

A Novel Technique for Modeling Non-Equilibrium Astrochemistry in Molecular Cloud Simulations

INAUGURAL-DISSERTATION

ZUR

ERLANGUNG DES DOKTORGRADES
DER MATHEMATISCH-NATURWISSENSCHAFTLICHEN FAKULTÄT
DER UNIVERSITÄT ZU KÖLN



vorgelegt von

Marco Panessa
aus New York, USA

Köln, 2023

Berichterstatter (Gutachter):

Dr. Daniel Seifried

Prof. Dr. Peter Schilke

Vorsitzender der Kommission:

Prof. Dr. Dennis Mücher

Examined on 3 May 2023

ABSTRACT

The interstellar medium (ISM) contains numerous chemical species whose distribution can give clues to how the ISM will evolve in time. However, modeling these species self-consistently in 3D-MHD simulations is computationally expensive, so simulations are generally restricted to species whose presence affects the thermal balance of the gas. This approach is cost-effective, but sacrifices the possibility of learning more about the ISM from the excluded species. This thesis presents a novel approach to post-processing the chemistry of 3D-MHD molecular cloud simulations. The approach uses the microphysics package KROME to post-process the chemical histories of massless tracer particles in four well-resolved 3D-MHD SILCC-Zoom simulations. After post-processing, the tracer data is used to reconstruct volume-filling density grids of species which have never been modeled in a self-consistent, time-dependent manner to date, due to their computational overhead. The modeling pipeline is applied in two papers to the molecular gas tracers HCO^+ and OH , the emission of which is associated with CO-bright and CO-dark molecular gas respectively. Unprecedented column density maps of these species at a spatial resolution of 0.125 pc are presented and shown to agree with observations. The time-dependent nature of the post-processing algorithm permits the analysis of the formation of HCO^+ and OH , in particular their peak abundance regimes and growth timescales. In conjunction with column density maps of H_2 , the extinction-dependent relationship between the densities of OH and H_2 can be mathematically fit from a 3D-MHD simulation for the first time. Finally, the potential application of this method to measuring the age of molecular clouds via studies of the deuterium fractionation in the gas is explored.

CONTENTS

1	INTRODUCTION	1
2	PHYSICS OF THE INTERSTELLAR MEDIUM	4
2.1	Components of the ISM	5
2.2	Heating and cooling processes	6
2.3	The multiphase model	9
2.4	Molecular clouds	9
2.4.1	Formation	10
2.4.2	Evolution	11
2.4.3	Destruction	12
2.4.4	Chemistry	13
3	SIMULATING THE CHEMISTRY OF THE ISM	16
3.1	Ideal Magnetohydrodynamics (MHD)	16
3.2	FLASH	18
3.2.1	Physics of the simulation	19
3.2.2	Chemical rate equations	20
3.2.3	Tracer particles	20
3.3	The SILCC simulations	21
3.3.1	SILCC-Zoom	22
3.4	Chemical post-processing	24
3.4.1	Post-processing paradigms	24
3.4.2	KROME	25
4	OVERVIEW OF RESEARCH	27
4.1	Notes Concerning Co-Authorship	28
4.1.1	Paper I	28
4.1.2	Paper II	29
4.2	Additional research	29
5	PAPER I	30
6	PAPER II	55
7	INVESTIGATING DEUTERIUM FRACTIONATION	76

7.1	Deuteration as a chemical clock	76
7.2	Role of post-processing	78
8	CONCLUSIONS AND OUTLOOK	83
A	POST-PROCESSING PIPELINE DESCRIPTION	87
A.1	POSTP.F90	87
A.2	REGRID.F90	91
A.3	Minor Routines	93
A.3.1	UNIFORM.PY	94
A.3.2	SNAPWRITER.F90	94
A.3.3	PROJECTOR.F90	95
B	THE STATISTICAL RIGOR OF THE TRACER POPULATION	96

1

INTRODUCTION

The question of what the heavens and the Earth are made of has vexed thinkers since antiquity. Classical philosophers concluded that because everything they could touch in daily life inevitably changed or decayed, while the heavens seemed to be cyclical and incorruptible, different laws of nature must apply to the earthly and celestial spheres. The sun, moon, planets, and stars were said to be composed of a 'quintessence' that was beyond human understanding. Conversely, earthly materials were composed of the four fundamental elements of air, earth, fire, and water, which could not be turned into each other. The element of earth was subdivided into categories like gold, iron, copper, and so on, their properties fixed immutably by a divine hand. Alchemists working to change one element to another were mysticists, their work more like magic than science.

In modernity, as technology and science advanced, we slowly learned that these simplistic and phenomenological descriptions of astronomy and chemistry were incorrect. The Danish observer Tycho Brahe recorded a supernova that appeared in the supposedly unchanging heavens, and proved that the Great Comet of 1577 was not an atmospheric occurrence but something farther away than the moon. Soon after these observations, Galileo observed the physical properties of objects in the solar system. The laws of motion put forward by Isaac Newton explicitly rejected the notion that the heavens obeyed different laws from Earth: our planet orbits the sun by the same force that keeps us fixed to the ground.

In the same decade that Newton first derived his Law of Gravitation, the German alchemist Henning Brand isolated the element phosphorus. This was the first new element discovered since antiquity, and it could be reliably produced by following a recipe, with no mysticism required. Over the following centuries, experimentalists discovered that numerous everyday materials were composed of a smaller list of isolated elements, each with characteristic properties. Mendeleev organized the elements according to these properties, and the empty spaces in this periodic table led to predictions about the properties of yet-undiscovered elements based on their neighbors. Finally, in the twentieth century, the field of quantum mechanics explained that all these seemingly-indivisible elements were built from different numbers and configurations of the same few fundamental particles.

These intertwined developments in astronomy and chemistry have led to the modern understanding of the nature of matter: everything visible in the universe is composed of the same basic particles, obeying one set of laws. These particles can gather in complex systems, from the small (life on Earth) to the largest imaginable (stars and galaxies), but we are now confident that Earth and human life were ultimately born from the same processes that produced the sun and all the stars in the sky. The question of where we came from can be answered with Carl Sagan's assertion, "We are made of star-stuff. We are a way for the universe to know itself."

CONTENTS OF THIS THESIS

The exact mechanisms by which stars and planets are born are topics of active and ongoing debate. Through observations of dense gas in the Milky Way and in other galaxies, we know that stars form via the conglomeration of gas into protostars, until their internal pressure rises enough to sustain energetic fusion processes. The elemental composition of stars is of great importance to their radiative properties and lifecycles. To understand the stars, therefore, we must understand the composition of the molecular clouds where stars form.

The temporal scales associated with molecular clouds and star formation far exceed the entire span of human existence on Earth, to say nothing of the length of time we have been able to observe molecular clouds with rigor. We cannot yet visit them for samples, and cannot wait long enough to watch them evolve in nature. Thus, we resort to modeling their physical and chemical evolution in simulations, using complicated numerical codes. However, self-consistently modeling the chemistry of molecular clouds can increase the difficulty of cloud simulations by orders of magnitude.

In this doctoral thesis, I offer a set of algorithms that I have developed in order to approach this tension between accuracy and computational expense. These algorithms sidestep the issue of properly modeling the chemistry everywhere inside a simulation at every timestep, instead using the abbreviated chemical models of the simulations as inputs to a set of routines which can then calculate a more robust chemical ecosystem. This is called "post-processing" the simulations.

This thesis contains two scientific papers for which I am the first author. The first, "The evolution of HCO^+ in molecular clouds using a novel chemical post-processing algorithm," (hereafter, Paper I) details and validates the post-processing pipeline which I built to address the aforementioned computational issues. This validation is performed by analyzing the formation, abundance, distribution, and time evolution of the molecule HCO^+ , which is found in the densest regions of molecular clouds. The second paper, "Tracing dark molecular gas in simulated clouds using post-processed non-equilibrium OH abundance," (hereafter, Paper II) applies the post-processing pipeline to multiple molecular cloud simulations to systematically characterize the distribution of the diffuse molecular gas tracer species OH, and relate it to the local density and observations of molecular hydrogen.

The organization of this thesis will be as follows. First, in Chapter 2, I will introduce the physics of the interstellar medium (ISM), where molecular clouds are found. This will include the components of the ISM (Section 2.1), the heating and cooling processes which impact the dynamics of the interstellar gas (2.2), the multiphase model of the ISM's density and temperature profiles (2.3), and finally the physics and chemistry of molecular clouds (2.4). Next, in Chapter 3, I will report on the essential computational concepts that underlie simulations of molecular cloud chemistry. This begins with an explanation of the equations and assumptions of ideal magnetohydrodynamics (MHD) in Section 3.1. This is followed with an explanation of the numerical code FLASH (3.2), which is used in the SILCC (3.3) and SILCC-Zoom (3.3.1) simulations. Finally, I summarize chemical post-processing (3.4) and the microphysics package KROME (3.4.2) which handles the chemical calculations in my work.

Chapter 4 introduces Paper I and Paper II, summarizing their findings and defining the extent of my coauthors' contributions to them. Chapter 5 contains Paper I, and Chapter 6 contains Paper II. To supplement the two papers, Chapter 7 intro-

duces the next scientific objective for my post-processing pipeline: learning how to infer the age of observed molecular clouds from measurements of their deuterium fractionation. Chapter 8 concludes the thesis and summarizes my results. Two appendices are attached thereafter. Appendix A details the various routines in the post-processing pipeline more fully than could fit into the papers, and Appendix B confirms the statistical rigor of the simulated particles which are the basic unit of my post-processing.

PHYSICS OF THE INTERSTELLAR MEDIUM

The visible universe contains some 200 billion galaxies ([Lauer et al., 2021](#)). Each contains up to hundreds of billions of stars, ranging from red dwarfs much smaller than our Sun, to supergiants containing tens of solar masses of matter. A significant portion of the universe's matter content is not found in stars at all. About 85% of the universe's matter is 'dark,' not interacting with electromagnetic waves in any discernible way and only detectable through its gravitational influence on galaxies' bulk motion and the radial velocities of their constituent stars ([Jarosik et al., 2011](#); [Planck Collaboration et al., 2014](#)). Almost all of the remaining 15% – so-called 'baryonic' matter – lies outside the star-forming regions of galaxies, in the diffuse circumgalactic medium or the extremely rarefied warm-hot intergalactic medium, where density can fall as low as $n \sim 10^{-6} \text{ cm}^{-3}$ ([Nicastro et al., 2008](#)).

The stars in the Milky Way contain 85–90% of the galaxy's visible matter, while the rest lies in the seemingly empty space between the stars: the 'interstellar medium' (ISM). This reservoir of gas provides the raw materials and environment necessary for star formation, a pivotal process in astrophysics. Studying the dynamical evolution of the ISM is essential to understanding both the evolution of the galaxy at large and the history and future of its stellar population.

Until the modern era, the concept that stars are physical objects which are born and die was not understood. Aristotle, for instance, insisted that the stars were perfect and unchanging, composed of aether or 'quintessence,' and orbited the Earth in circles ([De Caelo, 1995](#)). Even after the acceptance of the theory that stars are like our Sun except at a great distance, nobody could posit how stars shine (let alone how they might be formed) until ideas of nuclear fusion were developed. Theories of protostars remained theoretical until [Becklin and Neugebauer \(1967\)](#) observed an infrared blackbody source that barely emitted in visible wavelengths. Since then, we have observed a broad cross-section of protostars at various stages of formation, and have refined our theoretical models of their evolution.

The stellar lifecycle, particularly of very massive stars ($M > 8\text{--}10$ solar masses, M_{\odot}), plays a critical role in the long-term dynamics of the Milky Way and other galaxies. The formation and destruction of these massive stars regulate the composition and distribution of the gas and dust which compose the ISM. Because stars form via the coagulation of this gas and dust, they retain a signature of their birth environments. By linking the composition of massive stars observed today to the spectra of nearby sites of star formation, we can make deductions about the galaxy's past. By modeling how these stars affect the local ISM both during their lifetimes and in the course of their death, we can conjecture about the galaxy's future.

In this chapter, I will begin by introducing the components of the ISM, including its constituent matter, radiation environment, and forces and fields. Secondly, I will summarize the mechanisms by which the ISM temperature is regulated. The next section will introduce the canonical schema by which the ISM is divided into phases. Finally, I will explain in detail the dense regions known as molecular clouds, in particular their dynamical evolution and chemical contents.

2.1

COMPONENTS OF THE ISM

The interstellar medium is dominated by gaseous atoms and molecules. Hydrogen is the most common element in the universe, comprising some 90% of all atoms by number and 70% by mass (Draine, 2011). Its most common state in the Milky Way (filling 64% of the galaxy's ISM by volume) is as ionized H^+ , a bare proton. Another 31% of the ISM volume contains predominantly atomic H, with the remaining 5% containing the molecular form H_2 (Tielens, 2005).

The presence of H^+ can be readily traced by its H_α recombination emission (Tielens, 2005; Draine, 2011), and the presence of atomic H by the hyperfine 21 cm transition (Klessen and Glover, 2016). Conversely, observing H_2 in the ISM is difficult. Molecular hydrogen has no permanent electric dipole, and although it has a quadrupole moment, its transitions have a high excitation temperature compared to the temperature of the dense gas environment where H_2 is found. Because H_2 is usually indicative of the densities where star formation can occur, locating it is of paramount importance to understanding the dynamics of the galaxy. The best-studied approach is to discern which other chemical species are cospatially present alongside the H_2 , as further explored in Paper I (Chapter 5) and Paper II (Chapter 6).

Another 28% of the ISM mass consists of helium, which is generally inert (Kalberla and Kerp, 2009). The remaining 2% of the ISM mass comprises all the other, heavier elements, which are all categorized as 'metals' in astrophysical parlance. Practically all metals in the ISM were produced in thermonuclear processes inside aging or dying stars (rather than in primordial nucleosynthesis), and ejected into the ISM via stellar winds or supernovae (see Section 2.4.3). Despite the tiny proportionality of metals in the ISM, they play an unmistakable role in the thermal processes that regulate the temperature of the gas. Because of the aforementioned constraints on observing molecular hydrogen, detecting the spectral signatures of metal-bearing molecules is essential to understanding the composition of dense regions in the ISM (Wolfire et al., 2010; Smith et al., 2014; Li et al., 2015; Seifried et al., 2020).

In addition to its gas content, the ISM also contains particulates ranging in size from 50–2500 Å, collectively referred to as 'dust' (Draine and Lee, 1984; Weingartner and Draine, 2001). The total mass of these metal-bearing particles is about 1% of the ISM mass (Hildebrand, 1983; Klessen and Glover, 2016), and they include silicates, chondrites, water ice, and organic compounds like polycyclic aromatic hydrocarbons (PAHs). Despite their small mass contribution, the dust grains play a key role in dense regions of the ISM. Dust particles provide a large surface area on which chemical reactions can occur (van Dishoeck and Blake, 1998), including some that are disfavored in the gas phase. For instance, although two free hydrogen atoms can combine into H_2 in the gaseous ISM, the combination rate is too low to explain the observed molecular fraction. Hydrogen atoms can also stick to the surfaces of dust grains, where they have a much greater chance of finding each other and forming H_2 (Gould and Salpeter, 1963). These hydrogen molecules can then desorb from the grains and join the gas phase. Accordingly, we now understand most of the H_2 content in the ISM was formed via reactions on dust. Dust also readily absorbs incident radiation, providing significant shielding to the gas by preventing incoming high-energy photons from reaching the regions of highest density (Tielens, 2005).

The matter comprising the ISM is strongly influenced by ambient radiation. This radiation bath, collectively called the 'interstellar radiation field' (ISRF), ori-

ginates in numerous astrophysical processes (Draine, 2011). Very massive stars of the O- and B-type spectral class emit plentiful UV light, which can ionize hydrogen and dissociate molecules. The cosmic microwave background, with a frequency of $\sim 10^{10}$ Hz (corresponding to a blackbody temperature of 2.762 K), was released everywhere in the universe at the recombination epoch 360 kyr after the Big Bang, and fills all space with photons whose energy is around $\sim 10^{-3}$ eV (Fixsen and Mather, 2002, see also Penzias and Wilson 1965). Interstellar dust grains at the temperature of the ISM radiate with blackbody spectra peaking in the infrared regime. Nebulae also radiate, primarily in free-free bremsstrahlung and ionization lines of metals. Finally, the ISRF also contains radio waves from synchrotron emission and X-rays from very hot plasma and X-ray binaries.

When calculating the impact of the ISRF, we generally focus on the radiation with enough energy to dissociate molecular hydrogen or ionize atomic hydrogen (13.6 eV) (Tielens, 2005). The volumetric energy density of photons with energies between 4–13.6 eV is represented by the constant G_0 , which depends on local conditions. In the solar neighborhood, this is cited as $G_0 = 1.7$ in Habing units, for which 1 Habing is 5.29×10^{-4} ergs cm^{-3} (Draine, 1978). Closer to more energetic stars than in the solar neighborhood, the ISRF can be several orders of magnitude stronger.

The ISM is also filled with ‘cosmic rays’ (CRs). In 1912, Victor Hess discovered these were not emissions from Earth’s radioactive elements, but instead particles from space. Most cosmic rays consist of single protons, plus a small fraction of alpha particles (doubly-ionized helium nuclei), metal nuclei, and electrons (Draine, 2011; Klessen and Glover, 2016), accelerated to relativistic speeds by supernovae, active galactic nuclei, and other energetic sources. The energy distribution of CRs peaks around ~ 300 MeV, enough to ionize and/or dissociate any atom or molecule with which they interact. Since CRs have enough energy to penetrate even the densest gas in the ISM, they are usually modeled as a constant energy field which interacts with the interstellar gas at a ‘cosmic ray ionization rate’ (CRIR) between 10^{-17} – 10^{-14} s^{-1} , though work is ongoing to determine their attenuation profile toward density peaks (Gaches and Offner, 2018; Gaches et al., 2019).

Finally, the ISM is suffused with magnetic fields which affect the dynamical evolution of the interstellar gas (Crutcher et al., 1999; Bourke et al., 2001; Troland and Crutcher, 2008; Crutcher, 2012; Seifried et al., 2020; Ganguly et al., 2022). These fields exert a pressure which supports gas clouds against gravitational collapse on large scales, and deflect charged particles such as cosmic rays and ions like H^+ . In the solar neighborhood, the field strength is $\sim 5 \mu\text{G}$ (Crutcher, 2012), reaching higher values in denser gas. Though magnetic fields are invisible, we can detect their presence from the preferential alignment of elongated dust grains with the field lines, which polarizes background continuum sources; or Zeeman splitting of spectral features like the 21 cm atomic hydrogen hyperfine transition line.

2.2

HEATING AND COOLING PROCESSES

Numerous heating and cooling effects determine the thermal state of the ISM, the impact of each of which depends strongly on local parameters like the density and radiation environment. The net change in energy (per volume), \dot{u} , driven by all

heating and cooling processes is given by (Tielens, 2005):

$$\dot{u} = n^2\Lambda - n\Gamma, \quad (2.1)$$

where n is the number density, $n^2\Lambda$ is the net heating rate, and $n\Gamma$ is the net cooling rate. On large scales, the temperature gradient of the ISM is nonzero, driving dynamical movements in the gas.

Heating processes in the ISM can include:

- **Photoelectric heating.** Electrons on dust grains absorb UV radiation and become unbound in the gas phase, with a thermal velocity equal to the energy of the UV photon minus the grain's ionization barrier. These free electrons distribute their super-thermal kinetic energy to other gas particles through stochastic collisions, heating the environment overall (Draine, 1978; Bakes and Tielens, 1994; Wolfire et al., 2003). On the perimeter of dense regions in the ISM, the dust periphery 'self-shields' the dust deeper in the cloud, reducing the efficacy of photoelectric heating and permitting the survival of H₂ (Klessen and Glover, 2016).
- **H₂ dissociation.** An H₂ molecule is dissociated by UV radiation. The two free hydrogen atoms each gain kinetic energy equal to one-half times the difference between the energy of the UV photon and the dissociation barrier of H₂. This excess energy is distributed to the gas as heat by collisions. Each dissociation event contributes an average of 0.4 eV to the ISM (Black and Dalgarno, 1977; Draine and Bertoldi, 1996).
- **H₂ formation.** The combination of two hydrogen atoms is energetically favorable, freeing 4.48 eV per formed molecule (Goldsmith and Langer, 1978). This energy puts the H₂ in an excited vibrational or rotational state. Collisional de-excitation distributes this energy to the local gas, though the efficiency of this process is not well constrained (Klessen and Glover, 2016).
- **UV pumping.** An H₂ molecule is excited by incident radiation. The molecule de-excites by fluorescence of near-infrared photons, or preferentially by collisions if the gas density $n \gtrsim 10^3 \text{ cm}^{-3}$. Each pumping event contributes an average of 2 eV to the ISM (Burton et al., 1990; Klessen and Glover, 2016).
- **Photoionization.** Atomic hydrogen is ionized by photons with energy greater than 13.6 eV, with the excess acquired by the H⁺ as kinetic energy. Collisions with the gas distribute this energy as heat.
- **Cosmic ray heating.** In well-shielded dense gas, where the ISRF is attenuated, penetrating cosmic rays can still collisionally ionize and/or dissociate atoms and molecules. The products of these reactions gain enough excess kinetic energy from the collision that they can trigger secondary ionizations in the local gas (Glassgold and Langer, 1973; Dalgarno et al., 1999).
- **X-ray heating.** Like cosmic rays, X-rays can photoionize hydrogen and also deliver enough excess kinetic energy for secondary ionizations. However, because X-rays have significantly lower energy than cosmic rays, X-ray heating occurs in less dense gas than cosmic ray heating (Wolfire et al., 1995).
- **ISM dynamics.** Adiabatic compression of the ISM via gravitational instabilities or shocks dissipates the gas's bulk kinetic energy as heat to its constituent particles.

Opposing these heating effects, cooling processes in the ISM can include:

- **Permitted transitions.** In hot gas ($T \gtrsim 10^4$ K), electronic dipole transitions constitute a major source of cooling via the escape of high-energy photons. Cooling via Lyman- α emission (the de-excitation of an electron from the first excited state to the ground state) releases a UV photon with an energy of ~ 10.2 eV. In the temperature regime from 10^4 – 10^6 K, cooling lines from carbon and oxygen dominate, and then iron lines above 10^6 K (Gnat and Ferland, 2012).
- **Bremsstrahlung.** At even higher temperatures ($T < 10^7$ K), when iron is fully ionized, cooling is dominated by free-free bremsstrahlung between the electron population and ionized nuclei (mostly H^+) (Sutherland and Dopita, 1993).
- **Fine structure transitions.** Degeneracies between the energies of nuclear states can be broken by spin-orbit coupling, which can separate the states by $\sim 10^{-2}$ eV (Atkins and Friedman, 2011). Because these transitions are so low-energy, they can still occur in very cold gas ($T < 100$ K) where electronic transitions are disfavored. Fine structure transitions have low probability, but contribute significant cooling when other cooling avenues are restricted by temperature or shielding. Fine structure line emission is dominated by carbon and then oxygen (Wolfire et al., 1995; Glover and Mac Low, 2007; Glover et al., 2010).
- **H_2 rotational transitions.** Molecular hydrogen is found in some rotational quantum state defined by the rotational quantum number J . Transitions in which $J \rightarrow J \pm 1$ are strongly forbidden, so the lowest-energy permitted rotational transition is $J = 2 \rightarrow 0$, for which $\Delta E/k_B \simeq 500$ K. The energy barrier of the initial excitation limits the emissive cooling by these transitions in cold, dense gas (Hollenbach and McKee, 1979).
- **HD rotational transitions.** Unlike its isotopologue H_2 , the deuterated form HD has a permitted transition with $J = 1 \rightarrow 0$, for which $\Delta E/k_B \simeq 128$ K. Even though HD is rare compared to H_2 , HD provides more cooling than H_2 at $T < 50$ K due to this lower excitation barrier (Klessen and Glover, 2016).
- **CO rotational transitions.** The energy states of carbon monoxide are closely spaced with a small energy gap, so its emission can cool even very cold gas ($T < 20$ K). However, because CO only exists in well-shielded gas, its cooling efficiency is limited (Kramer et al., 1999; Goldsmith, 2001).
- **Dust cooling.** All dust grains radiate with blackbody spectra, peaking in the infrared. When gas and dust are thermodynamically coupled, energy distributed to the dust via collisions eventually radiates away as infrared photons. If the gas temperature is greater than the dust temperature, the system will seek equilibrium by increasing the dust temperature, ultimately cooling the whole system. This is particularly effective for cooling where $n > 10^5$ cm $^{-3}$ (Leung, 1975; Hollenbach and McKee, 1989; Goldsmith, 2001).

2.3

THE MULTIPHASE MODEL

The efficiencies of the heating and cooling processes of the ISM are temperature- and density-dependent. Over time, these processes sort the interstellar gas into ‘phases’ where the temperature and density occupy particular regimes. These phases are not entirely distinct. Inhomogeneities in the gas and dust distribution, and disruptive events like supernovae, can blur the boundaries between the phases as the gas seeks a new equilibrium. For this reason, to understand the ISM, the phases must all be considered together as parts of a whole, rather than cases to study in isolation.

Field et al. (1969) offered the first formal categorization of the phases of the ISM. They stated that if the gas is assumed to be neutral and in local thermal equilibrium, two phases result. The warmer phase, now called the Warm Neutral Medium (WNM), contains diffuse atomic gas with temperature $T \sim 10^4$ K and density $n \sim 1 \text{ cm}^{-3}$. The rest of the gas would be found in what is now called the Cold Neutral Medium (CNM), where $T \sim 100$ K and $n \sim 10\text{--}100 \text{ cm}^{-3}$. Gas between these temperature regimes was considered thermally unstable, gradually heating or cooling to the Warm or Cold phase.

In response to Field’s assumption of charge neutrality, McKee and Ostriker (1977) argued that energy injected into the ISM by supernova explosions would ionize the gas and raise the temperature. The resulting Hot Ionized Medium (HIM) would have $T \sim 10^6$ K and $n \sim 10^{-2} \text{ cm}^{-3}$, and due to the inefficiency of the available bremsstrahlung or iron cooling lines, would retain its temperature better than cooler gas that can cool via oxygen and carbon transitions. It has also been shown that the putatively neutral gas of the WNM can instead have a significant local ionization fraction due to collisions, detectable through galactic synchrotron absorption (Hoyle and Ellis, 1963), pulsar radio dispersion (Reynolds, 1989), and optical emission lines, such as from N^+ or O^+ (Reynolds et al., 1973; Mierkiewicz et al., 2006). This phase is called the Warm Ionized Medium (WIM).

Finally, the WNM can be profitably divided between the diffuse atomic gas (the modern definition of the WNM) and the denser, molecular gas, which clusters into ‘molecular clouds’ (MCs). These cold, dense agglomerations of gas ($n \gtrsim 10^2 \text{ cm}^{-3}$, $T \sim 10$ K) are the nurseries of star formation. By creating hot massive stars, MCs also set in motion the feedback effects like stellar wind and supernovae that ultimately destroy them, driving large-scale evolution in the density, temperature profile, and metallicity of the galaxy (Caselli et al., 1998; Wolfire et al., 2003).

2.4

MOLECULAR CLOUDS

All stars are born in molecular clouds. Therefore, to understand the life cycles of stars, we must understand the life cycles of molecular clouds, from formation all the way to destruction.

Descriptively, a molecular cloud is a region of the ISM with high density, low temperature, and (consequently) high molecular fraction. Most MCs contain between $10^3\text{--}10^7$ solar masses, with those containing more than 10^4 solar masses called ‘giant molecular clouds’ (GMCs) (Blitz et al., 2007; Murray, 2011; Dobbs et al., 2014). Typical clouds are about 100 pc wide, with many intricate substructures. It is now understood that clouds are composed of filaments, which are very dense tendrils

of gas ~ 0.1 pc in width and up to tens of parsecs long (Molinari et al., 2010; André et al., 2014). Overdense clumps of gas in these filaments undergo gravitational collapse into cores, some of which continue condensing into a protostar or a cluster of protostars. The gas and dust accumulated around the protostars is then cleared through a combination of condensation into planetesimals and protoplanets and radiative feedback from the star once it begins to shine. The feedback of the most massive stars ultimately destroys the cloud.

2.4.1

FORMATION

Matter in the ISM is always gravitationally self-attracted to a local center of mass. However, the infalling gas generates volume-crossing sound waves which impart an outward pressure that resists gravity. If the self-gravity is stronger than the force exerted by this pressure, the pressure will fail to support the gas against collapsing. The end result is a dense molecular cloud (Truelove et al., 1997; Tielens, 2005).

Because the outward pressure depends on non-scaling quantities like the density and sound speed, and the cloud's self-gravity grows with the spatial extent of the uniform density gas, the self-gravity will win if the gas agglomeration is wide enough. The critical radius is called the 'Jeans length,' λ_J , defined as:

$$\lambda_J = \sqrt{\frac{15}{4\pi} \frac{k_B T}{G m_p \mu \rho}}, \quad (2.2)$$

where k_B is Boltzmann's constant, G is the gravitational constant, m_p is the mass of a proton, μ is the mean molecular weight, and ρ is the cloud density. Modeling the gas as a sphere, we can define a corresponding Jeans mass M_J , greater than which a cloud will collapse:

$$M_J = \frac{4}{3} \pi \lambda_J^3 \rho = \frac{4}{3} \pi \left(\frac{15}{4\pi} \frac{k_B T}{G m_p \mu \rho} \right)^{\frac{3}{2}} \rho \quad (2.3)$$

For a given composition and temperature, a cloud smaller than λ_J is supported (Jeans, 1902; Tielens, 2005; Draine, 2011; Federrath et al., 2011). Since λ_J rises with temperature and declines with density, therefore, gas clouds which are cold and dense are most susceptible to form into molecular clouds, explaining the observed temperature and density profile of clouds in the Milky Way.

The timespan of MC formation is on the order of the freefall time t_{ff} , the time that a test mass dropped inward from the edge of the gas cloud would take to fall to the center of mass. This is given as (Tielens, 2005):

$$t_{ff} = \sqrt{\frac{3\pi}{32} \frac{1}{G \rho}}, \quad (2.4)$$

and for the average MC is ~ 1 Myr.

The given formulation of the Jeans instability criterion is an idealization, suffering in particular from not including the effects of supersonic turbulence, which seem to be ubiquitous in the ISM (see e.g. Zuckerman and Evans, 1974; Truelove et al., 1997; Walch et al., 2015).

2.4.2

EVOLUTION

Once the diffuse gas of the ISM condenses to form a molecular cloud, it does not continue condensing forever. The population of MCs in the galaxy follows a pair of size relations (Goldsmith and Langer, 1978), showing that the clouds we can observe seem to be constrained in their bulk properties. First, the masses M of observed MCs follow the relation (Solomon et al., 1987; Dame et al., 1987; Heyer and Dame, 2015):

$$\frac{dN}{dM} \propto M^{\eta_M}, \quad (2.5)$$

where N is the number of MCs, and η_M is the scaling index cited from -1.5 to -2.5 , depending on the H_2 distribution (Solomon et al., 1987; Heyer et al., 2001). Secondly, the sizes R of observed MCs follow the analogous relation:

$$\frac{dN}{dR} \propto R^{\eta_R}, \quad (2.6)$$

where the scaling index $\eta_R = -3.3$ to -3.9 (Heyer et al., 2001; Roman-Duval et al., 2010).

Because of these scale relations, the low observed star formation efficiency ($\sim 1\text{--}2\%$), and the lack of systematic redshift in MC spectra to indicate global collapse away from our point of view, Zuckerman and Evans (1974) rejected the notion from Goldreich and Kwan (1974) that MCs are continually condensing. Instead, they offer the theory of gravo-turbulent stability. This states that supersonic turbulence inside molecular clouds supports them against further collapse at the time that they reach the canonical density profile given by the scaling relations. Observed supersonic linewidths in MC spectra support the idea that the gas is in this turbulent motion. The repulsive kinetic pressure prevents densities in the cloud from approaching that of a prestellar core outside the narrow filamentary structures, explaining the low efficiency of star formation (see e.g. Mac Low and Klessen, 2004; McKee and Ostriker, 2007; Hennebelle and Falgarone, 2012).

More recently, others (e.g. Heitsch and Hartmann, 2008; Camacho et al., 2016; Vázquez-Semadeni et al., 2019, and more) have countered with the theory that molecular clouds actually are not supported against collapse. The theory of global hierarchical collapse instead posits that clouds are constantly condensing after all. Because different density regimes collapse at different rates, filaments and cores can quickly form in the heart of clouds while the external, diffuse medium collapses more slowly. Feedback from short-lived massive stars formed on the filamentary spatial scale arrests the collapse of the diffuse medium, keeping the star formation efficiency low, and eventually destroying the cloud before the diffuse medium can successfully condense. The global redshift whose absence was taken by Zuckerman and Evans (1974) as evidence of gravo-turbulent support may actually just be disguised by the highly inhomogeneous distribution of the gas.

Systematically assessing the age of observed molecular clouds might solve this mystery, since it seems clouds would be short-lived if the theory of global hierarchical collapse is true. The discovery of old clouds would argue in favor of internal support, presumably by turbulent pressure. However, measuring a developed cloud's age is not straightforward. Observations by Scoville and Hersh (1979) and Koda et al. (2009) of MCs crossing between spiral arms of the Milky Way and M51, respectively, indicate that these clouds must have an age on the order

of the inter-arm crossing time (~ 100 Myr). Conversely, plotting stars near small molecular clouds in the solar neighborhood on an Hertzsprung-Russell (HR) diagram gives ages on the order of only ~ 10 Myr (Elmegreen, 2000; Hartmann et al., 2001). Studies of molecular clouds in the PHANGS-ALMA survey by Chevance et al. (2020), meanwhile, find lifetimes as short as 1–5 Myr after the first massive stars appear.

With estimates for the ages of molecular clouds differing by orders of magnitude, the debate between gravo-turbulent support and global hierarchical collapse remains unresolved. Additional ways to measure the ages of clouds are still sought. One promising method could be to study the evolving ortho-to-para ratio of H_2 , gleaned from close examination of the rate of deuterium fractionation (Ceccarelli et al., 2014; Bovino et al., 2017; Giannetti et al., 2019; Bovino et al., 2021). For further explanation, as well as upcoming research I will undertake in this direction, see Chapter 7.

2.4.3

DESTRUCTION

Molecular clouds become victims of their own stars, destroyed through several processes categorized as ‘feedback.’ Most stars are small and do not disrupt the dynamics of their parent cloud. However, stars with mass $M \gtrsim 8 M_\odot$ are so luminous that their energy output can carve out ionized bubbles in the otherwise molecular gas. These stars’ deaths via supernovae can later destroy clouds completely. Feedback processes include:

- **Ionizing radiation.** Massive O- and B-class stars radiate $\sim 10^{53}$ ergs of ionizing Lyman continuum photons over their main sequence lifetimes (Vacca et al., 1996), surrounding themselves with HII regions in which all hydrogen takes the form H^+ . This region is idealized as the ‘Strömgren sphere,’ which extends to the distance from the parent star at which the ionization rate falls to equality with the recombination rate. Because MCs are inhomogeneous, HII regions generated by these stars are irregularly shaped and can extend farther than if the stars were isolated in a homogeneous medium. Excess energy in the Strömgren sphere (above the ionization threshold) is absorbed by the gas as heat, raising the pressure and pushing the cloud apart. This reduces the density, allowing destructive shocks and the effects of supernovae to even more efficiently disperse the cloud (Strömgren, 1939; Spitzer, 1978; Hanson et al., 2005; Murray, 2011).
- **Radiation pressure.** Photons with energy below hydrogen’s ionization barrier can still excite the gas outside the Strömgren sphere. The photons’ momentum may also drive a bulk momentum transfer to the cooler gas, though this is poorly constrained (Arthur et al., 2004; Sales et al., 2014). In diffuse gas, the momentum transfer effect would be minimal (Arthur et al., 2004; Krumholz and Matzner, 2009), but at the density of typical filaments ($n \gtrsim 10^4 \text{ cm}^{-3}$), it could drive turbulence that disrupts the gravitationally-bound substructures (Gritschneider et al., 2009).
- **Stellar wind.** Hot plasma and electrons in a star’s corona are accelerated by the corona’s very high temperature ($T \gtrsim 10^6 \text{ K}$), and expelled isotropically (Matzner, 2002; Krumholz, 2015). For very massive stars, this mass loss can amount to ~ 1 solar mass per Myr, at a velocity of $v \sim 2000 \text{ km s}^{-1}$, and a

total output of 10^{51} ergs over the star's short lifetime – comparable to a Type II supernova (Puls et al., 1996; Naab and Ostriker, 2017). As with ionizing radiation, the stellar wind increases local pressure and temperature while driving down density, dispersing the molecular gas.

- **Supernovae.** After running out of fusible hydrogen in their cores, very massive stars fuse a succession of heavier elements. This ends with iron, which is the first element (by atomic weight) not to release net energy via fusion. The core fusion terminates and the rest of the star collapses and rebounds explosively, in a core collapse or Type II supernova. The total energy released in a supernova is taken to be $\sim 10^{51}$ ergs, approximately as much as the star radiated in its whole lifetime. The surrounding medium is heated by the supernova's radiation and the kinetic energy of the expanding debris shell. The gas temperature reaches as high as 10^6 – 10^7 K, forming the Hot Ionized Medium (McKee and Ostriker, 1977). The energy injected into the cloud by a supernova is enough to disperse the gas (Iffrig and Hennebelle, 2015; Walch et al., 2015; Girichidis et al., 2016). Nevertheless, the supernova's shock front can continue to propagate elsewhere in the ISM and trigger turbulent instabilities in the local gas (Elmegreen and Scalo, 2004), setting in motion its condensation into new molecular clouds (Elmegreen and Lada, 1977; Wunsch et al., 2011).

2.4.4

CHEMISTRY

The chemistry inside molecular clouds is significantly more complex than the chemistry in the warmer, ionized ISM. The heavy radiation environment and high temperatures of the warmer and more diffuse ISM phases dissociates most molecules and ionizes most atoms into a plasma, producing a chemical ecosystem where relatively few processes need to be simultaneously accounted for. Because molecular bonds are delicate, the majority of them can only survive inside the relatively sedate environment of a molecular cloud. Inside molecular clouds, where $T \lesssim 50$ K and $n > 10^2 \text{ cm}^{-3}$, the conditions are right for electron recombination and the formation of a panoply of molecules. Since the first molecular detections in the ISM (Swings and Rosenfeld, 1937; Douglas and Herzberg, 1941), the number of species observed in the ISM has skyrocketed.

The defining feature of a molecular cloud is, tautologically, the presence of molecular gas. The H_2 density distribution is strongly correlated with the bulk density distribution of the molecular gas, since H_2 is by far the most common molecule (Glover et al., 2010). UV photons with $E > 13.6$ eV can ionize hydrogen and also have more than enough energy to photodissociate H_2 molecules (Tielens, 2005). Thus, H_2 will not survive unless it is shielded from the interstellar radiation field. The gas envelope of a molecular cloud is thick enough that radiation impinging upon its surface is depleted before it can penetrate too deeply and dissociate molecules closer to the local peaks of the density gradient. This 'self-shielding' of H_2 , as will be defined later in Eq. 3.10 in the simulation context (Glover et al., 2010; Walch et al., 2015), is essential to the long-term survival of molecular species.

The critical importance of the H_2 content in molecular clouds naturally raises the question of how H_2 forms. The simplest formation mechanisms are in the gas phase – for instance, via radiative association of two neutral hydrogen atoms or various ion-neutral reactions – but the reaction rates of these gas phase production

routes typically cannot sum to more than 1% of the total production rate that would be required to explain the observed molecular fraction in normal cloud conditions (Tegmark et al., 1997).

Instead, the most convincing argument is that H_2 is preferentially formed via the association of neutral hydrogen atoms on the surface of dust grains (Gould and Salpeter, 1963; Hollenbach and Salpeter, 1971). The complex physics underlying grain surface reactions require intensive modeling and the consideration of many disparate material factors. Generally, we can model the H_2 production rate R_G on grain surfaces as (Hollenbach and Salpeter, 1971; Hollenbach et al., 2009):

$$R_G = \frac{1}{2} \gamma v_H n_H n_d \sigma_d, \quad (2.7)$$

where γ is the proportion of successful hydrogen recombination, v_H is the (average) thermal velocity of hydrogen at the local temperature T_{gas} , n_H is the hydrogen number density, and the product $n_d \sigma_d$ (representing the product of the dust grain number density and the cross-section of interaction) is taken to be $2 \times 10^{-21} n_H$ following Hollenbach et al. (2009) and given a standard grain size distribution (Mathis et al., 1977). The H_2 is eventually desorbed from the grain and joins the gas phase.

In addition to providing a formation site for H_2 , dust grains also contribute significantly to the shielding of dense gas from the ISRF. Assuming a coupling between the dust and molecular gas distributions, the shielding contribution of the dust can be related to the total hydrogen column density $N(\text{H}_{\text{tot}})$ as in Draine and Bertoldi (1996):

$$A_V = (5.348 \times 10^{-22}) N(\text{H}_{\text{tot}}), \quad (2.8)$$

where A_V is called the visual extinction. This quantity describes the increase in apparent magnitude (i.e., dimming) imparted by foreground dust to a background emission source. In modern observations, A_V is used as a proxy for the local density, particularly in two dimensions. A 3D analogue of A_V is later employed (Section 3.2) to characterize the volumetric shielding of simulated gas in this work, but this distinction need not detain us for the moment, besides to note that these will be distinguished by their subscripts as $A_{V,2D}$ and $A_{V,3D}$.

Molecular hydrogen has enough shielding to survive by $A_V \simeq 0.5\text{--}1$, given typical cloud conditions. Unfortunately, as noted earlier, H_2 has no emission modes in the cold cloud environment. It cannot be observed directly. Instead, we must search for other molecules with detectable emission in molecular cloud conditions, and try to correlate their density regimes with that of H_2 . Historically, the principal choice for this has been carbon monoxide, CO, which is the next most common molecule after H_2 . It forms through a wide variety of pathways (Glover and Clark, 2012; Klessen and Glover, 2016), including a reaction chain beginning with the H_2 or the cosmic ray tracer H_3^+ , and then via reactions that produce other molecules like OH and HCO^+ . Other routes include through ionized hydrocarbons like CH_2^+ recombining with electrons to form CH and CH_2 , which can also be formed directly from neutral carbon at high densities.

Though CO can be produced through more distinctive pathways than H_2 can, the CO molecule is fragile. Photons with $E > 11.1$ eV can excite CO, which typically dissociates during the subsequent radiative decay (van Dishoeck and Black, 1988). The CO content depends on the shielding provided by the surrounding gas, and critically, by a surrounding H_2 envelope. This indicates that the molecular hydrogen is not spatially coincident with the CO distribution, since CO must be

surrounded by some molecular gas to survive. In terms of the visual extinction, CO is generally present when $A_V \gtrsim 3$. Thus, in the extinction range $A_V \simeq 1\text{--}3$, a molecular hydrogen envelope exists which cannot be traced by the emission of CO (van Dishoeck and Black, 1988; Wolfire et al., 2010; Valdivia et al., 2016; Gaches and Offner, 2018; Seifried et al., 2020). This ‘CO-dark’ gas can represent tens of percent of a molecular cloud’s H_2 content (Smith et al., 2014; Seifried et al., 2020), so CO emission alone cannot reliably reveal the extent (and thus the mass and density distribution) of a molecular cloud.

The search for alternative molecular gas tracer species is a topic of active debate. In this thesis, I focus on two candidates, the formyl cation HCO^+ (van Dishoeck and Black, 1988; Nikolic, 2007; Gerin and Liszt, 2021), and the hydroxyl radical OH (Weinreb et al., 1963; Wannier et al., 1993; Liszt and Lucas, 1996; Xu et al., 2016; Busch et al., 2019). Both species are present in some chief formation pathways of CO, and therefore trace the dense gas. HCO^+ in particular traces slightly denser gas than CO, and can be correlated with CO emission (Teague et al., 2015; Barnes et al., 2020; Yang et al., 2021). Conversely, OH has been observed at lower extinctions than are survivable for HCO^+ , and thus represents a promising tracer particularly of the CO-dark density regime (Neufeld et al., 2002; Allen et al., 2012, 2015; Li et al., 2015, 2018; Busch et al., 2019, 2021). The formation routes and density distribution of HCO^+ are explored thoroughly in Paper I, while the distribution and time evolution of OH are studied in Paper II.

SIMULATING THE CHEMISTRY OF THE ISM

Unlike the terrestrial sciences, astrophysics has few opportunities to perform experiments. The highest-quality vacuums on Earth still contain orders of magnitude more particles per volume than the interstellar medium. Molecular clouds in particular are hard to emulate in experiments on the ground, both due to the enormous spatial scale of their gravitational self-interaction, and the long temporal scale of their formation and evolution. The low speed of cloud evolution in human terms prevents us even from observing the evolution of a single cloud, instead restricting our data to current snapshots of a wide variety of molecular clouds and forcing us to deduce the sequence of evolutionary steps.

To understand the ISM, we instead rely on a cyclic loop of observations and simulations. Observations inform and constrain the parameters of simulations, the output of which is then examined for patterns that observers can later confirm or refute. Numerical simulations of the ISM are extremely complex and computationally expensive due to the number of forces and interactions involved, the long timescale of ISM evolution, and the wide domain of parameters of interest (e.g. density, which covers 25 orders of magnitude between the ISM and the interior of a star). Because of this complexity, we cannot afford to simulate the ISM with perfect accuracy.

A common sacrifice in ISM simulation is the accuracy of the chemical modeling in the gas. Solving the rate equations for a large number of chemical species in tandem with dynamically evolving the gas is quite expensive. Thus, simulations of ISM dynamics will, at best, run heavily simplified chemical networks ‘on-the-fly’ alongside the hydrodynamical calculations. These networks are often limited to the species relevant to the heating and cooling processes listed in Section 2.2. As such, additional information about molecular cloud evolution which could be learned from a more comprehensive set of chemical reactions is lost. Remedying this knowledge gap through the technique of chemical post-processing is the goal of this thesis and my ongoing work, as explored in Paper I and Paper II (Chapters 5 and 6).

Faithfully simulating the chemistry of the ISM requires a firm foundation in the principles of magnetohydrodynamics, in Section 3.1. Then, in Section 3.2, I will specifically outline the FLASH code underlying the SILCC (Section 3.3) and SILCC-Zoom (Section 3.3.1) simulations on whose data I performed my analyses. Lastly, in Section 3.4 I will explain the idea of chemical post-processing and the functionality of the KROME microphysics package, which underlies the post-processing code that I developed.

3.1

IDEAL MAGNETOHYDRODYNAMICS (MHD)

The ISM comprises an ensemble of unbound interacting particles. Each individual particle can be ascribed a trajectory, energy, and momentum as a function of time.

While the interactions among a small subset of particles could be simulated with ease, as the particle population grows to the number of particles contained within a region of the ISM, the computational difficulty becomes insurmountable. A useful simplification can be deployed to evade this issue. If we assume the ISM is in local thermal equilibrium and the mean free path of a particle is much shorter than the length scale of interest, we can model the ISM using the equations of fluid mechanics.

The generalized formation of fluid mechanics is found in the Navier-Stokes equations, which model viscous fluids (Landau and Lifshitz, 1959). In the astrophysical context, we can neglect viscosity, since the Reynolds number R of the ISM is estimated to be 10^5 – 10^7 (Elmegreen and Scalo, 2004), orders of magnitude greater than the regime where viscosity affects the fluid flow. Therefore, we can simplify further from the Navier-Stokes equations to the Euler equations for fluid flow (Choudhuri, 1998).

Assuming idealized conditions (see below), the four equations of ideal MHD are:

$$\frac{\partial \rho}{\partial t} + \nabla \cdot \rho \mathbf{v} = 0 \quad (3.1)$$

$$\frac{\partial \rho \mathbf{v}}{\partial t} + \nabla \cdot \left(\rho \mathbf{v} \otimes \mathbf{v} + \left(P + \frac{B^2}{8\pi} \right) \mathbf{I} - \frac{\mathbf{B} \otimes \mathbf{B}}{4\pi} \right) - \rho \mathbf{g} = 0 \quad (3.2)$$

$$\frac{\partial E}{\partial t} + \nabla \cdot \left((E + P) \mathbf{v} - \frac{(\mathbf{B} \cdot \mathbf{v}) \mathbf{B}}{4\pi} \right) - \rho \mathbf{v} \cdot \mathbf{g} - \dot{u} = 0 \quad (3.3)$$

$$\frac{\partial \mathbf{B}}{\partial t} - \nabla \times (\mathbf{v} \times \mathbf{B}) = 0, \quad (3.4)$$

which express the conservation respectively of mass, momentum, energy, and magnetic flux for a fluid element of density ρ , velocity vector \mathbf{v} , and total energy E . The magnetic field vector is \mathbf{B} , the gravitational acceleration vector is \mathbf{g} , the thermal pressure is P , and the net heating (or cooling) rate of the system is \dot{u} (see Equation 2.1). The magnetic divergence is set to zero ($\nabla \cdot \mathbf{B} = 0$) per Gauss's Law forbidding magnetic monopoles. E and P are respectively:

$$E = \frac{\rho v^2}{2} + \frac{B^2}{8\pi} + u \quad (3.5)$$

$$P = u(1 - \gamma), \quad (3.6)$$

where γ is the adiabatic index. Finally, the gravitational acceleration vector is found using Poisson's Equation:

$$\nabla^2 \Phi - 4\pi G \rho = 0, \quad (3.7)$$

where Φ is the gravitational potential and G is Newton's gravitational constant. In the ISM, Φ consists of the sum of the gravitational contributions from the self-gravity of the interstellar gas, point sources like stars and bound clusters, and an external galactic potential.

As stated above, the equations of ideal MHD require certain assumptions in order to be valid. In particular, they assume collisional coupling of the ions and neutral particles in the gas, and effectively infinite conductivity and zero resistance (Stahler and Palla, 2004). However, certain interactions of the interstellar gas with magnetic fields can violate these assumptions. In increasing order of the relevant

density regime, these interactions are as follows:

- **Ambipolar diffusion.** In the diffuse ISM, where the ionization fraction is high, the assumption that the magnetic field is well-coupled to the gas is reasonable. But in neutral atomic and molecular gas, ions are obviously rarer (Caselli et al., 1998; Goicoechea et al., 2009). This can decouple the magnetic field from dense gas in the hearts of clouds. As such, a numeric code using ideal MHD overestimates the magnetic support against collapse in dense neutral gas. This affects the density profile of simulated clouds around $n \gtrsim 10^6 \text{ cm}^{-3}$ (Mathis et al., 1977; Elmegreen, 1979).
- **Hall diffusion.** In dense gas, magnetic fields can drive ions perpendicular to both the field and the local current. This effectively introduces resistivity to the gas, violating the infinite conductivity assumption when $n \gtrsim 10^7 \text{ cm}^{-3}$ (Wardle, 2004).
- **Ohmic dissipation.** At very high gas densities, currents in the gas generated by changes in the magnetic field can experience resistive energy loss through heat, as in a circuit. This effect occurs at densities of $n \gtrsim 10^{11} \text{ cm}^{-3}$ (Nakano et al., 2002; Stahler and Palla, 2004).

These violations of the conditions of ideal MHD are important at the density regime of prestellar cores or protostars, but less so at the density regime of the broader molecular cloud, in which the density ranges between 10^1 – 10^6 cm^{-3} . Since this thesis focuses on the chemistry at the molecular cloud scale, the assumptions of ideal MHD are reasonable in this work.

Some further deviation from reality is expected not for nonideal physical reasons, but due to computational constraints. In particular, in a discretized numerical code as is used in this thesis, numerical discrepancies from the continuous solutions of the ideal MHD equations are inevitable. This can violate the $\nabla \cdot \mathbf{B} = 0$ condition. The simulations are run using the ES solver, which guarantees positive entropy and pressure. This will minimize but cannot eliminate these discretization errors (Derigs et al., 2016).

3.2

FLASH

The numerical code underlying the simulations analyzed in this thesis is FLASH 4.3, a highly parallelized, three-dimensional, magnetohydrodynamical code developed at the FLASH Center for Computational Science at the University of Chicago (Fryxell et al., 2000; Dubey et al., 2008). FLASH is a so-called ‘grid code,’ simulating a volume of interstellar gas by splitting it into cells which all report local parameters like the energy, momentum, and so on. This contrasts with codes based on smoothed particle hydrodynamics (SPH), which model a volume as a system of massive particles.

The simulation grid in FLASH is initialized with a particular resolution. As the simulation evolves, cells with high density are automatically subdivided into smaller, better-resolved cells. Each large cell can therefore contain progressively smaller ones, with the data saved in a ‘tree-like’ structure. This capability is called adaptive mesh refinement (AMR), and represents a compromise between modeling the physics with maximal resolution everywhere, and the reality that a globally

well-resolved simulation is unaffordable using contemporary computing methods (MacNeice et al., 2000).

3.2.1

PHYSICS OF THE SIMULATION

FLASH can employ a variety of tools and modules that enhance the fidelity of the simulated physics. First, the choice of Riemann solver for the grid depends on the presence or absence of a magnetic field. In the case of pure hydrodynamic simulations with no magnetic field, the MHD equations are solved using the directionally-split, five-wave Bouchut solver HLL5R with $\mathbf{B} = 0$ (Bouchut et al., 2007, 2010; Waagan et al., 2011). This solver ensures positive entropy and density even in highly supersonic gas flows. Magnetized MHD simulations instead use the ES solver, which can effectively minimize the discretization errors in the $\nabla \cdot \mathbf{B} = 0$ constraint described in the previous section (Derigs et al., 2016).

The gravity module calculates the gravitational force vector on each grid cell from three sources: an external potential, stellar object point sources in the domain, and the self-gravity of the gas. The external potential represents the influence of old halo stars, with no variations due to the presence of circumgalactic dark matter. The simulations in this thesis do not contain point source objects (e.g., sink particles), so the point source gravitational term will be dismissed going forward. The gas self-gravity is calculated using TreeRay, an OctTree solver which models gravity self-consistently within the hierarchical AMR data structure (Wünsch et al., 2018).

The Optical Depth module (Clark et al., 2012; Wünsch et al., 2018) in TreeRay calculates the attenuation of the interstellar radiation field (ISRF) in each cell (Habing, 1968; Draine, 1978). This is computed via the three-dimensional visual extinction $A_{V,3D}$ at each cell, by measuring the hydrogen column density $N(H_{\text{tot}})$ along n_{pix} equally-weighted directions (Górski and Hivon, 2011) as follows:

$$A_{V,3D} = \frac{-1}{\gamma} \ln \left(\frac{1}{n_{\text{pix}}} \sum_{i=1}^{n_{\text{pix}}} \exp(-\gamma A_{V,i}) \right), \quad (3.8)$$

where the factor γ is -2.5 (Bergin et al., 2004, and see also Glover and Clark 2012), $n_{\text{pix}} = 48$ in this work, and the unidirectional visual extinction $A_{V,i}$ is defined as (Draine, 1978):

$$A_{V,i} = \left(5.348 \times 10^{-22} \right) N(H_{\text{tot},i}) \quad (3.9)$$

The total attenuation due to dust in each cell is then $\exp(-\gamma A_{V,3D})$. The same calculation along n_{pix} sightlines is repeated with the column densities of H_2 and CO, to calculate the self-shielding contribution against the ISRF provided by those species. Specifically, the self-shielding coefficient f_{shield,H_2} is calculated as:

$$f_{\text{shield},H_2} = \frac{0.965}{(1 + x/b_5)^2} + \frac{0.035}{(1 + x)^{1/2}} \exp \left(-8.5 \times 10^{-4} (1 + x)^{1/2} \right), \quad (3.10)$$

where $x = N(H_2)/(5 \times 10^{14} \text{ cm}^{-2})$, $b_5 = b/(10^5 \text{ cm s}^{-1})$ (Glover et al., 2010), and b is the Doppler broadening parameter, $b = \sqrt{k_b T/m_H}$, with m_H being the mass of the hydrogen atom (Walch et al., 2015). The self-shielding coefficient for CO, $f_{\text{shield},CO}$, can be found tabulated in Lee et al. (1996) as a function of $N(H_2)$ and $N(CO)$, in Table 11.

3.2.2

CHEMICAL RATE EQUATIONS

At each hydrodynamic timestep, the FLASH code can also update values for the local chemistry simultaneously with the heating and cooling rates. This requires the preparation of a ‘chemical network,’ a self-consistent ecosystem of chemical reactions which controls the abundances of a set of included species. The following conservation equation is solved in each cell for each species i of density ρ_i :

$$\frac{\partial \rho_i}{\partial t} + \nabla \cdot (\rho_i \mathbf{v}) = C_i(\rho_i, T, \dots) - D_i(\rho_i, T, \dots), \quad (3.11)$$

where C_i and D_i are respectively the net creation and destruction rates of the species. The two sides are solved separately. First, the left side is solved as though the species’ abundance were a constant, or $C_i - D_i = 0$. Then the right side is solved as a set of coupled ordinary differential equations. Respectively, these solutions are:

$$\frac{\partial \rho_i}{\partial t} + \nabla \cdot (\rho_i \mathbf{v}) = 0, \quad (3.12)$$

$$\frac{d\rho_i}{dt} = C_i(\rho_i, T, \dots) - D_i(\rho_i, T, \dots) \quad (3.13)$$

Solving these sets of tightly-coupled, sparse, and stiff differential equations is extremely expensive with regard to computation time. For example, (Seifried and Walch, 2016) found that including even a limited chemical network in an idealized filament simulation using FLASH increased the computation time by a factor of 7, compared to including no network at all. Numerical ISM simulations are therefore usually run ‘on-the-fly’ with the simplest network possible. Because the heating and cooling effects of CO, C^+ , and oxygen play a pivotal role in the thermal (and subsequently dynamical) evolution of molecular clouds (van Dishoeck and Black, 1988; Wolfire et al., 2010; Glover and Mac Low, 2011; Bisbas et al., 2021), the on-the-fly network may include only enough reactions to properly model those species. The chemical network used on-the-fly in the reference simulations for this thesis is explained in Section 3.3.1.

3.2.3

TRACER PARTICLES

In conjunction with its grid calculations, FLASH can inject passive, massless ‘tracer particles’ into the computational domain. These tracers are not physical objects and do not affect the evolution of the interstellar gas in any way. Instead, they act like cameras released into the fluid flow, advecting with the gas by following the local velocity field at each dynamical timestep. They periodically record local simulation parameters like the density, temperature, and chemical abundances modeled in the on-the-fly chemical network.

To remedy the unphysical discontinuities that could otherwise result between the data of nearby tracers on either side of cell boundary, the tracers record data using a system called Cloud-in-Cell interpolation. This procedure models the tracer as occupying a space equal in size to one (local) cell, and saving a weighted average of the data in the grid cells that the tracer ‘cell’ is overlapping. This effectively gives the tracers a sub-grid resolution, which can be useful for resolving fluid flows in

very dense gas.

Released into a grid code domain, the tracers can follow the motion of gas ‘packets’ or fluid elements over time. The long-term gas flow dynamics in a simulation can be established by analyzing the tracers’ trajectories. Furthermore, by plotting the tracers’ trajectory in other dimensional spaces – for instance the space of $n(\text{HCO}^+)/n_{\text{H,tot}}$ vs. $A_{\text{V,3D}}$, as in Fig. 4 of Paper I – the complex chemical evolution of individual fluid elements can be understood. Finally, because the tracers save local chemical data over the entire lifetime of the simulation, their whole chemical histories can be post-processed in a time-dependent manner. This can unlock some information about the cloud chemistry which would be otherwise inaccessible, given the aforementioned computational constraints against running large networks on-the-fly.

The advection behavior of tracer particles does not perfectly match the behavior of the gas in all circumstances. For instance, Genel et al. (2013) show that ‘classical’ tracers of the sort used in FLASH have a tendency to accumulate in overdense regions. This property also reduces the tracer statistics in the diffuse gas outside those regions (see also Price and Federrath, 2010; Konstandin et al., 2012; Cadiou et al., 2019). Although reduced statistics do not affect the average properties of the remaining tracers which are not accumulated (see e.g. Ferrada-Chamorro et al., 2021), this increases the uncertainty of the distribution.

For more on tracer particles, see especially Section 2.2 in Paper I. For a study examining the effect of artificially reducing the tracer statistics on the ‘regridding’ code described in Paper I and also employed in Paper II, see Appendix B. I find among other things that even after randomly reducing the set of tracers used in regridding by 90%, the average abundances of H, H₂, C, CO, and C⁺ as a function of density remain consistent with the abundances found using the entire tracer population.

3.3

THE SILCC SIMULATIONS

The SILCC collaboration has produced a well-studied set of numerical simulations (Walch et al., 2015; Girichidis et al., 2016; Gatto et al., 2017, and more) which explore the evolution of the multiphase ISM. Based on the FLASH code, they employ rigorous physics modeling, AMR grid resolution, supernova feedback, an on-the-fly chemical network, and robust modeling of the heating and cooling processes in the interstellar gas. The simulations use a ‘stratified box’ setup with periodic boundary conditions, centered on the galactic midplane and covering a spatial domain of $500 \times 500 \times 5000$ pc. This domain is then evolved for ~ 100 Myr, to investigate the evolution of the ISM under solar neighborhood conditions (Walch et al., 2015).

Important parameters of the simulation are set as follows. The default resolution (before any mesh refinement) is set to 3.9 pc. At $t = 0$, the midplane density is set to $\rho_0 = 9 \times 10^{-24}$ g cm⁻³, with a Gaussian density profile of scale height 30 pc. The gas surface density is set to $\Sigma_{\text{gas}} = 10$ M_⊙ pc⁻². The stellar potential is set in accordance with a stellar surface density of $\Sigma = 30$ M_⊙ pc⁻², with a scale height of 100 pc. The metallicity is set to the solar fiducial value. In the gas phase, the fractional abundances (with respect to hydrogen) are set for helium to 0.1, carbon to 1.4×10^{-4} , and oxygen to 3.2×10^{-4} (Sembach et al., 2000). The ratio of gas mass to dust mass is 100:1.

The cosmic ray ionization rate (CRIR) for molecular hydrogen is set to $\zeta =$

$6 \times 10^{-17} \text{ cm}^{-1}$, without attenuation. The interstellar radiation field (ISRF) is set to a uniform strength of $G_0 = 1.7$ Habing units, as described in Section 2.1, and is attenuated using the Optical Depth module described in Section 3.2.1. In simulations including a magnetic field, the field is initialized along the x -direction, with $B_x = B_{x,0} \sqrt{\rho(z)/\rho_0}$ and a midplane magnetic field strength of $B_{x,0} = 3 \mu\text{G}$ in accordance with observations (Beck and Wielebinski, 2013). Supernovae are triggered in the ‘mixed driving’ configuration as discussed in (Walch et al., 2015), with half detonated at local density peaks, and half at random positions in the domain. The rate of supernova detonation is set in accordance with the gas surface density, as in the Kennicutt-Schmidt relation (Schmidt, 1959; Kennicutt, 1998).

3.3.1

SILCC-ZOOM

The SILCC simulations’ wide spatial extent provides fascinating models of the multiphase ISM on large scales, but due to resolution limits, the flagship SILCC setup is poor at modeling the intricacies of molecular cloud evolution. Since the characteristic width of a cloud is $\sim 100 \text{ pc}$, and the clouds contain star-forming cores in filaments with a width of $\sim 0.1 \text{ pc}$, the default SILCC resolution of 3.9 pc is insufficient to resolve the scale of star formation.

This gap in the SILCC model’s comprehensive ISM coverage is bridged by the SILCC-Zoom simulations. These simulations each reference the large-scale SILCC runs and re-simulate a patch of cold dense gas at a higher resolution, to more faithfully model the formation and evolution of molecular clouds. This thesis examines four such SILCC-Zoom simulations in detail, using their chemical histories and the aforementioned tracer particle capabilities of the FLASH code to reach new insights about the dense molecular gas. Two of the simulations are pure hydrodynamical (HD) runs without magnetic fields (originating in Seifried et al., 2017b), called MC1-HD and MC2-HD, and two full MHD runs (originating in Seifried et al., 2020), called MC1-MHD and MC2-MHD. All four simulations were rerun with some updates as explained in Seifried et al. (2021). Despite the similar names, these are four separate simulations with separate initial states.

The SILCC-Zoom simulations are initialized as follows. First, a SILCC simulation is evolved until cold and dense gas begins to coalesce. Isolated patches of dense gas are selected, so that the nascent cloud’s internal forces are the primary driver of its dynamical development. The simulation is then rewound to a time when the cloud’s density is around $\sim 10^1 \text{ cm}^{-3}$, now defined as $t_{\text{evol}} = t_0$. Next, the cloud is re-simulated at a higher resolution. Importantly, the cloud is evolved *in conjunction* with the surrounding multiphase ISM at the original SILCC resolution. Properly accounting for the evolution of the external gas has been shown to be critical to modeling the evolution of the dense cloud (Vázquez-Semadeni et al., 2000; Mac Low and Klessen, 2004; Brunt et al., 2009; Klessen and Glover, 2016; Seifried et al., 2017b).

Cells inside the SILCC-Zoom clouds are refined using a multi-step algorithm. First, a fixed region is defined (by eye) around the molecular cloud, measuring about $\sim 100 \text{ pc}$ in each dimension. This is the ‘zoom-in’ region, where the FLASH AMR process is permitted to increase the resolution above the initial SILCC limits. The simulation runs from t_0 , and the resolution in the zoom-in region is gradually refined through two methods. First, cells of increasing density are refined to a resolution of up to 0.5 pc , using the second derivative of the density field divided by

Table 3.1: The chemical species included in the NL99 network, which originated with [Nelson and Langer \(1999\)](#) with most recent updates by [Mackey et al. \(2019\)](#). The species CH_x and OH_x are defined as proxies for, respectively, simple hydrocarbons like CH, CH_2 , CH_3 , and similarly OH, H_2O , and so forth. The species M and its ionized state M^+ are proxies for metals like N, Mg, Si, S, and Fe.

e^-	H	H^+	H_2	He	He^+
H_2^+	H_3^+	O	O^+	OH_x	HCO^+
C	C^+	CO	CH_x	M	M^+

the average of the gradient ([Lohner, 1987](#)). These cells can then be further refined up to a resolution of 0.06 pc ([Seifried et al., 2021](#)), following the criterion that the local Jeans length (see Equation 2.2) is resolved by at least sixteen cells in each dimension ([Truelove et al., 1997](#); [Federrath et al., 2011](#)). At this resolution, filamentary structures can be resolved. The entire refinement process is performed in gradual steps until $t_{\text{evol}} = 1.65$ Myr, to suppress the development of spurious grid artifacts that would materially affect the gas evolution in a nonphysical way.

Originally, the SILCC-Zoom simulations were run using the chemical network (hereafter ‘NL97’) from [Nelson and Langer \(1997\)](#). In [Seifried et al. \(2021\)](#), the four simulations considered in this thesis were rerun, using instead the network ‘NL99.’ This network (an updated version of NL97) originated in [Nelson and Langer \(1999\)](#) ([Gong et al., 2017](#), and see also [Glover and Clark 2012](#)), with updates by [Glover et al. \(2010\)](#) and [Mackey et al. \(2019\)](#). Due to the computational expense of modeling chemistry on-the-fly as explained in Section 3.2.2, the NL99 network concentrates on modeling the abundances of C^+ , CO and atomic O, to account for these species’ thermal impact on the gas (see Section 2.2). The network resorts to numerous shortcuts and approximations to speed up its calculations, namely by not fully modeling some intermediate species in reactions that produce the aforementioned thermally-critical ones. Though NL99 succeeds at capturing most of the thermal impact on the gas from the chemistry, it has nothing – or at least, little that is trustworthy – to say about any number of other species of observational and theoretical interest. The list of included species is provided in Table 3.1. More details about NL99 can be found in Paper I, in Appendix A3.

A critical event of the SILCC-Zoom simulations for this thesis is the deployment of their massless tracer particles, as described in Section 3.2.3. The tracers are set loose to advect with the local gas flow, following it for ~ 4 Myr. The tracers are all injected in the simulations simultaneously at t_0 , in a uniform lattice spaced 1 pc apart. This lattice covers the entire zoom-in region evenly, plus extending outside the boundaries of the zoom-in region by 10 pc in each dimension. For the HD simulations considered in this thesis, this amounts to roughly 900,000 tracers. For the MHD simulations, which cover slightly larger spatial extents, this is roughly 2,000,000 tracers.

It can also be shown that the tracer population is large enough to statistically resolve chemical abundances across the whole density domain of the SILCC-Zoom simulations, following the application of the ‘regridding’ method explained in Section 5 of Paper I. In Appendix B of this thesis, I assess the statistical rigor of the tracer population by selecting 10% of them at random and following the entire post-processing and regridding pipeline using this subset. Repeating several validation tests from Paper I, I find negligible difference in the abundances and distribution

of major hydrogen- and carbon-bearing species when comparing the 10% subset to the full tracer population for each cloud.

3.4

CHEMICAL POST-PROCESSING

The high computational overhead of simulating robust chemical networks on-the-fly has driven a longstanding search for viable shortcuts. With the time and expense constraints on 3D-MHD simulations, these shortcuts take the general form of ‘post-processing’ the simulation’s dynamical, thermal, and (if applicable) limited chemical data. The local density, temperature, and chemical abundances are used to solve a system of reaction rate equations after the fact (see e.g. [Grassi et al., 2014, 2017](#)). This process is applied to a subset of data, like a spatial subdomain and/or a single snapshot, since post-processing the entire simulation would be no better in terms of computational expense than coupling the network to it on-the-fly.

3.4.1

POST-PROCESSING PARADIGMS

The simplest form of chemical post-processing is processing to equilibrium. This entails freezing the dynamical state of a simulation at a specific timestep, and using these frozen parameters to evolve a robust chemical network for a very long timescale, until chemical equilibrium is achieved (as in e.g. [Gong et al., 2018, 2020](#); [Li et al., 2018](#); [Keating et al., 2020](#)). There is no doubt that this technique is cheap and provides more information about ISM chemistry than the bare dynamical simulations ([Hu et al., 2021](#)), but because the chemical equilibrium timescale in the ISM is generally longer than the dynamical timescale, equilibrium post-processing can be gravely inconsistent with approaches that evolve the chemistry in a time-dependent way.

As an example of this inconsistency, [Hu et al. \(2021\)](#) find that in simulations of varying metallicity, the transition from atomic to molecular gas is a smooth gradient using time-dependent data, but becomes sharp when evolved to equilibrium. [Ebagezio et al. \(2022\)](#) and [Rybarczyk et al. \(2021\)](#) also show that the total abundances of H_2 and CO are overestimated by tens of percent at equilibrium compared to time-dependent results (see also Paper II, which finds the same). Even worse, the timescale of chemical equilibrium – shown in e.g. Paper II to be no less than 4 Myr for fiducially-parameterized SILCC-Zoom simulations – may exceed the lifetime of a molecular cloud altogether ($\sim 1\text{--}5$ Myr in [Chevance et al., 2020](#), or see also [Mac Low and Klessen 2004](#)), rendering equilibrium results moot.

Fortunately, non-equilibrium chemical modeling has mostly been accepted as a necessity in modern simulations, on scales ranging from galactic down to molecular clouds. Recent works employing non-equilibrium (or equivalently, time-dependent) chemical models include [Gnedin et al. \(2009\)](#); [Clark et al. \(2012\)](#); [Richings and Schaye \(2016\)](#); [Seifried and Walch \(2016\)](#); [Valdivia et al. \(2016\)](#); [Seifried et al. \(2017a\)](#); [Capelo et al. \(2018\)](#); [Lupi et al. \(2018\)](#); [Lupi and Bovino \(2020\)](#); [Hu et al. \(2021\)](#); [Ferrada-Chamorro et al. \(2021\)](#).

These works employ a wide variety of approaches to the problem of balancing the rigor of the post-processing against the computation time. In this thesis, I apply the strategy of post-processing the chemical abundances reported by the tracer particles inside SILCC-Zoom simulations (see Sections 3.2 and 3.3.1). These tracers

Table 3.2: The 39 chemical species included in my post-processing network, a modified version of `react_C0thin` as included in the `KROME` distribution (Grassi et al., 2017). The species `f-H2O` and `f-CO` represent `H2O` and `CO` frozen out onto dust grains, with their adsorption and desorption modeled as formation and destruction reactions.

e ⁻	H	H ⁺	H ⁻	H ₂	H ₂ ⁺	H ₃ ⁺
He	He ⁺	He ²⁺	C	C ⁺	C ⁻	C ₂
CH	CH ⁺	CH ₂	CH ₂ ⁺	CH ₃ ⁺	O	O ⁺
O ⁻	O ₂	O ₂ ⁺	OH	OH ⁺	H ₂ O	H ₂ O ⁺
H ₃ O ⁺	HCO	HCO ⁺	HOC ⁺	CO	CO ⁺	Si
Si ⁺	Si ²⁺	(f-H ₂ O)	(f-CO)			

represent consistent individual fluid elements in the grid throughout the simulation’s lifetime, recording the local dynamics as well as the on-the-fly chemistry. As such, the tracer histories can be individually post-processed in a fundamentally self-consistent way. Each tracer history is isolated, so post-processing them can be massively parallelized (as they were for Paper I) or done in batches to suit computational requirements. With appropriate statistical coverage from the tracers, the average values of dynamical parameters and (post-processed) chemical abundances can be recovered over the entire density range and temporal span of the simulation.

3.4.2

KROME

The post-processing algorithm applied to the tracer particles, as described in this thesis in Paper I and more thoroughly in Appendix A, employs the microphysics package `KROME` to calculate the time-dependent chemical evolution over the course of each tracer’s history. This package consists of a set of Python routines which take a user-provided chemical network and generate FORTRAN subroutines that can be coupled directly to simulation code, or to other user-generated routines as I have done. These FORTRAN subroutines provide stable solutions of the abundances of the chemical species included in the network, given a self-consistent ecosystem of formation and destruction reactions. The code flags charge and element conservation violations, as well as species which only have formation or destruction reactions (sources and sinks). Heating and cooling processes are modeled as well, to ensure the accuracy of the chemical models.

The chemical network given to `KROME` can be tuned to apply to the astrophysical problem of interest. Numerous networks are included in the package. In this thesis, I perform my post-processing exclusively using a slightly modified version of the `react_C0thin` network described in Grassi et al. (2014), including 37 gas phase species, two species representing `CO` and `H2O` which have frozen onto dust grains (with ‘formation’ and ‘destruction’ reactions modeling their adsorption and desorption respectively), and some 301 total reactions. Over the course of work for this thesis, a couple inconsequential errors in reaction rates were found and corrected. An audit of `HCO+` formation reactions performed during the writing of Paper I discovered that the reaction $\text{H}_2 + \text{CO}^+ \rightarrow \text{HCO}^+ + \text{H}$, as well as its counterpart reaction forming `HOC+`, were missing from the original network. This reaction is a dominant formation route for `HCO+` near the extinction boundary of the molecular gas (Sternberg and Dalgarno, 1995), necessitating adding it back in. The

full list of species in my post-processing network is given in Table 3.2, with further explanation (particularly of the freeze-out modeling) in Paper I, Appendix A1 and A2.

The high-order solver DLSODES (Grassi et al., 2013; Bovino et al., 2013) handles the matrix of rate equations associated with the formation and destruction routes in the network. The ordinary differential equation that solves for the net production rate of a species i with number density n_i is:

$$\frac{dn_i}{dt} = \sum_{j \in F_i} \left(k_j \prod_{r \in R_j} n_{r(j)} \right) - \sum_{j \in D_i} \left(k_j \prod_{r \in R_j} n_{r(j)} \right), \quad (3.14)$$

where F_i is the set of formation reactions for species i , D_i is the set of destruction reactions, R_j is the set of reactants in any one of the reactions j in F_i or D_i , $n_{r(j)}$ is the number density of a reactant r in a reaction from the set R_j , and k_j is the associated rate coefficient of each reaction. Thus, the rate of each reaction is equal to a rate coefficient times the product of the number densities of all reactants in that reaction. The left-hand term gives the sum of the formation reaction rates, and the right-hand term gives the sum of the destruction reaction rates, with dn_i/dt given by the difference of these.

These differential equations are very stiff, meaning small changes in the independent variables can cause large and unstable variations in the dependent variables, or equivalently, that the dependent and independent variables range over highly divergent scales (Press et al., 1992). Additionally, the solution matrix for these reactions can be very sparse in a realistic chemical network, with many values equal to zero, which affects the calculation of the Jacobian determinant needed to solve them. Reaching stable solutions of an interlinked set of stiff, sparse differential equations is a nontrivial problem. The KROME solver has proven very useful in approaching complex astrochemical questions (with early successes including Seifried and Walch, 2015; Schleicher et al., 2016; Grassi et al., 2017; Seifried et al., 2017a), validating its use as the mathematical engine of my chemical post-processing algorithm.

OVERVIEW OF RESEARCH

The following two chapters consist of two scientific articles which I wrote during the course of my doctoral studies:

THE EVOLUTION OF HCO^+ IN MOLECULAR CLOUDS USING A NOVEL CHEMICAL POST-PROCESSING ALGORITHM (PAPER I)

Coauthors: Daniel Seifried, Stefanie Walch, Brandt Gaches, Ashley Barnes, Frank Bigiel, Lukas Neumann

Summary: I introduce a novel post-processing scheme which I coded in FORTRAN, split into several modules. The SILCC-Zoom simulations contain tracer particles which record their local history. I post-process these histories with a robust chemical network, explaining in detail how the time-dependence is preserved. The tracer histories are then statistically examined, showing for instance the density regime of greatest HCO^+ formation. Then I explore HCO^+ formation routes, finding that the dominant formation reaction changes with visual extinction. I introduce a regridding algorithm which repopulates 3D density grids using the post-processed abundances of the relatively sparse tracer particles, and validate the accuracy of these grids. I produce column density maps of HCO^+ from these regridded results and compare them favorably to observations made by coauthors. Finally, I explore caveats and future steps.

TRACING DARK MOLECULAR GAS IN SIMULATED CLOUDS USING POST-PROCESSED NON-EQUILIBRIUM OH ABUNDANCE (PAPER II)

Coauthors: Daniel Seifried, Stefanie Walch

Summary: Using the same algorithms as Paper I, I systematically explore the abundance, distribution, and evolution of OH in four simulated SILCC-Zoom clouds. I examine the total mass of H_2 , CO, and OH in the clouds as a function of time, as a step towards tracing CO-dark gas with OH. Next I display the first self-consistent time-dependent column density maps of OH, and explore the characteristics of an MHD filament from one of these maps. I examine how the cumulative mass of OH and H_2 below various density thresholds changes as a function of time in the four clouds, in both 2D and 3D. Then I determine how the dark gas fraction relates to the extinction and the local OH content. With this information, I reject the use of $N(\text{OH})$ alone as an adequate tracer over a wide range of $N(\text{H}_2)$ which is consistent with the dark gas. However, I find that the ratio $N(\text{OH})/N(\text{H}_2)$ vs. visual extinction is time-invariant at CO-dark extinctions, providing a route to determine $N(\text{H}_2)$ if $N(\text{OH})$ and A_V are known. An equation is fit to $N(\text{OH})/N(\text{H}_2)$ vs. $A_{V,2D}$ in the diffuse molecular gas. Finally, the principal formation and destruction reactions for OH are examined.

These papers work to answer some of the questions previously raised in this thesis:

1. How do molecular clouds evolve chemically in time?
2. What can we infer about molecular cloud evolution from the distribution of its constituent chemical species, e.g. HCO^+ and OH ?
3. How well can alternative tracer candidate species like OH trace the limits of the CO-dark molecular gas?
4. How important is the pursuit of time-dependent chemistry compared to simpler equilibrium chemistry?

These questions are too great in scope to be answered by these papers alone. However, it is my hope that these works contribute to the debate and development in the field of astrochemistry.

To supplement the overview and validation of my post-processing code, especially the validation methods presented in Paper I, two appendices are attached to this thesis. The first (Appendix A) outlines the routines and subroutines which comprise my post-processing pipeline, in significantly greater detail than would fit in a scientific paper. Understanding the code in this level of detail is not necessary for appreciating its scientific output, but these descriptions are included for technical completeness.

The second appendix (Appendix B) explores the statistical rigor of the number of available tracer particles whose post-processed abundances provide the foundation of the regridding scheme laid out in Section 5 of Paper I. In that appendix, I find that even when the number of tracers is reduced by a factor of 10, the post-processing and regridding methods both continue to give valid results that are consistent with the results of the full tracer population. Reducing the tracer statistics increases the convergence time of the regridding algorithm but does not notably affect either the total mass of various species, or their distributions in either 2D or 3D.

4.1

NOTES CONCERNING CO-AUTHORSHIP

I am the first author on Paper I and Paper II, but both papers have been improved by contributions from coauthors. In this section, I will define the elements of the papers where my coauthors bear some responsibility.

4.1.1

PAPER I

- I wrote all text in the body of the paper, as well as all the appendices except Appendix A2 (Freeze-out), which was written by DS. Every figure is my own creation, and when those figures include data from other works, it is cited.
- All of the algorithms described in the paper are my creation, though they were developed in consultation with DS.
- The SILCC-Zoom data originates in [Seifried et al. \(2017b\)](#) and [Seifried et al. \(2020\)](#), with changes in accordance with the descriptions in [Seifried et al. \(2021\)](#).

- The KROME microphysics package originates from [Grassi et al. \(2014\)](#), and the YT Python package is an open-source distribution managed by the YT Project at <https://yt-project.org/>
- Data in Fig. 17 (a scatterplot of $N(\text{HCO}^+)$ vs. $N(\text{H}_2)$), namely the column density observations of HCO^+ in the W49A star-forming region, were specifically provided by FB and AB from the observations detailed in [Barnes et al. \(2020\)](#), following essential processing by LN.
- Comments and feedback provided especially by DS, as well as SW, BG, FB, and AB, were essential to the paper's development.

4.1.2

PAPER II

- I wrote all the text in the body of the paper, as well as all the appendices. Every figure is my own creation, and when those figures include data from other works, it is cited.
- All of the algorithms described in the paper are my creation, though they were developed in consultation with DS.
- The SILCC-Zoom data originates in [Seifried et al. \(2017b\)](#) and [Seifried et al. \(2020\)](#), with changes in accordance with the descriptions in [Seifried et al. \(2021\)](#).
- The KROME microphysics package originates from [Grassi et al. \(2014\)](#), and the YT Python package is an open-source distribution managed by the YT Project at <https://yt-project.org/>
- Comments and feedback provided by DS were essential to the paper's development.

4.2

ADDITIONAL RESEARCH

Following the two papers, I present another chapter exploring the topic of determining the age of molecular clouds through studies of their deuterium fractionation. This is a highly time-dependent problem requiring an advanced chemical network, and is not remotely feasible to study on-the-fly in 3D-MHD simulations given present-day computational constraints. Therefore, it makes an excellent science application for the methods that I introduce and explore in Papers I and II. I outline the scope of the chemical problem at hand, and explain the necessary features of a chemical network which my post-processing algorithm could apply to the SILCC-Zoom tracer particles.

The evolution of HCO^+ in molecular clouds using a novel chemical post-processing algorithm

M. Panessa,^{1*} D. Seifried,¹ S. Walch,¹ B. Gaches,^{1,2} A. T. Barnes,³ F. Bigiel,³ L. Neumann³

¹ Universität zu Köln, I. Physikalisches Institut, Zùlpicher Str. 77, 50937 Köln, Germany

² Department of Space, Earth & Environment, Chalmers University of Technology, SE-412 96 Gothenburg, Sweden

³ Argelander-Institut für Astronomie, Universität Bonn, Auf dem Hügel 71, 53121, Bonn, Germany

Accepted XXX. Received YYY; in original form ZZZ

ABSTRACT

Modeling the internal chemistry of molecular clouds is critical to accurately simulating their evolution. To reduce computational expenses, 3D simulations generally restrict their chemical modeling to species with strong heating and cooling effects. These simulations can be post-processed using more extensive chemical networks, but this approach usually evolves the chemical abundances to equilibrium. Time-dependent information about the evolution of species’ abundances is therefore lost. We address this gap by post-processing tracer particles in the SILCC-Zoom molecular cloud simulations. Using a chemical network of 39 species and 301 reactions (including freeze-out of CO and H_2O), and a novel iterative algorithm to reconstruct a filled density grid from sparse tracer particle data, we produce time-dependent density distributions for various species. We focus upon the evolution of HCO^+ , which is a critical formation reactant of CO but is not typically modeled on-the-fly. We analyse the evolution of the tracer particles to assess the regime in which HCO^+ production preferentially takes place. We find that $\sim 90\%$ of the HCO^+ content of the cold molecular gas forms in situ around $n_{\text{HCO}^+} \simeq 10^3\text{--}10^4\text{ cm}^{-3}$, over a time-scale of approximately 1 Myr. The remaining $\sim 10\%$ forms at high extinction sites, with minimal turbulent mixing out into the less dense gas. We further show that the dominant HCO^+ formation pathway is dependent on the visual extinction, with the reaction $\text{H}_3^+ + \text{CO}$ contributing 90% of the total HCO^+ production flux above $A_{V,3D} = 3$. Using our novel grid reconstruction algorithm, we produce the very first maps of the HCO^+ column density, $N(\text{HCO}^+)$, and show that it reaches values as high as 10^{15} cm^{-2} . We find that 50% of the HCO^+ mass is located in an A_V -range of $\sim 10\text{--}30$, and in a density range of $10^{3.5}\text{--}10^{4.5}\text{ cm}^{-3}$. Finally, we compare our $N(\text{HCO}^+)$ maps to recent observations of W49A and find good agreement.

Key words: ISM: clouds – ISM: molecules – methods: numerical – astrochemistry – stars: formation

1 INTRODUCTION

Astrophysical simulations have benefited enormously from modern advances in available computing power. Recent studies have shown that self-consistently tracking the chemical makeup of a molecular cloud is indispensable to understanding the cloud’s evolution (Walch et al. 2015; Girichidis et al. 2016). In particular, the abundances of common species like atomic carbon and carbon monoxide (CO) influence the cooling and heating rates via their line emission, in turn impacting the bulk dynamics of the cloud (van Dishoeck & Black 1988; Wolfire et al. 2010; Glover & Mac Low 2011; Bisbas et al. 2021).

Unfortunately, modeling the time-dependent chemistry of molecular clouds is both computationally expensive and theoretically challenging due to the sparsity and stiffness of the associated rate equations (Grassi et al. 2014). For instance, Seifried & Walch (2016) find that in a highly idealized filament simulation, the on-the-fly implementation of a chemical network of 37 species which self-consistently solves the CO abundance lengthens the computing time

by up to a factor of seven, compared to implementing no network at all. As such, the gas dynamics in molecular cloud simulations are typically coupled to extremely simple networks, or the chemistry is not even computed on-the-fly (Li et al. 2018; Gong et al. 2018, 2020; Keating et al. 2020). These minimal networks are restricted to the species which most strongly impact the cloud’s thermal state, with particular emphasis on modeling the abundance of CO through a limited ecosystem of reaction rates (see e.g. Nelson & Langer 1997, 1999; Glover & Clark 2012; Walch et al. 2015; Seifried et al. 2017a; Mackey et al. 2019; Hu et al. 2021).

While these networks suffice to model the bulk evolutionary dynamics of cold gas, they sacrifice the ability to study species which are dynamically less important but whose abundances and evolution could nevertheless supply further information about the molecular cloud. An example of a scientific question which restricted chemical networks cannot satisfactorily answer is the best way to trace ‘CO-dark’ molecular gas. The greater photodissociation energy of H_2 relative to CO causes the formation of an extended envelope of molecular hydrogen outside the denser regions in which CO can survive (van Dishoeck & Black 1988; Wolfire et al. 2010; Valdivia et al. 2016b; Gaches & Offner 2018). This envelope of H_2 , which

* panessa@ph1.uni-koeln.de

cannot be traced by CO emission, can represent several tens of percent of the cloud’s molecular hydrogen by mass (Wolfire et al. 2010; Smith et al. 2014; Seifried et al. 2020). Simulations using restricted chemical networks can model the CO-dark molecular gas, but cannot suggest alternative tracers for the molecular hydrogen due to the paucity of other species included in the network.

Because time-dependent networks are so costly to run on-the-fly, chemical post-processing is the chief way to investigate astrochemical problems. Typically, post-processing is performed by evolving a network to equilibrium given a set of fixed environmental parameters. But deferring analysis until equilibrium precludes any understanding of how the dynamical evolution of the cloud environment affects the chemistry.

Several recent works have performed time-dependent chemical post-processing of astrophysical simulations, specifically to correct for the shortcomings of the equilibrium approach. For instance, Ebagezio et al. (2022) compare time-dependent chemical data from SILCC-Zoom simulations of molecular clouds to the chemical outcome if the clouds are evolved to equilibrium. They find that evolving until equilibrium overestimates the total mass of H₂ and CO by up to 110 and 30 percent, respectively. The earlier in a cloud’s dynamical lifetime that its chemistry is evolved to equilibrium, the less accurate are the final abundances. The distribution of species has also been shown to differ between equilibrium and non-equilibrium results by Hu et al. (2021). They post-process a simulation using time-dependent chemistry, and find that the transitions between the ionized, atomic, and molecular gas phases are more shallow and gradual with time-dependent processing than when the chemistry is evolved to equilibrium. Ferrada-Chamorro et al. (2021), meanwhile, post-process the chemistry of a 3D-MHD simulation of a collapsing pre-stellar core. They account for the dynamical evolution of the simulation by post-processing abundances associated with passive tracer particles, which are free to advect with local density gradients in the gas. However, these simulations are isothermal and limited in size, and not run with any coupled chemistry network.

To accurately model the time-dependent chemistry of the multi-phase ISM on the scale of tens of parsecs, a simulation must be coupled to at least a simple network modeling the production of CO, such as discussed in Nelson & Langer (1997), Nelson & Langer (1999), Glover & Mac Low (2007a), Glover et al. (2010), and Glover & Mac Low (2011). Modeling a robust chemical network in the ISM requires an algorithm which accounts for the bulk motion of the gas, in a simulation which itself was already coupled to a simpler time-dependent network. Works which have made steps in this direction include Gnedin et al. (2009); Clark et al. (2012); Richings & Schaye (2016); Seifried & Walch (2016); Valdivia et al. (2016b); Seifried et al. (2017a); Capelo et al. (2018); Lupi et al. (2018); Lupi & Bovino (2020) and Hu et al. (2021).

We present here a novel, time-dependent chemical post-processing scheme, intended for the analysis of 3D magnetohydrodynamic (MHD) simulations. Although we apply the method here specifically to molecular clouds with masses of approximately $10^5 M_{\odot}$ over a timespan around 4 Myr, it could be further applied to any astrophysical simulation of arbitrary domain size or simulation timespan which includes passive tracer particles. We showcase the technique using a chemical network of 39 species and 301 reactions which is based on the network in Grassi et al. (2017), but the chemical network could also be of arbitrary size, provided all the included species are modeled comprehensively. Our method uses KROME (Grassi et al. 2014) to return the time-dependent density of every species in the chemical network, down to the scale of the individual gas elements associated with the simulation’s tracer particles. We additionally propose

an algorithm for recovering the density distribution over the entire domain for any species modeled in the post-processing network.

We validate each step of our methodology by investigating the non-equilibrium evolution of the formyl cation HCO⁺, a critical formation reactant of CO (van Dishoeck & Black 1988; Nikolic 2007; Gerin & Liszt 2021). These species generally share a density regime, with HCO⁺ most effectively tracing slightly denser gas than CO does (see e.g. Teague et al. 2015; Barnes et al. 2020; Yang et al. 2021; Jacob et al. 2022). Because the presence of HCO⁺ can regulate the production of CO, a deeper understanding of HCO⁺ evolution is critical to refining models of CO. However, HCO⁺ is not generally modeled on-the-fly in simulations. Therefore it is an excellent choice to showcase the scientific value of non-equilibrium chemical post-processing.

This paper is organized as follows. In Section 2, we summarize the initial conditions of the reference simulations, as well as the mechanics of their passive tracer particles and the limited chemical network which was coupled to the simulations. In Section 3, we discuss our more robust chemical network and the post-processing methodology. We then analyse the time-dependent evolution of the post-processed tracer abundances in Section 4, with the motivating example of the evolution of the dense-gas tracer HCO⁺. The algorithm for constructing a three-dimensional density grid from a snapshot of tracer abundances is explained in Section 5, and we present HCO⁺ column density maps and compare them to observations. Some caveats and opportunities for future improvements are outlined in Section 6. Finally, in Section 7 we summarize our work and briefly discuss potential future applications of our methodology.

2 THE SIMULATIONS

In this work, we apply our chemical post-processing methodology to four SILCC-Zoom simulations, part of the SILCC collaboration (Walch et al. 2015; Girichidis et al. 2016; Gatto et al. 2017). The two hydrodynamic (HD) simulations used here were first introduced in Seifried et al. (2017b), and later the MHD simulations in Seifried et al. (2020), with modifications to their original form described by Seifried et al. (2021). We will summarize here the details of these simulations most salient to the post-processing.

2.1 The reference simulations

The SILCC simulations model a part of a galactic disk with solar neighbourhood conditions using a stratified box centred on the galactic midplane. This box measures 500 pc × 500 pc × ±5 kpc, with a starting resolution of 3.9 pc. Particular subvolumes are selected for their propensity to form molecular clouds. Once these regions reach a density of $n \sim 10 \text{ cm}^{-3}$, they are then re-simulated with a higher resolution. These higher-resolution subvolumes (hereafter ‘zoom-in regions’) are simulated in tandem with the surrounding multi-phase ISM.

The SILCC-Zoom simulations are run using the adaptive mesh refinement (AMR) code FLASH v. 4.3 (Fryxell et al. 2000; Dubey et al. 2008). The zoom-in regions measure approximately 100 pc in each dimension, located within the broader SILCC domain. The full domain evolves for a startup time $t_0 = 11.9$ Myr for the HD clouds and $t_0 = 16.0$ Myr for the MHD clouds, after which the zoom-in process begins. The resolution inside the zoom-in region progressively increases to a maximal refinement of 0.06 pc over a total time of 1.65 Myr, to suppress the development of spurious turbulent grid artefacts. Outside the zoom-in regions, the broader simulation

continues at the initial resolution. In this paper, whenever we refer to an elapsed time value for a particular snapshot of a molecular cloud simulation, we expressly mean the time $t_{\text{evol}} = t - t_0$, or the time since the beginning of the simulation's zoom-in refinement.

The global parameters of the SILCC simulations are set to solar neighbourhood fiducial values as follows. At the galactic midplane, the bulk density is $\rho_0 = 9 \times 10^{-24} \text{ g cm}^{-3}$, in a Gaussian profile with a scale height of 30 pc transverse to the x-y plane. The gas surface density is set to $\Sigma_{\text{gas}} = 10 M_{\odot} \text{ pc}^{-2}$. Supernovae throughout the simulation volume are triggered in the 'mixed driving' configuration described in Walch et al. (2015) and Girichidis et al. (2016) until the zoom-in refinement begins at t_0 , at which point the supernova driving is deactivated altogether.

The cosmic ray ionization rate (CRIR) for molecular hydrogen is set to a constant value of $\zeta = 6 \times 10^{-17} \text{ s}^{-1}$, and the strength of the interstellar radiation field (ISRF) is set to the value of the Draine field (Draine 1978), which is $G_0 = 1.7$ in Habing units (Habing 1968). Attenuation of the ISRF is calculated using the TREE-RAY/OPTICAL-DEPTH module (Clark et al. 2012; Wünsch et al. 2018) with respect to the column densities of H₂, CO, and the dust distribution. This routine assigns each cell a three-dimensional visual extinction $A_{V,3D}$ by measuring the total gas column density $N(\text{H}_{\text{tot}})$ along n_{pix} equally-weighted sight lines (Górski & Hivon 2011), and then calculating:

$$A_{V,3D} = \frac{-1}{\gamma} \ln \left(\frac{1}{n_{\text{pix}}} \sum_{i=1}^{n_{\text{pix}}} \exp(-\gamma A_{V,i}) \right), \quad (1)$$

where each of the n_{pix} unidirectional extinction magnitudes are given by $A_{V,i} = (5.348 \times 10^{-22}) \times N(\text{H}_{\text{tot},i}) \text{ cm}^2$ (Draine & Bertoldi 1996), $\gamma = 2.5$ (Bergin et al. 2004, see also Glover & Clark 2012), and $n_{\text{pix}} = 48$ in the simulations used in this paper. Attenuation due to dust at a cell is then given by $\exp(-\gamma A_{V,3D})$. The self-shielding of H₂ and CO are analogously computed from those species' respective column densities.

The simulations are coupled on-the-fly to the chemical network first presented in Nelson & Langer (1999) (see also Glover & Mac Low 2007a,b; Glover & Clark 2012; Gong et al. 2017), which has been updated in accordance with Mackey et al. (2019). This network (hereafter 'NL99') contains only a few hydrogen and carbon species, and consolidates all metals (principally Si and Si⁺, by abundance) into the neutral and ionized placeholders M and M⁺. The full list of species in this network is provided in Appendix A3. The NL99 network's primary objective is to calculate the abundances of CO, C⁺, and O so that their heating and cooling contributions can inform the dynamical evolution of the gas.

We applied our post-processing scheme to four SILCC-Zoom simulations, two each including and not including magnetic fields, which originated in separate magnetized and unmagnetized SILCC runs. The two purely hydrodynamic (HD) clouds were first explored in Seifried et al. (2017b), and updated in Seifried et al. (2021) with a greater maximum refinement and the application of the chemical network derived from Mackey et al. (2019) instead of a precursor network (Nelson & Langer 1997). We denote these two simulations MC1-HD and MC2-HD. The two magnetohydrodynamic (MHD) clouds, which have also been updated in Seifried et al. (2021), originated in Seifried et al. (2020); we denote them MC1-MHD and MC2-MHD. Despite the similarities in their names, these are four separate simulations, evolved independently from the beginning of their runs. In the MHD simulations, the magnetic field was unidirectional and initialized at $B_x = B_{x,0} \sqrt{\rho(z)/\rho_0}$, where the mid-

plane magnetic field $B_{x,0} = 3 \mu\text{G}$, following observations (Beck & Wielebinski 2013).

2.2 Tracer particles

The FLASH code simulates astrophysical domains using a volume-filling Eulerian grid. However, the code can also inject tracer particles into the simulation volume. These tracers are passive and massless, with no dynamical impact upon the gas. At each time step, they are advected with the local density flow according to the velocity field of the gas at their particular location. When the zoom-in refinement begins, we initialize the tracers in a uniform lattice with a spacing in each dimension of 1 pc. The lattice covers the entire zoom-in region and an additional zone extending 10 pc out from the zoom-in region in the x, y, and z directions. The total number of tracers in the simulations is about 9×10^5 in both MC1-HD and MC2-HD, 2×10^6 in MC1-MHD, and 1.6×10^6 in MC2-MHD. The MHD zoom-in regions are slightly wider in each dimension than the HD regions (and therefore contain more tracers) because of their more diffuse distribution.

Every 3.3 kyr, a snapshot is taken of every tracer particle. The snapshot records each tracer's local values of the gas density, gas and dust temperature, self-shielding factors of H₂ and CO as well as $A_{V,3D}$, and the mass fractions of H, H₂, C, CO, and C⁺. These local readings proportionally represent those reported in a cell-sized box projected around the tracer particle, a system called Cloud-in-Cell interpolation. Because we simultaneously model the zoom-in region with the surrounding multi-phase ISM, some of the tracer particles move in or out of the zoom-in region over the simulation lifetime. Since the surrounding ISM is not well resolved, we restrict our analysis to particles which lie inside the zoom-in region at particular timesteps.

Post-processing the abundances reported by the tracer particles unlocks the time-dependent chemistry of individual gas complexes in the molecular cloud simulations (Genel et al. 2013; Ferrada-Chamorro et al. 2021). Prior works have shown the significant impact of turbulent mixing on the abundance distribution of H₂ (Glover et al. 2010; Valdivia et al. 2016b; Seifried et al. 2017b; Ebagezio et al. 2022). If we post-processed solely the simulation grids, we would be restricted to snapshots which do not preserve multi-timestep dynamical information, limiting us to equilibrium chemistry. Post-processing the chemical abundance evolution reported by the tracer particles gives a fuller picture of the simulated cloud's non-equilibrium chemical evolution than post-processing the AMR grids alone.

3 CHEMICAL POST-PROCESSING

Our post-processing calculations are handled by the chemistry and microphysics package KROME (Grassi et al. 2014). Rather than post-processing the full AMR grids, we apply the solver instead to the history files produced over the lifetime of each tracer particle. We take care to post-process each tracer individually. Because the tracers record the local values of the temperature, density, and radiation shielding, these time-dependent quantities can be used in KROME to solve the network of reaction rates. The chemical abundances recorded by the tracer particles at $t_{\text{evol}} = 0$ are used to initialize our post-processed chemistry network, but thereafter only the density, temperature, and shielding factors are used as inputs for each subsequent post-processing step.

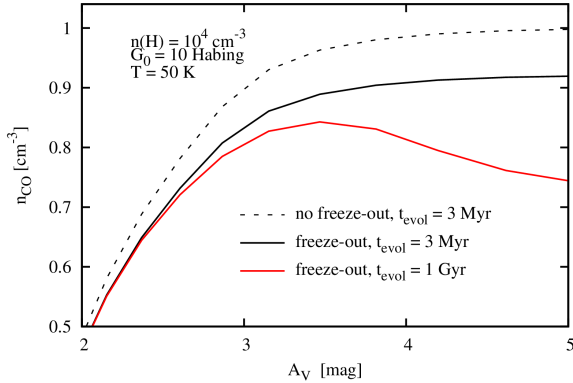


Figure 1. The carbon monoxide number density n_{CO} vs. the visual extinction A_V in a 1D-PDR setup, comparing our post-processing network with freeze-out reactions turned on (black solid line) and the same network with those reactions turned off (dashed). Freeze-out effects lead to a net decrease in n_{CO} starting around $A_V = 2$. By $A_V = 5$, the run where freeze-out is enabled has a CO abundance about 10% lower than the run where it is not. When the setup is run with freeze-out for $t_{\text{evol}} = 1$ Gyr (red), n_{CO} declines relative to the $t_{\text{evol}} = 3$ Myr result starting around $A_V \approx 2.5$.

3.1 The chemical network

For post-processing the abundances reported by the tracers, we use a chemical network containing 301 reactions, 37 gas-phase species, and 2 species frozen on to dust grains. The network is derived from the `react_COthin` network included with the `KROME` package and described in Grassi et al. (2017). The network solves for not only the simplest hydrogen and carbon species which were present in the simulation’s on-the-fly network (see Section 2.1), but also for HCO^+ , OH , CH , H_2O , the cosmic ray tracer H_3^+ , neutral and ionized silicon, and more. The full list of 39 species is included in Appendix A1. Our principal modification to the network comes in the addition of two species to represent CO and H_2O which have frozen on to grains, as well as reactions to model their adsorption and desorption rates (see Appendix A2 for details).

We show the importance of including these freeze-out effects in Fig. 1, where we plot the CO abundance vs. A_V for our network (solid lines) and with the freeze-out reactions turned off (dashed). We employ a 1D-PDR setup in which $n(\text{H}) = 10^4 \text{ cm}^{-3}$, $G_0 = 10$ in Habing units, $T = 50 \text{ K}$, and the evolution time is $t_{\text{chem}} = 3 \text{ Myr}$ (black). The inclusion of freeze-out starts to diminish the CO abundance around $A_V \approx 2$. By $A_V \approx 5$, the network with freeze-out has a CO abundance about ten percent lower than the network without freeze-out. We then repeat this test with freeze-out at $t_{\text{chem}} = 1 \text{ Gyr}$ (red), finding a decline in n_{CO} relative to the $t_{\text{chem}} = 3 \text{ Myr}$ case beginning at $A_V \approx 2.5$. The different outcomes for n_{CO} at different times underscore the importance of freeze-out effects to time-dependent chemistry.

3.2 The post-processing procedure

We post-process the chemical history of each tracer particle individually, using the post-processed abundances of each particle snapshot as the input state of the subsequent post-processing step. We will show a procedure to weight these abundances relative to the local bulk density around the tracer particle, which changes as the particle

advects throughout the simulation domain. Additionally, we employ a number of environmental parameters saved in the tracer histories as parameters in the chemical network’s reactions: the bulk density, the gas and dust temperatures, the 3D visual extinction $A_{V,3D}$, and the H_2 and CO self-shielding coefficients. When one of these environmental parameters p changes between successive snapshots by more than a specified threshold percent change s (in this work, 10%), we subdivide the inter-snapshot timestep of 3.3 kyr into smaller pieces based on a linear interpolation scheme. This safeguards the rate equation solver from large environmental shifts which may produce inaccurate solutions. The steps of this algorithm are described below.

3.2.1 Initialization

The output of our post-processing is an array of chemical number densities covering every species included in the chemical network. This evolving abundance array must be initialized before the first post-processing step at $t_{\text{evol}} = 0$. Each tracer particle history includes the on-the-fly values for the mass fractions of H, H_2 , C, CO, and C^+ at each snapshot time (separated by 3.3 kyr). We read these mass fractions from the first particle snapshot in the history, along with the local bulk density. The mass fractions are then converted to number densities via their respective molecular weights, and are saved to the evolving abundance array as the initial values for these species. We derive an initial value for the density of ionized hydrogen by the relation

$$n_{\text{H}^+} = n_{\text{H,tot}} - n_{\text{H}} - 2n_{\text{H}_2}. \quad (2)$$

Additionally, we set the initial number densities for helium, carbon, and oxygen to $n_{\text{He}} = 0.1n_{\text{H,tot}}$, $n_{\text{C}} = (1.4 \times 10^{-4})n_{\text{H,tot}}$, and $n_{\text{O}} = (3.2 \times 10^{-4})n_{\text{H,tot}}$, following the abundances given in Sembach et al. (2000). All other species in the evolving abundance array are initialized to number densities of 10^{-20} cm^{-3} ; tests indicate that after a few snapshots, the densities of species not initially set as a fraction of $n_{\text{H,tot}}$ are insensitive to their initial value. These arrays are established separately for every tracer particle in the simulation.

3.2.2 Iterating the post-processing

Fundamentally, our post-processing methodology tries to reach the most accurate chemical solution by advancing in incremental steps, rather than evolving the abundances over long time-scales to equilibrium. This is facilitated by always iterating the `KROME` solver by a time less than or equal to the time between two successive tracer snapshot times t_1 and t_2 , which are separated by 3.3 kyr. The decision of whether to advance the chemistry by less than $t_2 - t_1$, and if so, what fraction of that time to advance by instead, is made in the following way.

At t_1 , the procedure reads in the tracer particle’s saved values for $A_{V,3D}$, the bulk density, the gas and dust temperatures, and the self-shielding coefficients of H_2 and CO. These parameters are required to solve various reaction rates in the chemical network. We refer to an arbitrary member of this set of six environmental parameters at $t = t_1$ by p_1 . The parameter values for the subsequent timestep t_2 are then read as well.

Next, the code checks whether any of the parameters p_1 undergo a percent change exceeding some user-defined value s , that is:

$$p_2 > (1 + s)p_1 \quad \text{or} \quad p_2 < (1 - s)p_1, \quad (3)$$

if $p_2 > p_1$ or $p_2 < p_1$ respectively. These are the subcycling threshold conditions. If neither condition is fulfilled (that is, if none of p_1 experienced a percent change from t_1 to t_2 greater than s), the post-processing works as follows.

The KROME solver is passed the set of species number densities $n_{i,1}$ in its current state at t_1 , along with the values of p_1 . The solver then advances the chemistry for a time $\Delta t = t_2 - t_1$, keeping the parameters p_1 fixed, and reaches solutions for the number densities $n_{i,2}^*$. Then $n_{i,2}^*$ is multiplied by the inter-snapshot weight $W_{\Delta t}$, which is defined here as the ratio of the bulk densities ρ_2 and ρ_1 at t_2 and t_1 , respectively, such that each species number density n_i at t_2 is now given by:

$$n_{i,2} = n_{i,2}^* W_{\Delta t} = n_{i,2}^* \frac{\rho_2}{\rho_1}, \quad (4)$$

where $n_{i,2}$ is the set of weighted species number densities at t_2 . This weighting accounts for the motion of the tracer particle through regions of different density, corresponding to compression or rarefaction of the corresponding fluid element between t_1 and t_2 . After this, the post-processing is triggered anew for the timestep t_2 , and so forth, until the entire tracer history has been post-processed.

3.2.3 Subcycling

If, however, either of the aforementioned threshold conditions in Eq. 3 is fulfilled between two snapshots in a particle's history, a subcycling procedure is applied. This determines a smaller time over which to advance the chemistry $\Delta t < t_2 - t_1$, limiting the permissible amount of change in the parameters p given that they are held constant over Δt when solving the chemistry.

(i) In a first step, the code performs a linear interpolation for the values of the six environmental parameters p between t_1 and t_2 , and calculates the time it would take each p to undergo a relative change of exactly s . The smallest of these times is selected as the initial subcycle time $\Delta t_{\text{sub},1}$.

(ii) Next, for any additional necessary subcycling step j we determine the timestep as

$$\Delta t_{\text{sub},j} = (1 + s) \Delta t_{\text{sub},j-1}. \quad (5)$$

For the very first step ($j = 1$) we use $\Delta t_{\text{sub},1}$ (see below for an explanation of progressive increase).

(iii) We then advance the chemistry by the timestep $\Delta t_{\text{sub},j}$ from the current starting time of the subcycling step, $t_{\text{current},j}$ (i.e. t_1 for the first subcycling step, $j = 1$), to $t_{\text{current},j+1} = t_{\text{current},j} + \Delta t_{\text{sub},j}$ using the values of the parameters p at $t_{\text{current},j}$.

(iv) Next, using our linear interpolation from step (i), we calculate the values of the environmental parameters p at $t_{\text{current},j+1}$, to be used for the next subcycling timestep.

(v) The abundance array n^* obtained from step (iii) is multiplied by the timestep weight:

$$W_{\Delta t} = \frac{\rho_{t_{\text{current},j+1}}}{\rho_{t_{\text{current},j}}}. \quad (6)$$

This provides the properly weighted abundances for the next subcycling step.

We repeat steps (ii) to (v) until the next proper snapshot at t_2 is reached. For the very last subcycling timestep we take as the timestep the difference between t_2 and the end-time of the previous subcycle $t_{\text{current},2\text{nd-last}}$, i.e. $\Delta t_{\text{sub,last}} = t_2 - t_{\text{current},2\text{nd-last}}$ to assure that we end up exactly at t_2 .

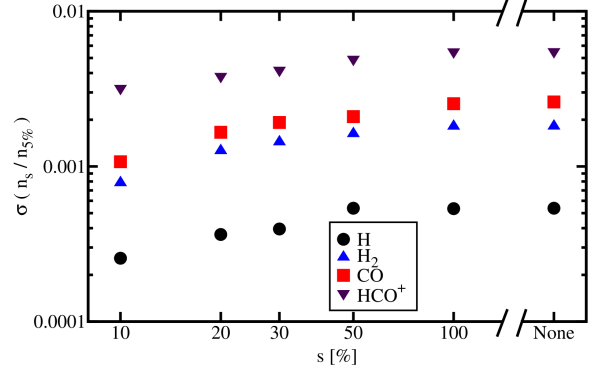


Figure 2. The standard deviations $\sigma(n_s/n_{5\%})$ of the distributions of the ratios of the number densities of H, H₂, CO, and HCO⁺, measured as a function of the selected subcycling threshold s , with respect to the results obtained for a threshold of $s = 5\%$ (see Eq. 7). Smaller subcycling thresholds correspond to smaller values of $\sigma(n_s/n_{5\%})$, but these standard deviations are all small or negligible. We therefore can select our subcycling threshold as $s = 10\%$ with confidence.

We note that we apply the iterative increase in the subcycling timestep (Eq. 5) to avoid the following edge case. If one of the environmental parameters undergoes a particularly large change between timesteps t_1 and t_2 , the linear interpolation described in step (i) will establish a particularly small $\Delta t_{\text{sub},1}$. If we were to advance the chemistry by only $\Delta t_{\text{sub},1}$ until t_2 is reached, and $\Delta t_{\text{sub},1}$ is very small, the subcycling procedure may impose as many as dozens of additional substeps before t_2 . In seeking a balance between small substeps which can properly shepherd the chemistry solver through rapid environmental changes, and the additional computational demands of solving the chemistry so many extra times, we found that iteratively increasing the substep size by factors of $(1 + s)$ is a viable compromise.

For the results presented in this paper, we use a subcycling threshold value $s = 0.1$, meaning a change of more than 10% in any environmental parameter would trigger subcycling. To validate this number, we post-process about 40,000 randomly selected tracer particles in MC1-HD (5% of its total particle population) with different values for the threshold: 5, 10, 20, 30, 50, and 100%. Additionally, we perform a test with subcycling deactivated, so that the solver would always iterate for $\Delta t = t_2 - t_1$ regardless of any changes in the environmental parameters between timesteps.

We concatenate the chemistry results from each test run with different values of s into snapshots at $t_{\text{evol}} = 2.5$ Myr. For each value of s , we denote the number densities of H, H₂, CO, and HCO⁺ as n_s . Next, for each particle we calculate the ratio $n_s/n_{5\%}$ and the standard deviation of this ratio for each species:

$$\sigma(n_s/n_{5\%}) = \left(\sum_i^N \frac{n_{i,s}}{n_{i,5\%}} - \left\langle \frac{n_s}{n_{5\%}} \right\rangle \right)^{\frac{1}{2}} N^{-\frac{1}{2}}, \quad (7)$$

where N is the number of tracers in the set and $\langle n_s/n_{5\%} \rangle$ is the mean of all particles' values for $n_s/n_{5\%}$. These standard deviations for each species and value for s are shown in Fig. 2. In general, the standard deviations are extremely small, on the order of 0.01 when considering the number densities of H, H₂, CO, and HCO⁺. The values of $\sigma(n_s/n_{5\%})$ decrease with decreasing s . Even for the run in

which subcycling is deactivated, the variation is marginal. Therefore, we feel secure in selecting a subcycling threshold of $s = 0.1$ as sufficient for post-processing.

3.3 Comparing on-the-fly and post-processed abundances

It can be instructive to compare the on-the-fly and post-processed abundances for certain hydrogen and carbon species which are present in the original simulations. In Fig. 3, we plot the average fractional abundances of H, H₂, C, CO, and C⁺ for the tracer particles before post-processing (left) and after (right), for the cloud MC1-HD at $t_{\text{evol}} = 2$ Myr, as a function of $n_{\text{H,tot}}$. The ratios of the post-processed mean fractional abundances to the unprocessed mean fractional abundances (i.e., the ratios of the abundances in the right and left panels of Fig. 3) are plotted in Appendix B, in the left panel of Fig. B1.

The post-processed abundances for these species are broadly similar to their original abundances. In particular, the fractional abundance profiles of H (black) and H₂ (purple) with respect to $n_{\text{H,tot}}$ are almost unchanged. Atomic hydrogen dominates at lower densities, and gradually diminishes in abundance as the density increases. At $n_{\text{H,tot}} \approx 3 \times 10^3 \text{ cm}^{-3}$, molecular hydrogen becomes the predominant hydrogen species. Atomic hydrogen continues to decline as H₂ nears saturation. Saturation occurs by $n_{\text{H,tot}} \approx 3 \times 10^4 \text{ cm}^{-3}$ both before and after post-processing.

The fractional abundances of C, CO, and C⁺ (shown with respect to the summed carbon density from those three species, rather than with respect to total hydrogen) undergo some changes during the post-processing. In the on-the-fly results, atomic carbon (green) dominates around $n_{\text{H,tot}} = 3 \times 10^3 \text{ cm}^{-3}$ before declining as CO (blue) predominates. However, in the post-processed results, the peak fractional abundance of atomic carbon occurs at the same $n_{\text{H,tot}}$ but only reaches 0.5. Consequently, C⁺ and CO reach higher fractional abundances in this density range for the post-processed results. We attribute this outcome to a well-known problem in the on-the-fly NL99 network, in which atomic carbon is overproduced. This problem has been discussed in a number of works (Glover & Clark 2012; Gong et al. 2017; Hu et al. 2021). A solution remains elusive, but is probably linked to the limited size of the network. In any case, as this problem appears to be alleviated by post-processing with our more extensive network, we are confident that it does not affect the analysis presented in this work.

Finally, we note that although the post-processing network includes additional carbon species (in particular, frozen-out CO), their abundances are low enough at most densities that their contribution to the total carbon can be neglected for this analysis. Around $n_{\text{H,tot}}$, the abundance of CO dips slightly, which we ascribe to an increase in the proportion of CO which has frozen onto dust at this density.

4 THE FORMATION OF HCO⁺

By post-processing the entire chemical histories reported by the tracers, we can now examine the full time-dependent evolution of interesting species rather than merely their equilibrium abundances. Because the tracers advect passively with the gas flow, they recount the full history of localized patches of gas. Analysing their bulk motion in conjunction with the post-processed chemistry can give us, for the first time, dynamical information about species only present in more extensive chemical networks than are run on-the-fly. In particular, we can analyse the formation rate, peak production density regime, and predominant creation pathways of interesting species.

4.1 HCO⁺ evolution

As a first scientific application, we consider the temporal and dynamical evolution of the HCO⁺ content in both hydrodynamic and magnetohydrodynamic molecular clouds. This species is present in some of the principal formation pathways for CO. Understanding the evolution of the HCO⁺ abundance can therefore provide time-dependent information about the CO content of molecular clouds and answer questions about how these species are related (van Dishoeck & Black 1988; Nikolic 2007; Papadopoulos 2007; Gerin & Liszt 2021).

In the background of Fig. 4, we plot a 2D-PDF of the fractional abundance of HCO⁺, f_{HCO^+} , vs. visual extinction $A_{\text{V},3\text{D}}$ for every tracer in the clouds MC1-HD (left) and MC1-MHD (right), at $t_{\text{evol}} = 4$ Myr. We see that the peak of f_{HCO^+} for both clouds at this time is found around $\log A_{\text{V},3\text{D}} \approx 0.5$. Because we post-process the entire history of every tracer in the clouds, we can investigate the time-dependent evolution of the particular tracers which achieve this peak f_{HCO^+} value. In particular, how do these particular tracers' values of $A_{\text{V},3\text{D}}$ change as they experience HCO⁺ formation, and what is the time-scale of that formation?

To answer these questions, we must first select an appropriate subset of tracer particles. We establish an HCO⁺ growth time-scale τ , defined as the time it takes a tracer particle to rise from just below an HCO⁺ fractional abundance of 10^{-12} to just above an abundance of 10^{-9} :

$$\tau = t(f_{\text{HCO}^+} = 10^{-9}) - t(f_{\text{HCO}^+} = 10^{-12}). \quad (8)$$

The upper threshold of 10^{-9} is chosen as it is approximately the minimum fractional abundance of HCO⁺ reported by any tracer with $A_{\text{V},3\text{D}} > 3$, which is roughly the $A_{\text{V},3\text{D}}$ -threshold in our post-processed chemistry above which high values of f_{HCO^+} begin to appear (Fig. 4, and see also Lucas & Liszt 1996). The tracers which fulfill the 'growth condition' of Eq. 8 and thus have a value for τ can be analysed as an ensemble. For the cloud MC1-HD, this comprises 27130 particles (3.1%), and for the cloud MC1-MHD, only 6420 (0.3%). The factor of ten smaller percentage of particles in MC1-MHD which fulfill our growth condition reflects the more diffuse nature of MHD clouds compared to pure HD ones (Seifried et al. 2020). Although the high-density regions of the HD and MHD clouds have similar properties (in contrast to their differently-distributed envelopes; see Ganguly et al. 2022), a smaller fraction of the MHD cloud's gas reaches a sufficient density for HCO⁺ formation, with a corresponding smaller number of tracer particles in dense gas.

We randomly select 50 particles in each cloud which fulfill the growth condition of Eq. 8, and plot the entire history of their values in the foreground of Fig. 4. These history trajectories are each split into four segments, color-coded according to their values for t_{evol} . For both clouds, the selected tracers linger at values for f_{HCO^+} below the lower threshold of 10^{-12} until around $t_{\text{evol}} = 2$ Myr (the blue and green segments). Then, the tracers ascend over the course of about 1 Myr (the orange and red segments) beyond the upper threshold of 10^{-9} without significant change to their visual extinction of about $A_{\text{V}} \approx 1-3$. After this, the gradual and ongoing gravitational contraction of these dense regions guides many of the tracers into higher density regions where $A_{\text{V}} \gtrsim 5$. However, this is after the time that the peak f_{HCO^+} has been attained. By repeating this plotting procedure for both molecular clouds several times with different random batches of particles that fulfill the growth condition, we find this pattern is consistent.

In the figure, we additionally plot the result of the PDF_{CHEM} model (solid black line) from Bisbas et al. (2022). This model corresponds

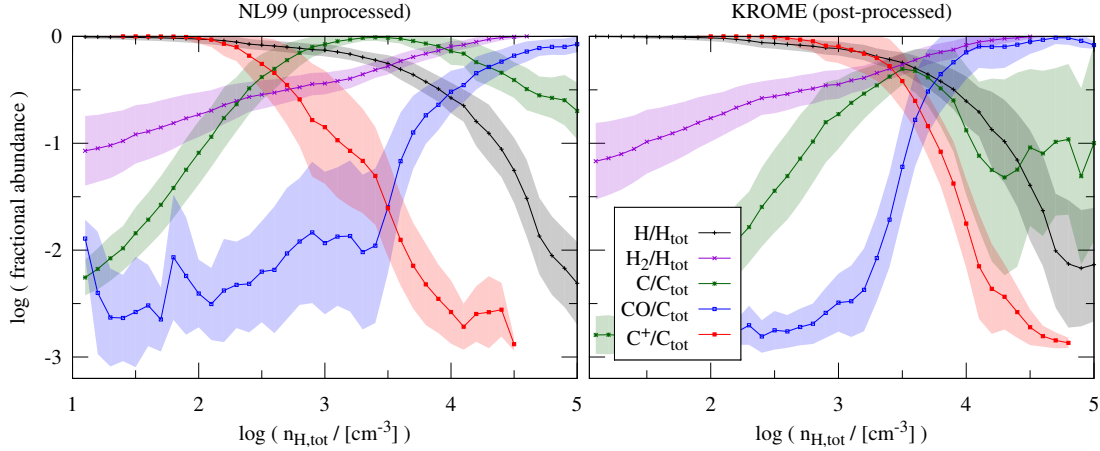


Figure 3. The average fractional abundances of H, H₂, C, CO, and C⁺ vs. the total hydrogen number density $n_{\text{H,tot}}$ of the molecular cloud MC1-HD at $t_{\text{evol}} = 2$ Myr, before post-processing (left) and after (right). The shaded areas represent one standard deviation around each species average. The abundance profiles of H (black) and H₂ (purple) do not change appreciably after post-processing. Post-processing reduces the saturation of atomic carbon (green) between $n_{\text{H,tot}} = 10^3$ – 10^4 cm⁻³. The bulk density at which the abundance of C⁺ (red) begins to decline is a magnitude higher after post-processing. CO (blue) becomes the dominant carbon species at a slightly lower bulk density after post-processing, primarily due to the reduction in atomic carbon.

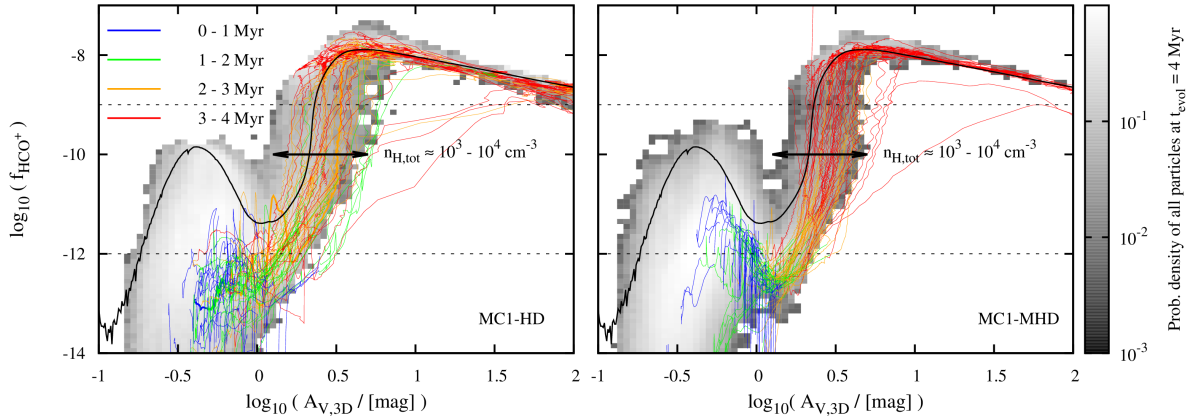


Figure 4. History tracks of a selection of 50 tracer particles that rise from a fractional abundance of 10^{-12} to 10^{-9} (indicated by horizontal black dashed lines) at some point during their lifetime, for MC1-HD (left) and MC1-MHD (right). The history tracks are colored according to the age of the particle at the time. Plotted beneath the tracks are 2D-PDFs of the HCO⁺ fractional abundance vs. visual extinction $A_{\text{V},3\text{D}}$ for all tracer particles in each simulation at $t_{\text{evol}} = 4$ Myr. The approximate $A_{\text{V},3\text{D}}$ range where $n_{\text{H,tot}} = 10^3$ – 10^4 cm⁻³ is indicated by a double-headed arrow. The f_{HCO^+} obtained from running a PDF_{CHEM} model (Bisbas et al. 2022) is plotted over the distribution (solid black line) to illustrate that the post-processed tracers comprehensively cover the extinction domain in which HCO⁺ is prevalent. Both molecular clouds contain similar distributions of tracer particles in this phase space. There is a sharp jump in fractional abundance between total hydrogen densities of 10^3 and 10^4 cm⁻³, where the tracer particles display local, in situ HCO⁺ production rather than turbulent mixing of HCO⁺ from deeper (i.e. from higher $A_{\text{V},3\text{D}}$) in the clouds. For both clouds, the selected tracers move from the lower to the upper threshold in a time-scale of about 1 Myr, corresponding to the typical HCO⁺ formation time. For the cloud MC1-HD, this growth mostly occurs some 2–3 Myr after the start of the zoom-in refinement, but for the cloud MC1-MHD, somewhat later, 3–4 Myr after the start of the refinement.

well to the tracer distribution, especially at $A_{\text{V},3\text{D}} \gtrsim 1$, validating the post-processed tracer chemistry in the extinction regime where HCO⁺ is found. The range $A_{\text{V},3\text{D}} \approx 1$ – 3 , in which the tracers experience most of their HCO⁺ growth, can be correlated with the total gas density. We examine again the tracer histories plotted in Fig. 4 but instead in the space of f_{HCO^+} vs. $n_{\text{H,tot}}$. By comparing the values for $n_{\text{H,tot}}$ and $A_{\text{V},3\text{D}}$ experienced by the tracers at different times, we can establish a rough correspondence between these two values. We

plot black arrows in Fig. 4 to indicate the approximate $A_{\text{V},3\text{D}}$ range in each cloud where $n_{\text{H,tot}}$ ranges from 10^3 to 10^4 cm⁻³. This result is in accordance with figure 12 in Seifried et al. (2017b).

Between $A_{\text{V},3\text{D}} \approx 5$ and the densest regions of the clouds where $A_{\text{V},3\text{D}} \approx 100$, f_{HCO^+} declines by approximately one order of magnitude in both MC1-HD and MC1-MHD. We posit that this results from a corresponding decline of one magnitude in f_{H^+} which we see over this extinction range, stemming from the constant number

density of H_3^+ in dense molecular clouds even as $n_{\text{H,tot}}$ increases (see e.g. Oka 2006; Le Petit et al. 2016). In Section 4.4, we will show that in our post-processing network at very high $A_{\text{V},3\text{D}}$, the primary formation pathway for HCO^+ is the reaction $\text{H}_3^+ + \text{CO}$. A decline in $f_{\text{H}_3^+}$ would lead to a bottleneck in that reaction and therefore a matching decline in f_{HCO^+} , as seen in Fig. 4. The possible impact of our constant value for the CRIR on the H_3^+ abundance is noted in Section 6.

4.2 Turbulent mixing

Recent works have discussed the role of turbulent mixing in distributing molecules like H_2 throughout molecular clouds from dense sites of peak formation (Seifried et al. 2017b, and see also Glover et al. 2010). For instance, Valdivia et al. (2017) (see also Valdivia et al. 2016a) and Godard et al. (2023) find that the presence of CH^+ in the diffuse ISM stems from advection and thermal instability in denser gas. It is natural to ask whether HCO^+ (which can be formed via CH^+ among other things; see next Section) is produced in dense gas and distributed around molecular clouds in the same fashion. By comparing each tracer’s time-dependent HCO^+ abundance to its local density, we can determine the dynamical backstory of gas which has a high HCO^+ abundance at late times.

We find that for both HD and MHD molecular cloud simulations, the tracer particles’ average separation in the high density regime is smaller than 0.1–0.2 pc, which is sufficient spatial resolution to resolve such turbulent flows. However, the representative particle history tracks in Fig. 4 do not exhibit this mixing action. For all clouds, about 90% of the tracers which fulfill the growth condition see HCO^+ formation in situ around $n_{\text{H,tot}} \lesssim 10^4 \text{ cm}^{-3}$ ($\log A_{\text{V},3\text{D}} < 0.7$). Only $\sim 10\%$ of the tracers first exceed $f_{\text{HCO}^+} = 10^{-9}$ while having $\log A_{\text{V},3\text{D}} \gtrsim 0.7$ (represented by the tracks moving diagonally to the upper right in Fig. 4), and practically all (99%) of these subsequently remain in the high density regime, rather than mix back out to regions of lower density. This may represent a lower limit on the mixing fraction, due to the propensity of tracer particles to become trapped at density peaks despite the presence of gas outflows (see e.g. Price & Federrath 2010; Konstandin et al. 2012; Genel et al. 2013; Cadiou et al. 2019).

4.3 The HCO^+ formation time-scale

The preceding analysis has shown that HCO^+ is preferentially formed in the density regime $n_{\text{H,tot}} \approx 10^3\text{--}10^4 \text{ cm}^{-3}$ with a time-scale on the order of 1 Myr. We will now analyse this formation time-scale in greater detail, in particular how it correlates with the abundances of various reactants in HCO^+ production pathways.

Examining the relationship between HCO^+ formation and the abundances of its formation reactants in the most simplistic way – within a single snapshot of all tracer particles – showcases the importance of a non-equilibrium approach to this problem. If there is a correlation between the densities of HCO^+ and some formation reactant, we can posit that that reactant’s pathway is an important source of HCO^+ . In Fig. 5, we compare n_{HCO^+} and n_{CO} in a 2D-PDF of cloud MC1-HD at $t_{\text{evol}} = 4$ Myr. Several lines of constant ratio are included. The two species have a tight, non-linear relationship across a large range of densities. But although the correlation of HCO^+ with CO is evident, the causal direction of this relationship, if there is any, is not. CO is present in both production and destruction reactions of HCO^+ , so a time-dependent perspective is required to understand how these two species are connected.

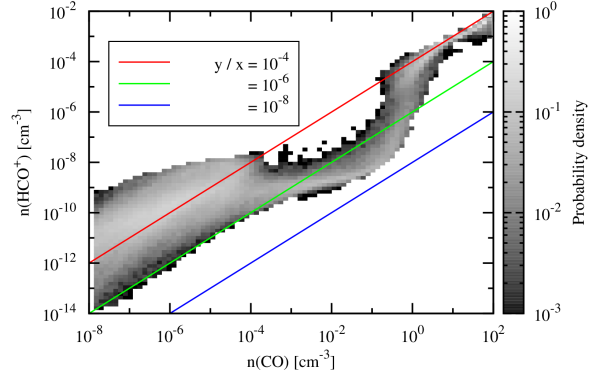


Figure 5. The number density of HCO^+ vs. the number density of CO, for all post-processed tracer particles in the zoom-in region of cloud MC1-HD at $t_{\text{evol}} = 4$ Myr, in the form of a 2D-PDF. Colored lines indicate different constant ratios. There is a close, but highly non-linear, relationship between the two species.

Table 1. List of the 11 reactions in our chemical network which produce HCO^+ .

1.	$\text{HOC}^+ + \text{H}_2 \rightarrow \text{HCO}^+ + \text{H}_2$
2.	$\text{HOC}^+ + \text{CO} \rightarrow \text{HCO}^+ + \text{CO}$
3.	$\text{CO}^+ + \text{H}_2 \rightarrow \text{HCO}^+ + \text{H}$
4.	$\text{CH} + \text{O} \rightarrow \text{HCO}^+ + \text{e}^-$
5.	$\text{CH}_2^+ + \text{O} \rightarrow \text{HCO}^+ + \text{H}$
6.	$\text{CH}_3^+ + \text{O} \rightarrow \text{HCO}^+ + \text{H}_2$
7.	$\text{H}_2\text{O} + \text{C}^+ \rightarrow \text{HCO}^+ + \text{H}$
8.	$\text{H}_3\text{O}^+ + \text{C} \rightarrow \text{HCO}^+ + \text{H}_2$
9.	$\text{CH}_2^+ + \text{O}_2 \rightarrow \text{HCO}^+ + \text{OH}$
10.	$\text{H}_3^+ + \text{CO} \rightarrow \text{HCO}^+ + \text{H}_2$
11.	$\text{HCO} + \gamma \rightarrow \text{HCO}^+ + \text{e}^-$

Our chemical network includes 11 reactions which form HCO^+ , listed in Table 1. We now go beyond the simple comparison of n_{HCO^+} with other n_i of the various reactants (O, CO^+ , H_3^+ , CH_3^+ , HOC^+ , H_2O , CH, and C^+), and consider the direct dependence of the formation time-scale of HCO^+ on these n_i . For this purpose, we again select the tracer particles which report over some period following $t_{\text{evol}} = 0$ that their HCO^+ fractional abundance ascended from below 10^{-12} to above 10^{-9} , the time-scale of which we defined as τ in Eq. 8. Over the period containing N particle snapshots between these two thresholds, we calculate the logarithmic-average number density of each reactant, $\langle \log n_i \rangle$, in the following way:

$$\langle \log n_i \rangle = \frac{1}{N} \sum_{j=1}^N \log n_{i,j}. \quad (9)$$

In Fig. 6, we plot 2D-PDFs of τ vs. $\langle \log n_i \rangle$ for H_{tot} , H_2 , CO, and HCO^+ itself, for the cloud MC1-HD. The over-plotted red points indicate the average τ for each density bin. The black over-plotted line in each 2D-PDF indicates a linear fit to the red points as follows:

$$\log \tau = m \langle \log n_i \rangle + C, \quad (10)$$

where C corresponds to the value of $\log \tau$ when $\langle \log n_i \rangle = 0$. The

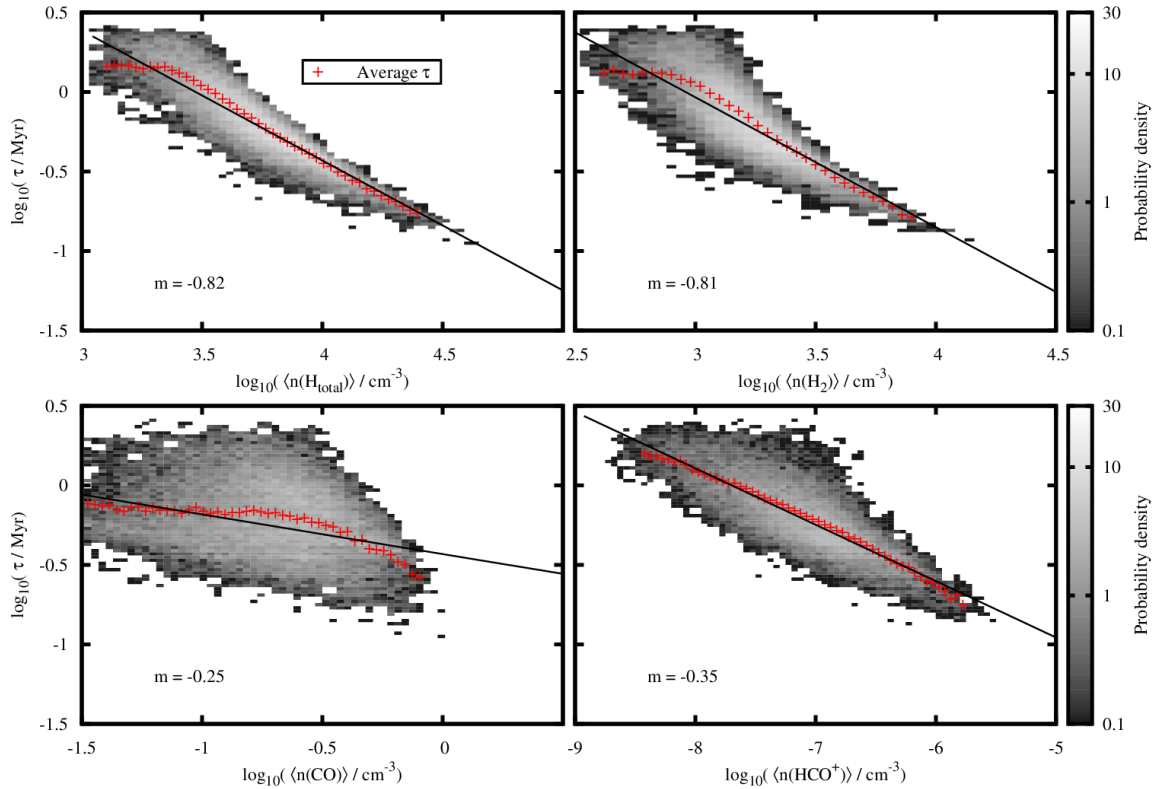


Figure 6. The 2D-PDF of the HCO⁺ growth time-scale τ (see Eq. 8), vs. the logarithm of the time-averaged mean density $\langle n_i \rangle$ (see Eq. 9), for the subset of tracers in MC1-HD which fulfill the HCO⁺ growth condition in Eq. 8. The red crosses denote the average τ for each density bin. The black line denotes a fit to these average points (see Eq. 10), for which the slope m is given in each panel. The higher the average density experienced by the tracer particles, the shorter the growth time-scale. The correlation is strongest with regard to $n_{\text{H,tot}}$, as HCO⁺ formation occurs predominantly in dense gas (see Fig. 4).

closer the slope m is to -1, the greater the correlation of a particular reactant with the overall HCO⁺ production rate.

As expected, a shorter time-scale τ corresponds to higher densities for these species, and thus also with higher $A_{\text{V,3D}}$. The correlation of τ with CO abundance is the smallest of these four species, with $m = -0.25$. This is likely due to the aforementioned presence of CO in both the creation and destruction reactions of HCO⁺. The correlations of τ with H_{tot} ($m = -0.82$) and H_2 ($m = -0.81$) are almost identical, which is reasonable given that HCO⁺ forms in the extinction regime of molecular gas (see Fig. 4). The correlation of the HCO⁺ number density with τ is weaker ($m = -0.35$), which means that the abundance of HCO⁺ is a less-reliable indicator of its own formation rate than are the abundances of H_2 and CO. Repeating this analysis for MC1-MHD shows almost identical correlations, with the average τ in each density bin almost unchanged, but with less spread in the underlying 2D distribution.

We can expand this analysis to other reactants listed in Table 1. In Fig. 7, we display the correlation of τ with $\langle n \rangle$ for O, CO⁺, H_3^+ , CH_3^+ , HOC^+ , H_2O , CH, and C^+ . Atomic oxygen, which can react to form HCO⁺ via several pathways, has the strongest correlation of these species with τ , with $m = -0.82$. Next we see that CO⁺ has a fitted slope of $m = -0.7$, corresponding to the high correlation of its reactant H_2 (see Table 1). The cosmic ray tracer H_3^+ has

$m = -0.66$, a stronger correlation than its reactant partner CO. CH_3^+ reacts with atomic oxygen and has a slope of $m = -0.65$. The isomer HOC^+ could form HCO⁺ by reacting with either H_2 or CO, and has a slope of $m = -0.62$. We ascribe the weaker correlation of H_2O with τ ($m = -0.31$) to the fact that its co-reactant, C^+ , connotes the presence of free electrons. Since electrons can recombine with and eliminate HCO⁺, it is sensible that the H_2O correlation is weak, and that the C^+ density is in fact anti-correlated ($m = +0.51$) with the HCO⁺ formation timescale. This also explains the anti-correlation of CH_2^+ density with τ ($m = +0.27$), in spite of the high correlation of its co-reactant O with τ (apparently due solely to the reaction with CH_3^+ ; its last co-reactant, CH, correlates poorly to τ with $m = +0.16$).

Qualitatively similar results are seen for these correlations in the other three molecular clouds. The ranges in the fitted slopes for these species for the four different molecular clouds, as well as for the species shown in Fig. 6, are reported in Table 2. Generally, the values for m are similar for all four molecular clouds and thus the range is limited. The MHD and HD clouds differ in the correlations of $\langle \log n_{\text{CO}^+} \rangle$ and $\langle \log n_{\text{H}_3^+} \rangle$ with τ . For instance, $\langle \log n_{\text{CO}^+} \rangle$ has a stronger correlation with τ in the HD clouds (e.g. $m = -0.7$ for MC1-HD) than in the MHD clouds (e.g. $m = -0.13$ for MC1-MHD).

Conversely, the correlation of τ with $\langle \log n_{\text{H}_3^+} \rangle$ is weaker in the HD clouds (e.g. $m = -0.6$ for MC1-HD) than in the MHD clouds (e.g.

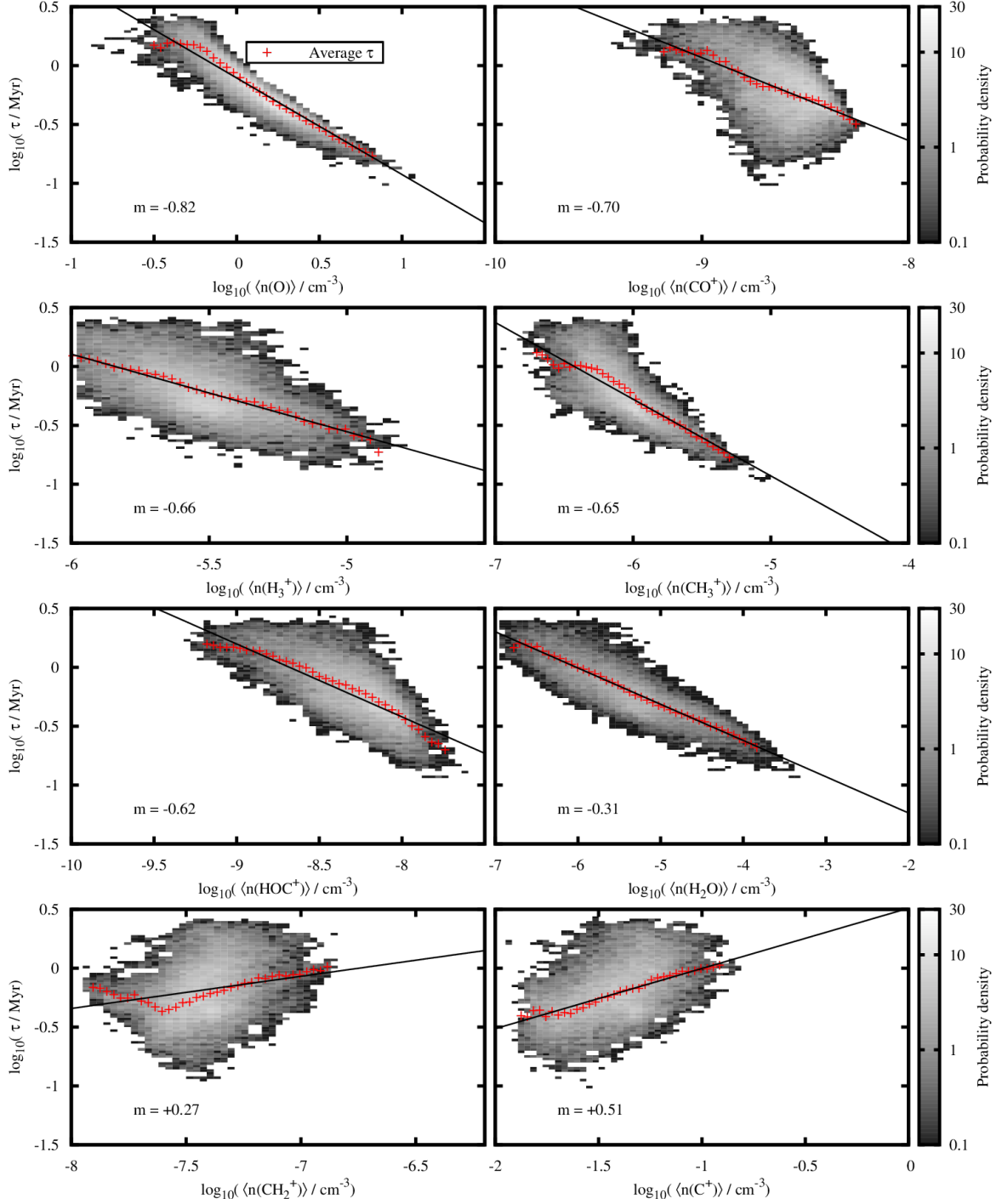


Figure 7. The 2D-PDF of the HCO^+ growth time-scale τ (see Eq. [refeq:tau](#)) vs. the time-averaged mean density $\langle \log n_i \rangle$ (see Eq. [9](#)) of various formation reactants of HCO^+ given in Table 1, for the subset of tracers in MC1-HD which fulfill the HCO^+ growth condition in Eq. [8](#). The red crosses denote the average τ for each density bin. The black line denotes a fit to these average points (see Eq. [10](#)), for which the slope m is given in each panel. Reactants which are abundant in the low-density (i.e. low- $A_{V,3D}$) regime, like C^+ and CH_2^+ , correlate poorly with τ (low values of $|m|$), partly because they imply the presence of electrons and unshielded radiation which both destroy HCO^+ . However, the formation species which are found at higher extinctions, like H_3^+ , are more strongly correlated.

Table 2. The minimum and maximum values of m for each HCO⁺ production reactant (see Eq. 10) for all four simulated clouds.

Species	m_{\min}	m_{\max}
H _{tot}	-0.95	-0.73
H ₂	-0.96	-0.75
CO	-0.25	-0.10
HCO ⁺	-0.43	-0.32
O	-0.82	-0.68
CO ⁺	-0.70	-0.13
H ₃ ⁺	-0.86	-0.60
CH ₃ ⁺	-0.65	-0.56
HOC ⁺	-0.62	-0.59
H ₂ O	-0.36	-0.30
CH	+0.11	+0.16
CH ₂ ⁺	-0.01	+0.27
C ⁺	+0.30	+0.51

$m = -0.86$ for MC1-MHD). This implies that the reaction CO⁺ + H₂ has greater influence during HCO⁺ formation in HD clouds than in MHD clouds. Conversely, the reaction H₃⁺ + CO has a somewhat greater influence in MHD clouds than in HD ones. Corroborating the latter point, we find that the reservoir of available H₃⁺ covers a greater spatial extent in the MHD clouds than in the HD clouds, since the MHD clouds also have a more extensive H₂ envelope in which H₃⁺ is formed via cosmic ray interactions. Thus, the H₃⁺ + CO reaction is an available formation pathway for HCO⁺ over a wider spatial extent in the MHD clouds than in the HD clouds.

Fully explaining these correlations requires us to explore the relative importance of the different pathways for HCO⁺ production. For the moment, we point out that the correlations are sensible in light of our prior discussion of the particle history tracks. Reactants which are prevalent in lower-extinction gas, such as C⁺ and CH, have poor correlations with τ . This is unsurprising given that Fig. 4 shows HCO⁺ formation is most prevalent in gas with total hydrogen density around 10^3 – 10^4 cm⁻³. Additionally, it is worth noting that for reactions where one reactant is more abundant than the other, the correlation with τ is stronger for the less-abundant reactant, as its limited supply constrains the rate of the reaction. For example, in the reaction H₃⁺ + CO, the less-abundant reactant is H₃⁺, which has a stronger correlation with τ than CO does.

4.4 HCO⁺ formation pathways

Figs. 6 and 7 show the correlation of individual reactants' number densities with the HCO⁺ formation time-scale, over the course of the entire simulation but only for the very small subset of particles which fulfill the growth condition of Eq. 8. It is natural to consider next all the tracer particles regardless of their lifetime peak HCO⁺ abundance, and what their individual chemical histories can tell us about the predominant modes of HCO⁺ formation: a topic that fundamentally requires time-dependent chemistry to properly explore.

Because all the tracer particles retain not only the species number densities, but also environmental parameters like the local temperature and visual extinction, we can re-calculate each tracer particle's reaction rate for all 11 HCO⁺ formation reactions listed in Table 1.

We calculate the production flux F_i of a given reaction i with R reactants and a temperature-dependent rate coefficient $k_i(T)$ as

$$F_i = k_i(T) \prod_{j=1}^R n_j. \quad (11)$$

We then assess the relative importance of each HCO⁺ formation reaction as a function of the local visual extinction $A_{V,3D}$. Rather than normalizing the reaction fluxes of the formation reactions on a per-particle basis (which would inaccurately suppress the contribution of tracers in regions of high absolute production flux), we first allocate F_i into bins of $A_{V,3D}$, and then normalize the flux contributions within each bin. We calculate this average normalized flux, $F_{i,\text{norm}}^{\text{avg}}$, for each reaction i in each $A_{V,3D}$ bin containing N_{bin} particles as follows:

$$F_{i,\text{norm}}^{\text{avg}} = \frac{1}{\sum_i F_i} \frac{1}{N_{\text{bin}}} \sum_{j=1}^{N_{\text{bin}}} F_{i,j}. \quad (12)$$

We choose to analyse $F_{i,\text{norm}}^{\text{avg}}$ at $t_{\text{evol}} = 2$ Myr, rather than at the later time $t_{\text{evol}} = 4$ Myr as with most of the other analysis in this work, in order to capture the state of the HCO⁺ formation reactions at the beginning of the principal formation epoch (see Fig. 4), rather than after the global HCO⁺ quantity has reached its final state.

In Fig. 8, we show these normalized reaction fluxes, $F_{i,\text{norm}}^{\text{avg}}$, for MC1-HD at $t_{\text{evol}} = 2$ Myr. The solid colored lines indicate the average value of each reaction in the local $A_{V,3D}$ -bin, with color-matched shading imposed to indicate one standard deviation above and below the mean. The reactions CH + O (Reaction 4 in Table 1), CH₂⁺ + O₂ (Reaction 5), HOC⁺ + CO (Reaction 2), H₃O⁺ + C (Reaction 8), and the cosmic ray interaction HCO + γ (Reaction 11) have been neglected due to their consistently minimal contributions to the total reaction flux in comparison to the other six remaining reactions across multiple snapshots and simulations. The relative fluxes of the non-negligible reactions achieve stable values by $A_{V,3D} = 10$. We have confirmed these values hold up to $A_{V,3D} = 100$, and leave out the final magnitude for purposes of readability.

It is clear that particular HCO⁺ formation reactions predominate in different visual extinction regimes. Up to $A_{V,3D} \approx 0.4$, HCO⁺ is chiefly generated via CH₂⁺ + O \rightarrow HCO⁺ + H and the unidirectional isomerization reaction HOC⁺ + H₂ \rightarrow HCO⁺ + H₂. However, the absolute quantity of HCO⁺ remains negligible in this poorly-shielded extinction regime due to efficient photodissociation by incident radiation.

From $A_{V,3D} \approx 0.4$ to 3, the reaction CO⁺ + H₂ \rightarrow HCO⁺ + H contributes about 75% of the total HCO⁺ production flux. The remaining 25% of the HCO⁺ contribution in this range comes from H₂O + C⁺ \rightarrow HCO⁺ + H (up to $A_{V,3D} \approx 1.5$) or the isomerization of HOC⁺ ($A_{V,3D} \approx 1.5$ –3). HOC⁺ is also produced by both the water reaction and the CO⁺ reaction at an approximately equal rate to HCO⁺ (Gerin et al. 2019; Gerin & Liszt 2021). However, because of the isomerization reaction, some of this HOC⁺ becomes HCO⁺ anyway. There is no equivalent route backwards for HCO⁺ to isomerize to HOC⁺, resulting in an abundance ratio $n_{\text{HCO}^+}/n_{\text{HOC}^+} \sim 100$ beginning around $A_{V,3D} \approx 1$.

The preceding reactions all decline in importance around $A_{V,3D} \approx 3$, as the reaction H₃⁺ + CO \rightarrow HCO⁺ + H₂ rapidly becomes, and then remains, the dominant one. This corresponds to a transition from an $A_{V,3D}$ regime dominated by photochemistry to a regime where the chemistry is driven by cosmic ray interactions. The H₃⁺ + CO reaction contributes more than 90% of the total HCO⁺

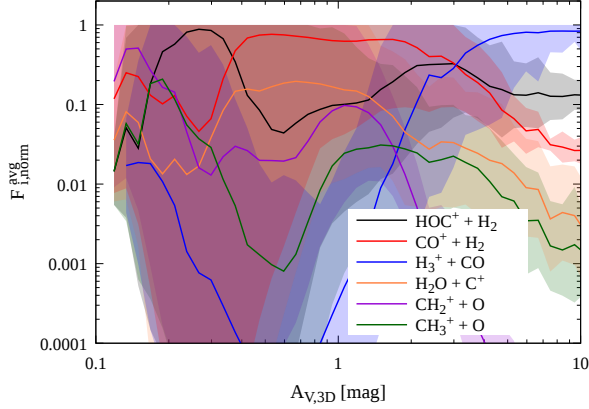


Figure 8. The normalized average reaction flux $F_{i, \text{norm}}^{\text{avg}}$ (see Eq. 12) of reactions in the post-processing network which produce HCO^+ , vs. visual extinction, for cloud MC1-HD at $t_{\text{evol}} = 2$ Myr. We have neglected the contributions of reactions which are generally subdominant in their impact upon HCO^+ abundance. The dominant HCO^+ formation reaction is heavily dependent on the extinction. Up to $A_{V, 3D} \approx 0.4$, formation is dominated by $\text{HOC}^+ + \text{H}_2$ (black). Then up to $A_{V, 3D} \approx 3$, the reaction $\text{CO}^+ + \text{H}_2$ (red) is dominant. However, the actual production of HCO^+ below $A_{V, 3D} \approx 3$ is minimal: the formation species which contribute the greatest fraction of HCO^+ formation flux are uncommon at such low extinctions. Thus, most of the HCO^+ production in the cloud stems from the reaction $\text{H}_3^+ + \text{CO}$ (blue), which dominates above $A_{V, 3D} \approx 3$. This reaction represents more than 90% of the total production flux at the high extinctions where HCO^+ is actually present.

production flux by $A_{V, 3D} \approx 5$. This extinction magnitude is approximately where the tracer particles whose trajectories are plotted in Fig. 4 experience an epoch of in situ HCO^+ formation.

The H_3^+ reaction can also produce HOC^+ at an equal rate, the isomerization of which contributes most of the remaining HCO^+ production flux at $A_{V, 3D} \gtrsim 5$. Comparing the reaction rates, we attribute about half of the HOC^+ which is then isomerized to HCO^+ at very high extinction to the $\text{H}_3^+ + \text{CO}$ reaction. As will be shown in Section 5.3, more than 90% of all HCO^+ by mass is found above $A_{V, 3D} \approx 5$, meaning the $\text{H}_3^+ + \text{CO}$ reaction is by far the most important driver of the cloud’s total HCO^+ content.

To further investigate this reaction, in Fig. 9 we analyse the distribution and evolution of H_3^+ in cloud MC1-HD. We again investigate the history of the H_3^+ distribution using the tracks followed by the same 50 tracer particles as in Fig. 4. Comparing the two figures, we see that the selected tracers (which were chosen for having a high value of $f(\text{HCO}^+)$ at late times) display the same bulk behavior in the growth of their H_3^+ content. Assuming the chemical state is near equilibrium at late times, the density of H_3^+ is decoupled from $n_{\text{H, tot}}$ (Oka 2006), explaining why $f(\text{H}_3^+)$ declines later in the simulation at high density ($\log A_{V, 3D} \approx 0.5$). This decline may explain some of the corresponding decline in $f(\text{HCO}^+)$ above $\log A_{V, 3D} \approx 0.5$ seen in Fig. 4, given that the reaction $\text{H}_3^+ + \text{CO}$ contributes the most to the HCO^+ formation in this $A_{V, 3D}$ regime (see Fig. 8). Since H_3^+ is less abundant than CO, the decline in H_3^+ would bottleneck this reaction.

When the reaction flux analysis is repeated for cloud MC1-MHD at $t_{\text{evol}} = 2$ Myr, the relative importance of the reactions is unchanged from the HD case. However, the crossover point where $\text{H}_3^+ + \text{CO}$ becomes the dominant reaction is instead at visual ex-

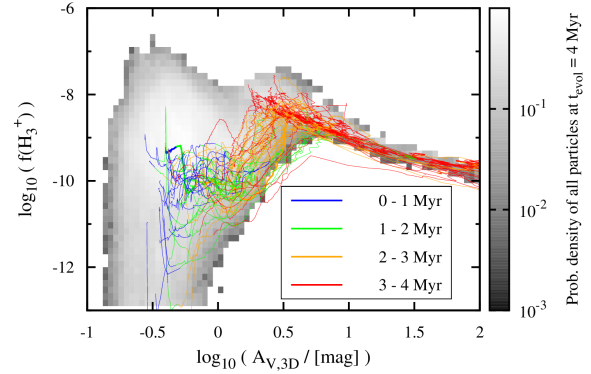


Figure 9. Same as Fig. 4, but showing tracer history tracks of H_3^+ fractional abundance vs. $A_{V, 3D}$ in cloud MC1-HD for the same representative random sample of tracer particles, plotted over a 2D probability density function of $f(\text{H}_3^+)$ vs. $A_{V, 3D}$ for every tracer particle in the simulation at $t_{\text{evol}} = 4$ Myr. As the less abundant reactant in the $\text{H}_3^+ + \text{CO}$ reaction, the available H_3^+ content bottlenecks the formation of HCO^+ by this route.

tingtion $A_{V, 3D} \approx 4$. Later, at $t_{\text{evol}} = 4$ Myr, this reaction becomes dominant at $A_{V, 3D} \approx 3$, the same as cloud MC1-HD. We attribute this effect to the slower coalescence rate of the MHD clouds compared to the HD clouds (Seifried et al. 2020). The ongoing cloud coalescence increases the abundances of H_3^+ and CO, fueling this reaction at lower and lower extinctions as time passes. We note that we find analogous results for the flux of $\text{H}_3^+ + \text{CO}$ vs. time in the clouds MC2-HD and MC2-MHD.

5 WHERE CAN HCO^+ BE FOUND?

In the previous section, we use our non-equilibrium chemical post-processing tools to explore the formation density regime, the formation time-scale, and the visual extinction-dependent dominant formation reactions of HCO^+ . Next, we wish to compare the distribution of HCO^+ to molecular cloud observations (e.g. Sanhueza et al. 2012; Gerin et al. 2019; Goicoechea et al. 2019; Barnes et al. 2020; Liu et al. 2020a,b; Nayana et al. 2020; Yun et al. 2021; Yang et al. 2021, and others). To do so, however, we must transform our ensemble of passive tracer particles into a comprehensive, space-filling array of number densities (hereafter ‘density grid’). Unlike SPH particles, these tracers do not represent mass and cannot be regridded the same way as SPH particles. A different approach is necessary, which we present in Section 5.1, followed by validations in Section 5.2. Finally, in Section 5.3, we present HCO^+ column density projections and compare them to observations.

5.1 The regridding algorithm

Because passive tracer particles – as opposed to particles in SPH simulations – do not represent fluid elements and thus are not associated with a certain quantity of mass or volume, we have developed a novel algorithm which maps the tracer particle back on a volume-filling grid. This procedure has several steps:

- (i) Generation of a blank, uniformly-resolved grid whose spatial extent matches the zoom-in region.

- (ii) Assignment of a desired species' fractional abundance from the tracer particles to the spatially-corresponding blank cells.
- (iii) Interpolation and extrapolation of the fractional abundance values of cells containing tracer particles into adjacent empty cells.
- (iv) Repetition of the interpolation procedure (iii) until the entire grid is filled with fractional abundance values.
- (v) Multiplication of the volume-filling fractional abundance grid with a corresponding, congruent grid of $n_{\text{H,tot}}$, generating a volume-filling, uniform number density grid of the considered species.

We now describe these steps in more detail. First, we define a grid domain and a uniform cell resolution, and select a time snapshot. The natural domain choice for this study is the exact extent of each zoom-in region. To explore the relationship between the resolution and the obtained species masses of the final grid, we tested uniform cell resolutions of 1, 0.5, 0.25, and 0.125 pc, for which the regridding procedure is conceptually identical.

A blank grid of the selected shape and resolution is initialized. We assign the particle's saved value for f_i to the corresponding cell in the blank grid. We choose to assign the fractional abundance values, rather than the naively more obvious choice of the number densities n_i , to avoid overestimating species densities at the diffuse frontiers of the molecular cloud. This will be explained in the interpolation phase of the algorithm. When $N > 1$ tracer particles occupy the same grid cell, their f_i values are logarithmically averaged:

$$\langle f_i \rangle = \exp \left(\frac{1}{N} \sum_j^N \ln f_{i,j} \right) \quad (13)$$

This logarithmic average prevents the higher f_i of two (or more) tracers from dominating the average abundance in a cell. This helps to avoid an overestimation of the total species mass in the given cell (see Section 5.2).

Merely regridding the tracer particle data is insufficient to fill the entire zoom-in domain due not only to the limited number of particles contained in the simulations, but also to the aforementioned tendency of tracer particles to congregate as the clouds contract over time. The densest regions of the clouds exhibit the best number statistics, but even here some cells lack direct tracer data. This issue worsens with increasing resolution. For instance, at a resolution of 0.125 pc, the zoom-in region for MC1-HD is split into more than 3×10^8 cells, but at an elapsed time of 2 Myr, only contains about 3×10^5 particles. Even neglecting the congregation of particles at density peaks, this represents a maximal filled proportion of 0.1%.

To remedy this, we iteratively interpolate the *fractional abundances* into adjacent empty cells, until the entire grid is filled. In this phase of the algorithm, each empty cell checks all 26 neighbouring cells for a nonzero value. If a single nonzero neighbour is found, that neighbour's f_i value is copied into the empty cell. If there are nonzero $N_{\text{neighbour}} > 1$, we calculate the final f_i value as:

$$\langle f_i \rangle = \exp \left(\frac{1}{\sum_j \frac{1}{d_j}} \sum_j^{N_{\text{neighbour}}} \frac{\ln f_{i,j}}{d_j} \right), \quad (14)$$

where d_j is the distance between the centroids of the empty cell and each neighbouring cell, divided by the cell resolution. During our tests, we found that the logarithmic averages recover the masses better than simple averages.

We emphasize that during each interpolation pass, the empty cells all assess their neighbours independently. If a pair of adjacent empty cells A and B share a single nonzero neighbour C, the value interpolated into A on this step from C will not simultaneously be considered

by B as it looks for its own nonzero neighbours. This avoids any dependence on the sweeping order of the interpolation, i.e., whether the pixels are interpolated, for instance, in the order x - y - z as opposed to z - y - x .

Since the density of tracer particles is lower in regions of low gas density, the interpolation procedure might need to assign values to empty grid cells from a tracer that is located several cells away, in a higher density region. Hence, if we had tried to generate a uniform grid by interpolating values for the *number density* of a target species, we would have unrealistically filled diffuse zones with gas that was not present in the SILCC-Zoom simulations of the same clouds, violating mass conservation. To avoid this, we found it to be crucial to interpolate merely f_i , and generate the number densities in a final step as follows.

The interpolation procedure repeats until the entire uniform grid is filled with nonzero values for f_i , and no empty cells remain. To convert this grid to the desired final n_i distribution, we multiply the filled grid of f_i values by another grid of identical size and resolution, which contains $n_{\text{H,tot}}$ obtained from the original simulation data. Since the identity of the target species is irrelevant to the operation of this algorithm, we can thus produce self-consistent density distributions for *any* species whose abundances are saved to the tracer particles.

Compared to the chemical post-processing of the tracer particle data, this regridding procedure has a negligible computational cost even at our highest resolution of 0.125 pc. Critically, the regridding cost is independent of the complexity of the post-processing network. Time-dependent density distributions for even the most exotic species can therefore be computed with great efficiency.

5.2 Validation

A critical validation of the interpolation procedure is whether it conserves the total hydrogen and carbon in the molecular cloud. The post-processing procedure allocates the hydrogen and carbon atoms into more species than were originally present in the on-the-fly network, but the total quantity of each element is unchanged by that procedure. Failures in conservation due to the interpolation process must be well-understood and minimized.

To check this, we revisit the original SILCC-Zoom simulations and calculate the total mass of hydrogen, $M_{\text{SILCC,H,tot}}$ from the sum of the masses of H, H₂, and H⁺; as well as the carbon mass, $M_{\text{SILCC,C,tot}}$, from the sum of C, C⁺, and CO (subtracting the mass of the oxygen atom). The SILCC-Zoom simulation grids, which contain cells with volumes dV_i that depend on the refinement level, report the mass density ρ_i in each cell for a given species. We calculate the total masses of hydrogen and carbon reported by the SILCC-Zoom grids at a given time as:

$$M_{\text{SILCC,H,tot}} = \sum_i^N (\rho_{\text{i,H}} + \rho_{\text{i,H}_2} + \rho_{\text{i,H}^+}) dV_i, \quad (15)$$

$$M_{\text{SILCC,C,tot}} = \sum_i^N \left(\rho_{\text{i,C}} + \frac{12}{28} \rho_{\text{i,CO}} + \rho_{\text{i,C}^+} \right) dV_i, \quad (16)$$

where the prefactor on $\rho_{\text{i,CO}}$ accounts for only considering the mass of the molecule's carbon atom.

We wish to compare these total mass values to those of our regridded, interpolated data. Because the regridded data are in units

of number density, the total regridded hydrogen and carbon mass equations are of a different form:

$$M_{\text{regrid,H,tot}} = m_p \sum_i^N (n_{\text{i,H}} + 2n_{\text{i,H}_2} + n_{\text{i,H}^+}) dV_i, \quad (17)$$

$$M_{\text{regrid,C,tot}} = m_p \sum_i^N 12 \left(n_{\text{i,C}} + n_{\text{i,CO,gas}} + n_{\text{i,CO,frozen}} + n_{\text{i,C}^+} \right) dV_i, \quad (18)$$

where the coefficients correspond to each term's molar mass contribution to the total hydrogen and carbon masses respectively, and m_p is the proton mass. We include the post-processed number density of the CO frozen onto dust grains because this can be comparable to the gas-phase density of CO in the densest regions of the cloud, particularly at late t_{evol} . None of the other carbon-bearing species contain more than 0.1% of the total carbon mass, and can be safely neglected when comparing $M_{\text{SILCC,C,tot}}$ and $M_{\text{regrid,C,tot}}$.

First, we analyse the regridded masses of CO and C as a function of the regridding resolution. We find that for resolutions coarser than 0.125 pc, the regridded CO mass – and to a lesser extent also the regridded mass of atomic carbon – do not converge well for either HD or MHD clouds (not shown here), falling below their values in the 0.125 pc resolution grid by up to a factor of 2. We attribute this to the highly concentrated nature of the CO content. If the cells are too large to resolve sub-parsec scale density peaks, the tracer averaging procedure will smooth out these peaks and report a peak value for n_{CO} which is too low. As we have shown, HCO^+ and CO occupy similar density regimes, and we would therefore expect errors of a similar magnitude in HCO^+ at low resolutions. Thus, we restrict ourselves hereafter to our maximal regridding resolution of 0.125 pc.

Next, we assess the effectiveness of the regridding procedure at recovering the total hydrogen and carbon masses of the simulated clouds by taking the ratio of $M_{\text{regrid}}/M_{\text{SILCC}}$ for different clouds at different timesteps. We display these results in Fig. 10, as a function of the number of interpolation steps, n_{steps} . Results are presented at $t_{\text{evol}} = 2$ Myr (dashed lines) and $t_{\text{evol}} = 4$ Myr (solid lines). Finally, we include the results when the tracers' unprocessed, NL99 abundances are regridded directly (dotted lines), without any of the post-processing described in Section 3. This separates the mass conservation impact of the regridding procedure from the question of redistribution of hydrogen and carbon atoms into other species that are only present in the post-processing network, and not in NL99.

For cloud MC1-HD, the total hydrogen mass is recovered to impressive accuracy at $t_{\text{evol}} = 2$ Myr, within 1% for both the unprocessed and post-processed tracers. The carbon mass represented by C, CO, and C^+ at the same time converges to within 5% of the original M_{SILCC} , and the NL99 value to within 3%, indicating that about 1–2% of the carbon has been distributed to other species by post-processing. This difference is not seen in the more diffuse cloud MC1-MHD at $t_{\text{evol}} = 2$ Myr, where the total regridded carbon masses from both the NL99 and post-processed grids are about %2 below the SILCC carbon total. It therefore appears that the redistribution of carbon is occurring in very dense gas, which MC1-MHD at $t_{\text{evol}} = 2$ Myr almost entirely lacks.

At $t_{\text{evol}} = 4$ Myr, the accuracy of the regridding process is lower. The total regridded hydrogen mass of both MC1-HD and MC1-MHD converges to 2–3% below the SILCC hydrogen mass. Carbon performs worse than hydrogen at this late time, with the total regridded carbon mass falling below the SILCC mass by $\sim 8\%$ in MC1-HD

and $\sim 17\%$ in MC1-MHD. We attribute this to the aforementioned importance of high resolution in the neighbourhood of dense peaks, which are well-developed by this point in both the HD and MHD clouds. Even in the densest regions of the clouds, the tracers occupy only a small fraction of the cells at the 0.125 pc resolution, and the interpolation procedure may miss some dense pockets of CO.

We find that M_{regrid} converges by the eighth interpolation step to within one percent of their final values when the grid is totally full. This suggests the remainder of the interpolation procedure, which is predominated by interpolation into low-density cells on the frontier of the zoom-in region (and takes between 70 and 200 more interpolation steps at a resolution of 0.125 pc), could be skipped without sacrificing precision in the final total mass. For the clouds MC1-HD and MC1-MHD at $t_{\text{evol}} = 2$ Myr, this respectively amounts to 87% and 94% interpolation steps which we perform but which have a minimal impact upon the final result.

We can validate the method further by another plot of the average fractional abundance of H, H_2 , C, CO, and C^+ vs. $n_{\text{H,tot}}$ for the molecular cloud MC1-HD at $t_{\text{evol}} = 2$ Myr, this time analysing the interpolated grids (Fig. 11). In general, we find similar outcomes to the post-processed particle results shown in the right panel of Fig. 3. The ratios of these mean fractional abundances after regridding to the mean fractional abundances of the post-processed tracers before regridding are plotted in Appendix B, in the right panel of Fig. B1.

For each carbon species, the similarity is lowest in the regime where the species is not the dominant representative of that element. Hence, the interpolated grid reflects the tracer values for CO least well at low densities where CO is rare, and the values for atomic carbon least well at high densities, where CO is saturated. We speculate that this occurs because the interpolation process introduces a certain degree of noise into the abundance profiles, which can be commensurate in scale to the true signal of a species in a regime where its fractional abundance is low.

The accuracy of the regridding technique at preserving species' fractional abundances in their dominant density regimes supports our approach described in Section 5.1, in spite of the shortcomings we have discussed. The computational cost of simulating larger chemical networks on-the-fly is simply prohibitive at this time. Therefore, we choose to accept a certain degree of inaccuracy and uncertainty as this is the only way to obtain filled, 3D density data for complex species that are not present in smaller chemical networks.

Finally, in Fig. 12, we show the time-dependent total mass of H_2 (top), CO (middle, the sum of the gaseous and frozen-out states), and HCO^+ (bottom) inside each simulation's zoom-in region. The masses are given at $t_{\text{evol}} = 2, 3$, and 4 Myr. The exception is MC2-HD, which terminated at a final time of $t_{\text{evol}} = 3.76$ Myr. The total masses of H_2 and CO at the different time snapshots correspond to the masses given for the clouds in their originating papers (Seifried et al. 2017b, 2020, especially figure 2 of the latter), with deviations of $\sim 10\%$ ascribed to the effects of post-processing and the uncertainties introduced in the regridding process.

In the bottom panel of Fig. 12, we report the time-dependent total mass of HCO^+ in the four simulated clouds, a novel result. The increase in HCO^+ mass resembles the increase in CO mass, underscoring the close link between the two species. The HD clouds already possess some HCO^+ at $t_{\text{evol}} = 2$ Myr, but the MHD clouds have negligible HCO^+ content. Only at later times have the MHD clouds condensed enough that their cores are sufficiently well-shielded for the formation of CO, and also of HCO^+ . The fractional abundance of HCO^+ (with respect to all hydrogen nuclei) averaged over each cloud is as low as $\sim 10^{-12}$ (the MHD clouds at early times) and as high as $\sim 1.3 \times 10^{-9}$ (the HD clouds at late times).

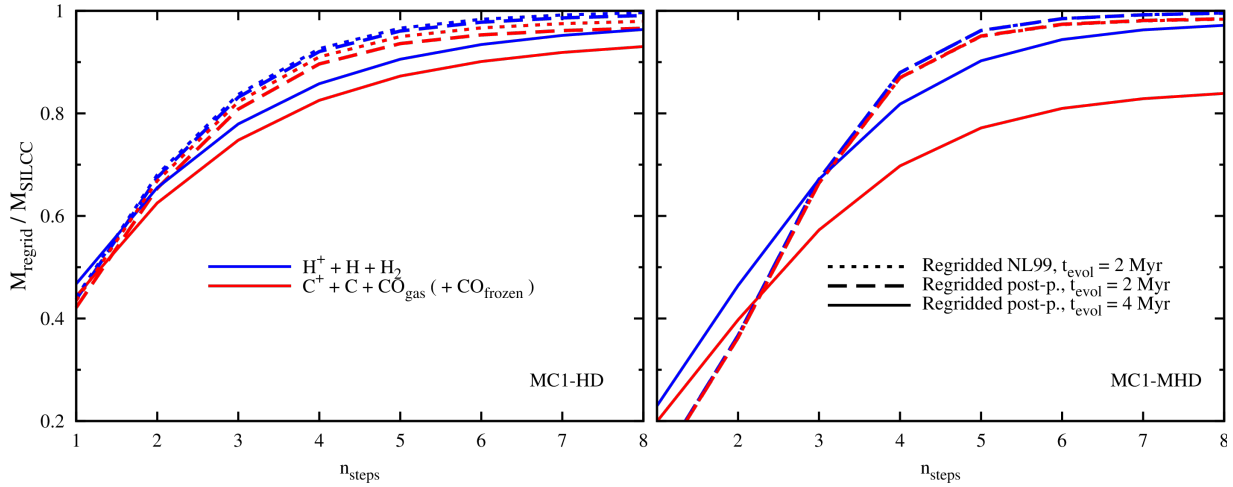


Figure 10. The ratios $M_{\text{regrid},\text{H,tot}}/M_{\text{SILCC},\text{H,tot}}$ (blue) and $M_{\text{regrid},\text{C,tot}}/M_{\text{SILCC},\text{C,tot}}$ (red) from Eqs. 15–18, vs. the cumulative number of interpolation steps, n_{steps} , for MC1-HD (left) and MC1-MHD (right). Results are provided for the post-processed tracers at $t_{\text{evol}} = 2$ Myr (dashed) and 4 Myr (solid), along with the result after regridding the tracer particles’ unprocessed NL99 abundances (dotted). The contribution of frozen-out CO is included for $M_{\text{regrid},\text{C,tot}}$, since the species contains a non-negligible amount of the total carbon after post-processing. For MC1-MHD, the 2 Myr results for NL99 and the post-processed data are virtually indistinguishable. In general, the regridding reproduces the masses with an accuracy of $\sim 10\%$.

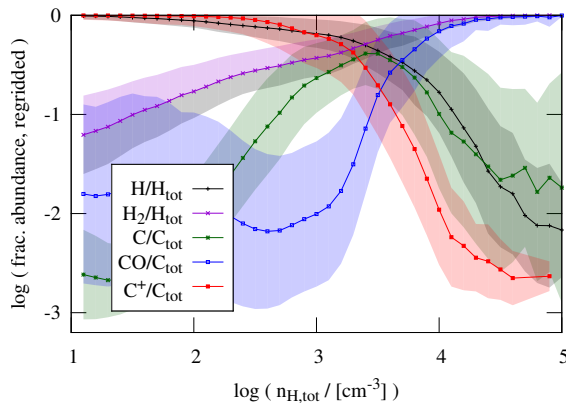


Figure 11. Same as Fig. 3, but for the post-processed abundances from the reconstructed grids after the interpolation is complete. Comparing to the right-hand panel of Fig. 3, which shows the post-processed tracer abundances, our regridding algorithm is generally successful at recovering f_i for each species in the regime where that species is most abundant. However, the two data sets are less congruent for each species in regimes where the species is less abundant. In particular, CO is over-represented at lower densities, and C is under-represented at the highest densities.

5.3 The HCO⁺ column density

With these tracer-derived density grids, we can produce column density maps of species that were not present in the on-the-fly network. In Appendix C, we compare column density maps of the post-processed H_{tot} , H, H_2 , and CO abundances in cloud MC1-HD to the results shown in Seifried et al. (2017b). Our results are in good agreement with the original maps. As predicted in that work, post-processing the on-the-fly results for these species did not have a large impact upon the abundances.

Next, in Fig. 13, we show – to our knowledge – the first-ever maps of the HCO⁺ column density, $N(\text{HCO}^+)$, in simulated molecular clouds. Since we show in Fig. 4 that much of the HCO⁺ formation in both MC1-HD and MC1-MHD takes place around $t_{\text{evol}} \approx 2\text{--}3$ Myr with a formation time-scale of $\tau \approx 1$ Myr, we choose to examine the column density maps at $t_{\text{evol}} = 4$ Myr, i.e. after the principal epoch of HCO⁺ formation. The distributions of HCO⁺ in MC1-HD (top row) and MC1-MHD (bottom row) showcase the ‘fluffier’ distribution seen in MHD simulations compared to hydrodynamic ones (Seifried et al. 2020; Ganguly et al. 2022). Regions with $N(\text{HCO}^+) < 10^9 \text{ cm}^{-2}$ have been masked in white. The maximal HCO⁺ column density in both clouds is on the order of 10^{15} cm^{-2} . The dense regions ($N(\text{HCO}^+) > 10^{12} \text{ cm}^{-2}$) in MC1-HD are clumpy, with lower-density regions (where $N(\text{HCO}^+) = 10^9\text{--}10^{11} \text{ cm}^{-2}$) only extending short distances from the peak sites. On the other hand, in MC1-MHD, the HCO⁺ is far more extended, forming a diffuse envelope tens of parsecs out from the filamentary structures where $N(\text{HCO}^+)$ is maximal.

In Fig. 14, we contextualize our findings for $N(\text{HCO}^+)$ in relation to the column densities of other species. The average values of $N(\text{HCO}^+)$ from the y - z projections of MC1-HD (red) and MC1-MHD (green) at $t_{\text{evol}} = 4$ Myr are plotted against $N(\text{H}_{\text{tot}})$ (left), $N(\text{H}_2)$ (middle), and $N(\text{CO})$ (right). The results for MC1-HD at $t_{\text{evol}} = 2$ Myr (black) are plotted as well. Most pixels with $N(\text{H}_{\text{tot}}) \approx N(\text{H}_2) \approx 10^{21} \text{ cm}^{-2}$ have $N(\text{HCO}^+)$ values between 10^9 and 10^{11} cm^{-2} . For $N(\text{H}_{\text{tot}}) \gtrsim 10^{21} \text{ cm}^{-2}$ and $N(\text{CO}) \gtrsim 10^{17} \text{ cm}^{-2}$, $N(\text{HCO}^+)$ increases to maximal values of around 10^{15} cm^{-2} . Comparing the results at $t_{\text{evol}} = 2$ Myr and $t_{\text{evol}} = 4$ Myr for MC1-HD, we see that $N(\text{HCO}^+)$ increases over time, as expected following the results in Section 4. The values of $N(\text{H}_{\text{tot}})$, $N(\text{H}_2)$, and $N(\text{CO})$ above which $N(\text{HCO}^+)$ quickly reaches its peak remain constant in time, however.

A systematic comparison of our results with observations is reserved for Section 5.3.3, but we provide some measurements by Yang et al. (2021) in the middle panel of Fig. 14. They measured $N(\text{HCO}^+)$

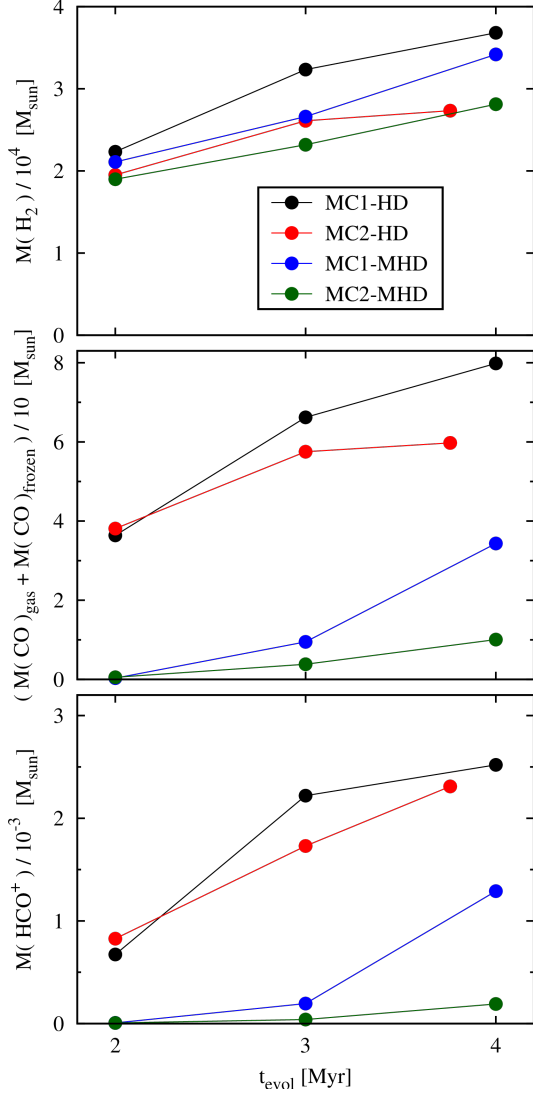


Figure 12. The masses of H_2 (top), all CO (middle), and HCO^+ (bottom) in the zoom-in regions of the four simulated clouds, vs. t_{evol} . These values are calculated by summing over the density grids produced by regriding the post-processed tracer particles. The CO mass represents the sum of the gaseous and frozen-out states. The masses of H_2 and CO generally correspond to the values in the SILCC-Zoom clouds themselves (Seifried et al. 2017b, 2020). The character of the HCO^+ growth resembles that of the CO growth, emphasizing that they exist in the same extinction regime.

for infalling cores, vs. $N(\text{H}_2)$ derived from dust continuum measurements. We find that our data match their observations well, with peak values of $N(\text{HCO}^+) \approx 10^{15} \text{ cm}^{-2}$ around $N(\text{H}_2) \approx 10^{22} \text{ cm}^{-2}$.

5.3.1 The distribution of HCO^+

Next, we study the cumulative mass distribution of HCO^+ as a function of the observed visual extinction using the relation $N(\text{H}_{\text{tot}}) = (1.87 \times 10^{21} \text{ cm}^{-2}) A_V$ (Draine & Bertoldi 1996, also as used in the SILCC-Zoom chemical network; see Section 2.1). In Fig. 15 we show the fraction of mass sitting below a certain A_V -threshold for the

cloud MC1-HD at $t_{\text{evol}} = 2$ Myr (solid lines) and $t_{\text{evol}} = 4$ Myr (long dashes), and cloud MC1-MHD at $t_{\text{evol}} = 4$ Myr (short dashes). Each color represents a different projection. We see that for MC1-HD at $t_{\text{evol}} = 2$ Myr, the HCO^+ distribution varies for different projections, with the first quartile being reached at A_V values of 8–20. The third quartile is typically reached around $A_V = 20$ –50. At $t_{\text{evol}} = 4$ Myr, the different projections correspond much more closely. The third quartile value remains almost unchanged, but the first quartile value is now systematically lower, around $A_V \approx 5$. This indicates that a significant amount of HCO^+ has formed between the two snapshots at lower extinctions, widening the average interquartile range. We repeat this procedure for the other simulated clouds, and found similar results. The lines for the three projections for the MHD clouds are still dissimilar at $t_{\text{evol}} = 4$ Myr, as expected given these clouds’ longer time-scale of gravitational collapse compared to the HD case. On average, we find that 50% of the HCO^+ mass – corresponding to the average interquartile range – lies between $A_V \sim 10$ and ~ 30 .

In the right-hand panel of Fig. 15, we plot again the cumulative mass of HCO^+ , but this time using the values of n_{HCO^+} and $n_{\text{H,tot}}$ from the 3D density grids rather than column density projections. The same time-dependent qualitative relationship is seen as in the left-hand panel. This indicates again that HCO^+ is being formed over time outside the very dense regions. Overall, we find that 50% of the HCO^+ is located at $n_{\text{H,tot}} \sim 10^{3.5} - 10^{4.5} \text{ cm}^{-3}$.

5.3.2 Resolution effects

Our resolution in the maps in Fig. 13 is 0.125 pc, up to one or two orders of magnitude higher than what is available in many observations (e.g. Barnes et al. 2020; Sanhueza et al. 2012; Nayana et al. 2020). To improve the comparison of our data to such observations, we convolve our maps of $N(\text{HCO}^+)$ with a Gaussian filter. By selecting the size of the filter, we can emulate any coarser resolution.

In Fig. 16, we show one of our 0.125 pc resolution $N(\text{HCO}^+)$ maps altered in this way to emulate resolutions of 3 pc (top) and 10 pc (bottom). We apply these convolution to the y - z projection of MC1-HD at $t_{\text{evol}} = 4$ Myr, corresponding to the top right panel of Fig. 13. As the resolution decreases, the filamentary-scale structures (~ 0.1 pc) lose their intricate detail, and adjacent density peaks (for instance the two small neighbouring peaks in the upper left of the cloud) become unresolved. The complex distribution of HCO^+ in the more diffuse areas where $N(\text{HCO}^+) = 10^9 - 10^{11} \text{ cm}^{-2}$ becomes smoother as well. The peak $N(\text{HCO}^+)$ value remains around 10^{15} cm^{-2} for all resolutions. However, at a resolution of 10 pc, only the very densest and clumpiest regions retain this peak column density, which is found along the lengths of the filamentary structures in the 0.125 pc resolution map.

Next, in Fig. 17 we repeat the comparison of $N(\text{HCO}^+)$ with $N(\text{H}_{\text{tot}})$, $N(\text{H}_2)$, and $N(\text{CO})$ which we performed in Fig. 14. This time, however, we restrict ourselves to the y - z projection of MC1-HD at $t_{\text{evol}} = 4$ Myr, and compare the average column densities at a resolution of 0.125 pc (black) to the column densities from maps emulating resolutions of 3 pc (red) and 10 pc (green). Decreasing the resolution causes the ratios between $N(\text{HCO}^+)$ and the other column densities to increase, due to the Gaussian broadening of the central features with high HCO^+ density. This effect implies that low-resolution observations outside the densest regions of a molecular cloud would measure higher values for $N(\text{HCO}^+)$ than are physically present.

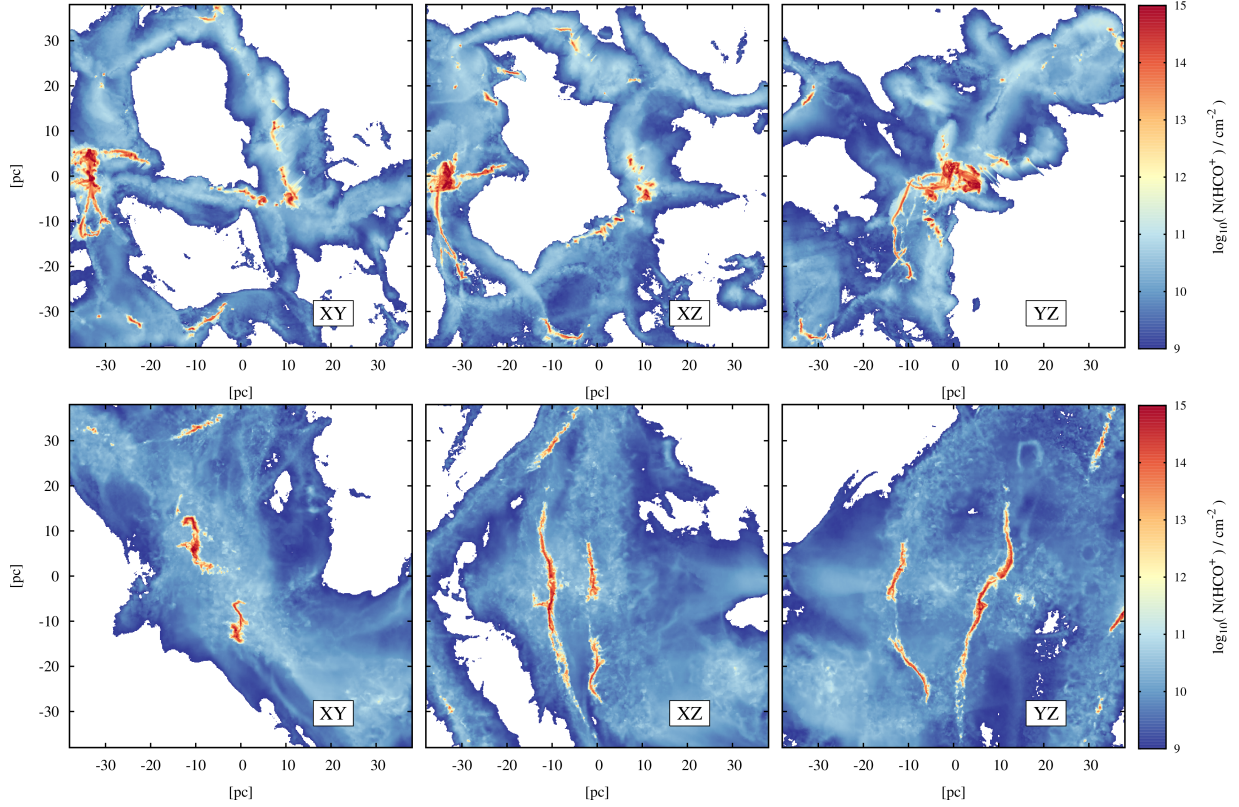


Figure 13. Maps of the column density of HCO⁺ for clouds MC1-HD (top row) and MC1-MHD (bottom row) at $t_{\text{evol}} = 4$ Myr. The three columns show projections in the x - y , x - z , and y - z planes respectively. Both clouds reach maximal values of $N(\text{HCO}^+) \approx 10^{15} \text{ cm}^{-2}$. The dense regions traced by HCO⁺ in MC1-HD are clumpy in shape, while the core distributions in MC1-MHD are more filamentary. Regions with $N(\text{HCO}^+) < 10^9 \text{ cm}^{-2}$ have been masked in white, underlining the more diffuse distribution of the molecular gas in the MHD simulation compared to the HD simulation.

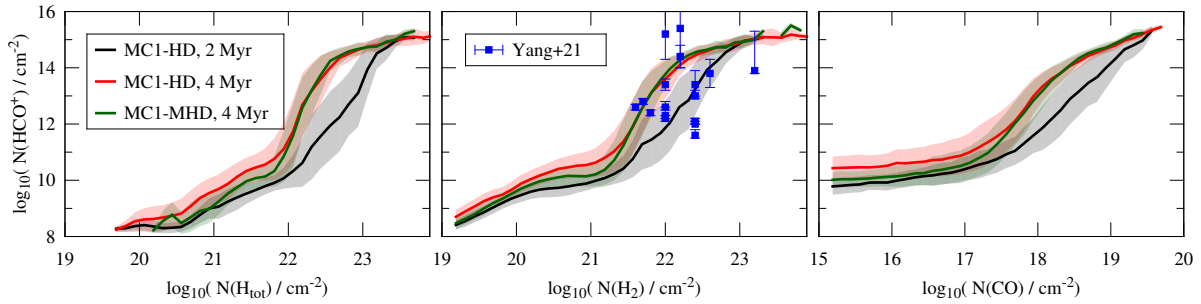


Figure 14. The average column densities of HCO⁺ for the y - z projection of the molecular clouds MC1-HD at 2 Myr (black) and 4 Myr (red) and MC1-MHD at 4 Myr (green), vs. the column densities of H_{tot} (left), H_2 (middle), and CO (right). The shaded areas represent one standard deviation from the respective average. In the middle panel, we overplot the observations of Yang et al. (2021) of infalling prestellar cores. Overall, we can see a significant increase in $N(\text{HCO}^+)$ for $N(\text{H}_{\text{tot}}) \sim N(\text{H}_2) \gtrsim 10^{21} \text{ cm}^{-2}$, and $N(\text{CO}) \gtrsim 10^{17} \text{ cm}^{-2}$. Clouds at later evolutionary stages have somewhat more HCO⁺ at given H_{tot} , H_2 , and CO column densities.

5.3.3 Comparison to observations of W49A

Transforming our column density results to match the resolution of observations allows us to make direct comparison to measurements of $N(\text{HCO}^+)$ in nature. For this purpose, we present values for $N(\text{HCO}^+)$

in the massive star-forming region W49A, as observed during the LEGO project (Barnes et al. 2020; see also Kauffmann et al. 2017).

The W49A observations were performed by the IRAM 30m telescope at a resolution of $\sim 30''$, then smoothed to $60''$, which corresponds to physical scales of ~ 3 pc at the cloud's distance of 11 kpc

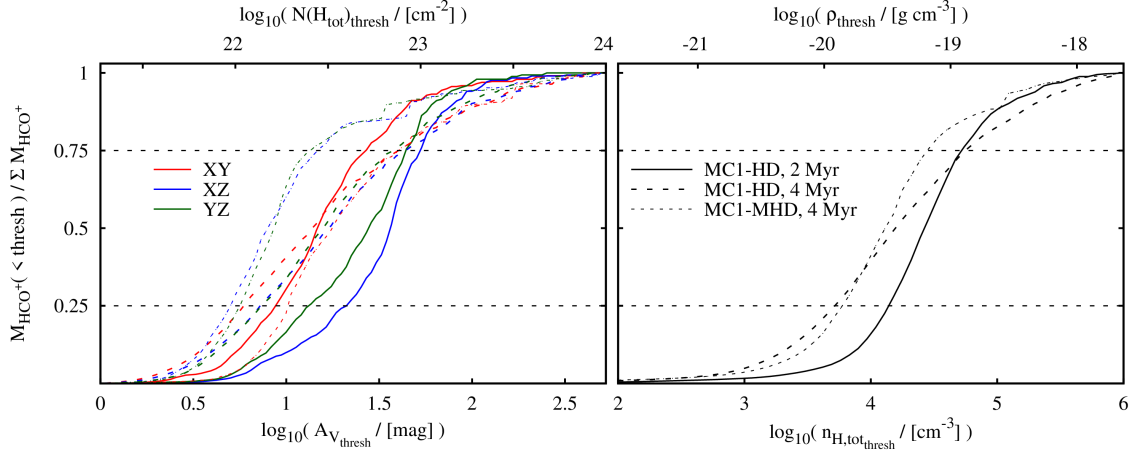


Figure 15. The cumulative mass fraction of HCO^+ vs. A_V (left) and $n_{\text{H,tot}}$ (right) for molecular cloud MC1-HD at $t_{\text{evol}} = 2$ Myr (solid lines) and $t_{\text{evol}} = 4$ Myr (large dashes), and cloud MC1-MHD at $t_{\text{evol}} = 4$ Myr (small dashes). The three colors in the left-hand plot indicate different projections. The values for A_V are calculated from projections of $N(\text{H}_{\text{tot}})$ via the relation $N(\text{H}_{\text{tot}}) = (1.87 \times 10^{21} \text{ cm}^{-2}) A_V$ (Draine & Bertoldi 1996), and the corresponding HCO^+ mass is calculated from the projections of $N(\text{HCO}^+)$. In the right-hand plot, the values for $n_{\text{H,tot}}$ are given by a 3D density grid, and the corresponding HCO^+ mass is calculated from a 3D grid of n_{HCO^+} . At $t_{\text{evol}} = 2$ Myr, the cumulative distribution of the HCO^+ is highly dependent on the viewing angle. At $t_{\text{evol}} = 4$ Myr, the HCO^+ distributions have become considerably more similar. The average interquartile range (containing 50% of the HCO^+ mass) for A_V ranges from ~ 10 to ~ 30 increasing slightly over time. Corresponding relations between the HCO^+ mass and $n_{\text{H,tot}}$ are seen in the right-hand plot. Cloud MC1-MHD, which condenses more slowly than the hydrodynamic cloud MC1-HD, contains a greater fraction of its total HCO^+ at lower A_V or $n_{\text{H,tot}}$.

(Zhang et al. 2013). We calculate the values of $N(\text{HCO}^+)$ from the $\text{HCO}^+ J = 1 \rightarrow 0$ emission (Neumann et al. in prep.), which has a high signal-to-noise ratio across much of the W49 region. We calculate the optical depth of the line using corresponding observations of $\text{H}^{13}\text{CO}^+(1-0)$ emission. Where the H^{13}CO^+ emission is below the noise level (corresponding to $N(\text{H}_2) \lesssim 10^{22} \text{ cm}^{-2}$), we make the assumption that the line is optically thin to approximate the lower limit of the column density. We determine the excitation temperature of HCO^+ by minimizing the column density equation when using both the $J = 1 \rightarrow 0$ line from LEGO-IRAM (Barnes et al. 2020) and $J = 3 \rightarrow 2$ line from LEGO-APEX (Neumann et al. in prep.), since $N(\text{HCO}^+)$ should be the same when determined from both lines. We complement these data with dust continuum observations from the *Herschel Space Observatory* large program Hi-Gal (Molinari et al. 2011), also smoothed to a matched resolution of $60''$, to recover the molecular hydrogen column density (see Barnes et al. 2020). The complete details of the APEX observations and full calculation of the column densities will be presented in a future work (Neumann et al. in prep.).

In Fig. 18, we plot $N(\text{HCO}^+)$ vs. $N(\text{H}_2)$ for these observations, and for our simulations at resolutions of 0.125 pc and 3 pc (using Gaussian convolution as previously explained). For $N(\text{H}_2) \gtrsim 10^{22} \text{ cm}^{-2}$, our simulations match the observed values quite well. At the peak values of $N(\text{H}_2)$, our simulated data at a resolution of 3 pc (matching the physical resolution of the observations) are in slightly better agreement than at the original 0.125 pc resolution. The regions where $N(\text{H}_2) \lesssim 10^{22} \text{ cm}^{-2}$ are in less good agreement with our simulations. We attribute this to the fact that below $N(\text{H}_2) \approx 10^{22} \text{ cm}^{-2}$, the observed $N(\text{HCO}^+)$ were calculated with an optically thin assumption due to the lack of significant H^{13}CO^+ emission in that column density regime. An improved approximation for the optical depth where $N(\text{H}_2) \lesssim 10^{22} \text{ cm}^{-2}$ would likely lead to higher values of $N(\text{HCO}^+)$ there, thus presumably in better agreement with our simulated data.

6 CAVEATS AND FUTURE DIRECTIONS

Via comparison to column density observations of HCO^+ , we have shown that our post-processing and regridding algorithms can reconstruct the HCO^+ abundance in molecular clouds. Moreover, by post-processing the tracer particle abundances over individual timesteps, we consider the chemistry in a non-equilibrium approach and utilize the momentary environmental parameters like the density and temperature in our solutions to the rate equations. These factors are essential to a truly time-dependent chemistry. Despite our post-processing and regridding routines giving robust results when compared with theoretical benchmark results and observations, some caveats should be kept in mind.

The clearest formal inconsistency to our approach is the impact that post-processing could have on the local temperature and shielding. Our method fixes these values at each timestep, and does not attempt to update or re-model them based on the output abundances from post-processing. In principle, changing the abundance profile of e.g. CO could shift the thermal equilibrium of the gas. This could lead to dynamic motions, altering the shielding profile. We recognize this could be an issue with our method in general, but basing our chemistry on the NL99 network should alleviate the problem. Glover et al. (2010) list the numerous, well-studied thermal processes modeled in NL99 in their Table 1. Post-processing the NL99 chemistry does not much impact the abundances of species like C, C^+ , and CO which were already modeled in the original network (see Fig. 3). Thus, we assert that post-processing NL99 should not radically alter the density profiles of these thermally-relevant species. However, applying our post-processing method to a simulation with an on-the-fly network that has less-robust thermal modeling may lead to inconsistencies.

Before further work with this method is contemplated, it must be noted that the chemical network employed here to showcase the post-processing is still small. Containing only 37 gas-phase species, the

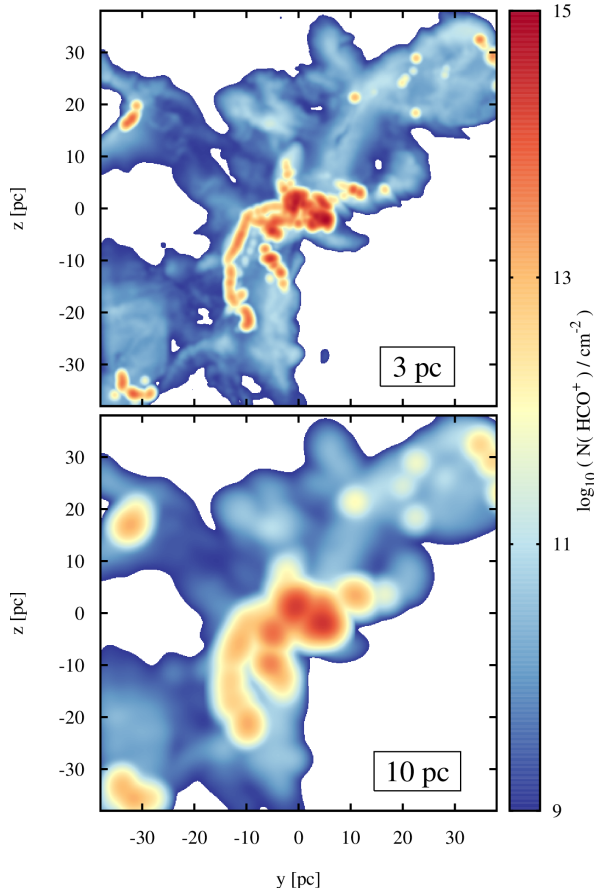


Figure 16. Column density maps of $N(\text{HCO}^+)$ from cloud MC1-HD at $t_{\text{evol}} = 4$ Myr (same as the top right panel of Fig. 13), but convolved with Gaussian filters of increasing beam size to emulate resolutions of 3 pc (top), and 10 pc (bottom). As resolution decreases, filamentary-scale structures become unresolved, and the peak $N(\text{HCO}^+)$ decreases as the beam samples surrounding areas of lower column density.

network most particularly lacks nitrogen, meaning that we cannot use this network to assess nitrogen-bearing dense gas tracers like HCN (Papadopoulos 2007; Godard et al. 2010; Kauffmann et al. 2017; Goicoechea et al. 2019). Silicon is included, but only in its elemental form rather than any molecular states. Overall, our network reproduces HCO⁺ observations well, but new, larger networks will need to be developed and validated with this method before the analysis techniques in this work can be applied more broadly.

However, ultimately one must balance the comprehensiveness of a chemical network with its practical usability in astrophysical simulations, which are already computationally expensive even before considering coupled or post-processed chemistry. Developing and validating this post-processing scheme required a chemical network with a reasonably short convergence time (Seifried & Walch 2016). Future works – for instance analysis of the time-dependent nature of deuterium fractionation, or the evolution of diffuse molecular gas tracers (Panessa et al., in prep) – will need larger and more comprehensive networks, which will need to be validated in turn.

We include a freeze-out approximation in our network, which

creates a noticeable difference in CO and H₂O abundance when compared to networks lacking these approximations (see Fig. 1, and Borchert et al. 2022), but the impact of grain chemistry on chemical abundances is complex (Flower et al. 2005; Bovino et al. 2017). In our network, the grains themselves are treated in a simple manner neglecting subtleties like ionization of the grains or changing sticking coefficients due to, e.g., the time-dependent variation in the composition of the ice mantles.

Another major factor in the post-processing outcome is the modeling of the CRIR. In our work, to assure that the thermal environment is mostly unchanged after post-processing, we must copy the value of the CRIR, $\zeta = 6 \times 10^{-17} \text{ s}^{-1}$, used in the reference SILCC-Zoom simulations. This is set to be constant, whereas Padovani et al. (2018) suggest a decrease in deeply embedded structures. A model for the CRIR which diminishes with (column) density would, for instance, impact the abundance profile of H₃⁺. As discussed in Section 4.4, the H₃⁺ abundance bottlenecks the high-extinction HCO⁺ abundance in our post-processing network via the dominant reaction H₃⁺+CO. Attenuation of the cosmic rays would diminish the H₃⁺ balance in dense gas and likely decrease the HCO⁺ density. Testing the importance of this effect will require new simulations run on-the-fly with an attenuated CRIR model.

Looking ahead, we intend to create synthetic emission maps from our regridded species data. This would provide us with a more direct comparison to observations, and properly account for the optical depth effects discussion in Section 5.3.3.

7 CONCLUSIONS

We present our novel chemical post-processing methodology for 3D-MHD simulations of the ISM and molecular clouds. This methodology provides non-equilibrium abundances for any species present in a chemical network of arbitrary complexity. In this work, we have applied our methods to investigating the time-dependent evolution of HCO⁺ in molecular clouds modeled in the SILCC-Zoom project. We summarize the methodology itself as follows:

- (i) Rather than post-process the instantaneous abundances of simulation snapshots, we post-process the abundances on tracer particles which are injected into the simulation. Because these tracers follow the gas flow, they report the time-dependent chemistry and dynamics of the local fluid environment.
- (ii) We use a chemical network of 39 species and 301 reactions to post-process the tracer particles' chemical abundances. This network includes many species of astrochemical interest, in particular HCO⁺. It also models the freeze-out of CO and H₂O on to dust grains.
- (iii) We use the chemical rate equation solver KROME (Grassi et al. 2014) to post-process the tracer abundances from the SILCC-Zoom simulations. The on-the-fly abundances of the hydrogen and carbon species are used to initialize the post-processing of each tracer particle. From that point on, we post-process the updated abundances directly at each time step.
- (iv) By advancing the chemistry over timesteps matching those of the simulation's particle snapshots, and using the time-dependent environmental parameters of the simulated cloud as inputs to the chemical network, we recover the non-equilibrium chemical state of the tracer particles over the entire history of the simulation.
- (v) We implement a subcycling routine to correct for large changes in the environmental parameters. This subdivides a tracer's evolution timestep if the local environmental parameters experience more than a user-defined percent change s . We show that the post-processed

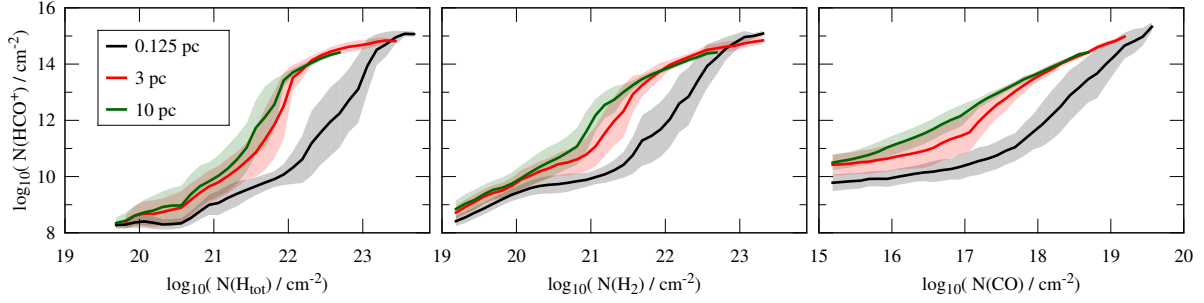


Figure 17. Same as Fig. 14, but only for the y - z projection of MC1-HD at $t_{\text{evol}} = 4$ Myr, convolved with Gaussian filters of increasing beam size to emulate resolutions of 3 pc (red) and 10 pc (green). The original resolution of 0.125 pc is repeated for comparison (black). As resolution decreases, higher values of $N(\text{HCO}^+)$ are found at given values of $N(\text{H}_{\text{tot}})$, $N(\text{H}_2)$, and $N(\text{CO})$.

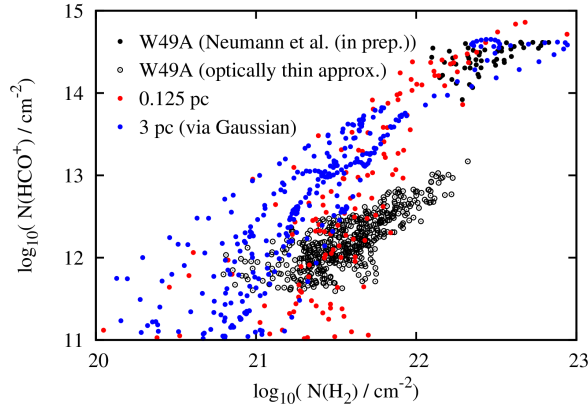


Figure 18. $N(\text{HCO}^+)$ vs. $N(\text{H}_2)$ for the y - z projection of MC1-HD at $t_{\text{evol}} = 4$ Myr at the original resolution of 0.125 pc (red) and convolved with a Gaussian filter to emulate a resolution of 3 pc (blue), compared to observations of the star-forming region W49A (Neumann et al. in prep.; see also Barnes et al. 2020) at a physical resolution of ~ 3 pc. Above $N(\text{H}_2) \approx 10^{22} \text{ cm}^{-2}$, the intensity of H^{13}CO^+ emission is sufficient to constrain the optical depth for the calculation of $N(\text{HCO}^+)$ (solid black). Below $N(\text{H}_2) \approx 10^{22} \text{ cm}^{-2}$, we approximate the emission as optically thin (empty black). The approximation represents a lower limit to the actual value of $N(\text{HCO}^+)$, and gradually conforms better to reality as $N(\text{H}_2)$ decreases further. Our simulations are in very good agreement with observations above $N(\text{H}_2) \approx 10^{22} \text{ cm}^{-2}$ where the optical depth is calculated explicitly, as well as around $N(\text{H}_2) \approx 10^{21} \text{ cm}^{-2}$ where the optically thin approximation is relatively accurate. Reducing the resolution of the modeled map to 3 pc (the same as the observations) with Gaussian convolution slightly improves the correspondence between the modeled and observed column densities.

abundances are generally converged for any value of s , and select a value of $s = 10\%$.

(vi) We present a novel algorithm to regrid a snapshot of the post-processed tracer abundances, using an iterative scheme to recover a volume-filling density grid, from which we make column density maps. We benchmark this algorithm against the masses of hydrogen and carbon in the original simulations, indicating an overall accuracy of better than $\sim 10\%$.

We can thus calculate non-equilibrium abundances for any species

in a chemical network of arbitrary size, for a fraction of the computational cost of running that network on-the-fly in 3D-MHD simulations. Throughout this paper, we have explored the evolution of the HCO^+ abundance in HD and MHD molecular clouds simulated in the SILCC-Zoom project. Our results include:

- (i) We find that HCO^+ predominantly forms at densities of $n_{\text{H,tot}} = 10^3\text{--}10^4 \text{ cm}^{-3}$. The formation of HCO^+ occurs in situ in this density range, rather than in a high density regime followed by turbulent mixing into lower-density regions. We show that the typical time-scale of HCO^+ formation is on the order of 1 Myr.
- (ii) We show that the HCO^+ formation time τ is inversely correlated with the abundances of species that are present in the high density regime and also participate in a formation pathway of HCO^+ .
- (iii) We show that different formation pathways of HCO^+ predominate in different A_V regimes. Up to $A_{V,3D} \approx 0.4$, the dominant reaction is $\text{HOC}^+ + \text{H}_2$, although it contributes very little to the total HCO^+ mass due to the rarity of these reactants in the low extinction environment. From $A_{V,3D} \approx 0.4\text{--}3$, the dominant reaction is $\text{CO}^+ + \text{H}_2$. Above $A_{V,3D} \approx 3$, the dominant reaction is $\text{H}_3^+ + \text{CO}$, contributing more than 90% of the total HCO^+ production. This system of dominant reactions is established very quickly for HD clouds, but takes a few Myrs longer for more slowly evolving clouds containing magnetic fields.
- (iv) We produce the to-date first column density maps of HCO^+ of simulated molecular clouds. We show that around $N(\text{H}_{\text{tot}}) \sim 10^{21} \text{ cm}^{-2}$ and $N(\text{CO}) \sim 10^{17} \text{ cm}^{-2}$, $N(\text{HCO}^+)$ rises quickly from values of $10^{10\text{--}11} \text{ cm}^{-2}$ to peak values as high as 10^{15} cm^{-2} .
- (v) We find that in MHD clouds, the distribution of HCO^+ is more diffuse than in the HD clouds. The results match well with recent observations of HCO^+ .
- (vi) We find that 50% of the HCO^+ mass is found at visual extinctions between ~ 10 and ~ 30 , or at values of $n_{\text{H,tot}}$ between $\sim 10^{3.5}$ and $\sim 10^{4.5} \text{ cm}^{-3}$.

Because our post-processing method is much faster than directly coupling large chemical networks to MHD simulations, it can be profitably applied to astrophysical problems which require complex, time-dependent chemical modeling. It is our hope that these tools can be used to support and guide future observational campaigns.

ACKNOWLEDGEMENTS

MP, DS, SW, and BG would like to acknowledge funding support from the Deutsche Forschungsgemeinschaft (DFG) via the Sonderforschungsbereich (SFB) 956, *Conditions and Impact of Star Formation* (projects C5 and C6). The SILCC-Zoom simulations were performed on SuperMUC at the Leibniz Computing Centre, and the post-processing and additional analysis were performed on ODIN at the Regionales Rechenzentrum der Universität zu Köln (RRZK). The FLASH code was developed partly by the DOE-supported Alliances Center for Astrophysical Thermonuclear Flashes (ASC) at the University of Chicago. ATB and FB would like to acknowledge funding from the European Research Council (ERC) under the European Union's Horizon 2020 research and innovation programme (grant agreement No.726384/Empire).

DATA AVAILABILITY

The data underlying this paper can be shared for scientific purposes after request to the authors.

REFERENCES

- Aikawa Y., Miyama S. M., Nakano T., Umemayashi T., 1996, *ApJ*, **467**, 684
- Barnes A. T., et al., 2020, *MNRAS*, **497**, 1972
- Beck R., Wielebinski R., 2013, in Oswald T. D., Gilmore G., eds., *Planets, Stars and Stellar Systems: Volume 5: Galactic Structure and Stellar Populations*. Springer Netherlands, Dordrecht, pp 641–723, doi:10.1007/978-94-007-5612-0_13
- Bergin E. A., Hartmann L. W., Raymond J. C., Ballesteros-Paredes J., 2004, *ApJ*, **612**, 921
- Bisbas T. G., Tan J. C., Tanaka K. E. I., 2021, *MNRAS*, **502**, 2701
- Bisbas T. G., van Dishoeck E., Hu C.-Y., Schruha A., 2022, in *European Physical Journal Web of Conferences*. p. 00013, doi:10.1051/epjconf/20226500013
- Borchert E. M. A., Walch S., Seifried D., Clarke S. D., Franek A., Nürnberger P. C., 2022, *MNRAS*, **510**, 753
- Bovino S., Grassi T., Schleicher D. R. G., Caselli P., 2017, *ApJ*, **849**, L25
- Cadiou C., Dubois Y., Pichon C., 2019, *A&A*, **621**, A96
- Capelo P. R., Bovino S., Lupi A., Schleicher D. R. G., Grassi T., 2018, *MNRAS*, **475**, 3283
- Clark P. C., Glover S. C. O., Klessen R. S., Bonnell I. A., 2012, *MNRAS*, **424**, 2599
- Draine B. T., 1978, *ApJS*, **36**, 595
- Draine B. T., Bertoldi F., 1996, *mnras*, **468**, 269
- Dubey A., et al., 2008, *Astronomical Society of the Pacific Conference Series*, **385**, 145
- Ebagezio S., Seifried D., Walch S., Nürnberger P. C., Rathjen T. E., Naab T., 2022, arXiv e-prints, p. arXiv:2206.06393
- Ferrada-Chamorro S., Lupi A., Bovino S., 2021, *MNRAS*, **505**, 3442
- Flower D. R., G. Pineau des Forêts Walmsley C. M., 2005, *A&A*, **436**, 933
- Fryxell B., et al., 2000, *ApJS*, **131**, 273
- Gaches B. A. L., Offner S. S. R., 2018, *ApJ*, **854**, 156
- Ganguly S., Walch S., Clarke S. D., Seifried D., 2022, arXiv e-prints, p. arXiv:2204.02511
- Garrod R. T., Herbst E., 2006, *A&A*, **457**, 927
- Gatto A., et al., 2017, *MNRAS*, **466**, 1903
- Genel S., Vogelsberger M., Nelson D., Sijacki D., Springel V., Hernquist L., 2013, *MNRAS*, **435**, 1426
- Gerin M., Liszt H., 2021, arXiv:2102.09861 [astro-ph]
- Gerin M., Liszt H., Neufeld D., Godard B., Sonnentrucker P., Pety J., Roueff E., 2019, *A&A*, **622**, A26
- Girichidis P., et al., 2016, *MNRAS*, **456**, 3432
- Glover S. C. O., Clark P. C., 2012, *MNRAS*, **421**, 116
- Glover S. C. O., Mac Low M., 2007a, *ApJS*, **169**, 239
- Glover S. C. O., Mac Low M., 2007b, *ApJ*, **659**, 1317
- Glover S. C. O., Mac Low M.-M., 2011, *MNRAS*, **412**, 337
- Glover S. C. O., Federrath C., Mac Low M.-M., Klessen R. S., 2010, *MNRAS*, **404**, 2
- Gnedin N. Y., Tassis K., Kravtsov A. V., 2009, *ApJ*, **697**, 55
- Godard B., Falgarone E., Gerin M., Hily-Blant P., De Luca M., 2010, *A&A*, **520**, A20
- Godard B., Pineau des Forêts G., Hennebelle P., Bellomi E., Valdivia V., 2023, *A&A*, **669**, A74
- Goicoechea J. R., Santa-Maria M. G., Bron E., Teyssier D., Marcelino N., Cernicharo J., Cuadrado S., 2019, *A&A*, **622**, A91
- Gong M., Ostriker E. C., Wolfire M. G., 2017, *ApJ*, **843**, 36
- Gong M., Ostriker E. C., Kim C.-G., 2018, *ApJ*, **858**, 16
- Gong M., Ostriker E. C., Kim C.-G., Kim J.-G., 2020, *ApJ*, **903**, 142
- Górski K. M., Hivon E., 2011, HEALPix: Hierarchical Equal Area isoLatitude Pixelization of a sphere (ascl:1107.018)
- Grassi T., Bovino S., Schleicher D. R. G., Prieto J., Seifried D., Simoncini E., Gianturco F. A., 2014, *MNRAS*, **439**, 2386
- Grassi T., Bovino S., Haugbølle T., Schleicher D. R. G., 2017, *MNRAS*, **466**, 1259
- Habing H. J., 1968, *Bull. Astr. Inst. Netherlands*, **19**, 421
- Hasegawa T. I., Herbst E., 1993, *MNRAS*, **261**, 83
- Herbst E., Cuppen H. M., 2006, *Proceedings of the National Academy of Science*, **103**, 12257
- Hollenbach D., Kaufman M. J., Bergin E. A., Melnick G. J., 2009, *ApJ*, **690**, 1497
- Hu C.-Y., Sternberg A., van Dishoeck E. F., 2021, *ApJ*, **920**, 44
- Jacob A. M., et al., 2022, *ApJ*, **930**, 141
- Kauffmann J., Goldsmith P. F., Melnick G., Tolls V., Guzman A., Menten K. M., 2017, *A&A*, **605**, L5
- Keating L. C., et al., 2020, *MNRAS*, **499**, 837
- Konstantin L., Federrath C., Klessen R. S., Schmidt W., 2012, *Journal of Fluid Mechanics*, **692**, 183
- Le Petit F., Ruaud M., Bron E., Godard B., Roueff E., Languignon D., Le Bourlot J., 2016, *A&A*, **585**, A105
- Leger A., Jura M., Omont A., 1985, *A&A*, **144**, 147
- Li Q., Narayanan D., Davè R., Krumholz M. R., 2018, *ApJ*, **869**, 73
- Liu T., et al., 2020a, *MNRAS*, **496**, 2790
- Liu T., et al., 2020b, *MNRAS*, **496**, 2821
- Lucas R., Liszt H., 1996, *A&A*, **307**, 237
- Lupi A., Bovino S., 2020, *MNRAS*, **492**, 2818
- Lupi A., Bovino S., Capelo P. R., Volonteri M., Silk J., 2018, *MNRAS*, **474**, 2884
- Mackey J., Walch S., Seifried D., Glover S. C. O., Wunsch R., Aharonian F., 2019, *MNRAS*, **486**, 1094
- Mathis J. S., Rimpl W., Nordsieck K. H., 1977, *ApJ*, **217**, 425
- Molinari S., et al., 2011, *ApJ*, **735**, L33
- Nayana A. J., et al., 2020, *ApJ*, **902**, 140
- Nelson R. P., Langer W. D., 1997, *ApJ*, **482**, 796
- Nelson R. P., Langer W. D., 1999, *ApJ*, **524**, 923
- Nikolic S., 2007, *Serbian Astro. J.*, **175**, 1
- Oka T., 2006, *Proceedings of the National Academy of Science*, **103**, 12235
- Padovani M., Galli D., Ivlev A. V., Caselli P., Ferrara A., 2018, *A&A*, **619**, A144
- Papadopoulos P. P., 2007, *ApJ*, **656**, 792
- Price D. J., Federrath C., 2010, *MNRAS*, **406**, 1659
- Richings A. J., Schaye J., 2016, *MNRAS*, **458**, 270
- Sanhueza P., Jackson J. M., Foster J. B., Garay G., Silva A., Finn S. C., 2012, *ApJ*, **756**, 31
- Seifried D., Walch S., 2016, *MNRAS*, **459**, L11
- Seifried D., Sánchez-Monge A., Suri S., Walch S., 2017a, *MNRAS*, **467**, 4467
- Seifried D., et al., 2017b, *MNRAS*, **472**, 4797
- Seifried D., Haid S., Walch S., Borchert E. M. A., Bisbas T. G., 2020, *MNRAS*, **492**, 1465
- Seifried D., Beuther H., Walch S., Syed J., Soler J. D., Girichidis P., Wunsch R., 2021, arXiv:2109.10917 [astro-ph]
- Sembach K. R., Howk J. C., Ryans R. S. I., Keenan F. P., 2000, *ApJ*, **528**, 310

- Smith R. J., Glover S. C. O., Clark P. C., Klessen R. S., Springel V., 2014, *MNRAS*, 441, 1628
- Teague R., Semenov D., Guilleaume S., Henning T., Dutrey A., Wakelam V., Chapillon E., Pietu V., 2015, *A&A*, 574, A137
- Valdivia V., Godard B., Hennebelle P., Gerin M., Lesaffre P., 2016a, p. 5
- Valdivia V., Hennebelle P., Gerin M., Lesaffre P., 2016b, *A&A*, 587, A76
- Valdivia V., Godard B., Hennebelle P., Gerin M., Lesaffre P., Le Bourlot J., 2017, *A&A*, 600, A114
- Walch S., et al., 2015, *MNRAS*, 454, 238
- Wolfire M. G., Hollenbach D., McKee C. F., 2010, *ApJ*, 716, 1191
- Wünsch R., Walch S., Dinnbier F., Whitworth A., 2018, *MNRAS*, 475, 3393
- Yang Y., Jiang Z., Chen Z., Ao Y., Yu S., 2021, *ApJ*, 922, 144
- Yun H.-S., et al., 2021, *ApJS*, 256, 16
- Zhang B., Reid M. J., Menten K. M., Zheng X. W., Brunthaler A., Dame T. M., Xu Y., 2013, *The Astrophysical Journal*, 775, 79
- van Dishoeck E. F., Black J. H., 1988, *ApJ*, 334, 771

Table A1. The 39 chemical species included in our post-processing network, which is modified from the react_COthin network included in the KROME distribution (Grassi et al. 2017). The last two species (in parentheses) represent H₂O and CO which have frozen out onto dust grains, and have no further chemical interactions with the medium until they have thawed again.

e ⁻	H	H ⁺	H ⁻	H ₂	H ₂ ⁺	H ₃ ⁺
He	He ⁺	He ²⁺	C	C ⁺	C ⁻	C ₂
CH	CH ⁺	CH ₂	CH ₂ ⁺	CH ₃ ⁺	O	O ⁺
O ⁻	O ₂	O ₂ ⁺	OH	OH ⁺	H ₂ O	H ₂ O ⁺
H ₃ O ⁺	HCO	HCO ⁺	HOC ⁺	CO	CO ⁺	Si
Si ⁺	Si ²⁺	(f-H ₂ O)	(f-CO)			

Table A2. The chemical species included in the NL99 network, which originated with Nelson & Langer (1999) with updates by Glover & Clark (2012) and Mackey et al. (2019). The species CH_x and OH_x are defined as proxies for, respectively, simple hydrocarbons like CH, CH₂, CH₃, and similarly OH, H₂O, and so forth. The species M and its ionized state M⁺ are proxies for metals like N, Mg, Si, S, and Fe.

e ⁻	H	H ⁺	H ₂	He	He ⁺
H ₂ ⁺	H ₃ ⁺	O	O ⁺	OH _x	HCO ⁺
C	C ⁺	CO	CH _x	M	M ⁺

APPENDIX A: CONTENTS OF CHEMICAL NETWORKS

A1 The post-processing network

Our post-processing method was tested and validated using a modified version of the react_COthin chemical network (Grassi et al. 2017), updated to include reactions that model the adsorption and desorption of CO and H₂ from dust grains. The chemical species included in this network are listed in Table A1, consisting of 37 gas-phase species and 2 proxy species for frozen-out CO and H₂O. We refer the reader to Grassi et al. (2017) or the Appendix materials of Seifried & Walch (2016) for additional details regarding the performance of and the reactions included in this network. The freeze-out modeling in our modified version of this network is described below.

A2 Freeze-out

We model the freeze-out of CO and H₂O as well as its desorption from dust grains as follows. The adsorption (freeze-out) occurs with a rate of

$$k_{\text{ads},i} = \sigma_d n_d c_{s,i} n_i S, \quad (\text{A1})$$

where $c_{s,i}$ and n_i are the sound speed and particle density of the considered species i , respectively, and S is the sticking coefficient. For the product $\sigma_d n_d$, representing the cross-section and density of dust particles, we adopt the value of $2 \times 10^{-21} n_{\text{H,tot}}$ given by Hollenbach et al. (2009) for a standard dust grain size distribution (Mathis et al. 1977).

For desorption from dust grains, we consider thermal and cosmic-ray induced desorption. The thermal desorption rate is given by

$$k_{\text{des,therm},i} = \nu_i e^{-E_{\text{D},i}/T_d}, \quad (\text{A2})$$

where ν_i is the vibrational frequency of the species i in the surface potential well, and $E_{\text{D},i}$ is its adsorption binding energy (e.g. Hasegawa & Herbst 1993). For $E_{\text{D},i}$ we used the values of 1150 K and 5700 K for CO and H₂O, respectively, given by Garrod & Herbst (2006). Using eq. 6 of Aikawa et al. (1996), we obtain ν_i of $1.01593 \times 10^{12} \text{ s}^{-1}$ and

$2.82095 \times 10^{12} \text{ s}^{-1}$ for CO and H₂O, respectively. For the desorption by cosmic rays we follow the approach of Hasegawa & Herbst (1993), giving a rate of $k_{\text{des,cr}} = f(70 \text{ K}) \cdot k_{\text{des,therm}}(T_d = 70 \text{ K}) \cdot \text{CRIR}$. This is based on the fraction of time that a dust grain reaches a temperature of 70 K due to heating by cosmic ray impacts (Leger et al. 1985), with updates for CO desorption as given by Herbst & Cuppen (2006).

A3 The on-the-fly network ‘NL99’

The SILCC-Zoom simulations on which we employ our post-processing method were run coupled to the chemical network ‘NL99.’ This network combines a model for CO chemistry by Nelson & Langer (1999) with a hydrogen model by Glover & Mac Low (2007a,b). The full network was first advanced by Glover & Clark (2012) and then modified by Mackey et al. (2019). The chemical species whose abundances are calculated in this network are listed in Table A2. Most of these species’ abundances are calculated on-the-fly using an ODE solver or through conservation equations. The exceptions are H₂⁺, which is assumed to immediately react further; and O, O⁺, and H₃⁺, which are evolved to equilibrium values.

For simplification, the proxy species CH_x and OH_x have been introduced. These represent families of carbon- and oxygen-bearing species with different numbers of hydrogen atoms, e.g., CH, CH₂, and CH₃, or OH, H₂O, and H₃O, and ionized states of these species as appropriate.

Rather than treat metal elements separately, the network combines various metals which contribute non-negligibly to the electron density into a proxy species M, as well as its singly-ionized state M⁺. By number density, this mostly comprises Si, but also N, Mg, S, and Fe.

The primary purpose of including the NL99 network in the SILCC-Zoom simulations is to properly model the heating and cooling effects of C⁺, CO, and atomic oxygen, which thermally impact the bulk gas distribution. As such, the limited other species in the network are not really modeled comprehensively. In particular, we stress that NL99 does not model the full set of creation and destruction reactions for HCO⁺ in a self-consistent, trustworthy way. This necessitates our post-processing, and precludes us from comparing the NL99 and post-processed abundances of HCO⁺ in this work.

APPENDIX B: RATIOS OF UNPROCESSED AND POST-PROCESSED ABUNDANCES

In Fig. B1, we present two sets of ratios of the means of fractional abundances at different stages in the post-processing algorithm, for cloud MC1 at $t_{\text{evol}} = 2 \text{ Myr}$.

In the left panel, we show the ratio of the mean post-processed fractional abundances (of H, H₂, C, CO, and C⁺) reported by the tracer particles (the right panel of Fig. 3), to the mean unprocessed (NL99) fractional abundances reported by the tracer particles (the left panel of Fig. 3), vs. $n_{\text{H,tot}}$. The post-processing changes the hydrogen abundances very little, but alleviates the problem of over-produced atomic carbon in NL99, as described in Section 3.3. In the right panel, we show the ratio of the mean post-processed fractional abundances after regridding (Fig. 11), to the mean post-processed fractional abundance reported by the tracer particles, that is, before regridding (the right panel of Fig. 3).

APPENDIX C: COLUMN DENSITY MAPS OF FUNDAMENTAL SPECIES

In Section 5, we discuss the algorithm by which we allocate and interpolate post-processed tracer abundances into a uniformly-resolved density grid. Line integration of these grids along a chosen line of sight produces column density maps. In the text we provide such maps for HCO⁺; here we present and discuss column density maps for atomic and molecular hydrogen, as well as CO, to validate our methods.

We present in Fig. C1 column mass density (Σ) maps for H, H₂, and CO (upscaled by 100) for the y-z projection of cloud MC1-HD at $t_{\text{evol}} = 4 \text{ Myr}$. These maps were presented at approximately the same t_{evol} in fig. 3 of Seifried et al. (2017b), the work from which this SILCC-Zoom simulation originated. Although our results here are post-processed using the more extensive chemical network which originated in Grassi et al. (2017), the distribution of different chemical species in the gas in Fig. C1 is approximately congruent with the original on-the-fly results, as predicted in Seifried et al. (2017b). The atomic hydrogen covers the entire domain and reaches a peak density around $10^{-2} \text{ g cm}^{-2}$. An envelope of H₂ with column densities between 10^{-6} and $10^{-3} \text{ g cm}^{-2}$ surrounds a dense core region where maximal values of $\Sigma(\text{H}_2) \approx 1 \text{ g cm}^{-2}$ are reached. CO is only abundant in these core regions, with column densities around $10^{-3} \text{ g cm}^{-2}$. The relative distributions of H₂ and CO reflect the extent of the CO-dark molecular gas. The close correspondence of these maps with the results from Seifried et al. (2017b) strongly supports the regridding algorithm by which we construct density grids from limited tracer particle data.

This paper has been typeset from a \LaTeX file prepared by the author.

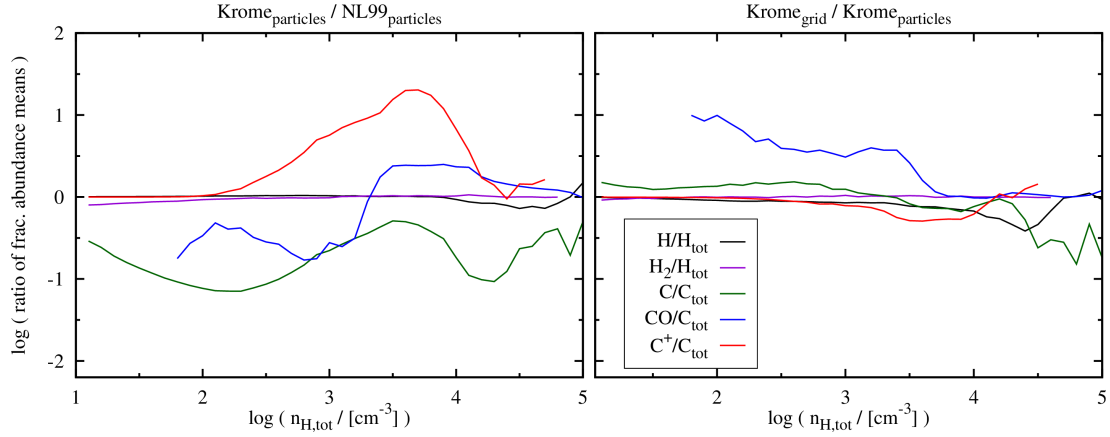


Figure B1. Left panel: the ratio of post-processed to unprocessed (NL99) mean fractional abundance reported by the tracer particles in MC1-HD at $t_{\text{evol}} = 2$ Myr, vs. $n_{\text{H,tot}}$. This corresponds to the ratio of the right and left panels of Fig. 3. Right panel: the ratio of post-processed mean fractional abundances after regridding to the post-processed mean fractional abundances from the tracer particles, vs. $n_{\text{H,tot}}$. This corresponds to the ratio of Fig. 11 with the right panel of Fig. 3.

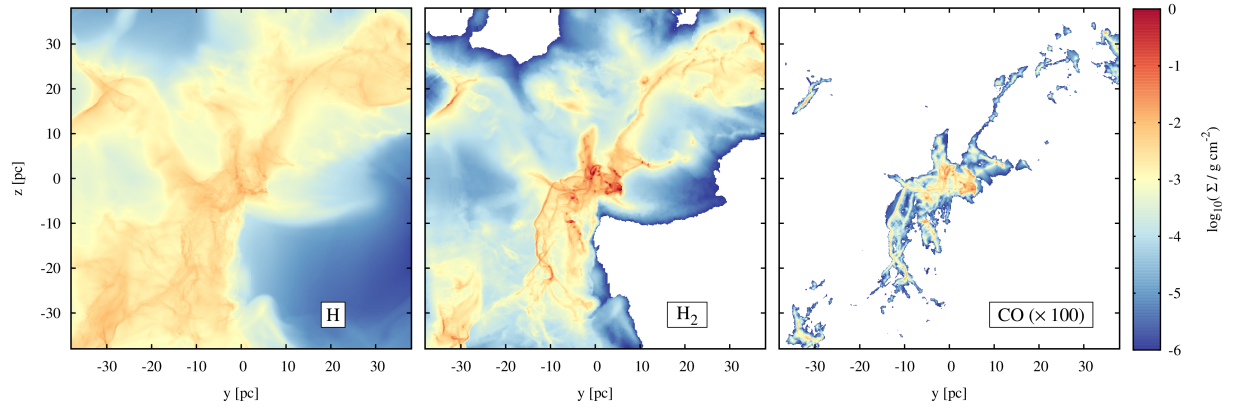


Figure C1. Projections along the x -direction of the column mass density of H, H₂, and CO (upscaled by 100), for MC1-HD at $t_{\text{evol}} = 4$ Myr, generated from the interpolated grids of post-processed tracer abundances. The maps are roughly centred on the densest region in the cloud. The atomic hydrogen (left) dominates in the more diffuse, outlying areas. Meanwhile, H₂ (centre) reaches its highest density in the heart of the cloud, but is also present in a diffuse envelope surrounding the core. CO (right) is only present in the densest parts of the cloud. These maps are very similar to the analogous AMR-derived maps in fig. 3 of Seifried et al. (2017b), supporting the accuracy of the regridding algorithm.

Tracing dark molecular gas in simulated clouds using post-processed non-equilibrium OH abundance

M. Panessa¹★, D. Seifried¹, S. Walch¹

¹ Universität zu Köln, I. Physikalisches Institut, Zùlpicher Str. 77, 50937 Köln, Germany

Accepted XXX. Received YYY; in original form ZZZ

ABSTRACT

The hydroxyl molecule (OH) is found in molecular clouds in comparable density and extinction regimes as molecular hydrogen, according to both observations and photodissociation region (PDR) chemical models. Consequently, OH is a candidate tracer for the so-called CO-dark molecular gas, where sufficient shielding exists for the survival of H₂, but not for CO, which is usually used to trace it. 3D magnetohydrodynamic (MHD) astrophysical simulations coupled on-the-fly to chemical networks which include OH could indicate the effectiveness of OH as a molecular gas tracer, but such time-dependent chemical models are computationally expensive. We bridge this computation gap with a non-equilibrium chemical evolution tool which post-processes the limited chemical data from four simulations of molecular clouds in the SILCC-Zoom project. We provide the density distributions for numerous chemical species, such as OH, whose abundances were not calculated on-the-fly. We present column density maps of OH at a spatial resolution of 0.125 pc, showing that $N(\text{OH})$ ranges from 10^{12} – 10^{14} cm^{−2} in diffuse molecular gas, with peaks around 10^{16} cm^{−2} in dense cores and filaments. We find that 50% of the OH mass in the molecular clouds lies between visual extinctions of $A_V = 1$ – 10 for non-magnetized, hydrodynamic (HD) simulations, and between $A_V = 0.6$ – 1.6 for the MHD simulations. We assess the relation of $N(\text{OH})$ to $A_{V,2D}$ and to $N(\text{H}_2)$, and plot the probability density functions of $N(\text{OH})$ over time. In addition, we show that equilibrium models overestimate the clouds’ total OH masses by up to a factor of 2, and similarly for the total H₂ and CO masses. We calculate the abundance ratio $N(\text{OH})/N(\text{H}_2)$ vs. A_V at disparate evolutionary timesteps, and find that the ratio is time-invariant and decreases from 5×10^{-7} to 5×10^{-8} as A_V increases from 0.1 to 3 magnitudes, then increases to 10^{-7} by $A_V = 15$, in line with observations. An exponential function is fit to $N(\text{OH})/N(\text{H}_2)$ for $\log A_{V,2D} < 0.5$. Finally, we infer that $N(\text{OH})/N(\text{H}_2)$ declines to a global minimum around $n_{\text{H,tot}}$ due to a combination of weakened formation routes and a strong rate of destruction via the OH + C⁺ reaction.

Key words: ISM: clouds – ISM: molecules – methods: numerical – astrochemistry – stars: formation

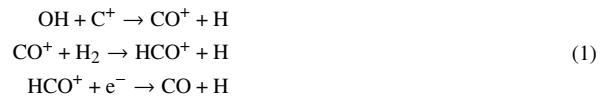
1 INTRODUCTION

Regions of the interstellar medium which are dominated by molecular hydrogen gas (H₂) are referred to as molecular clouds. The densest regions of these clouds undergo gravitational collapse into protostellar systems (André et al. 2014). To fully understand this dynamic process of star formation, we must understand the distribution and evolution of the clouds’ H₂ content.

Unfortunately, observing H₂ directly in molecular clouds is not possible. The molecule is symmetric and lacks a permanent dipole moment, and is essentially invisible in emission at the temperature range where it is present in the Galaxy (~ 10 – 100 K). Instead, we infer the presence of H₂ via the emission of other species which are present in the same location, and thus ‘trace’ the invisible H₂. The usual target species for this practice is carbon monoxide (CO), the most abundant molecule in the ISM besides H₂ (see Dobbs et al. 2014, for a review). The observed emission from the rotational transition ¹²CO(1–0) at $\lambda = 3$ mm has been related to the total hydrogen column density via the X_{CO} factor (see Bolatto et al. 2013, for a review).

Emission from CO cannot trace the complete extent of H₂ in a molecular cloud, however. Because CO has the lower dissociation energy of the two molecules, a significant region of H₂ exists on the perimeter of molecular clouds where the self-shielding against the interstellar radiation field (ISRF) is sufficient for H₂ to survive, but not CO (van Dishoeck & Black 1988; Wolfire et al. 2010; Valdivia et al. 2016; Gaches & Offner 2018). This outer envelope of H₂ which is untraced by CO can represent tens of percent of the cloud’s total H₂ content (Wolfire et al. 2010; Lee et al. 2012; Smith et al. 2014; Planck and Fermi Collaborations et al. 2015; Seifried et al. 2020), and is referred to as the ‘CO-dark gas’ (Lada & Blitz 1988; Grenier et al. 2005). Tracing the CO-dark gas requires an alternative chemical tracer whose emission can constrain the local H₂ density.

A promising CO-dark gas tracer is the hydroxyl radical, OH. First detected in the ISM by Weinreb et al. (1963), OH plays a critical role in the formation of CO via a carbon reaction chain (van Dishoeck & Black 1988; Li et al. 2018a):



★ panessa@ph1.uni-koeln.de

Therefore, we expect abundant OH within the molecular gas. The CO produced by these reactions in the CO-dark regime is quickly photodissociated, but the OH remains, with detectable emission in areas with minimal CO (Wannier et al. 1993; Liszt & Lucas 1996; Neufeld et al. 2002; Allen et al. 2012, 2015; Li et al. 2015, 2018a; Busch et al. 2019, 2021). Work has been done to analyze the utility of OH as an observational molecular gas tracer, particularly the systematic sub-parsec resolution observations by Xu et al. (2016) of the Taurus Molecular Cloud boundary, where the abundance ratio OH/H₂ was related to the visual extinction.

To support and guide these observations of OH, we desire a chemical model which can accurately simulate not just the H₂ content of molecular clouds, but also candidate tracers like OH. The CO-dark molecular hydrogen content of a simulation is known, and so these simulations provide important validation of techniques for tracing that dark gas via the presence of other species.

However, modeling the time-dependent chemistry of the ISM is both difficult and computationally expensive due to the stiffness and sparsity of the associated rate equations (Grassi et al. 2014). Coupling 3D-MHD astrophysical simulations on-the-fly even to a simple chemical evolutionary network can increase the simulation time by close to an order of magnitude (Seifried & Walch 2016). For this reason, some simulations do not even model coupled chemistry at all, or when they do, often limit the models to the ecosystem of C⁺ and CO formation and destruction reactions, to account for the dynamical impact of the heating and cooling effects of those species on the bulk gas (as in the networks of e.g. Nelson & Langer 1997, 1999; Glover & Mac Low 2007a,b; Glover et al. 2010; Glover & Mac Low 2011). But this frugal approach sacrifices the possibility of further astrochemical investigation via analysis of other reactions and chemical products which are less essential to the cloud’s dynamical evolution.

Some works (Gong et al. 2018, 2020; Li et al. 2018b; Keating et al. 2020) try to remedy both of these issues – the computational expense of time-dependent chemistry, and the desire to better understand the overall chemical picture of molecular clouds – by taking a snapshot of a cloud at a fixed dynamical state and evolving the chemistry of the gas to chemical equilibrium. However, it has repeatedly been shown that applying the equilibrium approximation to evolving clouds gives inaccurate results for the time-dependent abundances of H₂ and CO (Hu et al. 2021; Rybarczyk et al. 2021; Ebagezio et al. 2022).

We propose a compromise position between expensive on-the-fly modeling and inaccurate equilibrium modeling: a post-processing algorithm which evolves the chemistry of passive tracer particles inside 3D-MHD simulations, from which we reconstruct time-dependent grids using an interpolative method (Panessa et al. 2022). We employ this method on the SILCC-Zoom molecular cloud simulations (Seifried et al. 2017, 2020), which include passive tracer particles. These tracers advect with density gradients, and report the local chemical and dynamical condition of the nearby gas. By post-processing all of these tracer histories, we can produce a time-dependent chemical history of the entire cloud for any species in the post-processing network. Panessa et al. (2022) used this algorithm to examine the distribution and evolution of HCO⁺ in dense molecular gas. Here, we employ it to analyze the density regime containing CO-dark gas, for the specific purpose of investigating the utility of OH as a molecular gas tracer.

This paper is arranged as follows. In Section 2, we explain the setup of the SILCC-Zoom simulations and the operation of the chemical post-processing method. Then, in Section 3, we present the first fully self-consistent, time-dependent column density maps of OH, examine the distribution of OH throughout the molecular

cloud simulations, and contrast the time-dependent data with results from equilibrium chemistry. In Section 4, we assess the abundances of OH and H₂ in the CO-dark gas regime, as well as the abundance ratio $N(\text{OH})/N(\text{H}_2)$ as a function of the visual extinction $A_{V,2D}$. Finally, in Section 5 we summarize our results.

2 NUMERICAL METHODS

We apply our time-dependent chemical post-processing (Panessa et al. 2022) to four SILCC-Zoom simulations (Seifried et al. 2017, 2020), which are part of the SIMulating the LifeCycle of molecular Clouds (SILCC) project (Walch et al. 2015; Girichidis et al. 2016). We summarize the relevant details of these simulations in Section 2.1. Next, in Section 2.2, we briefly explain our time-dependent chemical post-processing algorithm, which is explored and validated in much greater detail in Panessa et al. (2022).

2.1 The SILCC-Zoom simulations

Four SILCC-Zoom molecular cloud simulations are examined in this work: two non-magnetized, hydrodynamic (HD) simulations, MC1-HD and MC2-HD (which originated in Seifried et al. 2017, and modified as in Seifried et al. 2021), and two magneto-hydrodynamic (MHD) simulations, MC1-MHD and MC2-MHD (which originated in Seifried et al. 2020, again modified as in Seifried et al. 2021). We emphasize that despite the analogous names, the MHD simulations are not simply magnetized versions of the HD simulations; all four simulations are completely separate and unique (M)HD runs.

The molecular clouds in the SILCC-Zoom simulations originate in full-scale SILCC simulations, which model the multi-phase ISM (Walch et al. 2015; Girichidis et al. 2016). The SILCC simulations are run using the adaptive mesh refinement (AMR) grid code FLASH v. 4.3 (Fryxell et al. 2000; Dubey et al. 2008). They model a section of the galactic disk using a midplane-centered stratified box that measures 500 pc × 500 pc × ± 5 kpc, at an initial spatial resolution of 3.9 pc. Regions of high molecular gas content are selected, and re-simulated at higher resolution. These constitute the SILCC-Zoom simulations. Outside the so-called ‘zoom-in’ regions, the evolution of the surrounding multi-phase ISM continues at 3.9 pc resolution.

The full SILCC domain evolves for a cloud-dependent startup time t_0 before the zoom-in refinement of the selected cloud complex begins, with $t_0 = 11.9$ Myr for the HD clouds and $t_0 = 16.0$ Myr for the MHD clouds. The greater value for t_0 in the MHD simulations is due to the influence of magnetic fields in supporting gas structures against collapse (Walch et al. 2015; Girichidis et al. 2018; Seifried et al. 2020). In this work, when considering timescales of evolution for the molecular clouds, we always mean the time $t_{\text{evol}} = t - t_0$, that is, the time since the beginning of zoom-in refinement. From t_0 up to $t_{\text{evol}} = 1.65$ Myr, the resolution inside the zoom-in region is increased to 0.06 pc. This increase is performed in successive stages to suppress the development of spurious resolution artifacts (Seifried et al. 2017). Consequently, even though the chemical post-processing begins at t_0 , in order to maintain consistency in the spatial resolution of our chemical data, we only analyze the chemistry after $t_{\text{evol}} = 1.65$ Myr, when the structure of the cloud is fully developed.

The physical parameters of the SILCC simulations, and thus of the SILCC-Zoom simulations as well, are set as follows. The initial midplane bulk density is set to $\rho_0 = 9 \times 10^{-24}$ g cm⁻³, with a Gaussian density profile that has a scale height of 30 pc. The gas surface density is $\Sigma_{\text{gas}} = 10 M_{\odot}$ pc⁻². For the MHD simulations, the magnetic field is unidirectional and initialized throughout the

Table 1. The chemical species included in the NL99 network (Nelson & Langer 1999, with updates by Glover & Clark 2012 and Mackey et al. 2019). Most abundances are calculated on-the-fly using an ODE solver or with conservation equations, except for H_2^+ (which is assumed to be immediately consumed in other reactions), and O^+ , and H_3^+ (which are evolved to equilibrium values). Hydrocarbons like CH and CH_2 are approximated by the single proxy species CH_x , and oxygen hydrides like OH and H_2O by OH_x . The species M and M^+ are proxies for higher atomic number metals like N , Mg , Si , S , and Fe .

e^-	H	H^+	H_2	He	He^+
H_2^+	H_3^+	O	O^+	OH_x	HCO^+
C	C^+	CO	CH_x	M	M^+

volume at $B_x = B_{x,0} \sqrt{\rho(z)/\rho_0}$. The initial midplane magnetic field strength is $B_{x,0} = 3 \mu\text{G}$ in accordance with observations (Beck & Wielebinski 2013).

The cosmic ray ionization rate (CRIR) for H_2 is set everywhere to $\zeta = 6 \times 10^{-17} \text{s}^{-1}$, without attenuation. The interstellar radiation field strength (ISRF) is initialized at $G_0 = 1.7$ in Habing units (Habing 1968), or one Draine field (Draine 1978). We handle attenuation of the ISRF with the TREE-RAY/OPTICAL-DEPTH module (Clark et al. 2012; Wünsch et al. 2018), taking into account the shielding properties of H_2 , CO , and the dust distribution. This module calculates the three-dimensional visual extinction $A_{V,3D}$ for every grid cell by measuring the total hydrogen column density $N(\text{H}_{\text{tot}})_i$ along n_{pix} sight lines (Górski & Hivon 2011), and calculating:

$$A_{V,3D} = \frac{-1}{\gamma} \ln \left(\frac{1}{n_{\text{pix}}} \sum_{i=1}^{n_{\text{pix}}} \exp(-\gamma A_{V,i}) \right), \quad (2)$$

where the factor $\gamma = 2.5$ (Bergin et al. 2004, and see Glover & Clark 2012), $n_{\text{pix}} = 48$ for these simulations, and the visual extinction $A_{V,i}$ and $N(\text{H}_{\text{tot},i})$ are related as in Draine & Bertoldi (1996):

$$A_{V,i} = (5.348 \times 10^{-22}) N(\text{H}_{\text{tot}})_i \quad (3)$$

The total attenuation due to dust experienced at a cell is $\exp(-\gamma A_{V,3D})$. This process is repeated at each cell using $N(\text{H}_2)$ and $N(\text{CO})$ to find the self-shielding contribution against the ISRF provided by those species.

All four simulations were coupled on-the-fly to a streamlined chemical network introduced by Nelson & Langer (1997), shortly updated in Nelson & Langer (1999), and modified further by Glover et al. (2010) and Mackey et al. (2019). The goals of this chemical network, hereafter called ‘NL99,’ are to model the formation of H_2 , and to approximate CO and C^+ so that the simulations can properly account for these species’ heating and cooling effects. A limited set of hydrogen- and carbon-bearing species are modeled fully (see Table 1), with numerous approximations. The time-dependent abundances reported by the network can be post-processed self-consistently with regard to a more robust network, as described in the next section.

The FLASH code primarily simulates the ISM with a volume-filling AMR grid. The code can also include passive tracer particles in the simulation. Unlike SPH particles, these passive tracers do not represent any mass or physical object inside the simulation. They are merely sensors that record the local state as they advect with the gas flow. At t_0 for each simulation, we generate the tracers in a uniform lattice with inter-particle spacing of 1 pc, covering the entire zoom-in region and a surrounding volume that extends 10 pc outward from each edge of the zoom-in region. This amounts to

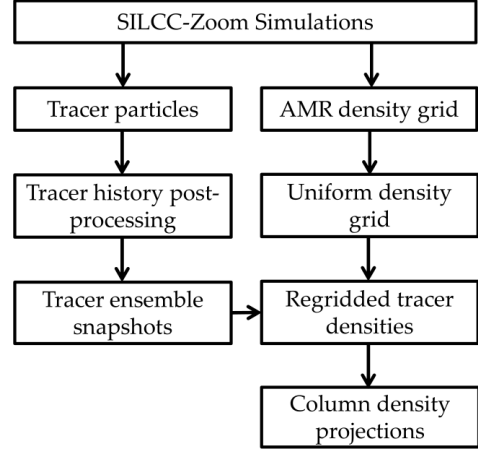


Figure 1. A schematic of the post-processing and regridding algorithm used in this work. The chemical histories of tracer particles from SILCC-Zoom simulations are post-processed with a robust chemical network. These tracers are ‘regridded’ with an interpolation method that fills every cell in the domain, weighted by the local density from the original simulation. Finally, we produce column density maps from these grids.

about 9×10^5 tracers for the clouds MC1-HD and MC2-HD, 2×10^6 tracers for MC1-MHD, and 1.6×10^6 tracers for MC2-MHD. The disparity between the HD and MHD particle counts stems from the more diffuse nature of the MHD clouds (Seifried et al. 2020; Ganguly et al. 2022) and the correspondingly larger zoom-in region needed to encapsulate their molecular content.

Every 3.3 kyr, until the simulations end around $t_{\text{evol}} \sim 4 \text{ Myr}$, the tracers record local values of numerous dynamical quantities, in particular the bulk density, gas and dust temperature, $A_{V,3D}$, and the self-shielding due to H_2 and CO . The tracers also record the local NL99 abundances of H , H_2 , C , CO , and C^+ . By post-processing these dynamically-evolving, time-dependent tracer histories – rather than dynamically-frozen snapshots of the AMR grid – we self-consistently analyze the time-dependent chemical evolution of the gas at a time resolution of 3.3 kyr.

2.2 The post-processing pipeline

We produce post-processed, 3D density distributions of chemical species using the algorithm first detailed in Panessa et al. (2022). This algorithm consists of two phases. First, the chemical histories of the tracers are individually post-processed timestep by timestep with regard to a larger chemical network. Second, the tracers are ‘regridded’ into 3D grids of uniform resolution via an iterative interpolation procedure, from which we derive column density projections. A flowchart of the algorithm’s operations is provided in Fig. 1. We summarize this pipeline below, followed by a validation of its accuracy in the regime of CO-dark gas.

2.2.1 Chemical post-processing

For our chemical post-processing, we employ the microphysics package KROME (Grassi et al. 2014). This package self-consistently evolves a chemical network for a user-specified timestep, given a set of initial abundances and the dynamical parameters (such as bulk density and gas temperature) that are relevant to the reactions.

In this work, as in Panessa et al. (2022), we employ a version

Table 2. The 39 chemical species included in our post-processing network, which is modified from the `react_COthin` network included in the `KROME` distribution (Grassi et al. 2017). The last two species (in parentheses) represent H_2O and CO which have frozen out onto dust grains, and have no further chemical interactions with the medium until they have thawed again.

e^-	H	H^+	H^-	H_2	H_2^+	H_3^+
He	He^+	He^{2+}	C	C^+	C^-	C_2
CH	CH^+	CH_2	CH_2^+	CH_3^+	O	O^+
O^-	O_2	O_2^+	OH	OH^+	H_2O	H_2O^+
H_3O^+	HCO	HCO^+	HOC^+	CO	CO^+	Si
Si^+	Si^{2+}	(f- H_2O)	(f-CO)			

of the `react_COthin` network introduced in Grassi et al. (2017), modified to contain 39 chemical species and 301 reactions. This network self-consistently evolves species like the cosmic ray tracer H_3^+ , the dense gas and CO tracer HCO^+ , diffuse gas tracers like OH and CH, and more. Two of the species correspond to CO and H_2O frozen onto dust grains, where they play no further role in the gas-phase chemistry until they are desorbed, either thermally or by cosmic ray interactions. Modeling the freeze-out of these species is critical to accurately modeling the molecular gas chemistry (Flower et al. 2005; Hollenbach et al. 2009; Wolfire et al. 2010). The full list of species in our post-processing network is presented in Table 2.

After compiling `KROME` with this network, we post-process the individual tracer histories from each molecular cloud. The abundances of H, H_2 , C, CO, and C^+ are initialized at t_0 at the NL99 values recorded by the tracer at t_0 . We derive an initial value for the number density of H^+ by the relation:

$$n_{\text{H}^+} = n_{\text{H,tot}} - n_{\text{H}} - 2n_{\text{H}_2}. \quad (4)$$

Relative to $n_{\text{H,tot}}$, we set the fractional abundance of helium to 0.1, carbon to 1.4×10^{-4} , and oxygen to 3.2×10^{-4} (Sembach et al. 2000). The number densities of all other species are initialized to 10^{-20} cm^{-3} . We find that after a few timesteps, these abundances which are not initialized to NL99 values or to a specific fractional abundance are insensitive to their initial value.

The chemistry of each tracer is evolved using `KROME` for at most 3.3 kyr per step, the interval at which the simulation’s tracer particle snapshots are written out. At each timestep, the system of chemical rate equations is solved with the chemical state from the previous timestep, using the tracers’ contemporaneous values for the dynamical parameters $A_{\text{V},3\text{D}}$, the bulk density, the gas and dust temperatures, and the self-shielding fractions for H_2 and CO. If any of these dynamical parameters change between successive timesteps by more than 10%, we apply a subcycling process which linearly interpolates the dynamical parameters between the timesteps. We then evolve the chemistry only long enough for the fastest-changing parameter to change by exactly 10%. Then the chemistry is evolved for gradually longer sub-steps until the next proper timestep is reached (i.e., 3.3 kyr after the previous proper timestep). This subcycling procedure is explored in detail in Panessa et al. (2022).

This post-processing algorithm repeats until the end of each tracer history (the end of the simulation, around $t_{\text{evol}} \sim 4 \text{ Myr}$). By evolving the chemistry in small time increments, and accounting for the changing dynamical state with each `KROME` update, we obtain the time-dependent chemical history of every tracer particle in each simulation. Because the tracers passively advect with local density flows, this amounts to the time-dependent chemical history of their associated fluid elements (Genel et al. 2013; Ferrada-Chamorro et al. 2021).

Chemical post-processing of ISM simulations is sometimes run until equilibrium is reached, assuming a fixed dynamical state. This methodology has been repeatedly shown to be questionable in evolving molecular clouds (Hu et al. 2021; Rybarczyk et al. 2021; Ebagezio et al. 2022). To compare our time-dependent data to the equilibrium approach, we follow a similar comparative method as Ebagezio et al. (2022). We take late snapshots of our tracer particles from each simulation ($t_{\text{evol}} = 4 \text{ Myr}$ for MC1-HD, MC1-MHD, and MC2-MHD; $t_{\text{evol}} = 3.76 \text{ Myr}$ for MC2-HD) and evolve them using `KROME`, this time for $\Delta t = 1 \text{ Gyr}$. This produces a snapshot of each cloud’s tracers at chemical equilibrium. In this work, we will supplement our time-dependent analysis by comparing to these equilibrium results.

2.2.2 Regridding

Once the tracer histories have been post-processed, we generate volume-filling, 3D density distributions for chemical species of interest. This ‘regridding’ procedure can be performed on a tracer snapshot at any timestep, although as noted above, we refrain from analyzing data before the conclusion of the zoom-in refinement at $t_{\text{evol}} = 1.65 \text{ Myr}$. We consider snapshots at $t_{\text{evol}} = 2, 3$, and 4 Myr . For MC2-HD, which was run for only 3.76 Myr, we consider this final time instead of 4 Myr. We also apply this regridding method to each cloud’s snapshot at equilibrium, to acquire comparative density distributions at equilibrium.

The regridding procedure for the tracers in each cloud works as follows. First, we create a blank grid of the same dimensions as, and cospatial with, the zoom-in region. The spatial resolution throughout is set uniformly to 0.125 pc. Next we consult the tracers’ spatial coordinates at the selected time. If a tracer is inside the zoom-in region at that time, its coordinates are translated into a corresponding cell in the grid. We assign to that cell the *fractional abundance* of the chemical species of interest, rather than the number density, because the latter leads to large overestimations of the density in the sparsely-sampled frontier regions in the interpolation steps to follow. If more than one particle occupies the same cell, their fractional abundances are logarithmically averaged.

Once every tracer’s fractional abundance has been written to the grid, we fill the empty pixels via an interpolation scheme. Each blank cell assesses the 26 cells surrounding it, and copies to itself a logarithmic average of the fractional abundances of all its neighbours, weighted by the inverse of the distance between the centroids of the blank cell and each neighbor. This process repeats until every cell has been assigned a nonzero fractional abundance value. Finally, we multiply the whole grid by a cospatial, uniform grid of $n_{\text{H,tot}}$ derived from the SILCC-Zoom density grid. This recovers a volume-filling, 3D, number density distribution of any species in the chemical network we like, at a spatial resolution of 0.125 pc.

2.2.3 Validation in the CO-dark density regime

Because the tracers are advected with the gas flow, they have a predilection for congregating in peak density regions, as explored in Genel et al. (2013). This improves the statistical reliability of the tracer-derived chemical abundances in dense gas, because the number of blank cells which must be filled by interpolation decreases in these areas. However, the congregation of tracers in dense gas corresponds to a decline in tracers in the intermediate- and low-density gas. This problem worsens as t_{evol} increases, and the molecular clouds continue to contract.

Because in Panessa et al. (2022) we focused on the dense gas tracer

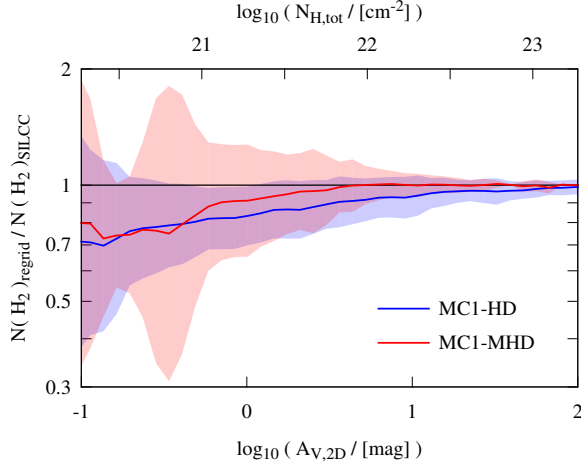


Figure 2. The ratio of the average $N(\text{H}_2)$ from regridding the NL99 tracer H_2 abundances, to the average $N(\text{H}_2)$ from the NL99 abundances in the original SILCC-Zoom grid, vs. the projected visual extinction $A_{V,2D}$, for the clouds MC1-HD (blue) and MC1-MHD (red) at $t_{\text{evol}} = 4$ Myr. The shaded areas represent one standard deviation from the respective average. The regridding method generally recaptures the H_2 abundance well, though with slight underestimation at all $A_{V,2D}$, especially in MC1-HD. Conversely, in MC1-MHD, the regridded $N(\text{H}_2)$ exceeds 90% of the original grid value down to $A_{V,2D} \sim 0.5$.

HCO^+ , here we first investigate the validity of the post-processing in the CO-dark, and thus more diffuse, gas. By taking projections of the regridded CO and H_2 abundances, we find that the CO-dark gas typically has visual extinctions below $A_{V,2D} \approx 3$ (see also Section 4.1).

The SILCC-Zoom simulations record their NL99 H_2 abundance in every AMR cell, which we process into a uniformly resolved grid using the YT Python package. This allows us to make a direct comparison of the original SILCC H_2 column density, $N(\text{H}_2)_{\text{SILCC}}$, to the post-processed H_2 column density after the regridding procedure, $N(\text{H}_2)_{\text{regrid}}$. We perform this comparison at $t_{\text{evol}} = 4$ Myr, as we have found that the disparity will be worst late in the simulations, when the tracers have had the maximum time to become locked in dense gas, e.g. molecular cloud cores and filaments.

In Fig. 2, we plot the average ratio $N(\text{H}_2)_{\text{regrid}}/N(\text{H}_2)_{\text{SILCC}}$ vs. $A_{V,2D}$ for the clouds MC1-HD (blue) and MC1-MHD (red), at $t_{\text{evol}} = 4$ Myr. The shaded regions indicate one standard deviation. For both clouds, the SILCC and regridded values of $N(\text{H}_2)$ correspond very well. In the CO-bright region with $A_{V,2D} \gtrsim 3$, the correspondence is within ten percent for the HD cloud, and within two percent for the MHD cloud. In the gas with visual extinctions from $A_{V,2D} \approx 1$ –3, the regridded values of $N(\text{H}_2)$ underestimate the molecular gas content by 10–20%. At a visual extinction of $A_{V,2D} \approx 0.1$, at which much of the gas is still atomic, the regridded tracers underestimate the SILCC grid values by about 30%.

Notably, the correspondence of $N(\text{H}_2)_{\text{regrid}}$ to $N(\text{H}_2)_{\text{SILCC}}$ is superior in MC1-MHD for $A_{V,2D} \gtrsim 0.3$. We ascribe this to the ‘fluffier’ distribution of MHD clouds compared to HD ones, the latter having more dense, well-shielded gas (see fig. 3 of Seifried et al. 2020). Because the MHD gas is more widely distributed, so are the tracers.

Keeping in mind that our method slightly underestimates the molecular gas content in the low-extinction regime, in the follow-

ing we analyze the abundance and distribution of OH over its entire density range.

3 THE DISTRIBUTION OF OH

3.1 Time-dependence of total OH, H_2 , and CO masses

Using the chemical density grids obtained in the regridding procedure (Section 2.2.2), we calculate each cloud’s total mass in H_2 , CO, and OH at $t_{\text{evol}} = 2, 3$, and 4 Myr.

After performing the regridding procedure outline in the previous section, we produce 3D density grids of n_{OH} , n_{H_2} , and n_{CO} for all four molecular clouds, at $t_{\text{evol}} = 2, 3$, and 4 Myr and at equilibrium. Because the density grids have a uniform spatial resolution of 0.125 pc, we can straightforwardly calculate the total mass of each species in each snapshot. Each cloud’s bulk mass is fairly static with time. The clouds MC1-MHD (blue) and MC2-MHD (green) are about twice as massive as MC1-HD (black) and MC2-HD (red) because the molecular gas in the MHD clouds is more widely distributed, and therefore the MHD zoom-in regions are larger than the HD ones.

In Fig. 3, we plot vs. time each cloud’s total mass in H_2 (top panel), CO (top middle), and OH (bottom middle). The masses of all three species increases in all four clouds over time, as the amount of dense gas increases. As Seifried et al. (2021) noted when examining these simulations, the HD and MHD clouds all have roughly equal masses of H_2 at $t_{\text{evol}} = 2$ Myr despite the factor of two greater mass in the MHD clouds. This indicates again that the MHD clouds have a more diffuse density profile, containing more atomic gas than the HD clouds. As a consequence, at $t_{\text{evol}} = 2$ Myr, the CO content of the MHD clouds is negligible. Only at later timesteps do the MHD clouds develop CO to the same order of magnitude as the HD clouds.

The clouds’ OH masses at $t_{\text{evol}} = 2$ Myr differ from each other in an analogous way to the clouds’ bulk masses: the MHD clouds are about twice as massive as the HD clouds and also contain twice as much OH. Over time, the OH content of the clouds increases by a factor of 1.5–2.8.

In the bottom panel of Fig. 3, we plot the ratio of the total mass of OH and H_2 in each cloud, $M_{\text{OH}}/M_{\text{H}_2}$. This ratio rises over time for the HD clouds, mostly due to the aforementioned quick rise in their OH content. The mass ratio for the MHD clouds remains more stable, as their OH and H_2 abundances grow in similar proportion to each other. At $t_{\text{evol}} = 4$ Myr, this ratio has an average value of 7×10^{-7} in the HD clouds, and an only slightly larger average of 1×10^{-6} in the MHD clouds. This is up to an order of magnitude greater than the value for $N(\text{OH})/N(\text{H}_2)$ of $\sim 10^{-7}$ which is common in observations (Liszt & Lucas 1996; Lucas & Liszt 1996; Liszt & Lucas 2002; Nguyen et al. 2018; Rugel et al. 2018; Jacob et al. 2019; Busch et al. 2021, see also Section 4).

3.2 Column density maps

We produce column density maps of OH for each cloud by summing the n_{OH} grids along each cardinal axis. In Fig. 4, we present maps of $N(\text{OH})$ from MC1-HD (top) and MC1-MHD (bottom) at $t_{\text{evol}} = 4$ Myr. All three projections are shown, revealing the shape of the clouds’ OH distributions. The column density ranges from $N(\text{OH}) \approx 10^{11} \text{ cm}^{-2}$ in the low-density gas (where $A_{V,2D} < 1$), to $N(\text{OH}) \approx 10^{16} \text{ cm}^{-2}$ in dense cores and filamentary structures.

The range of $N(\text{OH})$ is similar for the HD and MHD clouds, but with markedly different density distributions. Visually, these correspond to the differences in the bulk density distribution of the HD

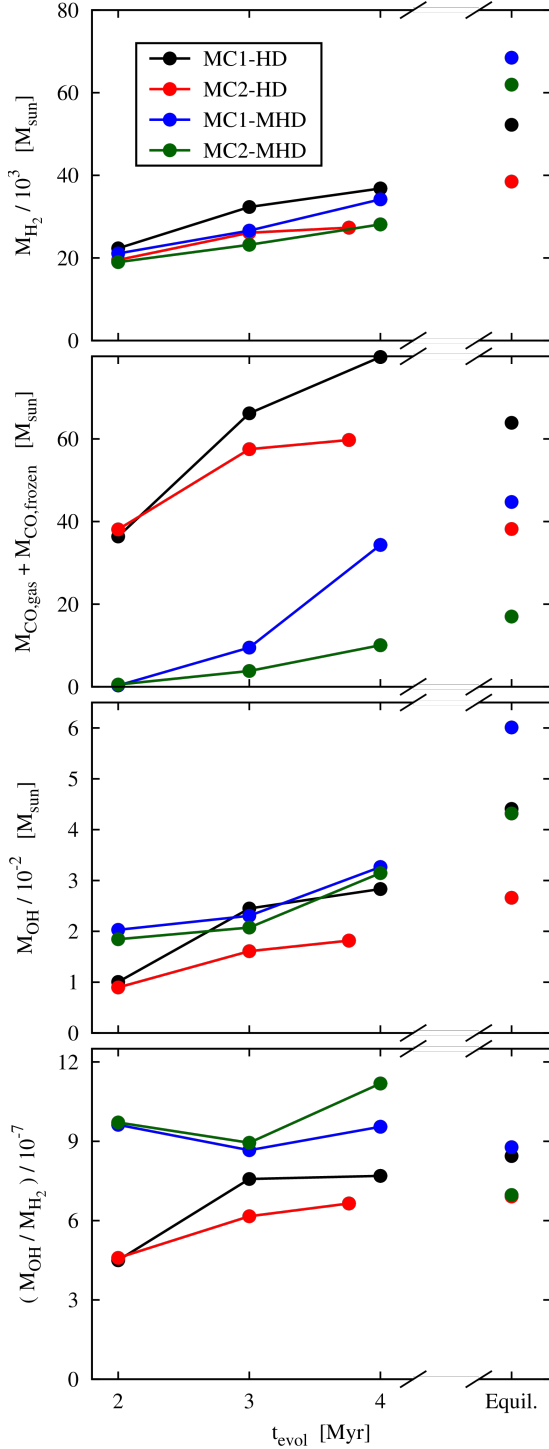


Figure 3. Evolution of each molecular cloud’s total mass of H_2 , CO, and OH (top, top middle, and bottom middle panels respectively), as well as the OH/ H_2 mass ratio (bottom panel) as a function of time. The CO mass includes contributions both from the gas phase and from the molecule frozen onto dust grains. As clouds evolve over time and become denser, the total H_2 , CO, and OH content all increase.

and MHD clouds (see Seifried et al. 2020; Ganguly et al. 2022; Ebagezio et al. 2022). The OH in the HD cloud is well-concentrated, with internal zones of low $N(\text{OH})$ that are tens of parsecs in scale and dense peaks with sharp column density gradients. The cores are generally clumpy, with $N(\text{OH})$ rising several orders of magnitude over just 1–3 pc. In contrast, the OH content of MC1-MHD is much more diffuse. The regions of peak $N(\text{OH})$ are not clumpy, but instead bundles of filaments with matching orientation. The value of $N(\text{OH})$ at the heart of these filaments approaches $N(\text{OH}) \approx 10^{16} \text{ cm}^{-2}$, as in the HD cloud, despite the great difference in the clouds’ respective column density distributions (again see Ganguly et al. 2022, for more comparisons of the bulk densities of HD and MHD SILCC-Zoom clouds).

The ranges and distributions of $N(\text{OH})$ in MC2-HD and MC2-MHD (not pictured) show the same differences seen in MC1-HD and MC1-MHD, with the caveat that MC2-MHD does not condense as much as the other clouds over the lifetime of the simulation. Thus, in MC2-MHD, $N(\text{OH})$ only rarely reaches the peak column density value of $N(\text{OH}) \approx 10^{16} \text{ cm}^{-2}$.

To illustrate the fine spatial resolution of our column density maps, in Fig. 5 we expand the inset box indicated in the y - z panel of MC1-MHD. The first panel repeats $N(\text{OH})$, with contours to indicate $A_{V,2D} = 1$ (blue) and $A_{V,2D} = 3$ (pink). At this scale, we find that $N(\text{OH})$ ascends rapidly through values around 10^{14} cm^{-2} to the peak of $N(\text{OH}) = 10^{16} \text{ cm}^{-2}$ in the heart of the filamentary bundle, i.e. within the $A_{V,2D} = 3$ contour. Individual filamentary structures can be distinguished inside the bundle, separated by pockets of slightly lower $N(\text{OH})$. At either end of the bundle, $N(\text{OH})$ does not taper off smoothly, but the structure instead breaks down into clumps with $N(\text{OH}) < 10^{15} \text{ cm}^{-2}$.

The second panel of Fig. 5 shows a typical measure of the OH abundance, the ratio $N(\text{OH})/N(\text{H}_2)$. We provide a high-resolution map on a similar physical scale as the Taurus Molecular Cloud observations by Xu et al. (2016). In the regions where $A_{V,2D} < 1$, the ratio is relatively high, approaching 10^{-6} . Then, transversely approaching the filament where $1 < A_{V,2D} < 3$, the abundance ratio shrinks toward 10^{-8} . Because the first panel shows that $N(\text{OH})$ is not declining in this region, the decline in $N(\text{OH})/N(\text{H}_2)$ is due to the increased H_2 abundance as shielding improves toward the filament. In the fully-shielded dense regions where $A_{V,2D} > 3$, the ratio increases again to over 10^{-7} . Dense regions in the other molecular clouds exhibit a similar relationship between $A_{V,2D}$ and $N(\text{OH})/N(\text{H}_2)$. A systematic exploration of this ratio, including its time-dependence and its relation to $A_{V,2D}$, is presented in Section 4.

In the third panel of Fig. 5, we map the ratio $N(\text{OH})/N(\text{CO})$. At the heart of the filamentary bundle, where the gas is fully molecular, this ratio is as low as 10^{-3} , in accordance with an $N(\text{OH})/N(\text{H}_2)$ ratio around 10^{-7} and a saturated CO abundance of 10^{-4} . However, outside the very dense gas, the value of $N(\text{OH})/N(\text{CO})$ plunges. The two species achieve parity around $A_{V,2D} = 1$. In the regions where $A_{V,2D} < 1$, $N(\text{OH})/N(\text{CO}) \sim 10$ or greater.

To supplement the three panels of this plot, in Appendix A we provide maps of $A_{V,2D}$, $N(\text{H}_2)$, and $N(\text{CO})$ over the same domain. These maps confirm that in MC1-MHD, the CO-dark gas lies between $A_{V,2D} \approx 1$ –3. We have confirmed that this CO-dark visual extinction regime holds for the other three simulated clouds as well (not shown).

In Fig. 6, we plot the time-dependence of $N(\text{OH})$ vs. $A_{V,2D}$ for the four molecular clouds. Along with results for $t_{\text{evol}} = 2, 3$, and 4 Myr (black, red, and blue), we provide the results when evolved to equilibrium (purple). From $A_{V,2D} = 0.1$ to 1, $N(\text{OH})$ increases from about 10^{12} to 10^{13} cm^{-2} for all four clouds. Between $A_{V,2D} \approx 1$ –3, $N(\text{OH})$

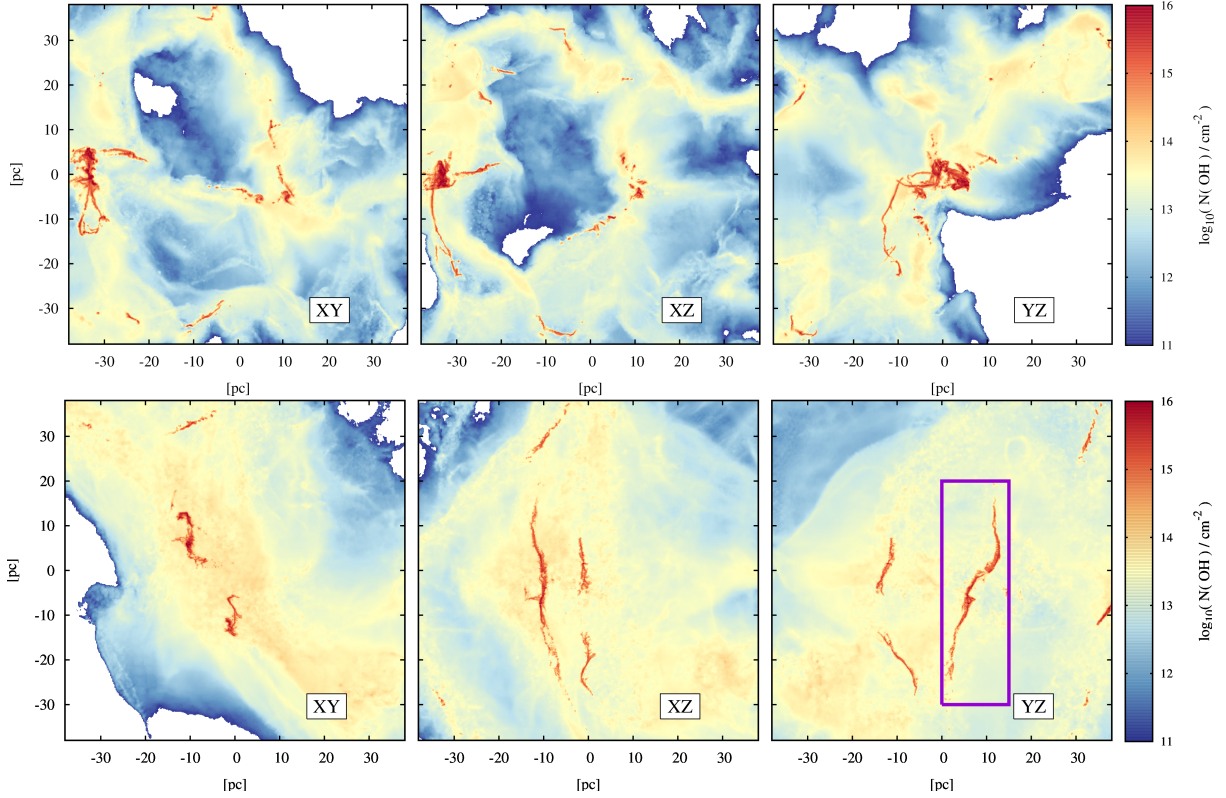


Figure 4. Maps of $N(\text{OH})$ from clouds MC1-HD (top) and MC1-MHD (bottom) at $t_{\text{evol}} = 4$ Myr for three lines of sight (left to right). The $N(\text{OH})$ distribution of the MHD cloud is much more diffuse than that of the HD cloud, with more filamentary structures instead of clumps. Both clouds have peak $N(\text{OH})$ values around 10^{16} cm^{-2} . The region indicated in the y-z projection of MC1-MHD is investigated in more detail in Fig. 5.

remains approximately constant. Above $A_{V,2D} \approx 3$, $N(\text{OH})$ resumes its increase, with peak values between $N(\text{OH}) \approx 10^{15} - 10^{16} \text{ cm}^{-2}$.

The value of $N(\text{OH})$ for any given $A_{V,2D}$ value increases by approximately 25% per 1 Myr of elapsed time. If evolved to equilibrium, $N(\text{OH})$ would increase at all $A_{V,2D}$ by up to an additional 25% compared to its reference value (i.e., the final point in time in the simulation). The peak value of $N(\text{OH})$ in all clouds at late times is around 10^{16} cm^{-2} , with variation of a factor of two. The value of $A_{V,2D}$ at which this peak $N(\text{OH})$ is reached decreases with later times. The MHD clouds reach the same peak $N(\text{OH})$ as the HD clouds do, but only at higher visual extinctions than in the HD clouds.

3.3 The distribution of OH

With the advantage of time-dependent data, in Fig. 7 we compare the cumulative distribution of the clouds' OH content at different timesteps within the simulation, as well as after evolving to equilibrium. Each row corresponds to a different molecular cloud. The left column plots the cumulative OH mass (solid lines) of each cloud's y-z column density projection below a given $A_{V,2D}$ threshold value, or equivalently below a threshold value of $N_{\text{H,tot}}$ (see Eq. 3). The right column plots the cumulative OH mass as a function of $n_{\text{H,tot}}$, or equivalently below a given bulk density $\rho = (1.4m_{\text{p}})n_{\text{H,tot}}$, where m_{p} is the proton mass. The black, red, and blue lines correspond to $t_{\text{evol}} = 2, 3$, and 4 Myr respectively; the tracers of MC2-HD did not reach $t_{\text{evol}} = 4$ Myr, so the final available timestep of $t_{\text{evol}} = 3.76$ Myr

is plotted instead, in green. The purple lines correspond to the result at equilibrium. The dashed lines indicate the cumulative H_2 mass of each cloud at each time.

The distribution of OH in projection (left column) differs dramatically between the HD and MHD clouds. In clouds MC1-HD and MC2-HD, at $t_{\text{evol}} = 2$ Myr, half of the OH content lies between $A_{V,2D} = 1-10$. As time passes, more OH forms in the very dense gas. The distribution at equilibrium resembles the distribution at 4 Myr, but differs significantly from the distribution at 2 Myr.

The MHD clouds, in contrast, have much more extensive OH envelopes. Half of the OH mass is found within the $A_{V,2D}$ interquartile range of 0.6–1.6. At all timesteps for both MHD clouds, half of the OH content is located outside $A_{V,2D} \approx 1$. The third quartile $A_{V,2D}$ value, outside which 75% of the OH lies, changes significantly for MC1-MHD over the time-dependent results (from $A_{V,2D} = 1$ to 8), but is almost unchanged for MC2-MHD.

Notably, the cumulative distributions of OH and H_2 evolve in similar ways over time. Both species are distributed over a narrower range in $A_{V,2D}$ at $t_{\text{evol}} = 4$ Myr than at $t_{\text{evol}} = 2$ Myr. Generally, each quartile of the OH distribution occurs at a lower density than the corresponding quartile in H_2 . This indicates that the cumulative OH content acts as a leading indicator of the H_2 content as the gas density increases, but is less useful for tracing the H_2 at very high densities, in particular above $n_{\text{H,tot}} = 10^2 - 10^3 \text{ cm}^{-3}$, and especially at earlier evolution times.

In Appendix B, we repeat the cumulative distribution of OH, but

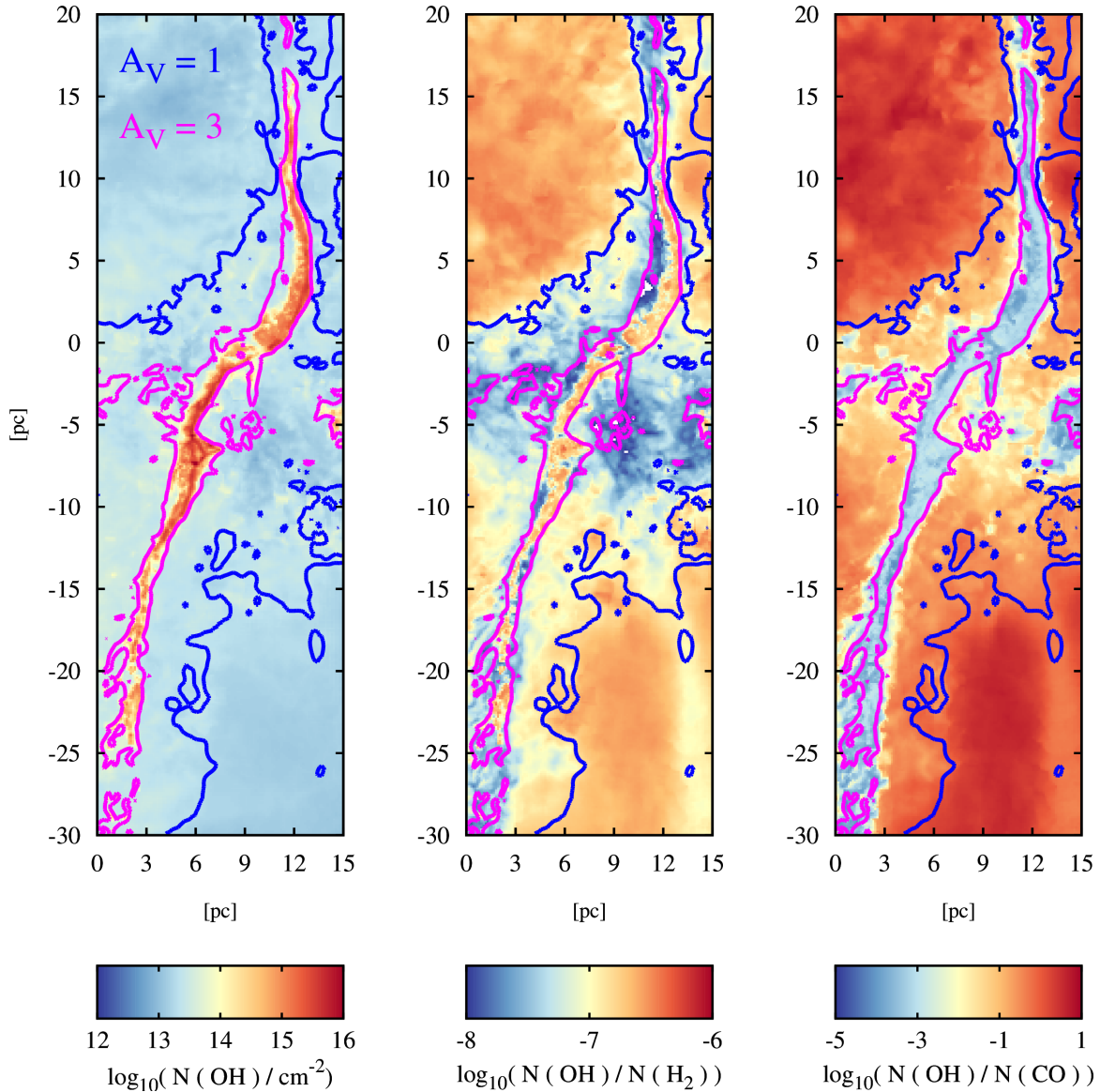


Figure 5. Zoomed-in detail from Fig. 4, in the y-z projection of $N(\text{OH})$ from MC1-MHD at $t_{\text{evol}} = 4$ Myr. Contours for $A_{V,2D} = 1$ (blue) and $A_{V,2D} = 3$ (pink) mark the rough lower and upper visual extinction bounds of the CO-dark gas. First panel: $N(\text{OH})$, showing the intricate filamentary detail of the simulation. Second panel: $N(\text{OH})/N(\text{H}_2)$, revealing the three distinct $A_{V,2D}$ regimes for this ratio. The ratio reaches its minimum value within $1 < A_{V,2D} < 3$, the CO-dark regime. Third panel: $N(\text{OH})/N(\text{CO})$, showing that within the CO-dark gas, the OH content exceeds the CO content by an order of magnitude.

compare it to the bulk gas distribution rather than the distribution of H_2 . We find that in the denser HD clouds, a larger fraction of the bulk mass lies at low densities (both column and volume), where OH is less abundant. By contrast, the bulk gas distribution aligns much better with the OH in the puffer MHD clouds. We find that the cumulative bulk mass distributions barely change as time passes, meaning that the clouds' changing OH distributions are due to the evolution of the chemical network, rather than a bulk shift in the dynamical environment affecting where OH can survive (e.g., by changes in the overall shielding).

To supplement the cumulative mass distributions of OH and H_2 , we provide in Fig. 8 the probability density functions (PDFs) of $N(\text{OH})$

for all four simulated clouds. A line corresponding to $\log N \propto -2$ (cyan) is provided for comparison. For all clouds and on all three sightlines, the highest probability density is found around $N(\text{OH}) \approx 10^{13} \text{ cm}^{-2}$. As t_{evol} increases, the peak probability column density increases by a factor of 2–5 depending on the cloud and sightline. The three sightlines at each timestep correspond more closely in the HD clouds than in the MHD clouds.

Following the peak, the PDF curves all decline sharply until $N(\text{OH}) \approx 10^{14} \text{ cm}^{-2}$. Above that column density, the probability curve rises again, to a local maximum around $N(\text{OH}) \approx 10^{15} \text{ cm}^{-2}$. The peak probability density in this local minimum rises by 0.5–1 order of magnitude over time, with the greatest increase seen for MC1-

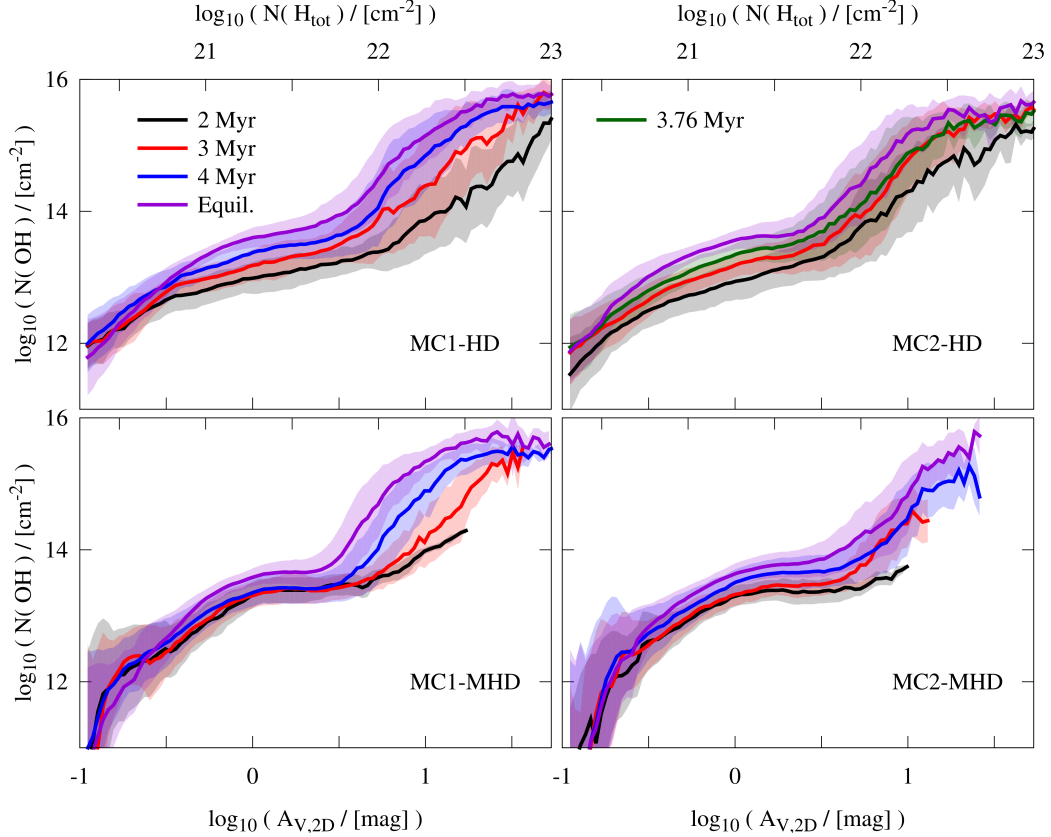


Figure 6. Average $N(\text{OH})$ vs. projected visual extinction $A_{V,2D}$ for the four molecular clouds at different times. The shaded areas represent one standard deviation from the respective average. $N(\text{OH})$ plateaus below 10^{14} cm^{-2} just below $A_{V,2D} \approx 3$, with the value of the plateau rising with time. Above $A_{V,2D} \approx 3$, $N(\text{OH})$ rises, the rise starting at lower $A_{V,2D}$ with increasing time. The equilibrium results have the highest $N(\text{OH})$ everywhere, and rise toward the max value of 10^{16} cm^{-2} at a lower $A_{V,2D}$ value than any time-dependent results.

MHD. We ascribe the development of this time-dependent feature to the gradual condensation of the densest regions of the clouds. The HD clouds are mostly condensed at t_0 , while MC1-MHD still shows rapid evolution and collapse after t_0 , and so its newly-dense core regions still experience significant OH growth at late times. Finally, MC2-MHD undergoes little dynamic collapse during the simulation lifetime, and so its probability peak at high $N(\text{OH})$ remains small.

Additional PDFs of the $N(\text{H}_{\text{tot}})$ for each cloud, time, and sightline are provided in Appendix C. Their shapes and peak values of $N(\text{H}_{\text{tot}}) \approx 10^{21} \text{ cm}^{-2}$ are consistent with other works, e.g. Bisbas et al. (2019).

3.4 The effect of equilibrium chemistry

Next, we consider how evolving the time-dependent chemical abundances to equilibrium affects the distributions of OH, H_2 , and CO. Ebagezio et al. (2022) and Seifried et al. (2021) have shown that equilibrium abundances for H_2 and CO overestimate the proper time-dependent results, and we investigate whether OH is similarly overestimated.

In Fig. 3, we plot for each cloud and species the total mass at equilibrium, represented by points after a break in the time axis. We find that the equilibrium result overestimates the total H_2 masses at $t_{\text{evol}} = 4 \text{ Myr}$ by 40–110%. Furthermore, the total CO masses

are overestimated by 8–60%. The OH masses at equilibrium are overestimated by 50–60%. For all three species, the upper limit of the overestimation range is provided by the MHD clouds. These overestimations increase by another factor of 2–3 when comparing the equilibrium results to the values at $t_{\text{evol}} = 2 \text{ Myr}$.

Because the H_2 and OH abundances suffer from similar overestimation errors, the equilibrium results for $M_{\text{OH}}/M_{\text{H}_2}$ are quite close to the values at $t_{\text{evol}} = 4 \text{ Myr}$ (3.76 Myr for MC2-HD). The exception to this is the mass ratio for MC2-MHD, which declines by almost a factor of two. Given that the two MHD clouds experienced the same proportional increase in H_2 from the last time-dependent snapshot to equilibrium, the decline in $M_{\text{OH}}/M_{\text{H}_2}$ for MC2-MHD stems from that cloud’s lower equilibrium value of OH.

These overestimations, and the degree to which they worsen when considering early timesteps in the clouds’ evolution, correspond closely to an analogous comparison in Ebagezio et al. (2022), which used the same simulated clouds, but an entirely distinct post-processing method from the one employed in this work. They find that after evolving equilibrium, the H_2 content in the HD clouds increases by up to 120%, and the CO content by up to 30%. This accords with the results in Gong et al. (2018) and Hu et al. (2021) as well, emphasizing that evolving these molecular species to equilibrium assuredly overestimates them.

Considering $N(\text{OH})$ vs. $A_{V,2D}$ in Fig. 6, we note that the equi-

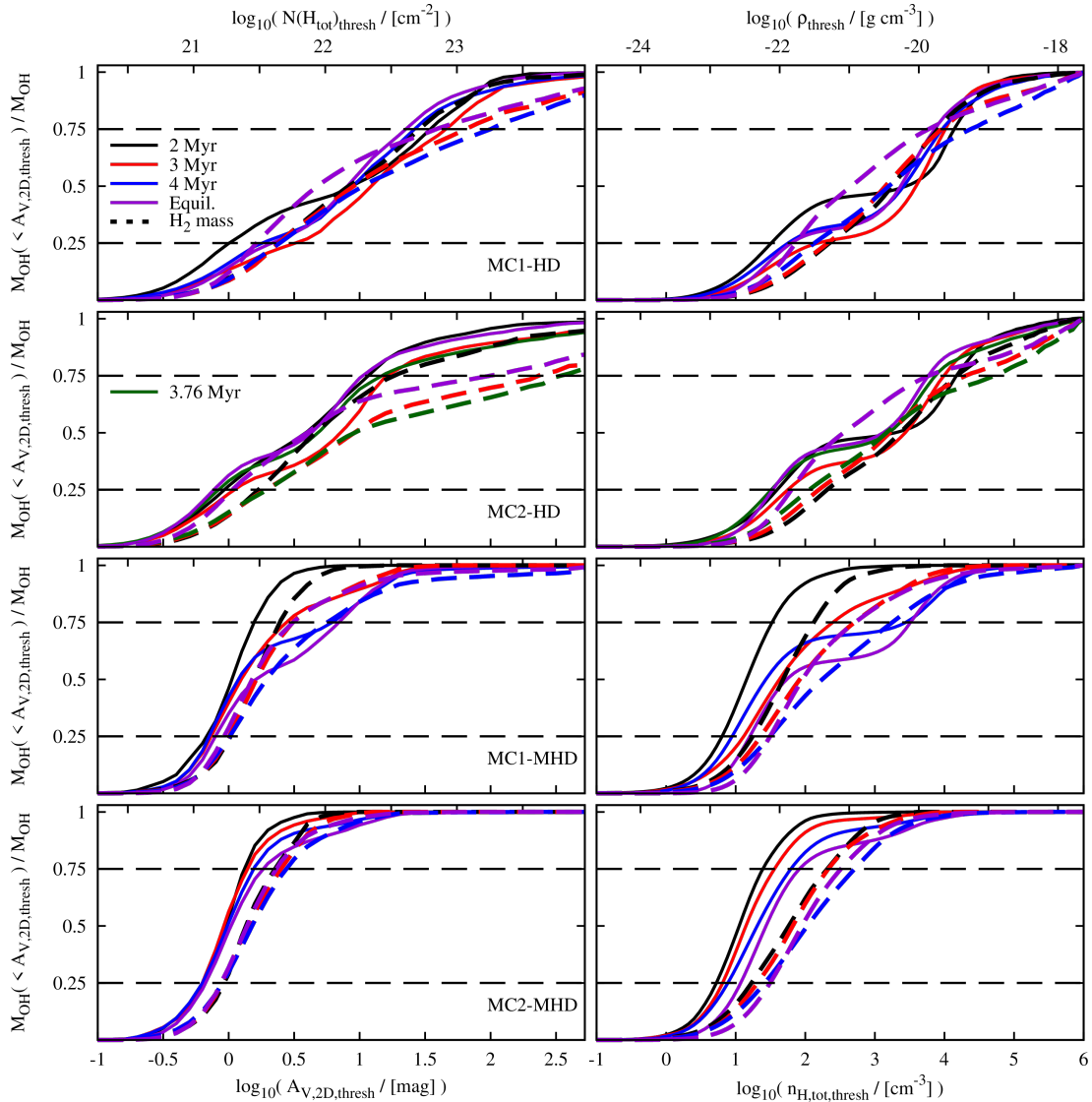


Figure 7. The normalized cumulative mass distribution of OH in each molecular cloud found below various density measures. The left column gives the fraction of OH mass in the y - z projections found below a threshold visual extinction $A_{V,2D,thresh}$. The right column gives the fraction of OH mass found below a threshold total hydrogen number density $n_{H,tot,thresh}$. The OH distributions (solid lines) are given at different values of t_{evol} , and at equilibrium. The cumulative fractions of the clouds’ H_2 masses are also provided (dashed lines).

librium value of $N(OH)$ is overestimated everywhere, in agreement with the overall increase in OH mass. Furthermore, the column density plateau that begins at $A_{V,2D} \approx 1$ resumes rising at a lower visual extinction at equilibrium than in the time-dependent results. Only where $A_{V,2D} \lesssim 0.3$ do the equilibrium and time-dependent values of $N(OH)$ correspond.

As seen in Fig. 7, evolving to equilibrium also changes the fraction of total OH in the CO-bright regime ($A_{V,2D} \gtrsim 3$) when compared to the time-dependent results. For the HD clouds, more OH is generated in the intermediate density regime and so the third quartile is reached at a lower $A_{V,2D}$ at equilibrium than in the time-dependent results. For the MHD clouds, which form dense gas mainly during later stages of their evolution ($t_{evol} \gtrsim 3$ Myr), the fraction of OH at high visual

extinction increases rather than decreases. These outcomes for OH mirror those for H_2 : the equilibrium H_2 in the HD clouds is more diffuse in the time-dependent results than at equilibrium, and vice versa for the MHD clouds.

To summarize, we find that the total masses and distributions of OH, H_2 , and CO under the assumption of chemical equilibrium differ significantly from the time-dependent results which properly track the dynamical evolution of the clouds. This underscores the care that must be taken when drawing conclusions from equilibrium chemistry about clouds that are still undergoing dynamical evolution, especially given such results as Chevance et al. (2020) which find that giant molecular clouds only live for 1–5 Myr after massive stars

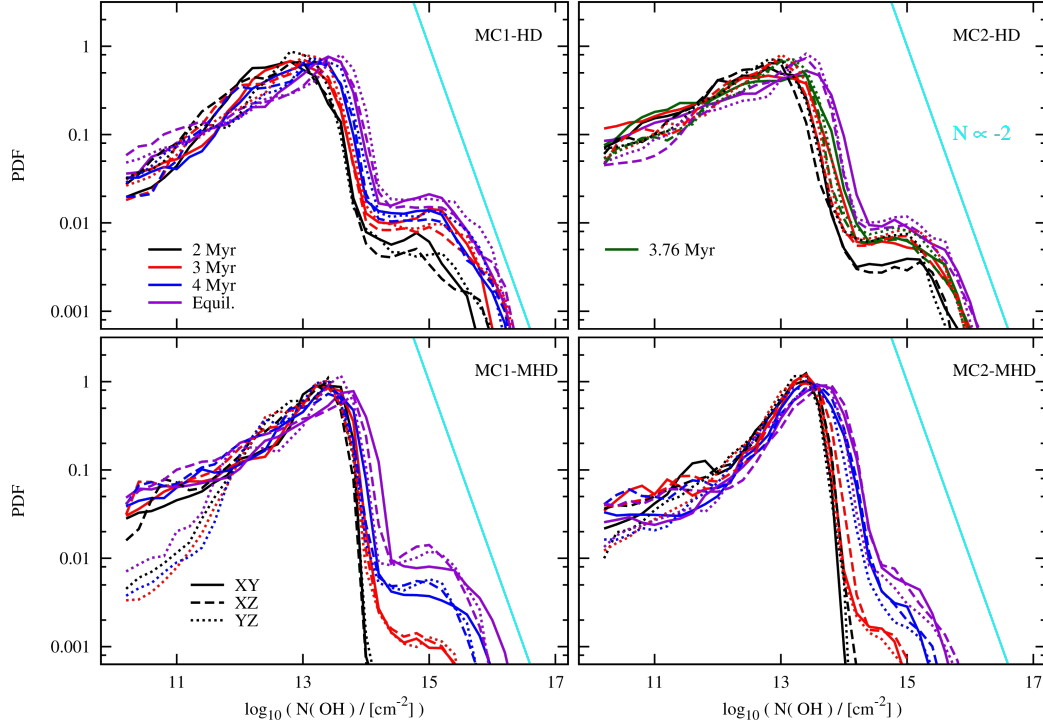


Figure 8. Probability density functions (PDFs) for $N(\text{OH})$ for the four simulated clouds at $t_{\text{evol}} = 2$ (black), 3 (red), and 4 Myr (blue), as well as at equilibrium (purple). For MC2-HD, the final timestep at $t_{\text{evol}} = 3.76$ Myr is provided. The different dash styles represent the three axes of column density projection. The cyan line represents the relationship $\log N \propto -2$. The highest probability density of $N(\text{OH})$ is consistently around $N(\text{OH}) \approx 10^{13} \text{ cm}^{-2}$. As time passes, a second local maximum develops at $N(\text{OH}) \approx 10^{15} \text{ cm}^{-2}$, most obviously in the HD clouds but eventually emerging in MC1-MHD as well.

are born. Our findings suggest that this may not be enough time for the clouds to ever reach equilibrium before they are dispersed.

4 TRACING MOLECULAR GAS WITH OH

Having established the abundance and distribution of OH in our simulated molecular clouds, we can now assess how OH traces the molecular hydrogen distribution. The value of $N(\text{H}_2)$ could be directly calculated from the emission of particular OH lines by way of an X_{OH} factor, analogous to the X_{CO} factor, as in [Xu & Li \(2016\)](#). As our post-processing and regridding method gives us direct access to the total species column densities without this observational error, we can directly compare $N(\text{H}_2)$ and $N(\text{OH})$ in the CO-dark gas regime, and try to relate the two without reference to emission.

4.1 The dark gas fraction

First, we must determine the visual extinction regime of the CO-dark gas in our molecular clouds. We calculate the ‘dark gas fraction’ (DGF) for each pixel in our column density maps using the relation

$$\text{DGF} = 1 - \frac{N(\text{CO}) \times \frac{1}{2.8 \times 10^{-4}}}{N(\text{H}_2)}, \quad (5)$$

which was also employed with these simulations in [Seifried et al. \(2020\)](#). In Fig. 9, we plot the average DGF vs. $A_{\text{V},2\text{D}}$ for the cloud MC1-HD at $t_{\text{evol}} = 2, 3$, and 4 Myr, and at equilibrium. Below $A_{\text{V},2\text{D}} \approx 1$ at all timesteps, the CO content is negligible, and the

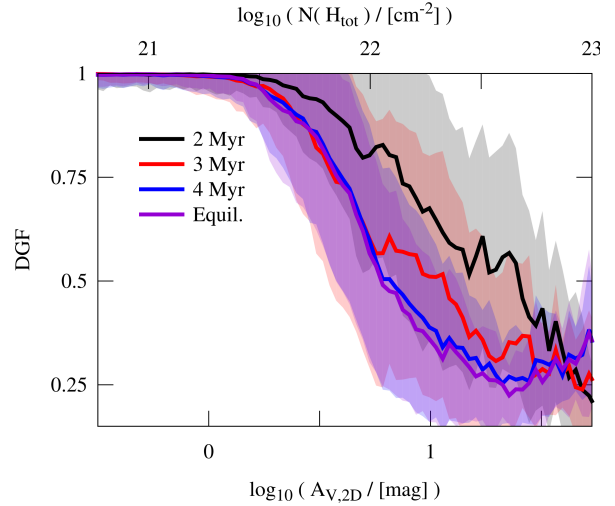


Figure 9. Average DGF as defined in Eq. 5, vs. projected visual extinction $A_{\text{V},2\text{D}}$ for MC1-HD at $t_{\text{evol}} = 2, 3$, and 4 Myr, and at equilibrium. The shaded areas represent one standard deviation from the respective average. The dark gas fraction falls over time for all visual extinctions above $A_{\text{V},2\text{D}} \approx 1$, but remains close to unity for $A_{\text{V},2\text{D}} \lesssim 3$ where shielding does not suffice for the survival of CO.

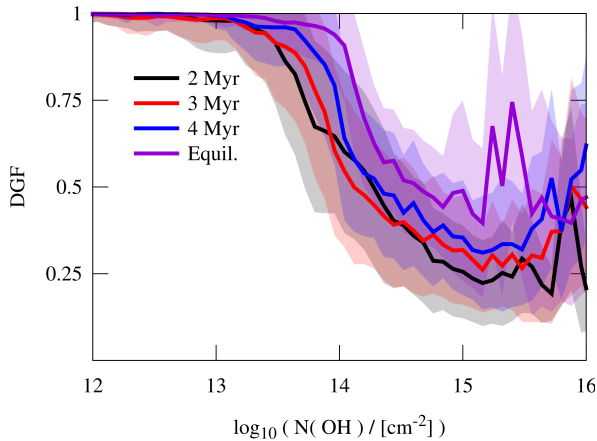


Figure 10. Same as Fig. 9, but plotting DGF against $N(\text{OH})$. In the CO-dark molecular gas, $N(\text{OH})$ is as high as 10^{14} cm^{-2} .

DGF does not decline below 50% until $A_{V,2D} \sim 5$. For the other clouds, the DGF curve behaves similarly, though it declines to 50% at $A_{V,2D} \sim 3$ in the MHD clouds.

In Fig. 6 we have seen that for all four clouds, $N(\text{OH})$ varies between about 10^{12} and 10^{14} cm^{-2} in this $A_{V,2D}$ range. To confirm the correspondence of this $N(\text{OH})$ range with the CO-dark gas, we plot in Fig. 10 the DGF vs. $N(\text{OH})$ for MC1-HD at different times. As OH broadly traces the molecular gas, unsurprisingly this relation looks similar to Fig. 9. At a high value of the DGF, $N(\text{OH})$ varies between 10^{12} and 10^{14} cm^{-2} . As time passes, and the cloud continues to condense, we find an increase in the threshold value of $N(\text{OH})$ at which the DGF begins to decline. At $t_{\text{evol}} = 4 \text{ Myr}$, the CO-dark gas contains a greater proportion of gas with higher values of $N(\text{OH})$ than it did at earlier times. Because of this time variance, tracing the CO-dark H_2 content in the clouds therefore requires a clear parameterization that links OH to H_2 up to $N(\text{OH}) \approx 10^{14} \text{ cm}^{-2}$.

4.2 Comparison of $N(\text{OH})$ with $N(\text{H}_2)$

Now that we have established the $A_{V,2D}$ and $N(\text{OH})$ regimes which correspond to the CO-dark gas, we can directly relate $N(\text{OH})$ with $N(\text{H}_2)$. We plot $N(\text{OH})$ vs. $N(\text{H}_2)$ in Fig. 11 for all four clouds at different times, and at equilibrium. Observations of OH have commonly reported the molecular abundance ratio $N(\text{OH})/N(\text{H}_2)$, derived using the OH transitions at 1665 and 1667 MHz, and generally around 10^{-7} (see e.g. Liszt & Lucas 1996, 2002; Nguyen et al. 2018; Rugel et al. 2018; Jacob et al. 2019; Busch et al. 2021). We plot this ratio in the figure (dashed, middle), as well as ratios of 10^{-6} (dotted) and 10^{-8} (dashed-dot).

Rather than a single value of 10^{-7} as in most sources, we find that the ratio $N(\text{OH})/N(\text{H}_2)$ exhibits non-linear behavior. At low $N(\text{H}_2)$ the ratio is above 10^{-7} , then dips as low as 10^{-8} when $N(\text{H}_2)$ is between $\sim 10^{20}$ – 10^{22} cm^{-2} , before rising to $\sim 10^{-7}$ at higher $N(\text{H}_2)$ until it declines below 10^{-7} at the highest column densities attained in the clouds. By approximating $N(\text{OH})/N(\text{H}_2)$ at a consistent value of 10^{-7} , given a certain value of $N(\text{OH})$, one would overestimate $N(\text{H}_2)$ at low densities by up to a factor of five, and underestimate it at medium densities up to a factor of ten. Furthermore, there is notable time variance in the $N(\text{OH})$ vs. $N(\text{H}_2)$ relationship, partic-

ularly for $N(\text{H}_2) \gtrsim 10^{20} \text{ cm}^{-2}$. Between $t_{\text{evol}} = 2$ – 4 Myr , the ratio $N(\text{OH})/N(\text{H}_2)$ grows by up to a factor 5–8.

We have shown that to trace H_2 in the CO-dark gas, we must relate the two species in the regime where $N(\text{OH})$ varies between 10^{12} and 10^{14} cm^{-2} . The relationship between the species seems consistent and time-invariant below $N(\text{H}_2) \lesssim 10^{20} \text{ cm}^{-2}$, but above this, $N(\text{OH})$ levels off around $5 \times 10^{13} \text{ cm}^{-2}$ up to $N(\text{H}_2) \approx 5 \times 10^{21} \text{ cm}^{-2}$. This is precisely in the CO-dark gas regime, and so taking OH in isolation, we do not find that $N(\text{OH})$ alone can reliably trace the $N(\text{H}_2)$ content of the CO-dark gas. However, we can propose an alternative molecular gas tracing procedure.

As mentioned above, the abundance ratio $N(\text{OH})/N(\text{H}_2)$ is usually reported as a single value over a field of view. Systematic analysis of this ratio as a function of visual extinction is less common, but has been performed by Xu et al. (2016), who made a series of Arecibo radio telescope observations along the boundary of the Taurus Molecular Cloud complex. By calculating the $N(\text{OH})/N(\text{H}_2)$ ratio as well as the visual extinction within each pointing, they found a functional relation whereby $N(\text{OH})/N(\text{H}_2)$ declines with increasing visual extinction, which corresponds to what we show in Fig. 12. They report this ratio declines from 8×10^{-7} to 1×10^{-7} from $A_{V,2D} = 0.4$ – 2.7 . They attribute the high value in $N(\text{OH})/N(\text{H}_2)$ (80 times greater than predicted in models) at low visual extinctions to a C-shock. Additional uncertainty in these observations stems from the uncertainties in the inference of $N(\text{H}_2)$ from dust continuum emission and the assumption that, in this visual extinction regime, the hydrogen is fully molecular. We can resolve both of these uncertainties with the full knowledge of $N(\text{H}_2)$ available in simulations.

We can plot $N(\text{OH})/N(\text{H}_2)$ vs. $A_{V,2D}$ for all four simulated clouds at several times, as well as after evolving to equilibrium. The outcome of this analysis is shown in Fig. 12. All four clouds display a functional relation between these quantities that matches the projection of $N(\text{OH})/N(\text{H}_2)$ in the zoomed-in filament detail in Fig. 5. Between $A_{V,2D} \approx 0.1$ – 3 , $N(\text{OH})/N(\text{H}_2)$ declines smoothly from 5×10^{-7} to 5×10^{-8} . This holds for both HD and MHD clouds. For the time-dependent results, this functional form is mostly time-invariant; at equilibrium, the ratio is slightly lower everywhere within this $A_{V,2D}$ range.

Above $A_{V,2D} \gtrsim 3$, we find that $N(\text{OH})/N(\text{H}_2)$ has strong time variation in both the value of $A_{V,2D}$ at which it begins rising again as well as the peak $N(\text{OH})/N(\text{H}_2)$ value that is then achieved. Later times correspond to a higher peak $N(\text{OH})/N(\text{H}_2)$ value and a lower visual extinction at which the ratio rises again. This time variance makes it more difficult to trace H_2 with OH at high $A_{V,2D}$ than at low $A_{V,2D}$.

We parameterize the change in the $N(\text{OH})/N(\text{H}_2)$ ratio as a function of $A_{V,2D}$ using an exponential fit (following the functional form of Xu et al. 2016), for $\log A_{V,2D} < 0.5$. This fit synthesizes 36 data sets from Fig. 12, comprising four clouds, three sightlines, and three non-equilibrium snapshots each. The fit equation takes the form:

$$\frac{N(\text{OH})}{N(\text{H}_2)} = (2.8 \times 10^{-8}) + (3.0 \times 10^{-7}) \exp(-A_{V,2D}/0.98) \quad (6)$$

and is plotted in Fig. 13 in red over the domain $\log A_{V,2D} \in [-1, 0.5]$. The 36 sets of source data for the fit are plotted in grey for comparison. Our fit coefficients roughly correspond to those in Xu et al. (2016), whose fit was taken over the $A_{V,2D}$ range 0.4–2.7 in the TMC boundary.

To supplement this 2D perspective with a 3D volumetric view, we additionally plot in Fig. 14 the ratio $n_{\text{OH}}/n_{\text{H}_2}$ vs. the total hydrogen density $n_{\text{H,tot}}$, for MC1-HD. We again see the abundance ratio decline from $\sim 5 \times 10^{-7}$ but now to a local minimum of $\sim 5 \times 10^{-9}$ (an order

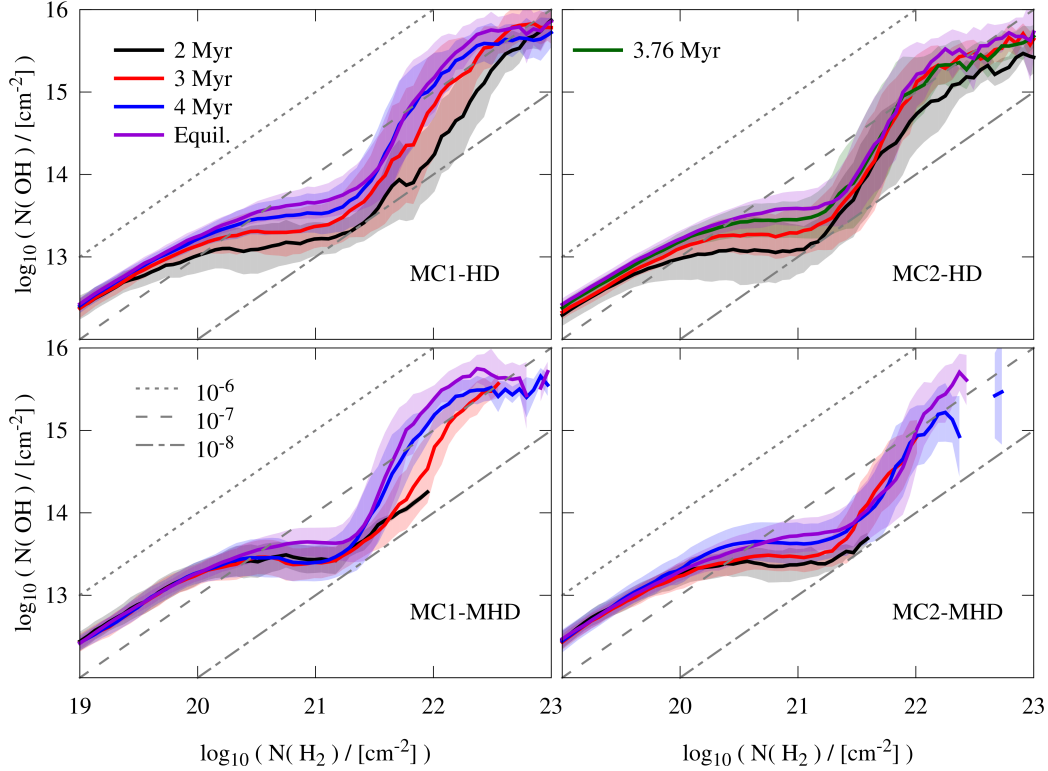


Figure 11. Average $N(\text{OH})$ vs. average $N(\text{H}_2)$ for the four molecular clouds at $t_{\text{evol}} = 2, 3$, and 4 Myr, and at equilibrium. For MC2-HD, the final timestep at $t_{\text{evol}} = 3.76$ Myr is provided. The shaded areas represent one standard deviation from the respective average. Abundance ratios of 10^{-6} , 10^{-7} , and 10^{-8} are plotted as different dashed lines. The abundance ratio of OH and H_2 varies with density, converging to the usual value of 10^{-7} only in the densest core regions. Because the relation between $N(\text{OH})$ and $N(\text{H}_2)$ is non-linear, it is difficult to trace the H_2 content using $N(\text{OH})$ alone.

of magnitude below the 2D case), over a change in $n_{\text{H,tot}}$ from 1 to 10^3 cm^{-3} . Above $n_{\text{H,tot}} \approx 10^3 \text{ cm}^{-3}$, the abundance ratio rises back to $\sim 5 \times 10^{-7}$ as it does in the 2D case. Based on the minimum's location, we infer that pixels in the 2D projections with $A_{\text{V,2D}} \approx 3$ have an average $n_{\text{H,tot}}$ of $\sim 10^3 \text{ cm}^{-3}$ along the line of sight.

4.3 Formation and destruction of OH

Inspecting the abundance ratio OH/ H_2 in both two and three dimensions indicates a global minimum around $A_{\text{V,2D}} \approx 3$ or $n_{\text{H,tot}} \approx 10^3 \text{ cm}^{-3}$. At both greater and smaller densities, the abundance ratio climbs to $\sim 10^{-7}$. We investigate the global minimum by studying the creation and destruction reactions for OH in our post-processing network, using a method employed in Panessa et al. (2022) to study the formation reactions of the dense gas tracer HCO^+ .

The post-processed tracer particles from the SILCC-Zoom simulations, from which we compose our 3D density distributions and column density maps, save all local chemical abundances and the temperature as a function of time. Thus, in a given snapshot, every tracer's local net production rate for OH can be solved by taking the difference of the summed creation reactions F and summed destruction reactions D for OH. These are calculated respectively as:

$$F_i = k_i(T) \prod_{j=1}^R n_j \quad (7)$$

$$D_i = k_i(T) \prod_{j=1}^R n_j \quad (8)$$

for each reaction i with reactants j , where $k_i(T)$ is the reaction rate coefficient. We calculate for each $n_{\text{H,tot}}$ bin the average rate F_i or D_i , and divide by $n_{\text{H,tot}}$ to normalize the reactions with respect to the density. This procedure (repeated from Panessa et al. 2022) allows for the comparison of the impact of different creation and destruction routes at different gas densities.

The results of this analysis are plotted in Fig. 15, showing the average normalized reaction rate for the 5 strongest formation paths and the 4 strongest destruction paths, for the cloud MC1-HD at $t_{\text{evol}} = 4$ Myr. All of the other, unplotted reactions are comparatively negligible. The OH formation reactions are split into two regimes. At densities $n_{\text{H,tot}} \lesssim 10^2 \text{ cm}^{-3}$, OH production is driven mostly by electron recombination with H_2O^+ . In denser gas, where $n_{\text{H,tot}} \gtrsim 10^4 \text{ cm}^{-3}$, the dominant production route is instead via two types of electron recombination with H_3O^+ , the reactions differing by producing two hydrogen atoms (#1) or one hydrogen molecule (#2) alongside the OH.

Between these low and high density regimes, the electron recombination routes with H_2O^+ and H_3O^+ are both disfavored, with the neutral-neutral $\text{O} + \text{H}$ reaction an order of magnitude weaker than the peak normalized rates of the recombination reactions. In this regime, where $n_{\text{H,tot}} \approx 10^3 \text{ cm}^{-3}$, most of the primary de-

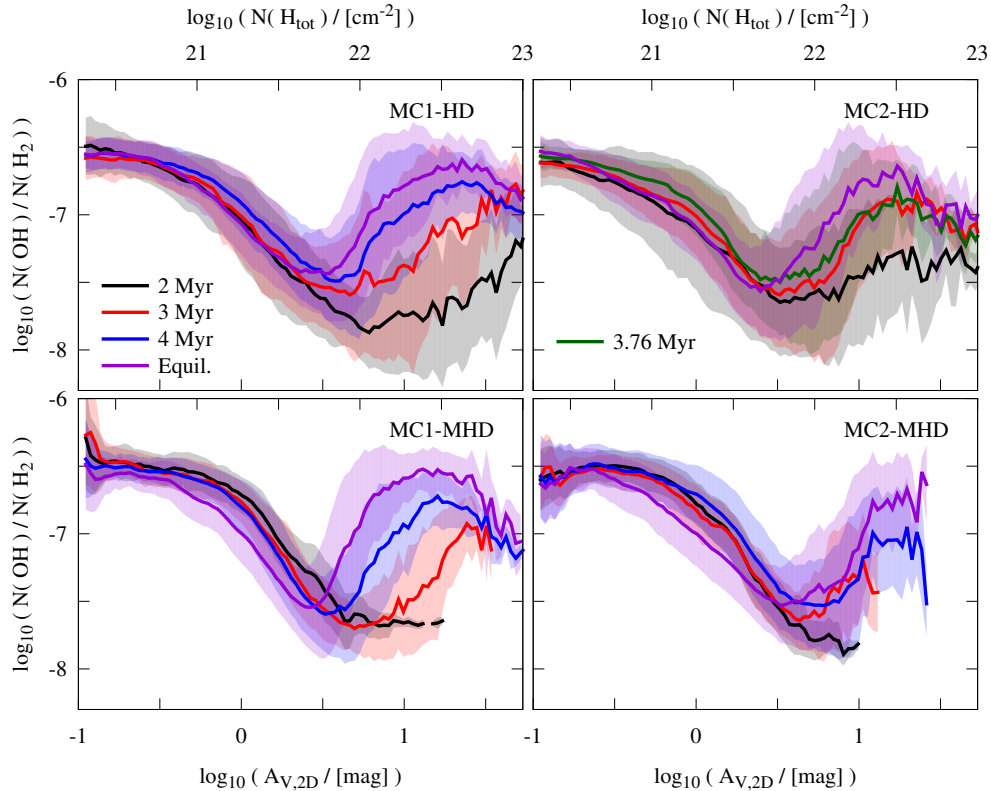


Figure 12. Average of the abundance ratio $N(\text{OH})/N(\text{H}_2)$ vs. visual extinction $A_{V,2D}$ in the y - z direction for the four molecular clouds at $t_{\text{evol}} = 2, 3$, and 4 Myr, and at equilibrium. For MC2-HD, the final timestep at $t_{\text{evol}} = 3.76$ Myr is provided. The shaded areas represent one standard deviation from the respective average. The ratio declines from 5×10^{-7} to 5×10^{-8} over the visual extinction range $A_{V,2D} \approx 0.1$ to 3, without much change in time. Above $A_{V,2D} \approx 3$, the abundance ratio rises. As time increases, the peak of this rise increases and the $A_{V,2D}$ value where the rise begins decreases. At equilibrium, $N(\text{OH})/N(\text{H}_2)$ is the same inside the densest peaks as it is outside the molecular gas regime.

struction routes are also curtailed, with one exception: the reaction $\text{OH} + \text{C}^+ \rightarrow \text{H} + \text{CO}^+$. This route strengthens with decreasing gas temperature and with increasing C^+ density. In Fig. 16, we plot these quantities and find that at $n_{\text{H,tot}} \approx 10^3 \text{ cm}^{-3}$ (the density of the global minimum in OH/H_2) the C^+ number density reaches its peak value of $\sim 10^{-1} \text{ cm}^{-3}$, and the gas temperature falls to $\sim 10 \text{ K}$ (the temperature regime of dense molecular gas). These conditions maximize the strength of the $\text{OH} + \text{C}^+$ reaction, explaining the observed minimum in the OH/H_2 ratio at the inner boundary of the CO-dark gas regime.

5 CONCLUSIONS

In this work, we have simulated the non-equilibrium abundance and distribution of OH throughout molecular clouds, with particular attention to the OH content of the dark molecular gas. We applied our time-dependent chemical post-processing and regridding algorithm (Panessa et al. 2022) to four SILCC-Zoom molecular cloud simulations, two HD (Seifried et al. 2017) and two MHD (Seifried et al. 2020). We tracked the distributions of OH as the clouds dynamically evolved. We have also compared these time-dependent results to the typical practice of evolving the chemistry of a dynamically-frozen snapshot to equilibrium. We summarize our results as follows:

(i) The regridding algorithm introduced in Panessa et al. (2022), which reconstructs 3D density distributions from chemically post-processed tracer particle histories, accurately models the diffuse molecular hydrogen distribution. The correspondence between H_2 abundance values from the original SILCC grids and the regridded tracers in the CO-dark gas regime is 10–15%.

(ii) The total mass of OH in all four molecular clouds grows by a factor of 2–3 from $t_{\text{evol}} = 2$ to 4 Myr, slightly exceeding the growth in total mass of H_2 in each cloud. The average OH mass fraction $M(\text{OH})/M(\text{H}_2)$ at $t_{\text{evol}} = 4$ Myr varies between $\sim 7 \times 10^{-7}$ (HD clouds) to $\sim 10^{-6}$ (MHD clouds).

(iii) We showcase unprecedented non-equilibrium column density maps of OH at a spatial resolution of 0.125 pc. In HD and MHD clouds, $N(\text{OH})$ ranges from 10^{11} – 10^{16} cm^{-2} . The regions of densest OH in the MHD clouds are less extensive than in the HD clouds, but show the same peak density. The OH distribution visually corresponds to the spatial extent of the simulations' H_2 distributions.

(iv) The overall distribution of OH differs between HD and MHD clouds. In HD clouds, half of the OH mass lies on average between $A_{V,2D} = 1$ –10, and for MHD clouds between $A_{V,2D} = 0.6$ –1.6. In all clouds, the OH fraction found at high density increases with time. The fraction of OH in the CO-dark gas regime remains fairly stable.

(v) Comparing $N(\text{OH})$ to $N(\text{H}_2)$ indicates that $N(\text{OH})$ plateaus around 10^{13} cm^{-2} while $N(\text{H}_2)$ rises from 10^{20} to 10^{21} cm^{-2} . Re-

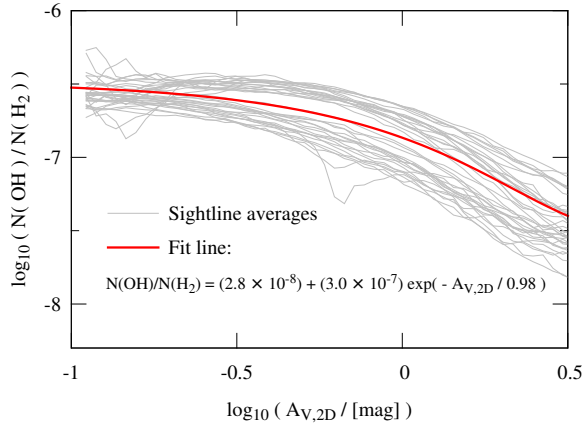


Figure 13. An exponential function (red) fit to $N(\text{OH})/N(\text{H}_2)$ vs. $A_{V,2D}$, for $\log A_{V,2D} < 0.5$. The 36 data sets from Fig. 12 which established the fit are plotted for comparison (grey).

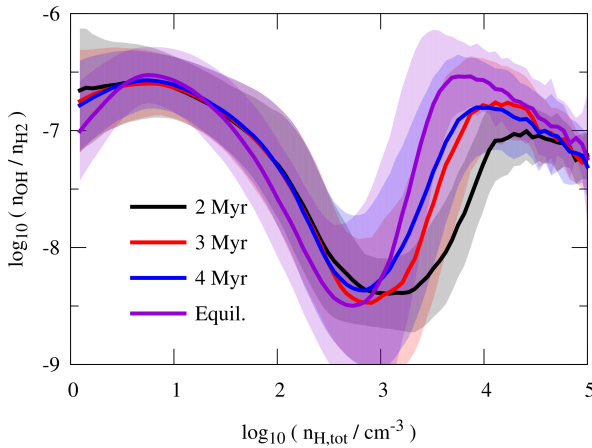


Figure 14. Average abundance ratio $n_{\text{OH}}/n_{\text{H}_2}$ vs. hydrogen number density $n_{\text{H,tot}}$, for cloud MC1-HD at $t_{\text{evol}} = 2, 3, \text{ and } 4$ Myr, and at equilibrium. The shaded areas represent one standard deviation from the respective average. We find that the OH and H_2 volume densities show the same qualitative behavior as in the 2D case of Fig. 12. The peak values of the abundance ratio are above 10^{-7} as in the 2D case, but the minimum ratio of about 5×10^{-9} , near $n_{\text{H,tot}} \sim 10^3 \text{ cm}^{-3}$, is an order of magnitude lower than in projection.

gions with this plateau value of $N(\text{OH})$ trace the physical extent of the CO-dark gas, but due to its flat profile in this range, $N(\text{OH})$ cannot be directly converted into $N(\text{H}_2)$.

(vi) In CO-dark gas ($A_{V,2D} \lesssim 3$), $N(\text{OH})/N(\text{H}_2)$ is time-invariant and consistent in all four molecular clouds, declining from 5×10^{-7} to 5×10^{-8} from $A_{V,2D} = 0.1$ to 3. At $A_{V,2D} > 3$, $N(\text{OH})/N(\text{H}_2)$ rises again to $\sim 10^{-7}$, and reaches its peak value at decreasing values of the visual extinction with increasing t_{evol} . For $\log A_{V,2D} < 0.5$, we parameterize the relationship with an exponential function.

(vii) The dominant formation and destruction reactions of OH are density-dependent. In diffuse gas, OH is formed mostly through electron recombination with H_2O^+ . In dense gas, electron recombination with H_3O^+ dominates OH production. In the middle

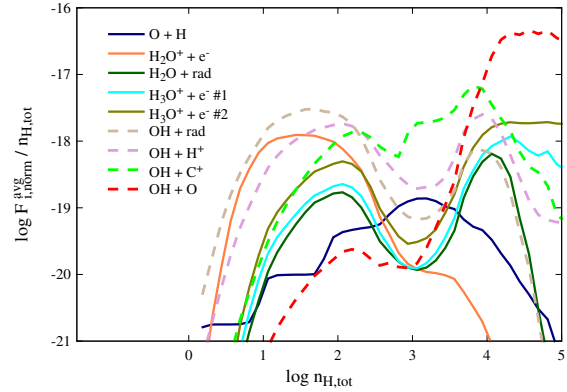


Figure 15. The density-normalized average reaction rate of some dominant formation (solid lines) and destruction reactions (dashed) of OH, vs. $n_{\text{H,tot}}$, for cloud MC1-HD at $t_{\text{evol}} = 4$ Myr. Electron recombinations dominate OH production in diffuse or dense gas, but production is suppressed at intermediate densities, while the destruction reaction $\text{OH} + \text{C}^+$ remains strong in this regime.

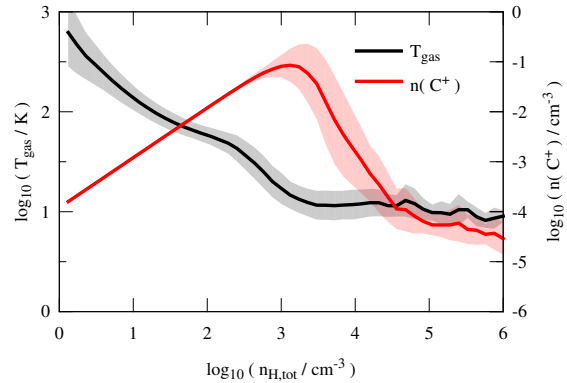


Figure 16. The average gas temperature T_{gas} and the number density of C^+ , both plotted against $n_{\text{H,tot}}$, from a snapshot of post-processed tracer particles of cloud MC1-HD at $t_{\text{evol}} = 4$ Myr. The shaded areas represent one standard deviation from the respective average. The reaction rate for $\text{OH} + \text{C}^+$ is proportional to the C^+ number density and inversely proportional to T_{gas} , and is therefore maximized around $n_{\text{H,tot}} \approx 10^3 \text{ cm}^{-3}$, where the OH/ H_2 ratio is minimized.

($n_{\text{H,tot}} \approx 10^3 \text{ cm}^{-3}$), both productive modes are suppressed but the destruction reaction $\text{OH} + \text{C}^+$ remains strong because this is the density regime of peak C^+ abundance. This explains the global minimum in the OH/ H_2 ratio seen around $n_{\text{H,tot}} \approx 10^3 \text{ cm}^{-3}$.

(viii) Evolving the tracer chemical histories to equilibrium overestimates the H_2 and CO masses with respect to the time-dependent results. The OH abundance at equilibrium is up to a factor of 3 larger than at $t_{\text{evol}} = 2$ Myr, and the total cloud $M(\text{OH})$ at equilibrium overestimates the value at $t_{\text{evol}} = 4$ Myr by 50–60%. Examining other measures like $N(\text{OH})$ or $N(\text{OH})/N(\text{H}_2)$ vs. $A_{V,2D}$, the functional forms are consistent between the equilibrium and non-equilibrium results, but with greater $N(\text{OH})$ everywhere at equilibrium, accounting for the mass overestimate.

Future work that examines the utility of OH as a dark gas tracer hinges upon direct comparison to observations. We intend to apply radiative transfer calculations which will generate self-consistent, time-dependent synthetic emission maps. These maps, in conjunction with the H₂ column density values reconstructed from our 3D density grids, can be used to establish an X_{OH} factor, analogous to the X_{CO} factor, which might help to assess the molecular hydrogen content at $A_{\text{V},2\text{D}} \lesssim 3$. Additionally, we look forward to investigating other chemical tracers and problems in astrochemistry using our post-processing methodology.

ACKNOWLEDGEMENTS

MP, DS, and SW would like to acknowledge funding support from the Deutsche Forschungsgemeinschaft (DFG) via the Sonderforschungsbereich (SFB) 956, *Conditions and Impact of Star Formation* (projects C5 and C6). The SILCC-Zoom simulations were performed on SuperMUC at the Leibniz Computing Centre, and the post-processing and additional analysis were performed on ODIN at the Regionales Rechenzentrum der Universität zu Köln (RRZK). The FLASH code was developed partly by the DOE-supported Alliances Center for Astrophysical Thermonuclear Flashes (ASC) at the University of Chicago.

DATA AVAILABILITY

The data underlying this paper can be shared for scientific purposes after request to the authors.

REFERENCES

- Allen R. J., Ivette Rodríguez M., Black J. H., Booth R. S., 2012, *AJ*, **143**, 97
- Allen R. J., Hogg D. E., Engelke P. D., 2015, *AJ*, **149**, 123
- André P., Di Francesco J., Ward-Thompson D., Inutsuka S. I., Pudritz R. E., Pineda J. E., 2014, in Beuther H., Klessen R. S., Dullemond C. P., Henning T., eds, *Protostars and Planets VI*. pp 27–51 ([arXiv:1312.6232](#)), doi:10.2458/azu_uapress_9780816531240-ch002
- Beck R., Wielebinski R., 2013, in Oswalt T. D., Gilmore G., eds, *Planets, Stars and Stellar Systems: Volume 5: Galactic Structure and Stellar Populations*. Springer Netherlands, Dordrecht, pp 641–723, doi:10.1007/978-94-007-5612-0_13
- Bergin E. A., Hartmann L. W., Raymond J. C., Ballesteros-Paredes J., 2004, *ApJ*, **612**, 921
- Bisbas T. G., Schruha A., van Dishoeck E. F., 2019, *MNRAS*
- Bolatto A. D., Wolfire M., Leroy A. K., 2013, *Annual Review of Astronomy and Astrophysics*, **51**, 207
- Busch M. P., Allen R. J., Engelke P. D., Hogg D. E., Neufeld D. A., Wolfire M. G., 2019, *ApJ*, **883**, 10
- Busch M. P., Engelke P. D., Allen R. J., Hogg D. E., 2021, [arXiv:2104.06538 \[astro-ph\]](#)
- Chevance M., et al., 2020, *MNRAS*, **493**, 2872
- Clark P. C., Glover S. C. O., Klessen R. S., Bonnell I. A., 2012, *MNRAS*, **424**, 2599
- Dobbs C. L., et al., 2014, in Beuther H., Klessen R. S., Dullemond C. P., Henning T., eds, *Protostars and Planets VI*. p. 3 ([arXiv:1312.3223](#)), doi:10.2458/azu_uapress_9780816531240-ch001
- Draine B. T., 1978, *ApJS*, **36**, 595
- Draine B. T., Bertoldi F., 1996, *mmras*, **468**, 269
- Dubey A., et al., 2008, *Astronomical Society of the Pacific Conference Series*, **385**, 145
- Ebagezio S., Seifried D., Walch S., Nürnberger P. C., Rathjen T. E., Naab T., 2022, [arXiv e-prints](#), p. [arXiv:2206.06393](#)
- Ferrada-Chamorro S., Lupi A., Bovino S., 2021, *MNRAS*, **505**, 3442
- Flower D. R., G. Pineau des Forêts Walmsley C. M., 2005, *A&A*, **436**, 933
- Fryxell B., et al., 2000, *ApJS*, **131**, 273
- Gaches B. A. L., Offner S. S. R., 2018, *ApJ*, **854**, 156
- Ganguly S., Walch S., Clarke S. D., Seifried D., 2022, [arXiv e-prints](#), p. [arXiv:2204.02511](#)
- Genel S., Vogelsberger M., Nelson D., Sijacki D., Springel V., Hernquist L., 2013, *MNRAS*, **435**, 1426
- Girichidis P., et al., 2016, *MNRAS*, **456**, 3432
- Girichidis P., Seifried D., Naab T., Peters T., Walch S., Wünsch R., Glover S. C. O., Klessen R. S., 2018, *MNRAS*, **480**, 3511
- Glover S. C. O., Clark P. C., 2012, *MNRAS*, **421**, 116
- Glover S. C. O., Mac Low M., 2007a, *ApJS*, **169**, 239
- Glover S. C. O., Mac Low M., 2007b, *ApJ*, **659**, 1317
- Glover S. C. O., Mac Low M.-M., 2011, *MNRAS*, **412**, 337
- Glover S. C. O., Federrath C., Mac Low M.-M., Klessen R. S., 2010, *MNRAS*, **404**, 2
- Gong M., Ostriker E. C., Kim C.-G., 2018, *ApJ*, **858**, 16
- Gong M., Ostriker E. C., Kim C.-G., Kim J.-G., 2020, *ApJ*, **903**, 142
- Górski K. M., Hivon E., 2011, *HEALPix: Hierarchical Equal Area isoLatitude Pixelization of a sphere* (ascl:1107.018)
- Grassi T., Bovino S., Schleicher D. R. G., Prieto J., Seifried D., Simoncini E., Gianturco F. A., 2014, *MNRAS*, **439**, 2386
- Grassi T., Bovino S., Haugbølle T., Schleicher D. R. G., 2017, *MNRAS*, **466**, 1259
- Grenier I. A., Casandjian J.-M., Terrier R., 2005, *Science*, **307**, 1292
- Habing H. J., 1968, *Bull. Astr. Inst. Netherlands*, **19**, 421
- Hollenbach D., Kaufman M. J., Bergin E. A., Melnick G. J., 2009, *ApJ*, **690**, 1497
- Hu C.-Y., Sternberg A., van Dishoeck E. F., 2021, *ApJ*, **920**, 44
- Jacob A. M., Menten K. M., Wiesemeyer H., Lee M.-Y., Güsten R., Durán C. A., 2019, *A&A*, **632**, A60
- Keating L. C., et al., 2020, *MNRAS*, **499**, 837
- Lada E. A., Blitz L., 1988, *ApJ*, **326**, L69
- Lee M.-Y., et al., 2012, *ApJ*, **748**, 75
- Li D., Xu D., Heiles C., Pan Z., Tang N., 2015, [arXiv:1503.02496 \[astro-ph\]](#)
- Li D., et al., 2018a, *ApJS*, **235**, 1
- Li Q., Narayanan D., Davè R., Krumholz M. R., 2018b, *ApJ*, **869**, 73
- Liszt H., Lucas R., 1996, *A&A*, **314**, 917
- Liszt H., Lucas R., 2002, *A&A*, **391**, 693
- Lucas R., Liszt H., 1996, *A&A*, **307**, 237
- Mackey J., Walch S., Seifried D., Glover S. C. O., Wunsch R., Aharonian F., 2019, *MNRAS*, **486**, 1094
- Nelson R. P., Langer W. D., 1997, *ApJ*, **482**, 796
- Nelson R. P., Langer W. D., 1999, *ApJ*, **524**, 923
- Neufeld D. A., Kaufman M. J., Goldsmith P. F., Hollenbach D. J., Plume R., 2002, *ApJ*, **580**, 278
- Nguyen H., et al., 2018, *ApJ*, **862**, 49
- Panessa M., Seifried D., Walch S., Gaches B., Barnes A., Bigiel F., Neumann L., 2022, in prep.
- Planck and Fermi Collaborations et al., 2015, *A&A*, **582**, A31
- Rugel M. R., et al., 2018, *A&A*, **618**, A159
- Rybarczyk D. R., et al., 2021, [arXiv:2112.05767 \[astro-ph\]](#)
- Seifried D., Walch S., 2016, *MNRAS*, **459**, L11
- Seifried D., et al., 2017, *MNRAS*, **472**, 4797
- Seifried D., Haid S., Walch S., Borchert E. M. A., Bisbas T. G., 2020, *MNRAS*, **492**, 1465
- Seifried D., Beuther H., Walch S., Syed J., Soler J. D., Girichidis P., Wünsch R., 2021, [arXiv:2109.10917 \[astro-ph\]](#)
- Sembach K. R., Howk J. C., Ryans R. S. I., Keenan F. P., 2000, *ApJ*, **528**, 310
- Smith R. J., Glover S. C. O., Clark P. C., Klessen R. S., Springel V., 2014, *MNRAS*, **441**, 1628
- Valdivia V., Hennebelle P., Gérin M., Lesaffre P., 2016, *A&A*, **587**, A76
- Walch S., et al., 2015, *MNRAS*, **454**, 238
- Wannier P. G., Andersson B. G., Federman S. R., Lewis B. M., Viala Y. P., Shaya E., 1993, *ApJ*, **407**, 163
- Weinreb S., Barrett A. H., Meeks M. L., Henry J. C., 1963, *Nature*, **200**, 829
- Wolfire M. G., Hollenbach D., McKee C. F., 2010, *ApJ*, **716**, 1191

Wünsch R., Walch S., Dinnbier F., Whitworth A., 2018, *MNRAS*, 475, 3393
 Xu D., Li D., 2016, *ApJ*, 833, 10
 Xu D., Li D., Yue N., Goldsmith P. F., 2016, *ApJ*, 819, 22
 van Dishoeck E. F., Black J. H., 1988, *ApJ*, 334, 771

APPENDIX A: FILAMENT DETAIL: $A_{V,2D}$, $N(H_2)$, AND $N(CO)$

In Fig. 5, we have shown $N(OH)$, $N(OH)/N(H_2)$, and $N(OH)/N(CO)$, with contour lines to indicate $A_{V,2D} = 1$ and $A_{V,2D} = 3$. We supplement that figure with Fig. A1, in which the same filament detail from MC1-MHD at $t_{evol} = 4$ Myr is shown, this time giving maps of $A_{V,2D}$, $N(H_2)$, and $N(CO)$.

We calculate the visual extinction $A_{V,2D}$ (left panel) from $N(H_{tot})$ using Eq. 3. The middle panel displays $N(H_2)$. Because $A_{V,2D}$ is a function of $N(H_{tot})$, and in the densest regions of a molecular cloud $N(H_{tot})$ is approximately twice $N(H_2)$, the maps of $A_{V,2D}$ and $N(H_2)$ closely correspond at the filament. On the edge of the map, where $A_{V,2D} < 1$, atomic hydrogen is dominant, and $N(H_2)$ declines relative to $A_{V,2D}$ as expected.

In the right panel, we provide $N(CO)$. Compared to H_2 , the CO content is much more concentrated in the filament. In the densest regions where $A_{V,2D} > 3$, the ratio of CO to H_2 abundance is close to the elemental carbon to hydrogen ratio of $\sim 10^{-4}$, with a peak column density of $N(CO) \approx 10^{19} \text{ cm}^{-2}$. Surrounding the filament, in the region where $A_{V,2D} \approx 1-3$, $N(CO)$ is between $10^{14}-10^{15} \text{ cm}^{-2}$. This CO-dark region (Seifried et al. 2020) contains a significant amount of molecular hydrogen in the second panel, underscoring the necessity for an alternative molecular tracer like OH in order to properly model the outer extent of the H_2 envelope. In regions exterior to this, where $A_{V,2D} < 1$, $N(CO)$ falls below $N(CO) < 10^{14} \text{ cm}^{-2}$. We have masked off values of $N(CO)$ below this limit in order to emphasize the differences between the three density regimes delineated by the extinction isolines.

APPENDIX B: COMPARISON OF CUMULATIVE OH MASS AND TOTAL MASS

The cumulative mass of OH vs. the (column) density of the four simulated clouds was shown in Fig. 7, along with the cumulative H_2 mass for comparison. In Fig. B1 we provide once more the cumulative OH mass vs. various measures of column and volume density, now alongside the cumulative bulk mass of the four clouds at each timestep. The bulk gas distribution at equilibrium is identical to the distribution at the final time-dependent timestep ($t_{evol} = 3.76$ Myr for MC2-HD, and 4 Myr for the others), and is not shown. The HD clouds, being clumpier in distribution than the MHD clouds, have more purely atomic gas with no OH. By contrast, the puffier density profile of the MHD clouds provides enough shielding for a significant OH reservoir to form at lower gas densities. Especially at early times the MHD clouds reach the third quartile in both the bulk gas and the OH at a lower density than the HD clouds.

For all three clouds, the time-dependence of the cumulative bulk mass is minimal in comparison to that of the cumulative OH and H_2 mass curves (see Fig. 7 for the latter). The cumulative OH curve for MC1-MHD changes to a much greater extent in the CO-dark gas regime over time, indicating that the shift in the OH distribution is not due to large-scale dynamical changes in the (column) density distribution but due to an ongoing chemical process.

APPENDIX C: PROBABILITY DENSITY FUNCTION OF $N(H_{TOT})$

In Fig. C1, we present a plot of the probability density function (PDF) of $N(H_{tot})$, to supplement the PDF of $N(OH)$ in Fig. 8. The PDF of $N(H_{tot})$ includes results from all three integration sightlines at $t_{evol} = 2, 3$, and 4 Myr. The cyan line corresponds to $\log N \propto -2$. The distribution peaks around 10^{21} cm^{-2} for all four clouds, similar to Bisbas et al. (2019).

This paper has been typeset from a \LaTeX file prepared by the author.

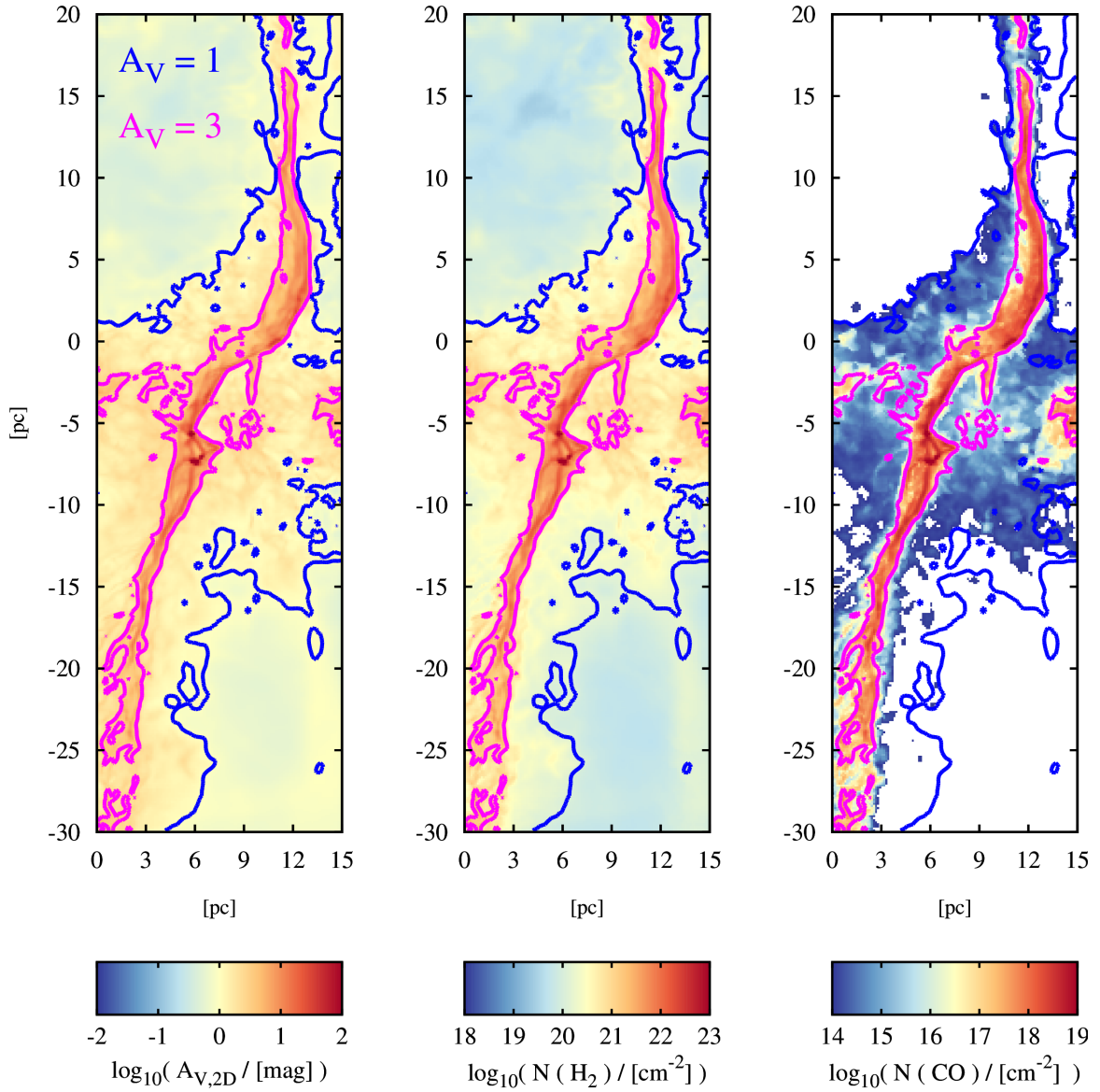


Figure A1. Zoom-in onto the highlighted box from Fig. 4, in the y-z projection of MC1-MHD at $t_{\text{evol}} = 4$ Myr. Contours for $A_{V,2D} = 1$ (blue) and $A_{V,2D} = 3$ (pink) mark the approximate boundaries of the CO-dark gas. First panel: the projected visual extinction $A_{V,2D}$. Second panel: $N(\text{H}_2)$, indicating a high molecular column density between $A_{V,2D} = 1$ and 3. Third panel: $N(\text{CO})$, which peaks in the body of the filament but rapidly declines when $A_{V,2D} < 3$. The H_2 outside this visual extinction boundary is the CO-dark molecular gas.

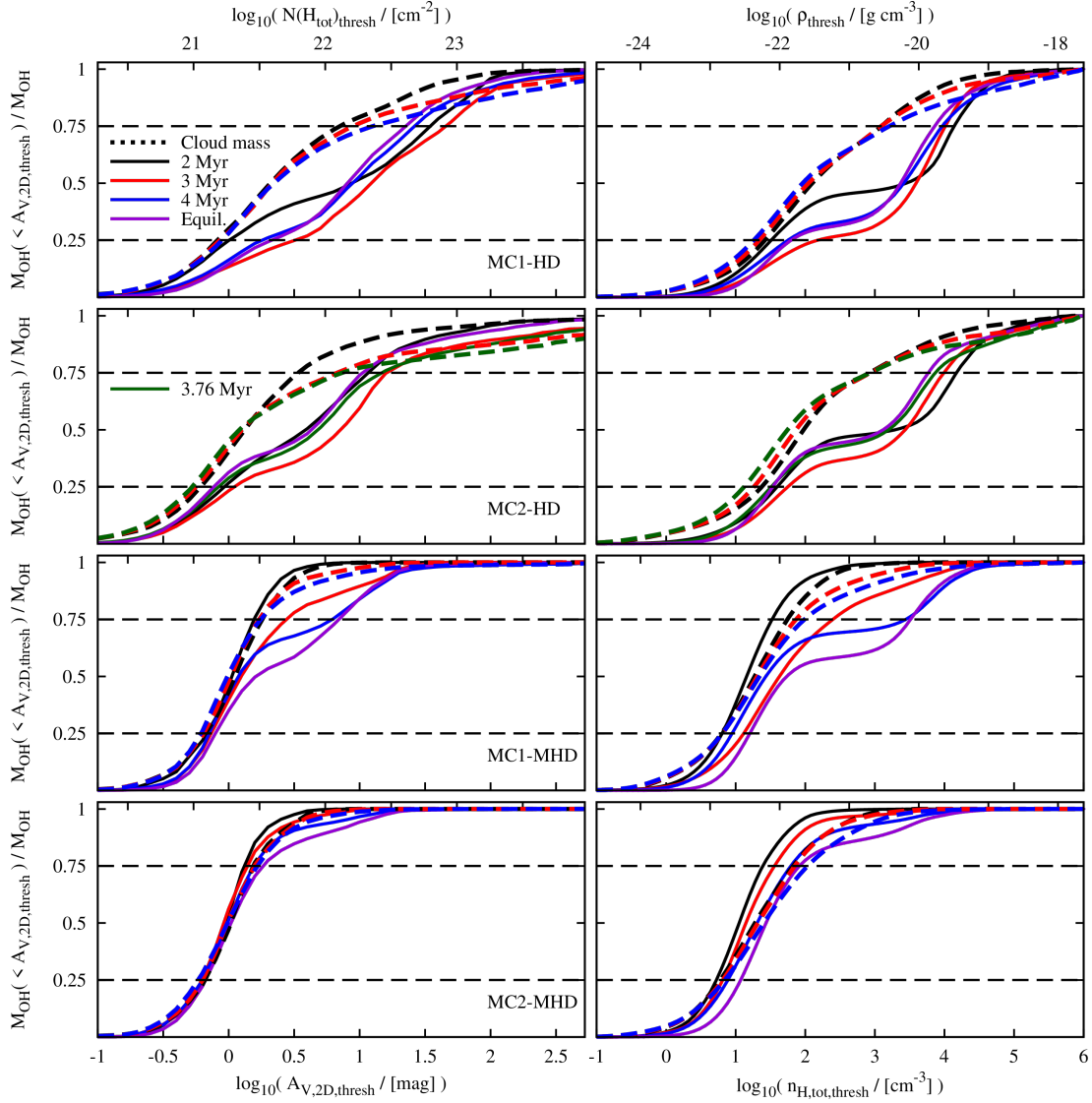


Figure B1. Same as Fig. 7, but comparing the cumulative OH mass below density thresholds (solid lines) to the cumulative total mass of each cloud below density thresholds (dashed lines), at each time snapshot. The bulk gas distribution at equilibrium is identical to the distribution at the final snapshot, and is not shown. The HD clouds are compact with significant atomic gas envelopes, so a greater fraction of the bulk gas mass is found at or below CO-dark visual extinctions compared to the OH fraction. The MHD clouds are much fluffier, with more extensive molecular envelopes, so the OH tracks the bulk gas distribution. As time passes in MC1-MHD, more OH forms at high $A_{V,2D}$, increasing the cumulative OH interquartile range, while the bulk gas distribution is unchanged.

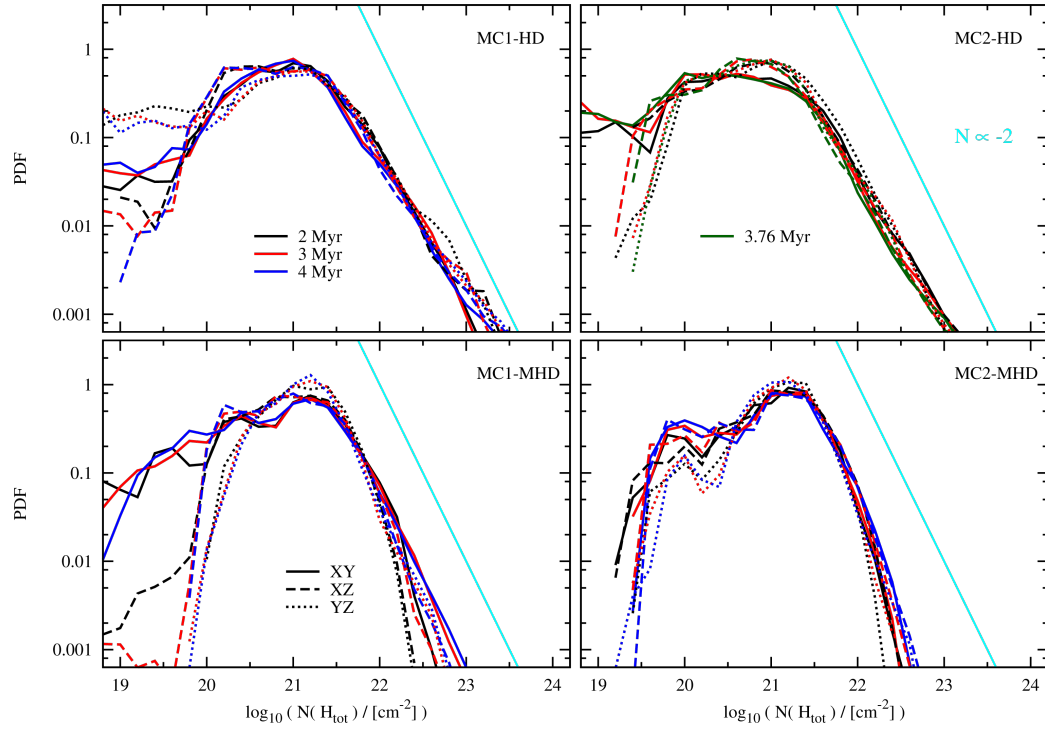


Figure C1. Same as Fig. 8, for $N(\text{H}_{\text{tot}})$.

INVESTIGATING DEUTERIUM FRACTIONATION

The preceding papers have explained and validated my post-processing and regrid-ding algorithms when applied to dense (Paper I) and diffuse (Paper II) molecular gas. In particular, the papers have shown that post-processing the tracer histories reveals the distribution and evolution of chemical species as a function of time. Paper I examined the growth timescale of HCO^+ , while Paper II compared the time-dependent abundances of H_2 , CO , and OH in different snapshots to the results after evolution of the chemical system to equilibrium. This chapter continues the theme of exploring time-dependent results, this time arguing that my algorithms will be particularly informative when applied to the question of measuring molecular cloud age as a function of deuterium fractionation. I will introduce the chemical argument, then briefly discuss steps that I have taken in this research direction.

7.1

DEUTERATION AS A CHEMICAL CLOCK

Chapter 2 of this thesis introduced the ongoing debate into whether molecular clouds are supported by supersonic internal turbulence (Zuckerman and Evans, 1974; Mac Low and Klessen, 2004), or are instead unsupported and form dense structures as a byproduct of global hierarchical collapse (Heitsch and Hartmann, 2008; Camacho et al., 2016; Vázquez-Semadeni et al., 2019). I briefly explored the notion of measuring the ages of molecular clouds to provide evidence in this debate. If surveys of molecular clouds determine they are all relatively youthful ($t \lesssim 10$ Myr), this would strongly imply that they are undergoing global collapse, since otherwise older clouds should be seen as well, if the physical constraints are properly understood. However, if these surveys identify clouds which are definitively older than ~ 10 Myr, this would rule out the pure global collapse models, even if it would not constitute proof that the gravo-turbulent theory fully explains why they are supported for so long.

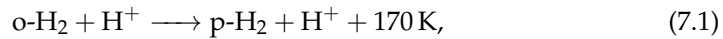
Unfortunately, measuring the age of a molecular cloud is nontrivial. To a human vantage point, molecular clouds are unchanging entities, only noticeably evolving over at least the kiloyear timescale (André et al., 2014). Therefore, we seek some verifiable and observable signature that could place at least either an upper or lower limit on cloud age: a so-called ‘chemical clock.’

It is not obvious where to look for such a signature. The molecular hydrogen in dense clouds does not emit, so the chemical signature would need to come from other species. Most reactions in molecular clouds are reversible, obscuring their time dependence. However, one class of reaction is strongly inhibited in the dense and cold environment of a molecular cloud: endothermic back-reactions. That is, if a reaction releases energy, it will be very difficult to find the energy in the cold molecular cloud to facilitate its reversal (Pagani et al., 2011; André et al., 2014). Correlating the product of such a reaction with cloud age (for instance, via simulations) would suffice for a chemical clock, but there is little *a priori* reason why the reactants

of these one-way routes would have predictable densities prior to the establishment of the cold cloud conditions which forbid their asymmetric back-reactions.

The spin-state transition of molecular hydrogen luckily fulfills this last critical requirement. H_2 forms on dust grains (Gould and Salpeter, 1963; Hollenbach and Salpeter, 1971) over a relatively short timescale in comparison to the age of a molecular cloud, and is inhibited from reaching a high abundance until the cloud density has increased enough to provide shielding against the ISRF. This results in most molecular hydrogen in a cloud being ‘born’ at the same time as the cloud that it constitutes. Furthermore, molecular hydrogen forms in one of two states due to its spin of $1/2$: the ortho- H_2 state which corresponds to odd rotational levels ($J = 1, 3, 5, \dots$) and the para- H_2 which corresponds to even rotational levels, including $J = 0$. The $J = 1$ ortho- H_2 state is energetically 170 K above the ground state (Pagani et al., 2011; Ceccarelli et al., 2014). The magnetic spin quantum number breaks the triple degeneracy of the $J = 1$ states, and so it is widely believed (though not entirely beyond doubt) that the H_2 in molecular clouds forms in ortho- and para- states at the ratio of their statistical weights, setting an initial ortho-to-para ratio (OPR) of 3:1.

Over time, the ortho- H_2 abundance (and thus the OPR) falls in molecular clouds. In the gas phase, ortho- H_2 can undergo the reaction:

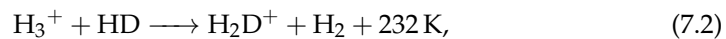


which is reversible in even slightly warmer conditions, but in the cold environment of the molecular cloud, is strongly disfavored. As a result, the OPR which begins at 3:1 declines over time to $\sim 10^{-3}$ or 10^{-4} (Pagani et al., 2011). This fulfills our desire for a species whose abundance is fixed and predictable at the birth of a molecular cloud, and changes in only one direction. Determining how the OPR falls in time should reveal the ages of molecular clouds based on their present OPR.

The issue with measuring the OPR is the impossibility of observing molecular hydrogen. Therefore, another mechanism is required which depends upon the ortho- or para- H_2 abundance, and results in something spectrally observable. Luckily again, such a mechanism exists. The presence of ortho- H_2 acts as a bottleneck for the ‘deuteration’ of molecular cloud species.

Deuteration is the hydrogen isotope that contains one proton and one neutron. The cosmic gaseous deuterium supply was set during primordial nucleosynthesis to a fractional abundance (relative to ^1H) of $\sim 1.6 \times 10^{-5}$ (Ceccarelli et al., 2014). However, many well-observed species – for instance HCO^+ and N_2H^+ – have deuterated isotopologues (like DCO^+ and N_2D^+) whose abundance in molecular clouds relative to the non-deuterated forms greatly exceeds this primordial number (Körtgen et al., 2017). Additional deuterium is produced in proton-proton chains in stellar cores, but this is consumed by fusion events. The last remaining explanation logically is that the deuterating reactions are one-way, like the ortho-to-para conversion.

This is not a coincidence; deuteration in molecular clouds is regulated by the OPR. The principal reaction series forming deuterated molecules like DCO^+ and so forth begins with the following reaction of the cosmic ray tracer H_3^+ with the HD reservoir (Pagani et al., 2011; Körtgen et al., 2017):



where the energy output assumes all species are in the ground state. The molecule H_2D^+ (as well as its own isotopologues HD_2^+ and D_3^+) facilitates deuterating reac-

tions which form DCO^+ and so on in the gas phase. Electron recombination with these isotopologues of H_3^+ also produces free neutral deuterium, which deposits on grains and leads to the formation of numerous deuterated species there as well, for instance deuterated water (HDO) and formaldehyde (HDCO) (Ceccarelli et al., 2014).

The reservoir of H_2D^+ , which is critical for deuteration of other molecules in the cloud, can be depleted two ways. The first is via reactions with gaseous CO (Bovino et al., 2019). In shielded gas, the reaction $\text{H}_3^+ + \text{CO} \longrightarrow \text{HCO}^+ + \text{H}_2$ is significantly preferred over reactions of H_3^+ with HD, keeping the H_2D^+ abundance low. In very dense gas, where $\gtrsim 90\%$ of the CO is depleted onto dust grains (Caselli et al., 2002), the remaining CO is insufficient to occupy all the H_3^+ , and a reservoir of H_2D^+ can form.

The other depleting factor for the H_2D^+ reservoir, which is much more important to this discussion, is the presence of ortho- H_2 (Pagani et al., 2011). As noted above, the $J = 1$ ortho- H_2 has an energy of 170 K, which is not far below the endothermic activation barrier of the back-reaction which returns H_2D^+ to H_3^+ and HD. The presence of ortho- H_2 destroys H_2D^+ and prevents deuteration. But as the cloud ages, the OPR falls as discussed, the H_2D^+ reservoir accumulates, and deuterated species like DCO^+ grow in abundance.

Measuring the age of a molecular cloud, therefore, requires relating the deuterium fractionation of species like HCO^+ and N_2H^+ (which can be observed) to the OPR (which cannot). We must also answer the question of how the OPR falls as a function of time, both with the assumed initial OPR of 3:1 and with other values to understand the functional relationship. Once we understand both of these questions, a cloud's observed deuterium fractionation can be systematically linked to its age, perhaps answering once and for all whether clouds are turbulently supported or undergoing global collapse.

7.2

ROLE OF POST-PROCESSING

The chemical post-processing and regridding algorithms that I have presented in this thesis provide the ability to simulate and test the assertions and hypotheses about cloud age, deuterium fractionation, and the OPR made in the previous section. Modeling deuterium fractionation is a decidedly nontrivial chemical problem, and networks which handle it self-consistently are vastly too complicated to run on-the-fly in modern 3D-MHD simulations with current hardware limits.

As deuterium fractionation and cloud age are inherently time-dependent problems, post-processing a system to equilibrium is quite pointless here. Therefore, to model deuterium fractionation and especially the evolution of the OPR, a time-dependent simulation technique is required. I submit that my post-processing algorithm using tracer particles is the correct approach. The SILCC-Zoom simulations are well-validated and well-studied. Because my post-processing method is applied to individual tracer particles, the computational load can be subdivided as necessary. Ferrada-Chamorro et al. (2021) show that post-processing even a percent-level subset of tracers recovers the average values of parameters and densities over the entire distribution. I confirm this to the 10% level for my post-processing method as well in Appendix B of this thesis.

Unlike in real observations, the molecular hydrogen in a simulation can be measured directly. A post-processing network which split hydrogen into its ortho- and

Table 7.1: The number of species and reactions in the four networks developed with Olli Sipilä toward deuterated post-processing. The networks contained a maximum of either 4- or 5-atom molecules, and did or did not include deuterium and spin isomer chemistry.

Network	Species	Reactions
4 atoms max, not deuterated	75	957
5 atoms max, not deuterated	83	1082
4 atoms max, deuterated	158	11910
5 atoms max, deuterated	194	12207

para- states, and evolved them self-consistently, could have its OPR tracked and related to the known simulation age. With four SILCC-Zoom simulations using the same fiducial solar neighborhood conditions, the correlation of the OPR with cloud age could be studied a little more systematically. Two of the simulations contain magnetic fields, and since magnetic support affects the density profile (Seifried et al., 2020; Ganguly et al., 2022), studies could be performed on the dependence of the rate of OPR decrease with the temperature and density. Finally, the construction of density grids and column density maps via the regridding method could provide a direct comparison between the simulated maps of deuterated species and real observations, helping to correlate the deuterium fractionation at various times with the measurable OPR.

The chemical network required for this science application would be extremely large. Three spheres of chemistry which are routinely neglected in simulated models would need to be included with sufficient rigor to capture their impact upon the relationship between the increasing deuterium fractionation and the decreasing OPR. First, grain-surface chemistry would have to be included. Models for the production of H_2 on grains would need to solve (or at worst, test a range of possibilities for) the initial OPR at the time of molecular cloud coalescence. The freezeout of CO onto dust grains must also be modeled carefully (Caselli et al., 2002), since gaseous CO depletes the H_2D^+ reservoir required for additional deuterating reactions (Bovino et al., 2019).

All reactions including more than one hydrogen or deuterium atom would need to be modeled separately for ortho- and para- states, to comprehensively track the OPR. Finally, all reactions including any hydrogen atoms would need counterparts included which cover every possible deuterated isotopologue. For instance, every single reaction with H_2 would need to be supplemented with reactions for HD and D_2 , and so forth. These last two requirements will exponentially increase the size of the chemical network compared to the relatively simple one employed in the papers in this thesis.

In the course of my doctoral work, I engaged with Olli Sipilä of the Max Planck Institute for Extraterrestrial Physics, whose expertise includes deuterated molecular cloud chemistry and the construction of chemical networks (Sipilä et al., 2015a,b, 2016, 2019). Together with Dr. Daniel Seifried, we worked to develop a chemical network that would suit all the above requirements. Several networks were constructed, with molecules up to either 4 or 5 atoms, and with and without deuterium and spin-state reactions. The count of species and reactions included in each network is reported in Table 7.1, to underscore the rapid growth in the size of such a

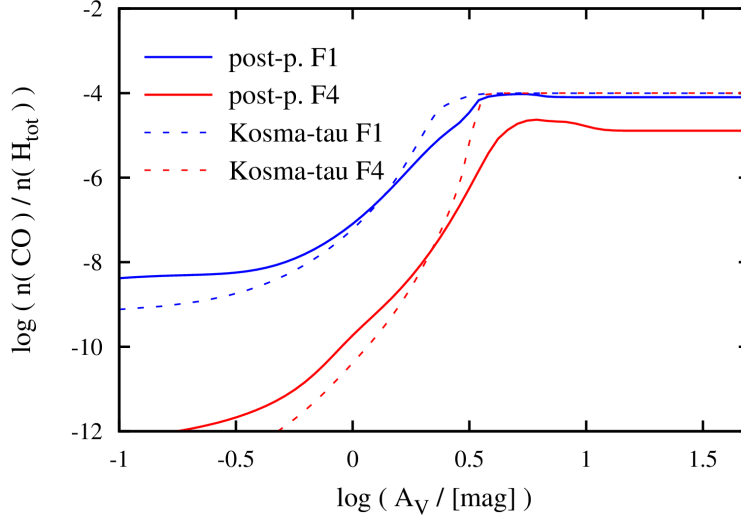


Figure 1: PDR benchmark tests of the 4-atom non-deuterated advanced network (see Table 7.1) for CO (solid lines), compared to results from the Kosma- τ PDR code, in the F1 (blue) and F4 (red) configurations described in Röllig et al. (2007).

network as more chemistry is modeled. The complete ecosystem of species in either deuterated network is too long to include here in full, in contrast to the 18 species included in NL99 (Table 3.1) or the 39 species in the post-processing network used in Paper I and Paper II (Table 3.2).

The non-deuterated networks have been validated using benchmark tests. These benchmark tests, which apply a chemical network to a photo-dissociation region (PDR) model developed in order to self-consistently compare different PDR codes (Röllig et al., 2007), report the density of certain species as a function of the visual extinction A_V . These PDR density profiles for the non-deuterated 4-atom post-processing network – developed as an essential testing item on the road to testing the deuterated networks – correlate reasonably well with the benchmark data sets provided from the Kosma- τ team.

In Fig. 1, the fractional abundance of CO vs. A_V is plotted in comparison with Kosma- τ PDR results. Two test configurations are shown: F1 ($n_{\text{H,tot}} = 10^3 \text{ cm}^{-3}$, ISRF volumetric energy density $G_0 = 17$ Habing, $T_{\text{gas}} = 50 \text{ K}$) and F4 ($n_{\text{H,tot}} = 10^{5.5} \text{ cm}^{-3}$, ISRF volumetric energy density $G_0 = 17 \times 10^5$ Habing, $T_{\text{gas}} = 50 \text{ K}$). The network under development includes detailed grain chemistry, which includes the adsorption of CO onto dust. This contributes to the lower CO abundance in the high-density F4 test as compared to Kosma- τ , which does not monitor freezeout. The same plot is offered in Fig. 2 for the cosmic ray tracer H_3^+ . Here, the high density test F4 sees more CO in Kosma- τ results than in the post-processing network. I again ascribe this to our inclusion of grain chemistry and freezeout. A strong destruction route for H_3^+ is via a reaction with CO to form HCO^+ , meaning that depletion of CO from the gas phase onto dust should increase the H_3^+ abundance, as seen in this F4 test. Finally, in Fig. 3 I plot the abundance profile for OH, to leverage the knowledge of OH gleaned from Paper II. Here, post-processed OH is diminished everywhere in the low density test F1 compared to the Kosma- τ results. I ascribe this to the strong destruction reaction $\text{OH} + \text{C}^+$, which is shown in Paper II to dominate the net OH destruction rate around $n_{\text{H,tot}} \sim 3 \text{ cm}^{-3}$, the exact density

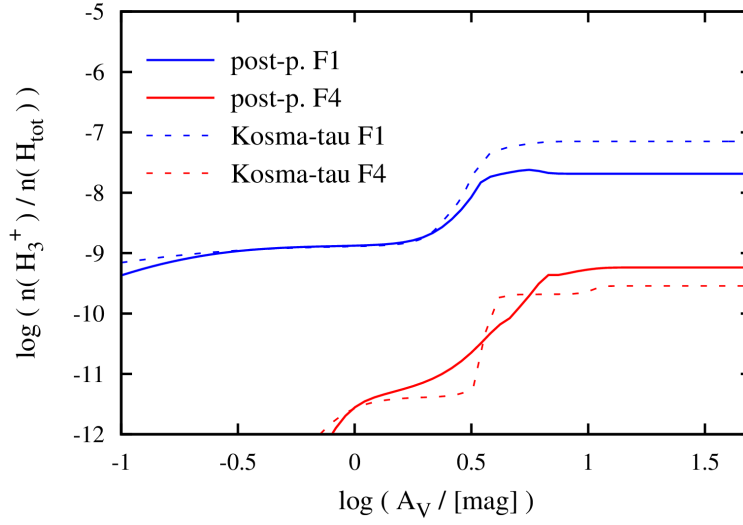


Figure 2: PDR benchmark tests of the 4-atom non-deuterated advanced network (see Table 7.1) for H_3^+ (solid lines), compared to results from the Kosma- τ PDR code, in the F1 (blue) and F4 (red) configurations described in Röllig et al. (2007).

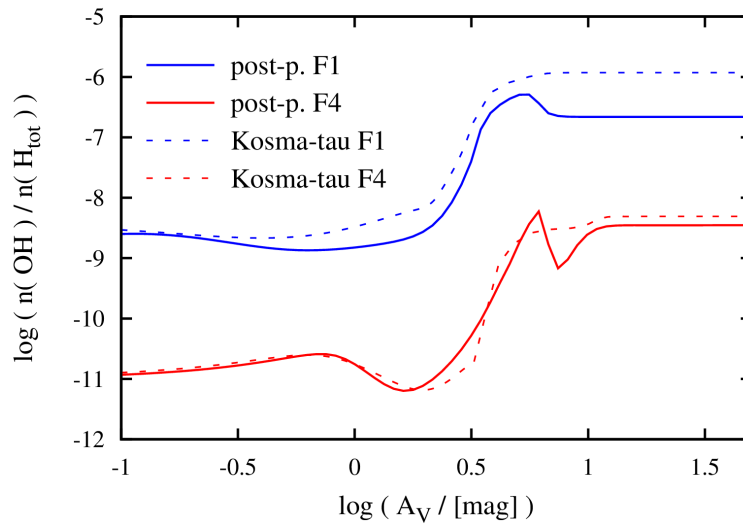


Figure 3: PDR benchmark tests of the 4-atom non-deuterated advanced network (see Table 7.1) for OH (solid lines), compared to results from the Kosma- τ PDR code, in the F1 (blue) and F4 (red) configurations described in Röllig et al. (2007).

setting for the F1 test.

Once my doctoral work is concluded, I intend to continue refining my post-processing and regridding algorithms, so they can be efficiently applied to the abundances of tracer particles whose histories have been post-processed with these deuterated networks. The tools presented in this thesis have a unique capability to simulate the time-dependent deuterium fractionation of a molecular cloud, which is still far beyond the present-day limits of traditional coupled simulations.

CONCLUSIONS AND OUTLOOK

This doctoral thesis has explored the varied and intricate frontiers of chemical modeling in astrophysical simulations. By contributing my chemical post-processing pipeline to the field, I aim to bridge the gap between the current limits on computational expense in simulations and the desire for well-resolved, 3D-MHD numerical simulations which are coupled to a realistic and comprehensive chemical network. In this concluding chapter, I will review the contents of the thesis, and briefly explain the outlook for future work.

INTRODUCTORY CHAPTERS

I began this thesis by introducing the physics of the interstellar medium, including its components, heating and cooling processes, and multiphase properties, in particular focusing on the dynamical and chemical development of molecular clouds. Next, I introduced the principles of ideal MHD underlying numerical codes like FLASH, which was used for the SILCC-Zoom simulations. Because these simulations were run coupled to a limited chemical network, I then proceeded to explore how chemical post-processing could unlock new information about the simulations' chemistry, especially in comparison to observed molecular clouds. I introduced the microphysics package KROME, which can post-process chemical inputs (in this case from the on-the-fly SILCC-Zoom network) with regard to a more robust network.

PAPER I

This paper introduced the two parts of my novel chemical post-processing scheme: first, processing the chemical histories of the tracer particles inside SILCC-Zoom 3D-MHD simulations using the KROME package and a more robust chemical network, and second, reconstructing volume-filling density distributions of any desired (post-processed) chemical species by 'regridding' the tracer particles and interpolating to fill empty cells in the domain. I began by describing the steps of the tracer chemical processing, including the use of subcycling to properly capture rapid changes in the tracers' dynamical states. The procedure was validated by comparing the on-the-fly abundances of certain species to their post-processed ones.

The dense molecular gas tracer HCO^+ was introduced. By plotting the full histories of the subset of post-processed tracers which eventually achieved high fractional abundance in HCO^+ , I determined that most HCO^+ is produced in the intermediate-density molecular gas, where $n \simeq 10^{3.5}-10^{4.5}$. A minimal amount of HCO^+ produced at greater densities in the cloud is redistributed via turbulent mixing. Next, I defined a timescale for HCO^+ formation for each tracer and correlated it with the logarithmic average of the densities of various formation reactants. I found that high densities of reactants which are primarily found in denser gas were

better correlated with a quick formation timescale than are reactants found in diffuse gas. A high density of C^+ was anti-correlated with HCO^+ formation, since the corresponding free electrons destroy HCO^+ . Following this analysis, I calculated the instantaneous reaction rates as a function of visual extinction for all 11 HCO^+ formation reactions in the post-processing network. I found that different formation routes are preferred depending on the extinction regime, with the reaction $H_3^+ + CO$ contributing 90% of the HCO^+ formation flux at high extinctions.

The next section of the paper introduced the regridding algorithm. I explained the setup and execution of the algorithm, then validated it by comparing reconstructed grids of some principal hydrogen and carbon species to their initial results from the SILCC-Zoom simulations. After this, I introduced the first-ever self-consistent, time-dependent column density maps of HCO^+ based on a physically realistic 3D-MHD molecular cloud simulation. Using these maps, I plotted the cumulative distribution of HCO^+ in different clouds at different times, finding that the bulk of the HCO^+ content of the HD clouds was found within a higher extinction regime than it is in MHD clouds, which have a shallower density gradient due to the presence of magnetic support.

I compared the column density $N(HCO^+)$ to the column densities of H_{tot} , H_2 , and CO , finding that $N(HCO^+)$ peaks around $\sim 10^{15} \text{ cm}^{-2}$. These column density measurements, especially in denser gas, compare very favorably with observations from the star-forming region W49A (Barnes et al., 2020, see also Kauffmann et al. 2017). Lastly, I studied the outcome of convolving a Gaussian kernel with the $N(HCO^+)$ maps, whose spatial resolution is 0.125 pc, to emulate coarser resolutions. This also accords with observations and provides a way to compare my chemical models (which require a high resolution to converge properly) with observations at any resolution.

PAPER II

This paper continues exploring the scientific possibilities of the post-processing and regridding algorithms introduced in Paper I, this time applying the tools to the diffuse molecular gas to investigate the CO-dark gas tracer candidate OH. Because the methods were mostly validated in Paper I using the dense gas tracer HCO^+ , I began by validating the algorithms at lower densities. The abundance of H_2 after regridding was comparable to the original SILCC-Zoom values, down to densities of $n \sim 1 \text{ cm}^{-3}$. The regridded H_2 abundance lags the original abundance at low densities, though the effect is lessened in the MHD simulations, due to their fluffier density profile compared to the HD simulations.

After confirming the algorithms work at low density, I applied them to four SILCC-Zoom molecular clouds and determined their constituent mass in H_2 , CO , and OH , both as a function of time and after evolving the chemistry to equilibrium to compare with other, less accurate models. I also explored the relationship between the OH abundance and the visual extinction, again comparing to equilibrium results. Evolving the chemistry to equilibrium was found to consistently overestimate the molecular hydrogen and OH content at high densities, underscoring the necessity of treating the chemistry in a time-dependent fashion.

The first-ever self-consistent simulated column density maps of OH were then introduced, followed by close examination of an MHD filament, in particular the OH and H_2 abundances in the CO-dark gas density regime. I analyzed the distribution of the clouds' OH content, both in the form of cumulative OH density vs.

cloud bulk density (using various 2D and 3D density measures) and in probability density functions (PDFs) of the four clouds' values for $N(\text{OH})$ at different times and along different sightlines, finding a global maximum around $\sim 10^{13} \text{ cm}^{-2}$ and a second smaller peak around $\sim 10^{15} \text{ cm}^{-2}$ whose probability density maximum increased by an order of magnitude as the clouds evolved in time.

In the following section, I quantified the dark gas fraction based on the H_2 and CO column densities as a function of extinction, and compared it to $N(\text{OH})$. Next, I determined that $N(\text{OH})$ plateaus in the CO-dark regime of $N(\text{H}_2)$, rejecting $N(\text{OH})$ alone as a molecular gas density tracer. However, I proceeded to find a definitive functional relationship between the ratio $N(\text{OH})/N(\text{H}_2)$ and the visual extinction, which I parameterized using a fit function in the domain where $\log A_{V,2D} < 0.5$. The paper concluded with a calculation of the relative strength of the many creation and destruction reactions for OH, as a function of visual extinction. A dip in OH fractional abundance around $A_{V,2D} \sim 3$ observed in my post-processed data was ascribed to a decline in the reaction rates of the chief OH formation routes.

DEUTERATION AS A CHEMICAL CLOCK

Following the presentation of my papers, I explored an additional science target for which my post-processing methods are well-suited: the questions surrounding molecular cloud age, the ortho-to-para ratio for H_2 , and deuterium fractionation. I systematically related these issues to each other, and advanced the argument that my chemical post-processing algorithm was positioned to study this highly time-dependent problem. I explained the chemical systems at hand, in particular the need for a thorough treatment of grain surface reactions, the splitting of all reactions involving more than one hydrogen atom into ortho- and para- configurations, the careful calibration of the irreversible (in cloud environments) exothermic reaction turning ortho- H_2 into para- H_2 , and the exponential growth of a network of reactions to handle all of these chemical species as well as their full complement of deuterated isotopologues. Early attempts to construct such a network were discussed.

FUTURE OUTLOOK

The chemical post-processing methods described in this thesis have strong potential to answer outstanding and unresolved questions in astrochemistry. In particular, the application of the methodology to questions of deuterium fractionation in molecular clouds could provide key evidence to one side or the other in the ongoing debate about whether molecular clouds are supported by gravo-turbulent instability or are instead undergoing global hierarchical collapse (Kong et al., 2016; Bovino et al., 2021). Calculating radiative transfer in the post-processed grids, using a tool like RADMC-3D (Dullemond et al., 2012), would give the ability to produce synthetic emission maps for the post-processed species – an unprecedented opportunity to compare real observations of molecules in the ISM to the output of a self-consistent 3D-MHD simulation.

Optimistically, the methods described in this thesis will not be necessary forever. The complexity of modern astrophysical questions has outstripped the capability of our computers to answer them efficiently enough for our liking. However, as time passes, we can remain hopeful that this bottleneck will eventually be cleared. Our modern 3D-MHD simulations were infeasible at their present scale as recently as ten to twenty years ago. As we wait for the strength of our computers to catch

up with the scale of our questions, algorithms like the post-processing and regrid-ding methods explored here will remain central to advancing our understanding in this field. Eventually, 3D-MHD simulations will handle their own chemistry, and present harmonious, unified models of how matter in the universe evolves over time. Until that day comes, I offer the post-processing tools in this thesis.

A

POST-PROCESSING PIPELINE DESCRIPTION

In this appendix, I will detail the operation of the chemical post-processing pipeline step by step. This pipeline consists of two major routines, both written by me in FORTRAN:

1. *POSTP.F90*: The chemical post-processing of the tracer particles' full histories using *KROME*, and
2. *REGRID.F90*: The regridding of the post-processed tracer particles into volume-filling, 3D number density distributions.

Additionally, after describing these two major routines in detail, I will briefly report on a few minor routines that I wrote which are also essential to the post-processing pipeline. These minor routines are mostly concerned with repackaging the existing data so that it can be read or analyzed further, and are included for the sake of completeness.

A.1

POSTP.F90

A routine to post-process the chemical history of tracer particles with respect to a different chemical network, via the microphysics package *KROME* ([Grassi et al., 2014](#)).

Fundamentally, *POSTP.F90* is structured to read the initial (i.e., direct from the simulation) chemical history of a single tracer particle step by step, and solve for the time-dependent abundances of every species in an alternative chemical network provided by the user. This is done on a per-particle basis. Using the OpenMP library to parallelize the operation of the code, the following steps are applied once to each and every tracer particle under consideration.

Before *POSTP.F90* can be run, a build of *KROME* must be compiled by the user, with a user-defined chemical network. In this work, I have exclusively performed my post-processing using the network `react_COthin_DUSTcool_new_freeze_extra`, which contains 37 gas-phase species and 2 species frozen onto dust grains, in 301 reactions. For more detail on *Krome*, see Section 3.4.2, and for more detail on the chemical networks, see especially Paper I (Chapter 5), Appendix A.

After compiling *KROME* with this chemical network, the necessary files and subroutines for post-processing are automatically generated. The routine *POSTP.F90* consists of a series of subroutines that call these *KROME* routines, taking care to use the tracer particles' local dynamics at each timestep to post-process them in a time-dependent manner. These subroutines are as follows.

PROGRAM SETUP

First, certain user-defined settings are initialized, in particular the subcycling threshold percent (see later subsection 'Subroutine: subcycle' or Section 3.2.3 of Paper I) and

the size of various arrays which will be needed to store tracer information later. These arrays are allocated a size equal to the number of written-out timesteps T (separated by 3.3 kyr) in the tracer histories. Currently, *POSTP.F90* must be hard-coded with T , depending on which simulation is being post-processed. A forthcoming update to the code will eliminate this dependence on hard-coding by requiring the user to supply a short list of simulation parameters, including T . For the SILCC-Zoom simulations, which run for ~ 4 Myr, $T \sim 1200$.

The user must also supply the number of tracer particles over which to loop the following subroutines, that is, how many tracers are expected to be post-processed. The identities (equivalently, file names) of these tracers must be contained in a file ‘partlist’ supplied by the user. A forthcoming update to the code will simply count the lines in ‘partlist’ and iterate over them all, without need for this variable to be changed.

SUBROUTINE: PARAM_SETUP_READFILE

The file ‘partlist’ is read to determine which tracer particle is to be post-processed. The tracer’s history file is opened and read in its entirety. The following values recorded in the history file are saved at every timestep to the aforementioned arrays of size T , for later use:

- The elapsed time of the SILCC simulation $t_0 + t_{\text{evol}}$ [s]
- The bulk gas density ρ [g/cm^{-3}]
- The visual extinction in three dimensions $A_{V,3D}$, calculated as in Section 2.1 of Paper I or Section 2.1 of Paper II [mag]
- The H_2 self-shielding fraction, as defined in [Glover et al. \(2010\)](#) [dimensionless]
- The CO self-shielding fraction, defined analogously to the H_2 self-shielding fraction ([Lee et al., 1996](#)) [dimensionless]
- The gas temperature [K]
- The dust temperature [K]
- The tracer’s spatial position inside the SILCC volume, split into x , y , and z coordinates [cm]
- The tracer’s velocity magnitude inside the SILCC volume, split into x , y , and z components [cm/s]
- The local mass fractions m (from NL99) of H, H_2 , C, CO, and C^+ [dimensionless]

From the local mass fractions m in the final item, their respective number densities n are calculated by multiplying each mass fraction with the bulk density ρ and dividing by their atomic weight. Using CO as an example,

$$n_{\text{CO}} = \frac{m_{\text{CO}} \times \rho}{28m_{\text{p}}}, \quad (\text{A.1})$$

where m_p is the mass of the proton and the atomic weight of CO is 28. The number densities of H, H₂, C, and C⁺ are computed analogously. Next, n_{H^+} is calculated as

$$n_{H^+} = n_{H,tot} - n_H - 2n_{H_2} \quad (A.2)$$

SUBROUTINE: CHEM_INIT

This subroutine prepares an initial chemical state for the tracer particle before post-processing, with respect to the chemical species present in the post-processing network rather than the simulation's on-the-fly network. In this work, this amounts to 39 chemical species to be initialized at t_0 .

The number densities of H, H₂, H⁺, C, CO, and C⁺ are initialized equal to the tracer's NL99 values at t_0 , described in the previous subsection. The number density of helium is set using the primordial hydrogen-to-helium ratio:

$$n_{He} = 0.1 \times n_{H,tot}, \quad (A.3)$$

and the number density of atomic oxygen is set according to [Sembach et al. \(2000\)](#), but subtracting the quantity of oxygen which is locked in CO:

$$n_O = (3 \times 10^{-4}) \times n_{H,tot} - n_{CO}. \quad (A.4)$$

The number densities of all other species in the post-processing network are initialized to 10^{-20} cm^{-3} . We find that after a few timesteps of post-processing (much earlier than any analysis performed in this work), the densities of these species are insensitive to this initial condition.

SUBROUTINE: GET_FILENAME

A trivial subroutine that creates the output file for the post-processed tracer history, naming it according to user-defined conditions. In this work, for simplicity, the tracer output files are named 'part_XXXXXXX', where the seven-digit latter part is replaced by the integer which is the particle's original identifier in the simulation.

SUBROUTINE: TRUE_SETUP

Unlike the previous subroutines, 'true_setup' is run for every timestep of post-processing, and constitutes the first half of each timestep's post-processing procedure. It is followed within the same timestep by the subroutine 'subcycle'.

In 'true_setup', a single array of environmental parameters is generated using the data saved from the tracer particle in 'param_setup_readfile'. This array contains the values *at the current timestep* t_1 of the bulk density, visual extinction $A_{V,3D}$, H₂ self-shielding coefficient, CO self-shielding coefficient, gas temperature, and dust temperature. Another array is made of these same parameters, but at the following timestep t_2 . A slope is calculated for the change in each of these environmental parameters between t_1 and t_2 . That is, for a parameter p , the rate of change m is

$$m = \frac{p_2 - p_1}{t_2 - t_1} \quad (A.5)$$

Lastly in this subroutine, the reference values for the cosmic ray ionization rate (CRIR) and interstellar radiation field (ISRF) are set for use in KROME. In this work, the CRIR is constant everywhere, and the ISRF is attenuated as described

in Chapter 3. These two parameters do not strictly need to be set again at every timestep when they remain constant in this work. However, the capability for such updates has been included so that this post-processing scheme can be more easily applied to other simulations which handle the CRIR and ISRF in a different way.

SUBROUTINE: SUBCYCLE

This subroutine checks whether the environmental parameters p change by more than a certain user-defined percent s between t_1 and t_2 , as described in detail in Section 3.2.3 of Paper I, and more briefly in Section 2.2.1 of Paper II.

If none of the environmental parameters p change by more than s (either increasing or decreasing), the routine proceeds directly to post-processing. `KROME` is called, and passed values for the gas density, the gas temperature, the other environmental parameters p , and the full set at t_1 of the number densities, n_1 . The solver then advances the chemistry by $\Delta t = t_2 - t_1$, holding all p constant. Then, the calculated number densities n_2^* are all multiplied by the ratio of the bulk densities at t_1 and t_2 , to properly weight the chemical number densities with respect to the changing bulk conditions around the tracer as it moves through the gas between timesteps:

$$n_2 = n_2^* \frac{\rho_2}{\rho_1}. \quad (\text{A.6})$$

If, however, one or more of the environmental parameters p_1 change by more than the percent threshold s (chosen in this work as 10%), a subcycling protocol is initiated instead. A linear interpolation is performed for all p between t_1 and t_2 , using the slopes m calculated in ‘true_init’. The code determines which parameter is changing the most quickly (i.e., which has the largest magnitude of m) and calculates how long, in the linear interpolation, that particular parameter would take to change by exactly s . This is some time $t_{sub,1} < (t_2 - t_1)$. `KROME` is called to iterate the chemistry, but this time is supplied with the linearly-interpolated parameters p at $t_1 + t_{sub,1}$, and advances the chemistry only by $t_{sub,1}$.

After a first subcycling step has been done, the chemistry is then advanced in the same fashion (using the linearly-interpolated parameters p) in steps that progressively increase in size by factors of $(1 + s)$, until the latest t_{sub} would advance the chemistry beyond the original t_2 . When that would happen, the chemistry is then only advanced to t_2 .

Once t_2 has been reached, the routine loops around to ‘true_init’, and post-processes every timestep in the tracer’s history file until the end of the simulation. This procedure repeats for every tracer until all of them have been post-processed.

WRITE-OUT

Once the post-processing is complete, the routine writes out the data. The following information about the post-processed tracer particle is written, for every timestep, to the output file initialized in ‘get_filename’, in the following order:

- The elapsed time of the SILCC simulation $t_0 + t_{evol}$ [s]
- The number density of hydrogen nuclei $n_{H,tot}$ [cm⁻³]
- The bulk gas density ρ [g/cm⁻³]
- The visual extinction in three dimensions $A_{V,3D}$, calculated as in Section 2.1 of Paper I or Section 2.1 of Paper II [mag]

- The H₂ self-shielding fraction, as defined in [Glover et al. \(2010\)](#) [dimensionless]
- The gas temperature [K]
- The dust temperature [K]
- The CO self-shielding fraction, defined analogously to the H₂ self-shielding fraction [dimensionless]
- The number densities (from NL99) of H, H₂, H⁺, C, CO and C⁺ calculated in 'param_setup_readfile' [cm⁻³]
- The tracer's spatial position inside the SILCC volume, split into x , y , and z coordinates [cm]
- The tracer's velocity magnitude inside the SILCC volume, split into x , y , and z components [cm/s]
- The number densities (from post-processing) of every species included in the post-processing network [cm⁻³]

These histories can be analyzed individually, or the data from a particular timestep can be concatenated into a snapshot using the minor routine *SNAPWRITER.F90* (see Section A.3.2).

A.2 REGRID.F90

A routine to transform a snapshot of the chemical states of tracer particles into a volume-filling, 3D number density distribution. This is called 'regridding' the tracers, so that they can be directly comparable to grid code results and to observations.

This routine uses the tracer snapshots created by *SNAPWRITER.F90* from the post-processed tracer histories (see Section A.3.2), along with the uniform grids of $n_{\text{H,tot}}$ from the SILCC-Zoom simulations created by *UNIFORM.PY* (see Section A.3.1), to generate number density grids of the same size and shape as the uniform grid of $n_{\text{H,tot}}$, but for a specific individual chemical species saved in the post-processed tracer histories. This volume-filling 3D density distribution can then be further processed with *PROJECTOR.F90* (see Section A.3.3) to create column density projections.

SETUP

In the current version of the code, a number of user settings are available which must be hard-coded and recompiled before each run of *REGRID.F90*. A forthcoming update to the code will set defaults as appropriate, and permit the user to supply the desired settings when calling the program, without need for recompilation. The settings defined by the user include the following.

- The identity of the chemical species for which a 3D density grid is desired. Density grids for only one chemical species can be created per run, though this may change in a forthcoming update.

- The cloud from which the snapshot to be regridded originated (can be looped in one run over multiple clouds).
- The desired final resolution of the 3D number density grid, with options of 1 pc, 0.5 pc, 0.25 pc, and 0.125 pc (can be looped in one run over multiple resolutions).
- The value of t_{evol} for the snapshot being regridded, with options of $t_{\text{evol}} = 2, 3, \text{ or } 4 \text{ Myr}$; or $t_{\text{evol}} = 3.76 \text{ Myr}$ for MC2-HD, where that is the final timestep (can be looped in one run over multiple times).
- The maximum number of interpolation steps to calculate, in the ‘interpolation’ subsection of the routine.
- Whether the snapshot being regridded comes from time-dependent post-processing, or represents the chemistry at equilibrium.

A blank grid is then created, which will eventually be filled with the regridded density data. This grid corresponds to the spatial extent of the zoom-in region for the cloud being considered (set above by the user), the coordinates of which are hard-coded in the current version. The grid consists of uniform cubic cells (of the resolution set above by the user) which cover the entire zoom-in region, and overlap the right-hand edge of each coordinate axis such that there are an integer number of cells. That is, the rightmost coordinate of the blank uniform grid ‘rounds up’ to the next integer multiple of the cell size.

Supplied with values for the cloud name, t_{evol} , and the desired resolution, the code then reads in another uniform grid of $n_{\text{H,tot}}$ from the original SILCC-Zoom simulation, which exactly corresponds spatially to the blank grid that has just been initialized, including the resolution and the overlap on the right-hand edge. This uniform grid of $n_{\text{H,tot}}$ must be prepared beforehand using *UNIFORM.PY* (see Section A.3.1). The $n_{\text{H,tot}}$ grid is essential for proper density weighting of the chemical abundances produced later in this routine, in the ‘interpolation’ module.

DIRECT REGRIDDING

Next, the code reads a (user-supplied) tracer snapshot which corresponds to the defined cloud name and t_{evol} value. Each line of the snapshot corresponds to the state of one tracer particle at this timestep. The intent of this module is to place the chemical abundances of these tracers back into the blank grid created in the previous steps.

For each tracer in the snapshot, the routine first checks its spatial coordinates to determine whether it was inside the zoom-in region at this time. If a tracer was outside the zoom-in region, the code cycles to the next tracer. If a tracer was inside the zoom-in region, the code then calculates the cell in the blank uniform grid that corresponds to its coordinates. Then, the *fractional abundance* ($n/n_{\text{H,tot}}$) of the chosen chemical species is assigned to that cell. The fractional abundance is used rather than the direct number density because (in a later step) this allows us to properly density-weight the interpolated abundances on the periphery of the zoom-in region, which would otherwise be overestimated.

This process loops over all tracers in the snapshot, until every tracer has been assigned to a cell (if in the zoom-in region) or rejected (if outside). If multiple tracers are located in the same cell, their fractional abundances are logarithmically

averaged to a single value for the cell. Logarithmic averages were found during testing to better capture the density distribution than simple averages.

INTERPOLATION

The tracers were initialized in the SILCC-Zoom simulations at a density of 1 pc^{-3} , covering the zoom-in region and extending a further 10 pc outside it in the x , y , and z directions. This comprises about one to two million tracers per cloud. However, since most analysis in this work is performed in clouds of size $\sim 100 \text{ pc}$ in each dimension at a resolution of 0.125 pc , the uniformly-resolved density grids contain up to a thousand times as many cells as tracer particles. Furthermore, since the molecular gas condenses into clumps over the simulation lifetime, so too do the tracers as they follow the gas flow (Genel et al., 2013, and see also Section 2.2.3 of Paper II). Therefore, to create a volume-filling density distribution from the relatively sparse tracer particle data, we must employ an interpolation and extrapolation scheme which reliably and robustly determines the chemical information of the blank cells, i.e. cells without tracers located inside their boundaries.

This method works as follows, and is explained more thoroughly in Section 5.1 of Paper I. Each blank cell in the grid checks its 26 immediate neighboring cells. If one of those neighboring cells has a nonzero fractional abundance value from a tracer, the value is copied to the blank cell, weighted by the normalized distance between the two cells' centroids. If more than one neighboring cell has a nonzero fractional abundance value, their (distance-weighted) values are logarithmically averaged before being copied to the blank cell. Every blank cell in the grid attempts to fill itself in this fashion independently. The blank cells disregard the values in other cells that have been filled by interpolation on the current step, to eliminate reliance on the sweeping order, e.g. whether the blank cells are filled in x - y - z order rather than, say, y - z - x order.

This interpolation process repeats as many times as necessary to fill the grid, which for the $\sim 100 \text{ pc}$ SILCC-Zoom zoom-in regions at a resolution of 0.125 pc ranges between 77–250 interpolation steps. Once the entire grid is filled with fractional abundance values, the grid is then multiplied by the aforementioned uniform grid of $n_{\text{H,tot}}$ (produced beforehand by the user with *UNIFORM.PY*). This produces a volume-filled, 3D number density distribution for the considered chemical species, which is then written to a file. Notably, this regridding procedure is identical for any species in the post-processing network. A 3D number density grid can therefore be straightforwardly produced for *any* species which is present in the post-processed tracer snapshots.

A.3 MINOR ROUTINES

Numerous additional routines were also written to facilitate the operation of the two main routines. These generally repackage or reorganize the data generated by the two main routines, so that it can be properly analyzed or plotted. Among others, these smaller routines include the following.

A.3.1

UNIFORM.PY

A routine that takes as its input a single SILCC-Zoom AMR grid, and produces a uniformly-resolved 3D grid of a subvolume within the AMR grid.

This routine can produce a uniform grid for any parameter reported by the AMR grid, but in this work, was primarily used to produce uniform grids of $n_{\text{H,tot}}$ for MC1-HD, MC2-HD, MC1-MHD, and MC2-MHD, as required by the regridding procedure (see Section 5.1 of Paper I). These grids were generated for $t_{\text{evol}} = 2, 3$, and 4 Myr, except for MC2-HD, where a grid at the final timestep of $t_{\text{evol}} = 3.76$ Myr was produced instead. I also produced several uniform grids of n_{H_2} for validating the regridding technique in the diffuse molecular gas (see Section 2.2.3 and Fig. 2 of Paper II).

The boundaries of the uniformly-resolved subvolume can be set manually, but were always selected in this work to be contiguous with each cloud’s zoom-in region, which are defined using coordinates within the larger SILCC domain. Because the size of the zoom-in region in each dimension is not necessarily equal to an integer multiple of the uniform resolution, the uniform grid ‘spills over’ the right-hand boundary of the zoom-in region by whatever fraction of one uniform cell falls outside the proper zoom-in boundaries. In effect, the uniform grid ‘rounds up’ to the nearest whole uniform cell size past the right edge.

This amounts, on average, to one-half of one uniform cell on the right-hand side of each dimension falling outside the exact zoom-in region boundary. At a resolution of 0.125 pc, this means the uniform grid exceeds the zoom-in region’s size by about 0.0625 pc in each dimension. The four clouds’ zoom-in regions are about 100 pc in each dimension, so this corresponds to an error of six-hundredths of one percent in the modeled width, and the negligible cube of this error in the total volume.

In any case, I stress that *REGRID.F90* produces 3D grids from the post-processed tracers using an identical approximation, with the coordinates of the ‘upper-right’ corner of the grid rounded up to the nearest whole uniform cell size in the same way as in *UNIFORM.PY*. Therefore, the uniform grid of $n_{\text{H,tot}}$ produced with this routine and the uniform fractional abundance grid produced via interpolation in *REGRID.F90* are spatially identical, and can be multiplied exactly to produce uniform number density grids of post-processed species from the tracer snapshots.

A.3.2

SNAPWRITER.F90

A routine that reads the entire history of each post-processed tracer particle and produces data snapshots.

These snapshots report the full state of every tracer particle at a single desired time, copied from their respective histories. These snapshots are generally taken at $t_{\text{evol}} = 2, 3$, and 4 Myr, except in the cloud MC2-HD, where a snapshot of the tracer particles at the final timestep of $t_{\text{evol}} = 3.76$ Myr was produced instead.

For the full list of items saved by the tracers and reproduced in the snapshot, see the prior section on *POSTP.F90*. Additionally, each line (that is, each particle) of each snapshot is appended with the particle’s number (which was previously only recorded in the filename of the particular particle’s history) and the value of the bulk density ρ_0 at $t_{\text{evol}} = 0$. Because the tracers advect along with local gas

packets, the relative proportion of gas mass associated with each tracer remains constant over the simulation lifetime, and so this initial bulk density can be used for mass-weighting the data from the tracers as an ensemble.

The routine is capable of producing these snapshots for any valid time $t_{\text{evol}} > 0$ defined by the user. It also has the ability to provide ‘next’ snapshots – that is, snapshots of the post-processed data from the timestep immediately after the primary time(s) set by the user. Since these two snapshots are separated by the smallest possible time (one write-out cycle for the tracer particles, which is ~ 3.3 kyr for the SILCC-Zoom simulations used here), these consecutive snapshots can be useful for approximating the instantaneous rate of change of the various tracer quantities.

A.3.3

PROJECTOR.F90

A routine that reads a single uniform 3D density grid (as produced by *REGRID.F90*), and produces 2D column density projections along the x , y , and z directions.

The line integration is performed manually along each direction. Because the density grid is uniformly resolved, and has already been prepared such that x , y , and z in the zoom-in region’s coordinate system are along the axes of the grid, each line integration N_{species} collapses to a brute force sum:

$$N_{\text{species}} = s \sum_i^T n_{i,\text{species}}, \quad (\text{A.7})$$

where s is the resolution-dependent cell size or depth (0.125 pc for all analysis in this work), T is the total number of cells along the desired direction (equal to the grid width along that direction divided by s , rounded up as described under *UNIFORM.PY*), and n_{species} is the number density of the species whose 3D grid is being considered.

For a given projection, this procedure repeats along the line of every 2D pixel until a projection map of the species column density, N , is produced, at a resolution of 0.125 pc. The spatial coordinates of each N are then calculated as the center of the corresponding 2D pixel. That is, for the bottom-left pixel in the x - y projection (along z) where the coordinates range from $x = y = 0$ pc to $x = y = 0.125$ pc, the coordinates of N in that cell are reported as $x = y = 0.0625$ pc, the middle point. These coordinates with their corresponding N values are then written out for the entire projection in a row-wise format, so they can be read by the plotting routines.

B

THE STATISTICAL RIGOR OF THE TRACER POPULATION

As described in Section 3.3.1, a uniform lattice of tracer particles is injected into each SILCC-Zoom simulation at $t_{\text{evol}} = t_0$. These tracers are spaced 1 pc apart in each dimension, and fill the entire zoom-in region as well as 10 pc outside the region in each direction. For the two pure hydrodynamic (HD) simulations considered in this thesis, this amounts to about 900,000 tracers per simulation. For the two MHD simulations including magnetic fields, which cover a broader spatial extent due to the more diffuse nature of the magnetically-supported gas (see e.g. [Seifried et al., 2020](#); [Ganguly et al., 2022](#)), this comes to about 2,000,000 tracers per simulation.

These tracer populations seem objectively large, but the number of tracers alone cannot tell us whether the density distributions of the simulated clouds are well-sampled by the tracer data. The post-processed tracers are regridded as described in Section 5 of Paper I, in a grid with a cell resolution of 0.125 pc. Even if all the tracers are distributed throughout the cloud without redundancy, they can only achieve a maximal cell-filling fraction of ~ 0.1 %.

Appendix C of Paper I shows that the regridding algorithm can recover the distributions of H, H₂, and CO seen in the original reference simulations, and throughout Paper I and Paper II, the column density projections of HCO⁺ and OH from the regridded tracers compare favorably to observations. Still, it is important to confirm whether the available number of tracer particles is statistically sufficient to accurately reconstruct the gas chemistry. To confirm the tracer count used in this thesis is more than sufficient, I have selected smaller percentages of the tracer particles at random from clouds MC1-HD and MC1-MHD, and subjected these subsets to a few of the validation methods seen in Paper I.

First, I selected random sets of tracers amounting to 50%, 33%, 25%, and 10% of the totals for each cloud. I calculated the average number densities of H₂, CO, C⁺, HCO⁺, and OH, and T_{gas} , all vs. $n_{\text{H,tot}}$ from these tracer subsets. These averages and corresponding standard deviations for MC1-HD at $t_{\text{evol}} = 4$ Myr are plotted in Fig. 4, along with the result from the full population (100%) of the tracers. The number densities are quite insensitive to the tracer number statistics, with the averages and standard deviations visually indistinguishable on the plots. This close correspondence is seen in other clouds at other times as well (not shown). The result accords with findings from [Ferrada-Chamorro et al. \(2021\)](#), who found the same insensitivity to tracer statistics down to a 1% subset of their full tracer populations. Consequently, I will restrict the subsequent analysis techniques to the smallest subset, 10%.

Next, I generate number density grids at a uniform 0.125 pc resolution for MC1-HD and MC1-MHD at $t_{\text{evol}} = 4$ Myr, for the species H, H₂, H⁺, C, C⁺, gaseous CO, and CO frozen onto dust grains. No other hydrogen- or carbon- bearing species contain more than 0.1% of the total hydrogen or carbon mass respectively, and are neglected here. Using the total masses of these grids, I repeat the analysis of Fig. 10 in Paper I. This sums the aforementioned hydrogen and carbon species and

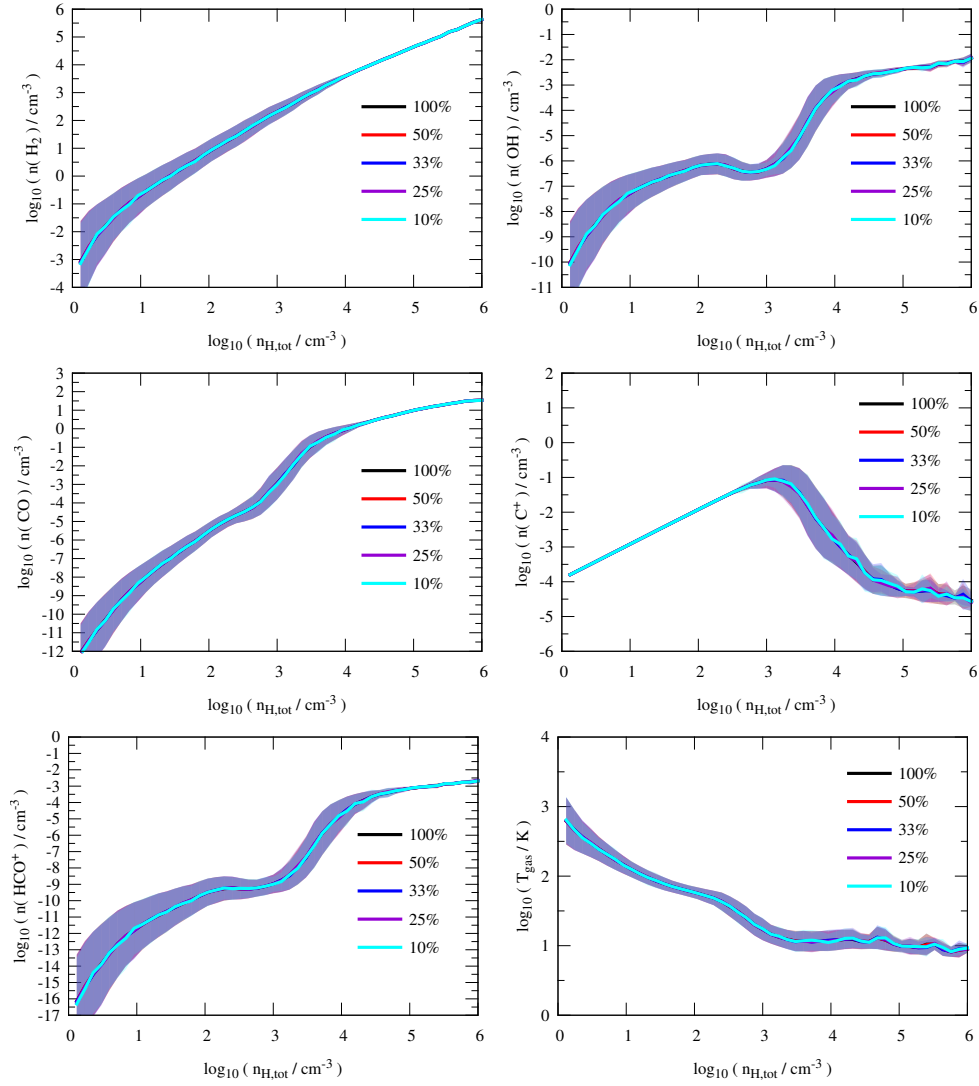


Figure 4: The average number densities of H_2 , OH , CO , C^+ , and HCO^+ , and the average value of T_{gas} , vs. $n_{\text{H,tot}}$ in MC1-HD at $t_{\text{evol}} = 4$ Myr. The shading indicates one standard deviation. Each color would correspond to a different subset of tracers, but their results are visually indistinguishable down to the 10% subset.

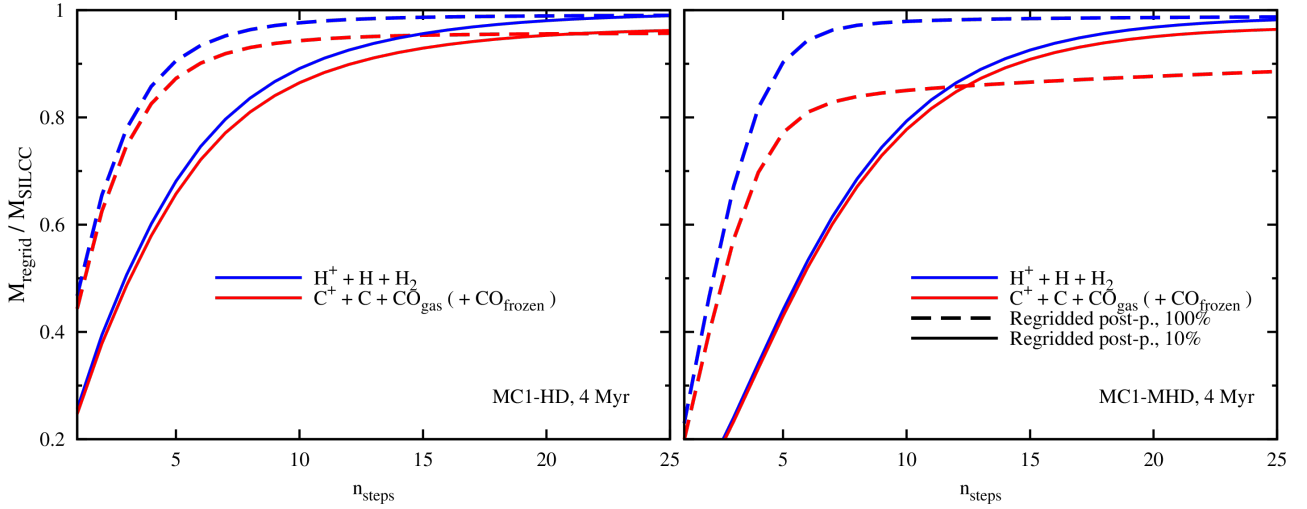


Figure 5: The ratio of regridded total hydrogen (blue) and carbon (red) masses to the total H and C masses from the SILCC grids, as a function of the number of interpolation steps. The left-hand panel shows MC1-HD, and the right-hand panel MC1-MHD, both at $t_{\text{evol}} = 4$ Myr. The convergences of both the full tracer population (solid lines) and the 10% subset (dashed) are shown. This corresponds to Fig. 10 from Paper I.

compares the total regridded H or C mass to the total H or C mass from the SILCC-Zoom grids, as a function of the number of interpolation steps taken in the course of filling in the entire regridded domain.

Each cloud’s results for the 10% subset are shown in Fig. 5, compared to the results for the full tracer population. In MC1-HD (left-hand panel), both the total hydrogen and total carbon masses from the 10% subset converge to the same values as the full tracer population. Convergence takes about twice as long for the 10% subset as for the full population. Reducing the tracers by a factor of ten would increase the average inter-tracer separation by $10^{1/3} \simeq 2$, so the doubled convergence time for the 10% subset implies that the inter-tracer separation is the controlling factor in the grid-filling timescale. This would indicate that running SILCC-Zoom simulations with another factor of ten increase in tracers (to $\sim 10^7$ per simulation) would only halve the interpolation convergence time, down to $n_{\text{steps}} \sim 5$. Assuming conservatively that this relationship between tracer number and inter-tracer separation continues to hold, an interpolative method like the one I have developed would be unavoidable unless the tracer count were multiplied by several more factors of ten.

In the right-hand panel of Fig. 5, the convergence results for MC1-MHD at $t_{\text{evol}} = 4$ Myr are shown. The hydrogen mass for the 10% subset still converges well, but the carbon mass overshoots the value for the full population. I posit that when 90% of the tracers are removed, different effects are seen in different density regimes. Minimal difference to the carbon quantity is made in the diffuse gas, where tracers are often separated by multiple cells anyway and significant interpolation is required to fill the grid even with the full population. Furthermore, cells with very dense gas can contain many tens of tracers, so the removal of 90% may still leave behind enough tracers to comprehensively sample these cells.

Conversely, in the intermediate density regime, many contiguous cells contain-

ing ~ 1 tracer may be left empty. The interpolation method fills these cells using the nearest surviving tracers, which may be those in very dense gas. As such, the regridded 10% subset would contain high densities of CO (both gaseous and frozen-out) in gas of intermediate bulk density. This effect would be greater in MHD clouds than in HD ones, as the MHD clouds have more diffuse gas in general and would suffer the greatest change by inaccurately interpolating the high-density CO outward from the local density peaks. The sharper density distribution of CO compared to H_2 (again see Appendix C of Paper I) makes this effect stronger for the total carbon mass than for the total hydrogen mass.

Next, in the top panel of Fig. 6, I repeat the analysis of Fig. 11 in Paper I. This plot gives the average fractional abundance of H and H_2 (relative to total hydrogen) and C, CO, and C^+ (relative to total carbon) as a function of $n_{\text{H,tot}}$. The original Fig. 11 in Paper I is provided in the bottom panel for comparison. As with the tracers, the average abundances of these species calculated from the grids are consistent between the 10% subset and the full population. At high density, the carbon species behave erratically, consistent with the prior hypothesis regarding the impact of the interpolation on the carbon species in particular. All in all, however, limiting the tracers to a 10% subset has minimal impact on the average abundances across a wide density domain.

Finally, I produce HCO^+ grids from the 10% tracer subset for MC1-HD and MC1-MHD at $t_{\text{evol}} = 4$ Myr, and take column density projections. In the top panel of Fig. 7, I plot the average $N(\text{HCO}^+)$ vs. $N(\text{H}_{\text{tot}})$, $N(\text{H}_2)$, and $N(\text{CO})$. This repeats the analysis of Fig. 14 of Paper I, which I repeat in the bottom panel for comparison. Again, the regridded 10% subset captures the same functional relationships as the regridded full tracer population. The value of $N(\text{HCO}^+)$ is slightly elevated at most densities in the 10% subset compared to the full population, which I ascribe to the same interpolation effect that impacted the carbon mass. The effect is barely noticeable, however.

In conclusion, I find that taking a subset of 10% of the tracer particles has reasonably small impacts upon the outcomes of the post-processing and regridding algorithms. The tracer averages are unaffected. Reducing the tracer statistics seems to cause the CO to be inaccurately interpolated farther out from dense cores than it should be. However, the effect is fairly small. The corresponding consistency of individual species' fractional abundances as a function of the total density, and of the HCO^+ column density as a function of the H_{tot} , H_2 , and CO column densities, shows that the regridding methods undertaken in this thesis are robust against a sharp reduction in the tracer number statistics. This indicates the current count of tracer particles from these simulations is statistically sufficient.

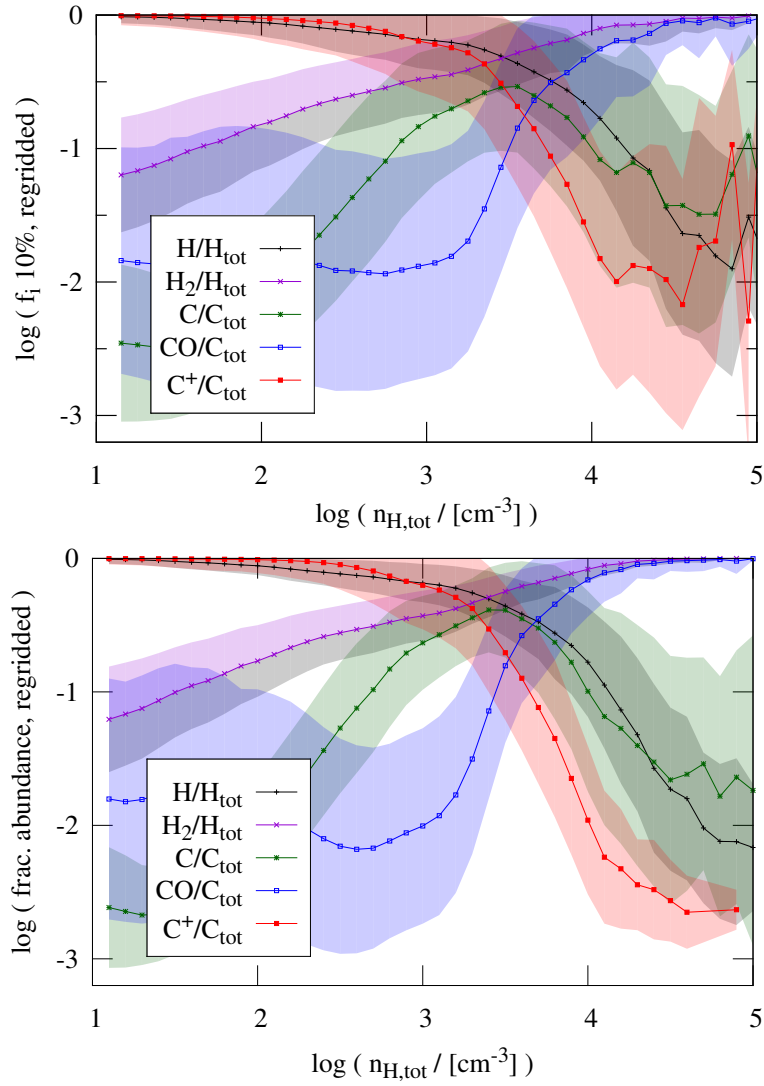


Figure 6: The fractional abundances (relative to hydrogen or carbon) of H, H₂, C, CO, and C⁺ vs. $n_{\text{H,tot}}$ for cloud MC1-HD at $t_{\text{evol}} = 2$ Myr, after regridding. Top panel: the result with the 10% subset of the tracers. Bottom panel: the result with the full tracer population for comparison, repeating Fig. 11 from Paper I.

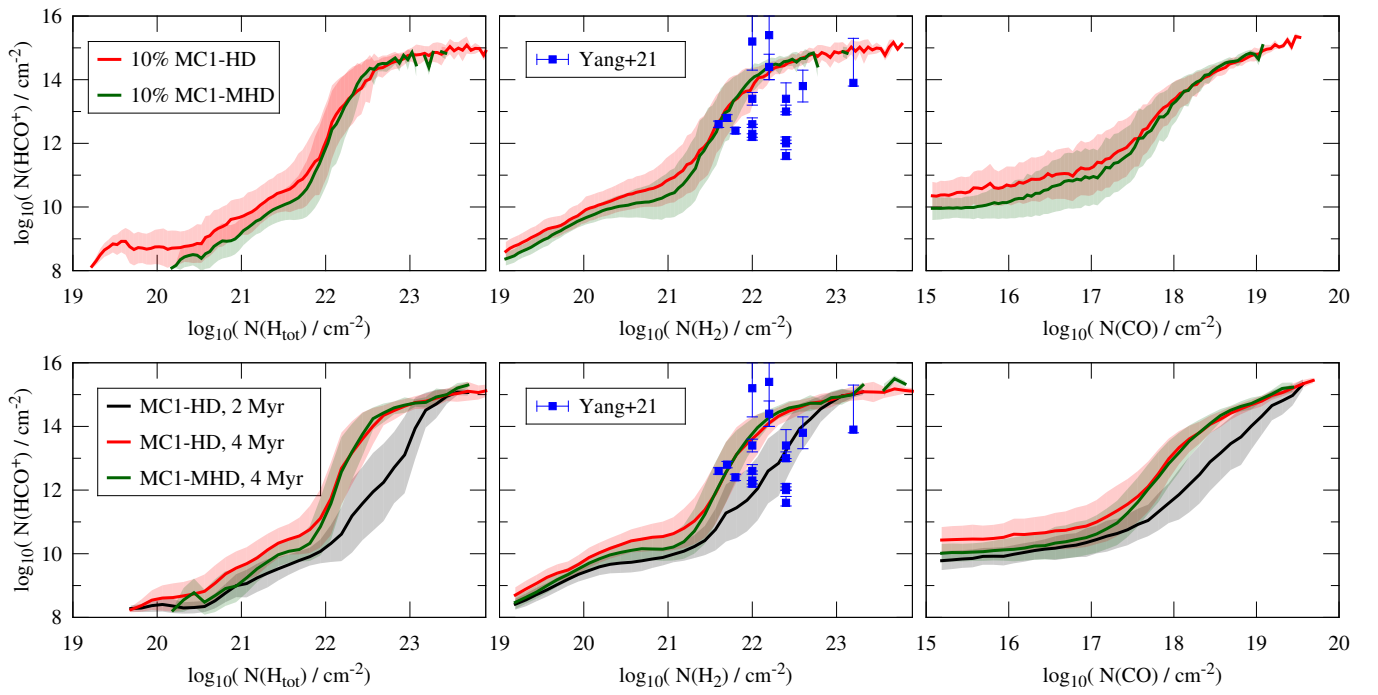


Figure 7: $N(\text{HCO}^+)$ (in the y - z direction) vs. the column densities of H_{tot} (left), H_2 (middle), and CO (right), for clouds MC1-HD and MC1-MHD at $t_{\text{evol}} = 4$ Myr. Top panel: the results using a 10% subset of the tracers. Bottom panel, the results using the full tracer population, repeating Fig. 14 of Paper I.

BIBLIOGRAPHY

- Ronald J. Allen, Mónica Ivette Rodríguez, John H. Black, and Roy S. Booth. Faint Extended OH Emission from the Local Interstellar Medium in the Direction $l \approx 108^\circ$, $b \approx 5^\circ$. *AJ*, 143(4):97, April 2012. doi: 10.1088/0004-6256/143/4/97.
- Ronald J. Allen, David E. Hogg, and Philip D. Engelke. The Structure of Dark Molecular Gas in the Galaxy. I. A Pilot Survey for 18 cm OH Emission Toward $l \approx 105^\circ$, $b \approx +1^\circ$. *AJ*, 149(4):123, April 2015. doi: 10.1088/0004-6256/149/4/123.
- P. André, J. Di Francesco, D. Ward-Thompson, S. I. Inutsuka, R. E. Pudritz, and J. E. Pineda. From Filamentary Networks to Dense Cores in Molecular Clouds: Toward a New Paradigm for Star Formation. In Henrik Beuther, Ralf S. Klessen, Cornelis P. Dullemond, and Thomas Henning, editors, *Protostars and Planets VI*, pages 27–51, January 2014. doi: 10.2458/azu_uapress_9780816531240-ch002.
- S. Jane Arthur, Stanley E. Kurtz, José Franco, and Marna Y. Albarrán. The Effects of Dust on Compact and Ultracompact H II Regions. *ApJ*, 608(1):282–296, June 2004. doi: 10.1086/386366.
- P. W. Atkins and Ronald Friedman. *Molecular quantum mechanics*. Oxford University Press, Oxford ; New York, 5th edition, 2011. ISBN 978-0-19-954142-3.
- E. L. O. Bakes and A. G. G. M. Tielens. The Photoelectric Heating Mechanism for Very Small Graphitic Grains and Polycyclic Aromatic Hydrocarbons. *ApJ*, 427: 822, June 1994. doi: 10.1086/174188.
- A T Barnes, J Kauffmann, F Bigiel, N Brinkmann, D Colombo, A E Guzmán, W J Kim, L Szűcs, V Wakelam, S Aalto, T Albertsson, N J Evans, S C O Glover, P F Goldsmith, C Kramer, K Menten, Y Nishimura, S Viti, Y Watanabe, A Weiss, M Wienen, H Wiesemeyer, and F Wyrowski. LEGO – II. A 3 mm molecular line study covering 100 pc of one of the most actively star-forming portions within the Milky Way disc. *MNRAS*, 497(2):1972–2001, September 2020. ISSN 0035-8711, 1365-2966. doi: 10.1093/mnras/staa1814. URL <https://academic.oup.com/mnras/article/497/2/1972/5880778>.
- Rainer Beck and Richard Wielebinski. Magnetic Fields in Galaxies. In Terry D. Oswalt and Gerard Gilmore, editors, *Planets, Stars and Stellar Systems: Volume 5: Galactic Structure and Stellar Populations*, pages 641–723. Springer Netherlands, Dordrecht, 2013. ISBN 978-94-007-5612-0. doi: 10.1007/978-94-007-5612-0_13.
- E. E. Becklin and G. Neugebauer. Observations of an Infrared Star in the Orion Nebula. *ApJ*, 147:799, February 1967. doi: 10.1086/149055.
- Edwin A. Bergin, Lee W. Hartmann, John C. Raymond, and Javier Ballesteros-Paredes. Molecular Cloud Formation behind Shock Waves. *ApJ*, 612(2):921–939, September 2004. ISSN 0004-637X, 1538-4357. doi: 10.1086/422578. URL <https://iopscience.iop.org/article/10.1086/422578>.

- Thomas G. Bisbas, Jonathan C. Tan, and Kei E. I. Tanaka. Photodissociation region diagnostics across galactic environments. *MNRAS*, 502:2701–2732, 2021. doi: 10.1093/mnras/stab121.
- J. H. Black and A. Dalgarno. Models of interstellar clouds. I. The Zeta Ophiuchi cloud. *ApJS*, 34:405–423, July 1977. doi: 10.1086/190455.
- L. Blitz, Y. Fukui, A. Kawamura, A. Leroy, N. Mizuno, and E. Rosolowsky. Giant Molecular Clouds in Local Group Galaxies. In Bo Reipurth, David Jewitt, and Klaus Keil, editors, *Protostars and Planets V*, page 81, January 2007. doi: 10.48550/arXiv.astro-ph/0602600.
- François Bouchut, Christian Klingenberg, and Knut Waagan. A multiwave approximate riemann solver for ideal mhd based on relaxation. i: Theoretical framework. *Numerische Mathematik*, 108:7–42, 11 2007. doi: 10.1007/s00211-007-0108-8.
- François Bouchut, Christian Klingenberg, and Knut Waagan. A multiwave approximate riemann solver for ideal mhd based on relaxation ii: Numerical implementation with 3 and 5 waves. *Numerische Mathematik*, 115:647–679, 06 2010. doi: 10.1007/s00211-010-0289-4.
- Tyler L. Bourke, Philip C. Myers, Garry Robinson, and A. R. Hyland. New OH Zeeman Measurements of Magnetic Field Strengths in Molecular Clouds. *ApJ*, 554(2):916–932, June 2001. doi: 10.1086/321405.
- S. Bovino, T. Grassi, M. A. Latif, and D. R. G. Schleicher. Impact of an accurate modelling of primordial chemistry in high-resolution studies. *MNRAS*, 434:L36–L40, July 2013. doi: 10.1093/mnras/slt072.
- S. Bovino, T. Grassi, D. R. G. Schleicher, and P. Caselli. H2 Ortho-to-para Conversion on Grains: A Route to Fast Deuterium Fractionation in Dense Cloud Cores? *ApJ*, 849(2):L25, November 2017. ISSN 2041-8213. doi: 10.3847/2041-8213/aa95b7. URL <https://iopscience.iop.org/article/10.3847/2041-8213/aa95b7>.
- S. Bovino, S. Ferrada-Chamorro, A. Lupi, G. Sabatini, A. Giannetti, and D.R.G. Schleicher. The 3D Structure of CO Depletion in High-mass Prestellar Regions. *ApJ*, 887(224):10, 2019. doi: 10.3847/1538-4357/ab53e4.
- Stefano Bovino, Alessandro Lupi, Andrea Giannetti, Giovanni Sabatini, Dominik R. G. Schleicher, Friedrich Wyrowski, and Karl M. Menten. Chemical analysis of prestellar cores in Ophiuchus yields short timescales and rapid collapse. *A&A*, 654:A34, October 2021. doi: 10.1051/0004-6361/202141252.
- C. M. Brunt, M. H. Heyer, and M. M. Mac Low. Turbulent driving scales in molecular clouds. *A&A*, 504(3):883–890, September 2009. doi: 10.1051/0004-6361/200911797.
- Michael G. Burton, D. J. Hollenbach, and A. G. G. M. Tielens. Line Emission from Clumpy Photodissociation Regions. *ApJ*, 365:620, December 1990. doi: 10.1086/169516.
- Michael P. Busch, Ronald J. Allen, Philip D. Engelke, David E. Hogg, David A. Neufeld, and Mark G. Wolfire. The Structure of Dark Molecular Gas in the Galaxy. II. Physical State of “CO-dark” Gas in the Perseus Arm. *ApJ*, 883(158):10, 2019. doi: 10.3847/1538-4357/ab3a4b.

- Michael P. Busch, Philip D. Engelke, Ronald J. Allen, and David E. Hogg. Observational Evidence for a Thick Disk of Dark Molecular Gas in the Outer Galaxy. *arXiv:2104.06538 [astro-ph]*, April 2021. URL <http://arxiv.org/abs/2104.06538>. arXiv: 2104.06538.
- Corentin Cadiou, Yohan Dubois, and Christophe Pichon. Accurate tracer particles of baryon dynamics in the adaptive mesh refinement code Ramses. *A&A*, 621: A96, January 2019. doi: 10.1051/0004-6361/201834496.
- Vianey Camacho, Enrique Vázquez-Semadeni, Javier Ballesteros-Paredes, Gilberto C. Gómez, S. Michael Fall, and M. Dolores Mata-Chávez. Energy Budget of Forming Clumps in Numerical Simulations of Collapsing Clouds. *ApJ*, 833(1): 113, December 2016. doi: 10.3847/1538-4357/833/1/113.
- Pedro R Capelo, Stefano Bovino, Alessandro Lupi, Dominik R G Schleicher, and Tommaso Grassi. The effect of non-equilibrium metal cooling on the interstellar medium. *MNRAS*, 475(3):3283–3304, April 2018. ISSN 0035-8711, 1365-2966. doi: 10.1093/mnras/stx3355. URL <https://academic.oup.com/mnras/article/475/3/3283/4793253>.
- P. Caselli, C. M. Walmsley, R. Terzieva, and Eric Herbst. The Ionization Fraction in Dense Cloud Cores. *ApJ*, 499(1):234–249, May 1998. doi: 10.1086/305624.
- P. Caselli, C. M. Walmsley, A. Zucconi, M. Tafalla, L. Dore, and P. C. Myers. Molecular Ions in L1544. II. The Ionization Degree. *ApJ*, 565(1):344–358, January 2002. doi: 10.1086/324302.
- Cecilia Ceccarelli, Paola Caselli, Dominique Bockelee-Morvan, Olivier Mousis, Sandra Pizzarello, Francois Robert, and Dmitry Semenov. Deuterium Fractionation: the Ariadne’s Thread from the Pre-collapse Phase to Meteorites and Comets today. *arXiv:1403.7143 [astro-ph]*, 2014. doi: 10.2458/azu_uapress_9780816531240-ch037. URL <http://arxiv.org/abs/1403.7143>. arXiv: 1403.7143.
- Mélanie Chevance, J. M. Diederik Kruijssen, Alexander P. S. Hygate, Andreas Schruba, Steven N. Longmore, Brent Groves, Jonathan D. Henshaw, Cinthya N. Herrera, Annie Hughes, Sarah M. R. Jeffreson, Philipp Lang, Adam K. Leroy, Sharon E. Meidt, Jérôme Pety, Alessandro Razza, Erik Rosolowsky, Eva Schinnerer, Frank Bigiel, Guillermo A. Blanc, Eric Emsellem, Christopher M. Faesi, Simon C. O. Glover, Daniel T. Haydon, I. Ting Ho, Kathryn Kreckel, Janice C. Lee, Daizhong Liu, Miguel Querejeta, Toshiki Saito, Jiayi Sun, Antonio Usero, and Dyas Utomo. The lifecycle of molecular clouds in nearby star-forming disc galaxies. *MNRAS*, 493(2):2872–2909, April 2020. doi: 10.1093/mnras/stz3525.
- Arnab Rai Choudhuri. *The physics of fluids and plasmas : an introduction for astrophysicists* /. 1998.
- Paul C. Clark, Simon C. O. Glover, Ralf S. Klessen, and Ian A. Bonnell. How long does it take to form a molecular cloud?: Molecular cloud formation time-scales. *MNRAS*, 424(4):2599–2613, August 2012. ISSN 00358711. doi: 10.1111/j.1365-2966.2012.21259.x. URL <https://academic.oup.com/mnras/article-lookup/doi/10.1111/j.1365-2966.2012.21259.x>.
- Richard M. Crutcher. Magnetic Fields in Molecular Clouds. *ARA&A*, 50:29–63, September 2012. doi: 10.1146/annurev-astro-081811-125514.

- Richard M. Crutcher, Thomas H. Troland, Bernard Lazareff, Gabriel Paubert, and Ilya Kazès. Detection of the CN Zeeman Effect in Molecular Clouds. *ApJ*, 514(2): L121–L124, April 1999. doi: 10.1086/311952.
- A. Dalgarno, Min Yan, and Weihong Liu. Electron Energy Deposition in a Gas Mixture of Atomic and Molecular Hydrogen and Helium. *ApJS*, 125(1):237–256, November 1999. doi: 10.1086/313267.
- T. M. Dame, H. Ungerechts, R. S. Cohen, E. J. de Geus, I. A. Grenier, J. May, D. C. Murphy, L. A. Nyman, and P. Thaddeus. A Composite CO Survey of the Entire Milky Way. *ApJ*, 322:706, November 1987. doi: 10.1086/165766.
- De Caelo. *Aristotle: On the Heavens I & II*. Liverpool University Press, 1995. ISBN 9780856686634. URL <http://www.jstor.org/stable/j.ctv1228h9n>.
- Dominik Derigs, Andrew R. Winters, Gregor J. Gassner, and Stefanie Walch. A novel high-order, entropy stable, 3D AMR MHD solver with guaranteed positive pressure. *Journal of Computational Physics*, 317:223–256, July 2016. doi: 10.1016/j.jcp.2016.04.048.
- C. L. Dobbs, M. R. Krumholz, J. Ballesteros-Paredes, A. D. Bolatto, Y. Fukui, M. Heyer, M. M. M. Low, E. C. Ostriker, and E. Vázquez-Semadeni. Formation of Molecular Clouds and Global Conditions for Star Formation. In Henrik Beuther, Ralf S. Klessen, Cornelis P. Dullemond, and Thomas Henning, editors, *Protostars and Planets VI*, page 3, January 2014. doi: 10.2458/azu_uapress_9780816531240-ch001.
- A. E. Douglas and G. Herzberg. Note on $\text{CH}^{\{+ \}}$ in Interstellar Space and in the Laboratory. *ApJ*, 94:381, September 1941. doi: 10.1086/144342.
- B. T. Draine. Photoelectric heating of interstellar gas. *ApJS*, 36:595–619, April 1978. ISSN 0067-0049, 1538-4365. doi: 10.1086/190513. URL <http://adsabs.harvard.edu/doi/10.1086/190513>.
- B. T. Draine and Frank Bertoldi. Structure of stationary photodissociation fronts. */mnras*, 468:269–289, 1996. URL <http://articles.adsabs.harvard.edu/pdf/1996ApJ...468..269D>.
- B. T. Draine and H. M. Lee. Optical Properties of Interstellar Graphite and Silicate Grains. *ApJ*, 285:89, October 1984. doi: 10.1086/162480.
- Bruce T. Draine. *Physics of the Interstellar and Intergalactic Medium*. 2011.
- A Dubey, R Fisher, C Graziani, G C Jordan, D Q Lamb, L B Reid, P Rich, D Sheeler, D Townsley, and K Weide. Challenges of Extreme Computing using the FLASH code. *Astronomical Society of the Pacific Conference Series*, 385(Numerical Modeling of Space Plasma Flows):145, 2008.
- C. P. Dullemond, A. Juhasz, A. Pohl, F. Sereshti, R. Shetty, T. Peters, B. Commercon, and M. Flock. RADMC-3D: A multi-purpose radiative transfer tool. *Astrophysics Source Code Library*, record ascl:1202.015, February 2012.
- S. Ebagezio, D. Seifried, S. Walch, P. C. Nürnbergger, T. E. Rathjen, and T. Naab. CO and [CII] line emission of molecular clouds – the impact of stellar feedback and non-equilibrium chemistry. *arXiv e-prints*, art. arXiv:2206.06393, June 2022.

- B. G. Elmegreen. Magnetic diffusion and ionization fractions in dense molecular clouds: the role of charged grains. *ApJ*, 232:729–739, September 1979. doi: 10.1086/157333.
- B. G. Elmegreen and C. J. Lada. Sequential formation of subgroups in OB associations. *ApJ*, 214:725–741, June 1977. doi: 10.1086/155302.
- Bruce G. Elmegreen. Star Formation in a Crossing Time. *ApJ*, 530(1):277–281, February 2000. doi: 10.1086/308361.
- Bruce G. Elmegreen and John Scalo. Interstellar Turbulence I: Observations and Processes. *ARA&A*, 42(1):211–273, September 2004. doi: 10.1146/annurev.astro.41.011802.094859.
- Christoph Federrath, Sharanya Sur, Dominik R. G. Schleicher, Robi Banerjee, and Ralf S. Klessen. A New Jeans Resolution Criterion for (M)HD Simulations of Self-gravitating Gas: Application to Magnetic Field Amplification by Gravity-driven Turbulence. *ApJ*, 731(1):62, April 2011. doi: 10.1088/0004-637X/731/1/62.
- Simón Ferrada-Chamorro, Alessandro Lupi, and Stefano Bovino. Chemical post-processing of magneto-hydrodynamical simulations of star-forming regions: robustness and pitfalls. *MNRAS*, 505(3):3442–3451, August 2021. doi: 10.1093/mnras/stab1525.
- G. B. Field, D. W. Goldsmith, and H. J. Habing. Cosmic-Ray Heating of the Interstellar Gas. *ApJ*, 155:L149, March 1969. doi: 10.1086/180324.
- D. J. Fixsen and J. C. Mather. The Spectral Results of the Far-Infrared Absolute Spectrophotometer Instrument on COBE. *ApJ*, 581(2):817–822, December 2002. doi: 10.1086/344402.
- B. Fryxell, K. Olson, P. Ricker, F.X. Timmes, M. Zingale, D.Q. Lamb, P. MacNeice, R. Rosner, J.W. Truran, and H. Tufo. FLASH: An Adaptive Mesh Hydrodynamics Code for Modeling Astrophysical Thermonuclear Flashes. *ApJS*, 131(1):273–334, 2000. doi: 10.1086/317361.
- Brandt A. L. Gaches and Stella S. R. Offner. A Model for Protostellar Cluster Luminosities and the Impact on the CO–H₂ Conversion Factor. *ApJ*, 854(2):156, February 2018. ISSN 1538-4357. doi: 10.3847/1538-4357/aaae2. URL <https://iopscience.iop.org/article/10.3847/1538-4357/aaae2>.
- Brandt A. L. Gaches, Stella S. R. Offner, and Thomas G. Bisbas. The Astrochemical Impact of Cosmic Rays in Protoclusters I: Molecular Cloud Chemistry. *ApJ*, 878(2):105, June 2019. ISSN 1538-4357. doi: 10.3847/1538-4357/ab20c7. URL <http://arxiv.org/abs/1905.02232>. arXiv: 1905.02232.
- S. Ganguly, S. Walch, S. D. Clarke, and D. Seifried. SILCC-Zoom: the dynamic balance in molecular cloud substructures. *arXiv e-prints*, art. arXiv:2204.02511, April 2022.
- Andrea Gatto, Stefanie Walch, Thorsten Naab, Philipp Girichidis, Richard Wunsch, Simon C. O. Glover, Ralf S. Klessen, Paul C. Clark, Thomas Peters, Dominik Derigs, Christian Baczynski, and Joachim Puls. The SILCC project – III. Regulation of star formation and outflows by stellar winds and supernovae. *MNRAS*, 466(2):1903–1924, April 2017. ISSN 0035-8711, 1365-2966. doi: 10.1093/mnras/stw3209.

- URL <https://academic.oup.com/mnras/article-lookup/doi/10.1093/mnras/stw3209>.
- Shy Genel, Mark Vogelsberger, Dylan Nelson, Debora Sijacki, Volker Springel, and Lars Hernquist. Following the flow: tracer particles in astrophysical fluid simulations. *MNRAS*, 435:1426–1442, 2013. doi: 10.1093/mnras/stt1383.
- Maryvonne Gerin and Harvey Liszt. CO+ as a probe of the origin of CO in diffuse interstellar clouds. *arXiv:2102.09861 [astro-ph]*, March 2021. URL <http://arxiv.org/abs/2102.09861>. arXiv: 2102.09861.
- A. Giannetti, S. Bovino, P. Caselli, S. Leurini, D. R. G. Schleicher, B. Körtgen, K. M. Menten, T. Pillai, and F. Wyrowski. A timeline for massive star-forming regions via combined observation of o-H₂D⁺ and N₂D⁺. *A&A*, 621:L7, January 2019. doi: 10.1051/0004-6361/201834602.
- Philipp Girichidis, Stefanie Walch, Thorsten Naab, Andrea Gatto, Richard Wünsch, Simon C. O. Glover, Ralf S. Klessen, Paul C. Clark, Thomas Peters, Dominik Dergis, and Christian Baczynski. The SILCC (Simulating the LifeCycle of molecular Clouds) project – II. Dynamical evolution of the supernova-driven ISM and the launching of outflows. *MNRAS*, 456(4):3432–3455, March 2016. ISSN 0035-8711, 1365-2966. doi: 10.1093/mnras/stv2742. URL <https://academic.oup.com/mnras/article-lookup/doi/10.1093/mnras/stv2742>.
- A. E. Glassgold and William D. Langer. Heating of Molecular-Hydrogen Clouds by Cosmic Rays and X-Rays. *ApJ*, 186:859–888, December 1973. doi: 10.1086/152552.
- S. C. O. Glover and M.-M. Mac Low. On the relationship between molecular hydrogen and carbon monoxide abundances in molecular clouds: H₂ versus CO abundance. *MNRAS*, 412(1):337–350, March 2011. ISSN 00358711. doi: 10.1111/j.1365-2966.2010.17907.x. URL <https://academic.oup.com/mnras/article-lookup/doi/10.1111/j.1365-2966.2010.17907.x>.
- S. C. O. Glover, C. Federrath, M.-M. Mac Low, and R. S. Klessen. Modelling CO formation in the turbulent interstellar medium. *MNRAS*, 404:2–29, April 2010. ISSN 00358711, 13652966. doi: 10.1111/j.1365-2966.2009.15718.x. URL <http://mnras.oxfordjournals.org/cgi/doi/10.1111/j.1365-2966.2009.15718.x>.
- Simon C. O. Glover and Paul C. Clark. Approximations for modelling CO chemistry in giant molecular clouds: a comparison of approaches: Approximations for CO chemistry. *MNRAS*, 421:116–131, January 2012. ISSN 00358711. doi: 10.1111/j.1365-2966.2011.20260.x. URL <https://academic.oup.com/mnras/article-lookup/doi/10.1111/j.1365-2966.2011.20260.x>.
- Simon C. O. Glover and Mordecai-Mark Mac Low. Simulating the Formation of Molecular Clouds. I. Slow Formation by Gravitational Collapse from Static Initial Conditions. *ApJS*, 169(2):239–268, April 2007. ISSN 0067-0049, 1538-4365. doi: 10.1086/512238. URL <https://iopscience.iop.org/article/10.1086/512238>.
- Orly Gnat and Gary J. Ferland. Ion-by-ion Cooling Efficiencies. *ApJS*, 199(1):20, March 2012. doi: 10.1088/0067-0049/199/1/20.
- Nickolay Y. Gnedin, Konstantinos Tassis, and Andrey V. Kravtsov. MODELING MOLECULAR HYDROGEN AND STAR FORMATION IN COSMOLOGICAL SIMULATIONS. *ApJ*, 697(1):55–67, May 2009. ISSN 0004-637X, 1538-4357. doi:

- 10.1088/0004-637X/697/1/55. URL <https://iopscience.iop.org/article/10.1088/0004-637X/697/1/55>.
- J. R. Goicoechea, J. Pety, M. Gerin, P. Hily-Blant, and J. Le Bourlot. The ionization fraction gradient across the Horsehead edge: an archetype for molecular clouds. *A&A*, 498(3):771–783, May 2009. doi: 10.1051/0004-6361/200811496.
- Peter Goldreich and John Kwan. Molecular Clouds. *ApJ*, 189:441–454, May 1974. doi: 10.1086/152821.
- P. F. Goldsmith and W. D. Langer. Molecular cooling and thermal balance of dense interstellar clouds. *ApJ*, 222:881–895, June 1978. doi: 10.1086/156206.
- Paul F. Goldsmith. Molecular Depletion and Thermal Balance in Dark Cloud Cores. *ApJ*, 557(2):736–746, August 2001. ISSN 0004-637X, 1538-4357. doi: 10.1086/322255. URL <https://iopscience.iop.org/article/10.1086/322255>.
- Munan Gong, Eve C. Ostriker, and Mark G. Wolfire. A Simple and Accurate Network for Hydrogen and Carbon Chemistry in the Interstellar Medium. *ApJ*, 843(38):36, 2017. doi: 10.3847/1538-4357/aa7561.
- Munan Gong, Eve C. Ostriker, and Chang-Goo Kim. The X_{CO} Conversion Factor from Galactic Multiphase ISM Simulations. *ApJ*, 858(1):16, May 2018. doi: 10.3847/1538-4357/aab9af.
- Munan Gong, Eve C. Ostriker, Chang-Goo Kim, and Jeong-Gyu Kim. The Environmental Dependence of the X_{CO} Conversion Factor. *ApJ*, 903(2):142, November 2020. doi: 10.3847/1538-4357/abbdab.
- K. M. Górski and Eric Hivon. HEALPix: Hierarchical Equal Area isoLatitude Pixelization of a sphere, July 2011.
- Robert J. Gould and Edwin E. Salpeter. The Interstellar Abundance of the Hydrogen Molecule. I. Basic Processes. *ApJ*, 138:393, August 1963. doi: 10.1086/147654.
- T. Grassi, S. Bovino, D. Schleicher, and F. A. Gianturco. Chemical complexity in astrophysical simulations: optimization and reduction techniques. *MNRAS*, 431(2):1659–1668, May 2013. doi: 10.1093/mnras/stt284.
- T Grassi, S Bovino, D R G Schleicher, J Prieto, D Seifried, E Simoncini, and F A Gianturco. KROME – a package to embed chemistry in astrophysical simulations. *MNRAS*, 439:2386–2419, 2014. doi: 10.1093/mnras/stu114.
- T. Grassi, S. Bovino, T. Haugbølle, and D. R. G. Schleicher. A detailed framework to incorporate dust in hydrodynamical simulations. *MNRAS*, 466(2):1259–1274, April 2017. ISSN 0035-8711, 1365-2966. doi: 10.1093/mnras/stw2871. URL <https://academic.oup.com/mnras/article-lookup/doi/10.1093/mnras/stw2871>.
- Matthias Gritschneder, Thorsten Naab, Stefanie Walch, Andreas Burkert, and Fabian Heitsch. Driving Turbulence and Triggering Star Formation by Ionizing Radiation. *ApJ*, 694(1):L26–L30, March 2009. doi: 10.1088/0004-637X/694/1/L26.
- H. J. Habing. The Interstellar Radiation Density between 912 Å and 2400 Å. *Bull. Astr. Inst. Netherlands*, 19:421–431, 1968. URL http://articles.adsabs.harvard.edu/cgi-bin/nph-iarticle_query?1968BAN...19..421H&defaultprint=YES&filetype=.pdf.

- M. M. Hanson, R. P. Kudritzki, M. A. Kenworthy, J. Puls, and A. T. Tokunaga. A Medium Resolution Near-Infrared Spectral Atlas of O and Early-B Stars. *ApJS*, 161(1):154–170, November 2005. doi: 10.1086/444363.
- Lee Hartmann, Javier Ballesteros-Paredes, and Edwin A. Bergin. Rapid Formation of Molecular Clouds and Stars in the Solar Neighborhood. *ApJ*, 562(2):852–868, December 2001. doi: 10.1086/323863.
- Fabian Heitsch and Lee Hartmann. Rapid Molecular Cloud and Star Formation: Mechanisms and Movies. *ApJ*, 689(1):290–301, December 2008. doi: 10.1086/592491.
- Patrick Hennebelle and Edith Falgarone. Turbulent molecular clouds. *A&A Rev.*, 20:55, November 2012. doi: 10.1007/s00159-012-0055-y.
- Mark Heyer and T. M. Dame. Molecular Clouds in the Milky Way. *ARA&A*, 53: 583–629, August 2015. doi: 10.1146/annurev-astro-082214-122324.
- Mark H. Heyer, John M. Carpenter, and Ronald L. Snell. The Equilibrium State of Molecular Regions in the Outer Galaxy. *ApJ*, 551(2):852–866, April 2001. doi: 10.1086/320218.
- R. H. Hildebrand. The determination of cloud masses and dust characteristics from submillimetre thermal emission. *QJRAS*, 24:267–282, September 1983.
- D. Hollenbach and C. F. McKee. Molecule formation and infrared emission in fast interstellar shocks. I. Physical processes. *ApJS*, 41:555–592, November 1979. doi: 10.1086/190631.
- David Hollenbach and Christopher F. McKee. Molecule Formation and Infrared Emission in Fast Interstellar Shocks. III. Results for J Shocks in Molecular Clouds. *ApJ*, 342:306, July 1989. doi: 10.1086/167595.
- David Hollenbach and E. E. Salpeter. Surface Recombination of Hydrogen Molecules. *ApJ*, 163:155, January 1971. doi: 10.1086/150754.
- David Hollenbach, Michael J. Kaufman, Edwin A. Bergin, and Gary J. Melnick. WATER, O₂, AND ICE IN MOLECULAR CLOUDS. *ApJ*, 690(2):1497–1521, January 2009. ISSN 0004-637X, 1538-4357. doi: 10.1088/0004-637X/690/2/1497. URL <https://iopscience.iop.org/article/10.1088/0004-637X/690/2/1497>.
- F. Hoyle and G. R. A. Ellis. On the Existence of an Ionized Layer about the Galactic Plane. *Australian Journal of Physics*, 16:1, March 1963. doi: 10.1071/PH630001.
- Chia-Yu Hu, Amiel Sternberg, and Ewine F. van Dishoeck. Metallicity Dependence of the H/H₂ and C⁺/C/CO Distributions in a Resolved Self-regulating Interstellar Medium. *ApJ*, 920(1):44, October 2021. doi: 10.3847/1538-4357/ac0dbd.
- Olivier Iffrig and Patrick Hennebelle. Mutual influence of supernovae and molecular clouds. *A&A*, 576:A95, April 2015. doi: 10.1051/0004-6361/201424556.
- N. Jarosik, C. L. Bennett, J. Dunkley, B. Gold, M. R. Greason, M. Halpern, R. S. Hill, G. Hinshaw, A. Kogut, E. Komatsu, D. Larson, M. Limon, S. S. Meyer, M. R. Nolte, N. Odegard, L. Page, K. M. Smith, D. N. Spergel, G. S. Tucker, J. L. Weiland, E. Wollack, and E. L. Wright. Seven-year Wilkinson Microwave Anisotropy Probe (WMAP) Observations: Sky Maps, Systematic Errors, and Basic Results. *ApJS*, 192(2):14, February 2011. doi: 10.1088/0067-0049/192/2/14.

- J. H. Jeans. The Stability of a Spherical Nebula. *Philosophical Transactions of the Royal Society of London Series A*, 199:1–53, January 1902. doi: 10.1098/rsta.1902.0012.
- Peter M. W. Kalberla and Jürgen Kerp. The HI Distribution of the Milky Way. *ARA&A*, 47(1):27–61, September 2009. doi: 10.1146/annurev-astro-082708-101823.
- Jens Kauffmann, Paul F. Goldsmith, Gary Melnick, Volker Tolls, Andres Guzman, and Karl M. Menten. Molecular Line Emission as a Tool for Galaxy Observations (LEGO): I. HCN as a tracer of moderate gas densities in molecular clouds and galaxies. *A&A*, 605:L5, September 2017. ISSN 0004-6361, 1432-0746. doi: 10.1051/0004-6361/201731123. URL <http://www.aanda.org/10.1051/0004-6361/201731123>.
- Laura C. Keating, Alexander J. Richings, Norman Murray, Claude-André Faucher-Giguère, Philip F. Hopkins, Andrew Wetzel, Dušan Kereš, Samantha Benincasa, Robert Feldmann, Sarah Loebman, and Matthew E. Orr. Reproducing the CO-to-H₂ conversion factor in cosmological simulations of Milky-Way-mass galaxies. *MNRAS*, 499(1):837–850, November 2020. doi: 10.1093/mnras/staa2839.
- Jr. Kennicutt, Robert C. The Global Schmidt Law in Star-forming Galaxies. *ApJ*, 498(2):541–552, May 1998. doi: 10.1086/305588.
- Ralf S. Klessen and Simon C. O. Glover. Physical Processes in the Interstellar Medium. In Yves Revaz, Pascale Jablonka, Romain Teyssier, and Lucio Mayer, editors, *Saas-Fee Advanced Course*, volume 43 of *Saas-Fee Advanced Course*, page 85, January 2016. doi: 10.1007/978-3-662-47890-5_2.
- Jin Koda, Nick Scoville, Tsuyoshi Sawada, Misty A. La Vigne, Stuart N. Vogel, Ashley E. Potts, John M. Carpenter, Stuartt A. Corder, Melvyn C. H. Wright, Stephen M. White, B. Ashley Zauderer, Jenny Patience, Anneila I. Sargent, Douglas C. J. Bock, David Hawkins, Mark Hodges, Athol Kembell, James W. Lamb, Richard L. Plambeck, Marc W. Pound, Stephen L. Scott, Peter Teuben, and David P. Woody. Dynamically Driven Evolution of the Interstellar Medium in M51. *ApJ*, 700(2):L132–L136, August 2009. doi: 10.1088/0004-637X/700/2/L132.
- Shuo Kong, Jonathan C. Tan, Paola Caselli, Francesco Fontani, Thushara Pillai, Michael J. Butler, Yoshito Shimajiri, Fumitaka Nakamura, and Takeshi Sakai. The Deuterium Fraction in Massive Starless Cores and Dynamical Implications. *ApJ*, 821(2):94, April 2016. doi: 10.3847/0004-637X/821/2/94.
- Lukas Konstandin, Christoph Federrath, Ralf S. Klessen, and Wolfram Schmidt. Statistical properties of supersonic turbulence in the Lagrangian and Eulerian frameworks. *Journal of Fluid Mechanics*, 692:183–206, February 2012. doi: 10.1017/jfm.2011.503.
- C. Kramer, J. Alves, C. J. Lada, E. A. Lada, A. Sievers, H. Ungerechts, and C. M. Walmsley. Depletion of CO in a cold dense cloud core of IC 5146. *A&A*, 342:257–270, February 1999.
- Mark R. Krumholz. Notes on Star Formation. *arXiv e-prints*, art. arXiv:1511.03457, November 2015. doi: 10.48550/arXiv.1511.03457.
- Mark R. Krumholz and Christopher D. Matzner. The Dynamics of Radiation-pressure-dominated H II Regions. *ApJ*, 703(2):1352–1362, October 2009. doi: 10.1088/0004-637X/703/2/1352.

- Bastian Körtgen, Stefano Bovino, Dominik R. G. Schleicher, Andrea Giannetti, and Robi Banerjee. Deuterium fractionation and H₂D⁺ evolution in turbulent and magnetized cloud cores. *MNRAS*, 469(3):2602–2625, August 2017. ISSN 0035-8711, 1365-2966. doi: 10.1093/mnras/stx1005. URL <http://arxiv.org/abs/1703.01201>. arXiv: 1703.01201.
- Lev Davidovich Landau and E. M. Lifshitz. *Fluid mechanics*. 1959.
- Tod R. Lauer, Marc Postman, Harold A. Weaver, John R. Spencer, S. Alan Stern, Marc W. Buie, Daniel D. Durda, Carey M. Lisse, A. R. Poppe, Richard P. Binzel, Daniel T. Britt, Bonnie J. Buratti, Andrew F. Cheng, W. M. Grundy, Mihaly Horányi, J. J. Kavelaars, Ivan R. Linscott, William B. McKinnon, Jeffrey M. Moore, J. I. Núñez, Catherine B. Olkin, Joel W. Parker, Simon B. Porter, Dennis C. Reuter, Stuart J. Robbins, Paul Schenk, Mark R. Showalter, Kelsi N. Singer, Anne J. Verbiscer, and Leslie A. Young. New Horizons Observations of the Cosmic Optical Background. *ApJ*, 906(2):77, January 2021. doi: 10.3847/1538-4357/abc881.
- H. H. Lee, E. Herbst, G. Pineau des Forets, E. Roueff, and J. Le Bourlot. Photodissociation of H₂ and CO and time dependent chemistry in inhomogeneous interstellar clouds. *A&A*, 311:690–707, July 1996.
- C. M. Leung. Radiation transport in dense interstellar dust clouds. *ApJ*, 199:340–360, July 1975. doi: 10.1086/153697.
- Di Li, Duo Xu, Carl Heiles, Zhichen Pan, and Ningyu Tang. Quantifying Dark Gas. *arXiv:1503.02496 [astro-ph]*, March 2015. URL <http://arxiv.org/abs/1503.02496>. arXiv: 1503.02496.
- Di Li, Ningyu Tang, Hiep Nguyen, J. R. Dawson, Carl Heiles, Duo Xu, Zhichen Pan, Paul F. Goldsmith, Steven J. Gibson, Claire E. Murray, Tim Robishaw, N. M. McClure-Griffiths, John Dickey, Jorge Pineda, Snežana Stanimirović, L. Bronfman, Thomas Troland, and The PRIMO Collaboration. Where is OH and Does It Trace the Dark Molecular Gas (DMG)? *ApJS*, 235(1):1, February 2018. ISSN 1538-4365. doi: 10.3847/1538-4365/aaa762. URL <https://iopscience.iop.org/article/10.3847/1538-4365/aaa762>.
- Qi Li, Desika Narayanan, Romeel Davè, and Mark R. Krumholz. Dark Molecular Gas in Simulations of $z \sim 0$ Disk Galaxies. *ApJ*, 869(1):73, December 2018. doi: 10.3847/1538-4357/aaec77.
- H. Liszt and R. Lucas. Galactic OH absorption and emission toward a sample of compact extragalactic mm-wave continuum sources. *A&A*, 314:917–926, October 1996.
- R. Lohner. An adaptive finite element scheme for transient problems in CFD. *Computer Methods in Applied Mechanics and Engineering*, 61(3):323–338, April 1987. doi: 10.1016/0045-7825(87)90098-3.
- Alessandro Lupi and Stefano Bovino. The [C ii]–SFR correlation in dwarf galaxies across cosmic time. *MNRAS*, 492(2):2818–2827, February 2020. ISSN 0035-8711, 1365-2966. doi: 10.1093/mnras/staa048. URL <https://academic.oup.com/mnras/article/492/2/2818/5700311>.
- Alessandro Lupi, Stefano Bovino, Pedro R Capelo, Marta Volonteri, and Joseph Silk. The natural emergence of the correlation between H₂ and star formation

- rate surface densities in galaxy simulations. *MNRAS*, 474(3):2884–2903, March 2018. ISSN 0035-8711, 1365-2966. doi: 10.1093/mnras/stx2874. URL <http://academic.oup.com/mnras/article/474/3/2884/4600559>.
- Mordecai-Mark Mac Low and Ralf S. Klessen. Control of star formation by supersonic turbulence. *Reviews of Modern Physics*, 76(1):125–194, January 2004. doi: 10.1103/RevModPhys.76.125.
- Jonathan Mackey, Stefanie Walch, Daniel Seifried, Simon C O Glover, Richard Wunsch, and Felix Aharonian. Non-equilibrium chemistry and destruction of CO by X-ray flares. *MNRAS*, 486:1094–1122, 2019. doi: 10.1093/mnras/stz902.
- Peter MacNeice, Kevin M. Olson, Clark Mobarry, Rosalinda de Fainchtein, and Charles Packer. PARAMESH: A parallel adaptive mesh refinement community toolkit. *Computer Physics Communications*, 126(3):330–354, 2000. ISSN 0010-4655. doi: [https://doi.org/10.1016/S0010-4655\(99\)00501-9](https://doi.org/10.1016/S0010-4655(99)00501-9). URL <https://www.sciencedirect.com/science/article/pii/S0010465599005019>.
- J. S. Mathis, W. Rumpl, and K. H. Nordsieck. The size distribution of interstellar grains. *ApJ*, 217:425–433, October 1977. doi: 10.1086/155591.
- Christopher D. Matzner. On the Role of Massive Stars in the Support and Destruction of Giant Molecular Clouds. *ApJ*, 566(1):302–314, February 2002. doi: 10.1086/338030.
- C. F. McKee and J. P. Ostriker. A theory of the interstellar medium: three components regulated by supernova explosions in an inhomogeneous substrate. *ApJ*, 218:148–169, November 1977. doi: 10.1086/155667.
- Christopher F. McKee and Eve C. Ostriker. Theory of Star Formation. *ARA&A*, 45(1):565–687, September 2007. doi: 10.1146/annurev.astro.45.051806.110602.
- E. J. Mierkiewicz, R. J. Reynolds, F. L. Roesler, J. M. Harlander, and K. P. Jaehnig. Detection of Diffuse Interstellar [O II] Emission from the Milky Way Using Spatial Heterodyne Spectroscopy. *ApJ*, 650(1):L63–L66, October 2006. doi: 10.1086/508745.
- S. Molinari, B. Swinyard, J. Bally, M. Barlow, J. P. Bernard, P. Martin, T. Moore, A. Noriega-Crespo, R. Plume, L. Testi, A. Zavagno, A. Abergel, B. Ali, L. Anderson, P. André, J. P. Baluteau, C. Battersby, M. T. Beltrán, M. Benedettini, N. Billot, J. Blommaert, S. Bontemps, F. Boulanger, J. Brand, C. Brunt, M. Burton, L. Calzolari, S. Carey, P. Caselli, R. Cesaroni, J. Cernicharo, S. Chakrabarti, A. Chrysostomou, M. Cohen, M. Compiegne, P. de Bernardis, G. de Gasperis, A. M. di Giorgio, D. Elia, F. Faustini, N. Flagey, Y. Fukui, G. A. Fuller, K. Ganga, P. Garcia-Lario, J. Glenn, P. F. Goldsmith, M. Griffin, M. Hoare, M. Huang, D. Ikhe-naode, C. Joblin, G. Joncas, M. Juvela, J. M. Kirk, G. Lagache, J. Z. Li, T. L. Lim, S. D. Lord, M. Marengo, D. J. Marshall, S. Masi, F. Massi, M. Matsuura, V. Minier, M. A. Miville-Deschênes, L. A. Montier, L. Morgan, F. Motte, J. C. Mottram, T. G. Müller, P. Natoli, J. Neves, L. Olmi, R. Paladini, D. Paradis, H. Parsons, N. Peretto, M. Pestalozzi, S. Pezzuto, F. Piacentini, L. Piazzo, D. Polychroni, M. Pomarès, C. C. Popescu, W. T. Reach, I. Ristorcelli, J. F. Robitaille, T. Robitaille, J. A. Rodón, A. Roy, P. Royer, D. Russeil, P. Saraceno, M. Sauvage, P. Schilke, E. Schisano, N. Schneider, F. Schuller, B. Schulz, B. Sibthorpe, H. A. Smith, M. D. Smith, L. Spinoglio, D. Stamatellos, F. Strafella, G. S. Stringfellow, E. Sturm,

- R. Taylor, M. A. Thompson, A. Traficante, R. J. Tuffs, G. Umana, L. Valenziano, R. Vavrek, M. Veneziani, S. Viti, C. Waelkens, D. Ward-Thompson, G. White, L. A. Wilcock, F. Wyrowski, H. W. Yorke, and Q. Zhang. Clouds, filaments, and protostars: The Herschel Hi-GAL Milky Way. *A&A*, 518:L100, July 2010. doi: 10.1051/0004-6361/201014659.
- Norman Murray. Star Formation Efficiencies and Lifetimes of Giant Molecular Clouds in the Milky Way. *ApJ*, 729(2):133, March 2011. doi: 10.1088/0004-637X/729/2/133.
- Thorsten Naab and Jeremiah P. Ostriker. Theoretical Challenges in Galaxy Formation. *ARA&A*, 55(1):59–109, August 2017. doi: 10.1146/annurev-astro-081913-040019.
- Takenori Nakano, Ryoichi Nishi, and Toyoharu Umebayashi. Mechanism of Magnetic Flux Loss in Molecular Clouds. *ApJ*, 573(1):199–214, July 2002. doi: 10.1086/340587.
- R. P. Nelson and W. D. Langer. The dynamics of low mass molecular clouds in external radiation fields. *ApJ*, 482:796–826, 1997. URL <https://iopscience.iop.org/article/10.1086/304167/pdf>.
- Richard P. Nelson and William D. Langer. On the Stability and Evolution of Isolated Bok Globules. *ApJ*, 524(2):923–946, October 1999. ISSN 0004-637X, 1538-4357. doi: 10.1086/307823. URL <https://iopscience.iop.org/article/10.1086/307823>.
- David A. Neufeld, Michael J. Kaufman, Paul F. Goldsmith, David J. Hollenbach, and René Plume. Submillimeter Wave Astronomy Satellite and Arecibo Observations of H₂O and OH in a Diffuse Cloud along the Line of Sight to W51. *ApJ*, 580(1): 278–284, November 2002. doi: 10.1086/343077.
- Fabrizio Nicastro, Smita Mathur, and Martin Elvis. Missing Baryons and the Warm-Hot Intergalactic Medium. *Science*, 319(5859):55, January 2008. doi: 10.1126/science.1151400.
- S Nikolic. HCO⁺ in dark molecular clouds. *Serbian Astro. J.*, 175:1–6, 2007. doi: 10.2298/SAJ0775001N.
- Laurent Pagani, Evelyne Roueff, and Pierre Lesaffre. Ortho-H₂ and the Age of Interstellar Dark Clouds. *ApJ*, 739(2):L35, October 2011. doi: 10.1088/2041-8205/739/2/L35.
- M. Panessa, D. Seifried, S. Walch, B. Gaches, A. Barnes, F. Bigiel, and L. Neumann. The Evolution of HCO⁺ in Molecular Clouds Using a Novel Chemical Post-processing Algorithm. *in prep.*, 2022.
- A. A. Penzias and R. W. Wilson. A Measurement of Excess Antenna Temperature at 4080 Mc/s. *ApJ*, 142:419–421, July 1965. doi: 10.1086/148307.
- Planck Collaboration, P. A. R. Ade, N. Aghanim, M. I. R. Alves, C. Armitage-Caplan, M. Arnaud, M. Ashdown, F. Atrio-Barandela, J. Aumont, H. Aussel, C. Baccigalupi, A. J. Banday, R. B. Barreiro, R. Barrena, M. Bartelmann, J. G. Bartlett, N. Bartolo, S. Basak, E. Battaner, R. Battye, K. Benabed, A. Benoît, A. Benoit-Lévy, J. P. Bernard, M. Bersanelli, B. Bertin-court, M. Bethermin, P. Bielewicz, I. Bikmaev, A. Blanchard, J. Bobin, J. J. Bock, H. Böhringer, A. Bonaldi, L. Bonavera, J. R. Bond,

- J. Borrill, F. R. Bouchet, F. Boulanger, H. Bourdin, J. W. Bowyer, M. Bridges, M. L. Brown, M. Bucher, R. Burenin, C. Burigana, R. C. Butler, E. Calabrese, B. Cappellini, J. F. Cardoso, R. Carr, P. Carvalho, M. Casale, G. Castex, A. Catalano, A. Challinor, A. Chamballu, R. R. Chary, X. Chen, H. C. Chiang, L. Y. Chiang, G. Chon, P. R. Christensen, E. Churazov, S. Church, M. Clements, D. L. Clements, S. Colombi, L. P. L. Colombo, C. Combet, B. Comis, F. Couchot, A. Coulais, B. P. Crill, M. Cruz, A. Curto, F. Cuttaia, A. Da Silva, H. Dahle, L. Danese, R. D. Davies, R. J. Davis, P. de Bernardis, A. de Rosa, G. de Zotti, T. Déchelette, J. Delabrouille, J. M. Delouis, J. Démoclès, F. X. Désert, J. Dick, C. Dickinson, J. M. Diego, K. Dolag, H. Dole, S. Donzelli, O. Doré, M. Douspis, A. Ducout, J. Dunkley, X. Dupac, G. Efstathiou, F. Elsner, T. A. Enßlin, H. K. Eriksen, O. Fabre, E. Falgarone, M. C. Falvella, Y. Fantaye, J. Fergusson, C. Filliard, F. Finelli, I. Flores-Cacho, S. Foley, O. Forni, P. Fosalba, M. Frailis, A. A. Fraisse, E. Franceschi, M. Freschi, S. Fromenteau, M. Frommert, T. C. Gaier, S. Galeotta, J. Gallegos, S. Galli, B. Gandolfo, K. Ganga, C. Gauthier, R. T. Génova-Santos, T. Ghosh, M. Giard, G. Giardino, M. Gilfanov, D. Girard, Y. Giraud-Héraud, E. Gjerløw, J. González-Nuevo, K. M. Górski, S. Gratton, A. Gregorio, A. Gruppuso, J. E. Gudmundsson, J. Haissinski, J. Hamann, F. K. Hansen, M. Hansen, D. Hanson, D. L. Harrison, A. Heavens, G. Helou, A. Hempel, S. Henrot-Versillé, C. Hernández-Monteagudo, D. Herranz, S. R. Hildebrandt, E. Hivon, S. Ho, M. Hobson, W. A. Holmes, A. Hornstrup, Z. Hou, W. Hovest, G. Huey, K. M. Huppenberger, G. Hurier, S. Ilić, A. H. Jaffe, T. R. Jaffe, J. Jasche, J. Jewell, W. C. Jones, M. Juvela, P. Kalberla, P. Kangaslahti, E. Keihänen, J. Kerp, R. Kesitalo, I. Khamitov, K. Kiiveri, J. Kim, T. S. Kisner, R. Kneissl, J. Knoche, L. Knox, M. Kunz, H. Kurki-Suonio, F. Lacasa, G. Lagache, A. Lähteenmäki, J. M. Lamarre, M. Langer, A. Lasenby, M. Lattanzi, R. J. Laureijs, A. Lavabre, C. R. Lawrence, M. Le Jeune, S. Leach, J. P. Leahy, R. Leonardi, J. León-Tavares, C. Leroy, J. Lesgourgues, A. Lewis, C. Li, A. Liddle, M. Liguori, P. B. Lilje, M. Linden-Vørnle, V. Lindholm, M. López-Caniego, S. Lowe, P. M. Lubin, J. F. Macías-Pérez, C. J. MacTavish, B. Maffei, G. Maggio, D. Maino, N. Mandolesi, A. Mangilli, A. Marcos-Caballero, D. Marinucci, M. Maris, F. Marleau, D. J. Marshall, P. G. Martin, E. Martínez-González, S. Masi, M. Massardi, S. Matarrese, T. Matsumura, F. Matthai, L. Maurin, P. Mazzotta, A. McDonald, J. D. McEwen, P. McGehee, S. Mei, P. R. Meinhold, A. Melchiorri, J. B. Melin, L. Mendes, E. Menegoni, A. Mennella, M. Migliaccio, K. Mikkelsen, M. Millea, R. Miniscalco, S. Mitra, M. A. Miville-Deschênes, D. Molinari, A. Moneti, L. Montier, G. Morgante, N. Morisset, D. Mortlock, A. Moss, D. Munshi, J. A. Murphy, P. Naselsky, F. Nati, P. Natoli, M. Negrello, N. P. H. Nesvadba, C. B. Netterfield, H. U. Nørgaard-Nielsen, C. North, F. Noviello, D. Novikov, I. Novikov, I. J. O'Dwyer, F. Orieux, S. Osborne, C. O'Sullivan, C. A. Oxborrow, F. Paci, L. Pagano, F. Pajot, R. Paladini, S. Pandolfi, D. Paoletti, B. Partidge, F. Pasian, G. Patanchon, P. Paykari, D. Pearson, T. J. Pearson, M. Peel, H. V. Peiris, O. Perdureau, L. Perotto, F. Perrotta, V. Pettorino, F. Piacentini, M. Piat, E. Pierpaoli, D. Pietrobon, S. Plaszczynski, P. Platania, D. Pogosyan, E. Pointecouteau, G. Polenta, N. Ponthieu, L. Popa, T. Poutanen, G. W. Pratt, G. Prézeau, S. Prunet, J. L. Puget, A. R. Pullen, J. P. Rachen, B. Racine, A. Rahlin, C. Räth, W. T. Reach, R. Rebolo, M. Reinecke, M. Remazeilles, C. Renault, A. Renzi, A. Riazuelo, S. Ricciardi, T. Riller, C. Ringeval, I. Ristorcelli, G. Robbers, G. Rocha, M. Roman, C. Rosset, M. Rossetti, G. Roudier, M. Rowan-Robinson, J. A. Rubiño-Martín, B. Ruiz-Granados, B. Rusholme, E. Salerno, M. Sandri, L. Sanselme, D. Santos, M. Savelainen, G. Savini, B. M. Schaefer, F. Schiavon, D. Scott, M. D. Seiffert,

- P. Serra, E. P. S. Shellard, K. Smith, G. F. Smoot, T. Souradeep, L. D. Spencer, J. L. Starck, V. Stolyarov, R. Stompor, R. Sudiwala, R. Sunyaev, F. Sureau, P. Sutter, D. Sutton, A. S. Suur-Uski, J. F. Sygnet, J. A. Tauber, D. Tavagnacco, D. Taylor, L. Terenzi, D. Texier, L. Toffolatti, M. Tomasi, J. P. Torre, M. Tristram, M. Tucci, J. Tuovinen, M. Türlér, M. Tuttlebee, G. Umana, L. Valenziano, J. Valiviita, B. Van Tent, J. Varis, L. Vibert, M. Viel, P. Vielva, F. Villa, N. Vittorio, L. A. Wade, B. D. Wandelt, C. Watson, R. Watson, I. K. Wehus, N. Welikala, J. Weller, M. White, S. D. M. White, A. Wilkinson, B. Winkel, J. Q. Xia, D. Yvon, A. Zacchei, J. P. Zibin, and A. Zonca. Planck 2013 results. I. Overview of products and scientific results. *A&A*, 571:A1, November 2014. doi: 10.1051/0004-6361/201321529.
- William H. Press, Saul A. Teukolsky, William T. Vetterling, and Brian P. Flannery. *Numerical recipes in FORTRAN. The art of scientific computing*. 1992.
- Daniel J. Price and Christoph Federrath. A comparison between grid and particle methods on the statistics of driven, supersonic, isothermal turbulence. *MNRAS*, 406(3):1659–1674, August 2010. doi: 10.1111/j.1365-2966.2010.16810.x.
- J. Puls, R. P. Kudritzki, A. Herrero, A. W. A. Pauldrach, S. M. Haser, D. J. Lennon, R. Gabler, S. A. Voels, J. M. Vilchez, S. Wachter, and A. Feldmeier. O-star mass-loss and wind momentum rates in the Galaxy and the Magellanic Clouds Observations and theoretical predictions. *A&A*, 305:171, January 1996.
- R. J. Reynolds. The Column Density and Scale Height of Free Electrons in the Galactic Disk. *ApJ*, 339:L29, April 1989. doi: 10.1086/185412.
- R. J. Reynolds, F. Scherb, and F. L. Roesler. Observations of Diffuse Galactic HA and [n II] Emission. *ApJ*, 185:869–876, November 1973. doi: 10.1086/152461.
- A. J. Richings and Joop Schaye. The effects of metallicity, UV radiation and non-equilibrium chemistry in high-resolution simulations of galaxies. *MNRAS*, 458(1):270–292, May 2016. ISSN 0035-8711, 1365-2966. doi: 10.1093/mnras/stw327. URL <https://academic.oup.com/mnras/article-lookup/doi/10.1093/mnras/stw327>.
- Julia Roman-Duval, James M. Jackson, Mark Heyer, Jill Rathborne, and Robert Simon. Physical Properties and Galactic Distribution of Molecular Clouds Identified in the Galactic Ring Survey. *ApJ*, 723(1):492–507, November 2010. doi: 10.1088/0004-637X/723/1/492.
- Daniel R. Rybarczyk, Munan Gong, Snezana Stanimirovic, Brian Babler, Claire E. Murray, Jan Martin Winters, Gan Luo, T. M. Dame, and Lucille Steffes. The role of neutral hydrogen in setting the abundances of molecular species in the Milky Way’s diffuse interstellar medium. II. Comparison between observations and theoretical models. *arXiv:2112.05767 [astro-ph]*, December 2021. URL <http://arxiv.org/abs/2112.05767>. arXiv: 2112.05767.
- M Röllig, N P Abel, T Bell, F Bensch, J Black, G J Ferland, B Jonkheid, I Kamp, M J Kaufman, J Le Bourlot, F Le Petit, R Meijerink, O Morata, V Ossenkopf, E Roue, A Sternberg, and J Stutzki. A photon dominated region code comparison study. *A&A*, 467:187–206, 2007. doi: 10.1051/0004-6361:20065918.
- Laura V. Sales, Federico Marinacci, Volker Springel, and Margarita Petkova. Stellar feedback by radiation pressure and photoionization. *MNRAS*, 439(3):2990–3006, April 2014. doi: 10.1093/mnras/stu155.

- Dominik R. G. Schleicher, Stefano Bovino, Muhammad A. Latif, Andrea Ferrara, and Tommaso Grassi. The chemical evolution of self-gravitating primordial disks. *A&A*, 585:A11, January 2016. doi: 10.1051/0004-6361/201526356.
- Maarten Schmidt. The Rate of Star Formation. *ApJ*, 129:243, March 1959. doi: 10.1086/146614.
- N. Z. Scoville and K. Hersh. Collisional growth of giant molecular clouds. *ApJ*, 229: 578–582, April 1979. doi: 10.1086/156991.
- D. Seifried and S. Walch. The impact of turbulence and magnetic field orientation on star-forming filaments. *MNRAS*, 452(3):2410–2422, September 2015. ISSN 0035-8711, 1365-2966. doi: 10.1093/mnras/stv1458. URL <https://academic.oup.com/mnras/article-lookup/doi/10.1093/mnras/stv1458>.
- D. Seifried and S. Walch. Modelling the chemistry of star-forming filaments – I. H₂ and CO chemistry. *MNRAS*, 459(1):L11–L15, June 2016. ISSN 1745-3925, 1745-3933. doi: 10.1093/mnrasl/slz035. URL <https://academic.oup.com/mnrasl/article-lookup/doi/10.1093/mnrasl/slz035>.
- D. Seifried, Á. Sánchez-Monge, S. Suri, and S. Walch. Modelling the chemistry of star-forming filaments – II. Testing filament characteristics with synthetic observations. *MNRAS*, 467(4):4467–4483, June 2017a. ISSN 0035-8711, 1365-2966. doi: 10.1093/mnras/stx399. URL <https://academic.oup.com/mnras/article-lookup/doi/10.1093/mnras/stx399>.
- D Seifried, S Walch, P Girichidis, T Naab, R Wunsch, R S Klessen, S C O Glover, T Peters, and P Clark. SILCC-Zoom: the dynamic and chemical evolution of molecular clouds. *MNRAS*, 472:4797–4818, 2017b. doi: 10.1093/mnras/stx2343.
- D Seifried, S Haid, S Walch, E M A Borchert, and T G Bisbas. SILCC-Zoom: H₂ and CO-dark gas in molecular clouds – the impact of feedback and magnetic fields. *MNRAS*, 492(1):1465–1483, February 2020. ISSN 0035-8711, 1365-2966. doi: 10.1093/mnras/stz3563. URL <https://academic.oup.com/mnras/article/492/1/1465/5681413>.
- D. Seifried, H. Beuther, S. Walch, J. Syed, J. D. Soler, P. Girichidis, and R. Wünsch. On the accuracy of HI observations in molecular clouds – More cold HI than thought? *arXiv:2109.10917 [astro-ph]*, October 2021. URL <http://arxiv.org/abs/2109.10917>. arXiv: 2109.10917.
- Kenneth R. Sembach, J. Christopher Howk, Robert S. I. Ryans, and Francis P. Keenan. Modeling the Warm Ionized Interstellar Medium and Its Impact on Elemental Abundance Studies. *ApJ*, 528(1):310–324, January 2000. doi: 10.1086/308173.
- O. Sipilä, P. Caselli, and J. Harju. Benchmarking spin-state chemistry in starless core models. *A&A*, 578:A55, June 2015a. doi: 10.1051/0004-6361/201424364.
- O. Sipilä, J. Harju, P. Caselli, and S. Schlemmer. Spin-state chemistry of deuterated ammonia. *A&A*, 581:A122, September 2015b. doi: 10.1051/0004-6361/201526468.
- O. Sipilä, P. Caselli, and V. Taquet. Effect of multilayer ice chemistry on gas-phase deuteration in starless cores. *A&A*, 591:A9, June 2016. doi: 10.1051/0004-6361/201628272.

- O. Sipilä, P. Caselli, and J. Harju. Modeling deuterium chemistry in starless cores: full scrambling versus proton hop. *A&A*, 631:A63, November 2019. doi: 10.1051/0004-6361/201936416.
- Rowan J. Smith, Simon C. O. Glover, Paul C. Clark, Ralf S. Klessen, and Volker Springel. CO-dark gas and molecular filaments in Milky Way-type galaxies. *MNRAS*, 441(2):1628–1645, June 2014. ISSN 1365-2966, 0035-8711. doi: 10.1093/mnras/stu616. URL <http://academic.oup.com/mnras/article/441/2/1628/1065660/C0dark-gas-and-molecular-filaments-in-Milky>.
- P. M. Solomon, A. R. Rivolo, J. Barrett, and A. Yahil. Mass, Luminosity, and Line Width Relations of Galactic Molecular Clouds. *ApJ*, 319:730, August 1987. doi: 10.1086/165493.
- Lyman Spitzer. *Physical processes in the interstellar medium*. 1978. doi: 10.1002/9783527617722.
- Steven W. Stahler and Francesco Palla. *The Formation of Stars*. 2004.
- A. Sternberg and A. Dalgarno. Chemistry in Dense Photon-dominated Regions. *ApJS*, 99:565, August 1995. doi: 10.1086/192198.
- Bengt Strömgren. The Physical State of Interstellar Hydrogen. *ApJ*, 89:526, May 1939. doi: 10.1086/144074.
- Ralph S. Sutherland and M. A. Dopita. Cooling Functions for Low-Density Astrophysical Plasmas. *ApJS*, 88:253, September 1993. doi: 10.1086/191823.
- P. Swings and L. Rosenfeld. Considerations Regarding Interstellar Molecules. *ApJ*, 86:483–486, November 1937. doi: 10.1086/143880.
- R. Teague, D. Semenov, S. Guilloteau, Th. Henning, A. Dutrey, V. Wakelam, E. Chapillon, and V. Pietu. Chemistry in disks: IX. Observations and modelling of HCO⁺ and DCO⁺ in DM Tauri*. *A&A*, 574:A137, February 2015. ISSN 0004-6361, 1432-0746. doi: 10.1051/0004-6361/201425268. URL <http://www.aanda.org/10.1051/0004-6361/201425268>.
- Max Tegmark, Joseph Silk, Martin J. Rees, Alain Blanchard, Tom Abel, and Francesco Palla. How Small Were the First Cosmological Objects? *ApJ*, 474:1, January 1997. doi: 10.1086/303434.
- A. G. G. M. Tielens. *The Physics and Chemistry of the Interstellar Medium*. 2005.
- Thomas H. Troland and Richard M. Crutcher. Magnetic Fields in Dark Cloud Cores: Arecibo OH Zeeman Observations. *ApJ*, 680(1):457–465, June 2008. doi: 10.1086/587546.
- J. Kelly Truelove, Richard I. Klein, Christopher F. McKee, II Holliman, John H., Louis H. Howell, and Jeffrey A. Greenough. The Jeans Condition: A New Constraint on Spatial Resolution in Simulations of Isothermal Self-gravitational Hydrodynamics. *ApJ*, 489(2):L179–L183, November 1997. doi: 10.1086/310975.
- William D. Vacca, Catharine D. Garmany, and J. Michael Shull. The Lyman-Continuum Fluxes and Stellar Parameters of O and Early B-Type Stars. *ApJ*, 460:914, April 1996. doi: 10.1086/177020.

- Valeska Valdivia, Patrick Hennebelle, Maryvonne Gérin, and Pierre Lesaffre. H₂ distribution during the formation of multiphase molecular clouds. *A&A*, 587: A76, March 2016. ISSN 0004-6361, 1432-0746. doi: 10.1051/0004-6361/201527325. URL <http://www.aanda.org/10.1051/0004-6361/201527325>.
- E. F. van Dishoeck and J. H. Black. The Photodissociation and Chemistry of Interstellar CO. *ApJ*, 334:771–802, November 1988. URL <http://articles.adsabs.harvard.edu/pdf/1988ApJ...334..771V>.
- Ewine F. van Dishoeck and Geoffrey A. Blake. Chemical Evolution of Star-Forming Regions. *ARA&A*, 36:317–368, January 1998. doi: 10.1146/annurev.astro.36.1.317.
- Enrique Vázquez-Semadeni, Adriana Gazol, and John Scalo. Is Thermal Instability Significant in Turbulent Galactic Gas? *ApJ*, 540(1):271–285, September 2000. doi: 10.1086/309318.
- Enrique Vázquez-Semadeni, Aina Palau, Javier Ballesteros-Paredes, Gilberto C. Gómez, and Manuel Zamora-Avilés. Global hierarchical collapse in molecular clouds. Towards a comprehensive scenario. *MNRAS*, 490(3):3061–3097, December 2019. doi: 10.1093/mnras/stz2736.
- Knut Waagan, Christoph Federrath, and Christian Klingenberg. A robust numerical scheme for highly compressible magnetohydrodynamics: Nonlinear stability, implementation and tests. *J. Comput. Phys.*, 230:3331–3351, 2011.
- S Walch, P Girichidis, T Naab, A Gatto, S C O Glover, R Wunsch, R S Klessen, P C Clark, T Peters, D Derigs, and C Baczynski. The SILCC (Simulating the LifeCycle of molecular Clouds) project – I. Chemical evolution of the supernova-driven ISM. *MNRAS*, 454:238–268, 2015. doi: 10.1093/mnras/stv1975.
- Peter G. Wannier, B. G. Andersson, S. R. Federman, B. M. Lewis, Y. P. Viala, and E. Shaya. Warm Neutral Halos around Molecular Clouds. V. OH (1665 and 1667 MHz) Observations. *ApJ*, 407:163, April 1993. doi: 10.1086/172502.
- Mark Wardle. Star Formation and the Hall Effect. *Ap&SS*, 292(1):317–323, August 2004. doi: 10.1023/B:ASTR.0000045033.80068.1f.
- Joseph C. Weingartner and B. T. Draine. Dust Grain-Size Distributions and Extinction in the Milky Way, Large Magellanic Cloud, and Small Magellanic Cloud. *ApJ*, 548(1):296–309, February 2001. doi: 10.1086/318651.
- S. Weinreb, A. H. Barrett, M. L. Meeks, and J. C. Henry. Radio Observations of OH in the Interstellar Medium. *Nature*, 200(4909):829–831, November 1963. doi: 10.1038/200829a0.
- M. G. Wolfire, D. Hollenbach, C. F. McKee, A. G. G. M. Tielens, and E. L. O. Bakes. The Neutral Atomic Phases of the Interstellar Medium. *ApJ*, 443:152, April 1995. doi: 10.1086/175510.
- Mark G. Wolfire, Christopher F. McKee, David Hollenbach, and A. G. G. M. Tielens. Neutral Atomic Phases of the Interstellar Medium in the Galaxy. *ApJ*, 587(1): 278–311, April 2003. doi: 10.1086/368016.
- Mark G Wolfire, David Hollenbach, and Christopher F McKee. The dark molecular gas. *ApJ*, 716(2):1191–1207, 2010. doi: 10.1088/0004-637X/716/2/1191.

- Richard Wünsch, Sergiy Silich, Jan Palouš, Guillermo Tenorio-Tagle, and Casiana Muñoz-Tuñón. Evolution of Super Star Cluster Winds with Strong Cooling. *ApJ*, 740(2):75, October 2011. doi: 10.1088/0004-637X/740/2/75.
- R Wünsch, S Walch, F Dinnbier, and A Whitworth. Tree-based solvers for adaptive mesh refinement code flash – I: gravity and optical depths. *MNRAS*, 475(3):3393–3418, April 2018. ISSN 0035-8711, 1365-2966. doi: 10.1093/mnras/sty015. URL <https://academic.oup.com/mnras/article/475/3/3393/4795314>.
- Duo Xu, Di Li, Nannan Yue, and Paul F. Goldsmith. Evolution of OH and CO-dark molecular gas fraction across a molecular cloud boundary in Taurus. *ApJ*, 819(1):22, February 2016. ISSN 1538-4357. doi: 10.3847/0004-637X/819/1/22. URL <https://iopscience.iop.org/article/10.3847/0004-637X/819/1/22>.
- Yang Yang, Zhibo Jiang, Zhiwei Chen, Yiping Ao, and Shuling Yu. In Search of Infall Motion in Molecular Clumps. III. HCO⁺ (1-0) and H¹³CO⁺ (1-0) Mapping Observations toward Confirmed Infall Sources. *ApJ*, 922(2):144, December 2021. doi: 10.3847/1538-4357/ac22ab.
- B. Zuckerman and II Evans, N. J. Models of Massive Molecular Clouds. *ApJ*, 192:L149, September 1974. doi: 10.1086/181613.

DATA AVAILABILITY

All data and code routines used in this thesis can be made available upon request to the relevant authors:

- **Post-processed tracer histories, snapshots, reconstructed grids, column density projections, and all numeric code described in Appendix A.** Produced by me, reported upon in Paper I ([Panessa et al., 2022](#)) and Paper II (Panessa, 2023 in prep.), and shareable upon request. 1st. Physics Institute, University of Cologne.
- **SILCC-Zoom simulations and tracers.** The pure HD simulations originate in [Seifried et al. \(2017b\)](#), and the MHD simulations in [Seifried et al. \(2020\)](#). Both sets of simulations were rerun using updates as reported in [Seifried et al. \(2021\)](#). 1st. Physics Institute, University of Cologne.
- **HCO⁺ column density observations.** Intensity maps of HCO⁺ are reported in [Barnes et al. \(2020\)](#) (and see also [Kauffmann et al., 2017](#)), and processed to their column density form by Neumann et al. (in prep). Argelander Institute for Astronomy, University of Bonn.
- **Deuterated chemical networks.** The networks described in Chapter 7 were compiled initially by Olli Sipilä of the Max Planck Institute for Extraterrestrial Physics, in consultation with Daniel Seifried and myself in November 2019.

ACKNOWLEDGEMENTS

Nobody who works on a project as big as earning a PhD does it alone. I owe a debt of gratitude to everyone who's supported me through this seemingly endless journey, as it finally comes to a close.

First, I offer sincere thanks to my supervisor, Dr. Daniel Seifried. His dedication to cultivating the skills of his supervisees is matched only by his commitment to strong and novel science. The insights developed in this thesis, and in the publications it contains, would not have been possible without his consistent availability and generosity. Prof. Dr. Stefanie Walch-Gassner taught me a great deal about academic leadership. Thanks are also due to Prof. Dr. Peter Schilke, for his advice as a member of my TAC, and to Prof. Dr. Dennis Mücher, for chairing my thesis committee.

Working at home through quarantine was a challenging experience. I did not realize how much I enjoyed spending my workdays with my officemates and colleagues until I couldn't anymore, and I'm grateful to be back with them daily as my doctoral work concludes. In particular, I want to thank Shashwata Ganguly and Nassim Tanha for their support and friendship.

The support of my friends and family has been a constant through my PhD, and any list of those to whom I am grateful would be incomplete: John and Lynn Pullan, for their acceptance, hospitality, and advice; Monica and George Woodard, for always being there over the last thirteen years no matter how our families grew and changed or where we moved; Caitlin and Cadence Loria, for always being a joy whenever we visit each other; Barbara Ellynes Zucchi Nobre Silva and Tommaso Frassetto, for feeling like family no matter how much time passes or how many plans fall through; and Ceren Çevik and Xingzhe Zhou for validation and encouragement, and a steady supply of cats.

But most of all, I know I'd never have succeeded without the unflagging love, support, and patience of my partner, Danielle Pullan. Through all the challenges of these past four years, she's always believed in me and what I could achieve. Here's to many more years of shared adventures, learning, delicious food, and growth together.

Erklärung zur Dissertation
gemäß der Promotionsordnung vom 12. März 2020

Diese Erklärung muss in der Dissertation enthalten sein.
(This version must be included in the doctoral thesis)

„Hiermit versichere ich an Eides statt, dass ich die vorliegende Dissertation selbstständig und ohne die Benutzung anderer als der angegebenen Hilfsmittel und Literatur angefertigt habe. Alle Stellen, die wörtlich oder sinngemäß aus veröffentlichten und nicht veröffentlichten Werken dem Wortlaut oder dem Sinn nach entnommen wurden, sind als solche kenntlich gemacht. Ich versichere an Eides statt, dass diese Dissertation noch keiner anderen Fakultät oder Universität zur Prüfung vorgelegen hat; dass sie - abgesehen von unten angegebenen Teilpublikationen und eingebundenen Artikeln und Manuskripten - noch nicht veröffentlicht worden ist sowie, dass ich eine Veröffentlichung der Dissertation vor Abschluss der Promotion nicht ohne Genehmigung des Promotionsausschusses vornehmen werde. Die Bestimmungen dieser Ordnung sind mir bekannt. Darüber hinaus erkläre ich hiermit, dass ich die Ordnung zur Sicherung guter wissenschaftlicher Praxis und zum Umgang mit wissenschaftlichem Fehlverhalten der Universität zu Köln gelesen und sie bei der Durchführung der Dissertation zugrundeliegenden Arbeiten und der schriftlich verfassten Dissertation beachtet habe und verpflichte mich hiermit, die dort genannten Vorgaben bei allen wissenschaftlichen Tätigkeiten zu beachten und umzusetzen. Ich versichere, dass die eingereichte elektronische Fassung der eingereichten Druckfassung vollständig entspricht.“

Teilpublikationen:

The evolution of HCO⁺ in molecular clouds using a novel chemical post-processing algorithm
Panessa et al. 2022, submitted to MNRAS

Tracing dark molecular gas in simulated clouds using post-processed non-equilibrium OH abundance
Panessa et al. 2023, in prep.

Datum, Name und Unterschrift

27.01.2023

Marco Panessa



Marco Panessa

PhD Researcher | Adjunct Instructor | Tutor | Science Fiction Author
marco.panessa@gmail.com - marcopanessa.com - Located in Cologne, Germany

Education

Universität zu Köln, Cologne, Germany

Doctoral Researcher since April 2019.

Catholic University of America, Washington, DC, USA

M.S. in Physics received May 2015. One year of PhD research completed.

Honors: Knights of Columbus Fellowship, awarded to top two GRE scorers of CUA's incoming graduate students

American University, Washington, DC, USA

B.S. in Physics received May 2013.

Honors: University Honors Program participant, Dean's List, Presidential Scholar.

University College London, London, UK

Study Abroad program, September 2011 – June 2012. Primary Department: Physics and Astronomy.



Scientific Writing

"The Evolution of HCO^+ in Molecular Clouds Using a Novel Chemical Post-Processing Algorithm"

- Authors: Marco Panessa, Daniel Seifried, Stefanie Walch, Brandt Gaches, Ashley Barnes, Frank Bigiel, and Lukas Neumann
- Submitted MNRAS October 2022

"Tracing Dark Molecular Gas in Simulated Clouds Using Post-Processed Non-Equilibrium OH Abundance"

- Authors: Marco Panessa, Daniel Seifried, and Stefanie Walch
- 2023, in prep.

"A Novel Technique for Modeling Non-Equilibrium Astrochemistry in Simulated Molecular Clouds"

- Doctoral thesis, 2023

Research Projects

Deuteration in molecular clouds: what advanced chemical tracers tell us about the lifetime of molecular clouds. *April 2019 – June 2023.*

- Doctoral research at University of Cologne Institute for Astrophysics (1. Physikalisches Institut). SFB 956/C6, Principal Investigator: Daniel Seifried.
- Developed, coded, and calibrated a novel chemical post-processing pipeline, in which tracer particles in 3D-MHD molecular cloud simulations are post-processed with KROME chemical analysis package using robust new chemical networks.

Symbiotic Flaring Variable Binary MWC 560. *April – August 2016.*

- Doctoral research in conjunction with Catholic University of America and NASA Goddard Space Flight Center Astrophysics Science Division. Collaborator: Fred Bruhweiler.
- Analyzed data collected by the International Ultraviolet Explorer satellite on binary system MWC 560, a unique example of a two-star system in outburst aimed at Earth.

High Energy X-ray Imaging Technology (HEXITEC). *September 2014 – March 2016.*

- Doctoral research at NASA Goddard Space Flight Center Heliophysics Science Division, HEXITEC project team. Principal Investigator: Steven Christe.
- Calibration and testing on small-pixel Cadmium Telluride detectors intended for later use on solar X-ray imaging missions.

Solar Aspect and Alignment System (SAAS). *August 2014.*

- Master's research with NASA Goddard Space Flight Center Heliophysics Science Division, Focusing Optics X-ray Solar Imager (FOXSI) mission. Collaborators: Steven Christe, Lindsay Glesener.
- Aligned and tested the solar alignment system used aboard the FOXSI-2 sounding rocket.

Statistical Analysis of Quasi-Periodic Pulsations in Solar Flares. *June – December 2012, September 2013 – August 2014.*

- Masters research and bachelors thesis, in conjunction with NASA Goddard Space Flight Center Heliophysics Science Division, Reuven Ramaty High Energy Solar Spectrographic Imager (RHESSI) Mission. Collaborator: Brian R. Dennis.
- Examined highly-energetic solar eruptive events for evidence of pulsation behavior in the delivery of energy into solar flares during their impulsive phases.

Conference Presentations

Wheel of Star Formation, *September 12-16, 2022.* Prague, Czechia. Talk: "The Time-Dependent Evolution of Post-Processed OH and HCO⁺ in Molecular Clouds"

Astronomische Gesellschaft 2020 Annual Meeting, *September 21-25, 2020.* Online. Talk: "Investigating HCO⁺ and OH in 3D-MHD Simulations of Molecular Cloud Evolution"

American Geophysical Union 2015 Fall Meeting, *December 14-18, 2015.* San Francisco, CA, USA. Poster: "HEXITEC: A Next Generation Hard X-ray Detector for Solar Observations"

Teaching and Tutoring Experience

University Course	Role	Student Level	Times Taught
Astrophysics	Adjunct Instructor	Advanced Bachelors	2
Applied Calculus	Adjunct Instructor	Early Bachelors	1
Introductory Physics	Adjunct Instructor	Early Bachelors	1
Astronomy	Lab Instructor	Early Bachelors	8
	Teaching Assistant	Early Bachelors	4

Adjunct Instructor. **American University Department of Physics,** Washington, DC. *August 2015 – May 2018.*

- Lectured and developed syllabus, lesson plans, homework assignments, and exams for astrophysics, applied calculus, and introductory physics courses for bachelors students.

Graduate Record Examination (GRE) Tutor. **Griffon Preparation Services,** Washington, DC. *June 2016 – June 2018.*

- Taught Mathematics, Verbal Reasoning, and Analytical Writing skills and strategies to aspiring graduate students from a variety of educational, professional, and linguistic backgrounds in a classroom setting
- Tutored individuals seeking improvement in their GRE scores, applying a specialized lesson plan and pedagogical approach tailored to each student
- Assist in the refinement of the core curriculum by writing new lesson plans and material, testing problems for educational effectiveness, and recommending the difficulty level for homework in individual subjects

Self-employed **Tutor.** Washington, DC. *June 2013 – June 2018.*

- Subjects offered include: Standardized Tests (SAT, PSAT, SAT Subject Tests, AP Tests), Physics/Astronomy, Math, English/Writing, History, Introductory Computer Programming

Teaching Assistant. **American University Department of Physics,** Washington, DC. *August 2012 – July 2013.*

Creative Publications

"The Lone and Level Sands." Short story and accompanying podcast on [Escape Pod](#).

"TOP SECRET: The Union Station Hypersphere Incident." Short story on [Fantasy Scroll Magazine](#).

Computer Skills

Proficient in FORTRAN, Python, LaTeX, IDL, Arduino, C++, Wolfram Mathematica, HTML.

Languages

English: Native. German: A2. Italian: A1.